

Max-Planck-Institut für Astrophysik

On the Stability of Thermonuclear Flames in Type Ia Supernova Explosions

Friedrich Konrad Röpke

Vollständiger Abdruck der von der Fakultät für Physik der Technischen Universität München
zur Erlangung des akademischen Grades eines

Doktors der Naturwissenschaften

genehmigten Dissertation.

Vorsitzender: Univ.-Prof. Dr. L. Oberauer

Prüfer der Dissertation:

1. Hon.-Prof. Dr. W. Hillebrandt

2. Univ.-Prof. Dr. M. Lindner

Die Dissertation wurde am 3. 7. 2003 bei der Technischen Universität München eingereicht und durch die Fakultät für Physik am 24. 7. 2003 angenommen.

*The phenomenon of combustion exerts
a lifelong fascination over us.*

— Ya. B. Zel'dovich (1980)

Contents

1. Prologue	1
1.1. Observational facts on Type Ia supernovae	2
1.2. Astrophysical implications	3
1.2.1. Conclusions from the observations	3
1.2.2. Constraints for the astrophysical models	4
1.2.3. Possible progenitor scenarios	4
1.2.4. Pre-ignition evolution	6
1.2.5. Astrophysical relevance of Type Ia supernovae	7
1.3. Current status of Type Ia supernova research	8
1.4. Objectives of this work	10
1.5. Organization of the thesis	13
2. Theoretical Considerations	15
2.1. Reactive fluid dynamics	15
2.1.1. General form of a balance equation	16
2.1.2. The Euler equations	17
2.1.3. The Navier-Stokes equations	18
2.1.4. General reactive flow equations	18
2.1.5. Nondimensional representation of the general reactive flow equations	20
2.1.6. Source terms for nuclear reactions	21
2.2. Combustion theory	23
2.2.1. The discontinuity approximation of burning fronts and modes of propagation	23
2.2.2. Internal structure of detonation and deflagration waves	27
2.2.3. Laminar flames	30
2.2.4. Phenomenological description according to Markstein	31
2.2.5. Thermonuclear deflagration in C+O white dwarf matter	31
2.3. Flame instabilities	33
2.3.1. Linear stability analysis	34
2.3.2. Corollaries from the flame instabilities	40
2.4. Analytical studies of nonlinear flame propagation	44
2.4.1. Stability analysis after Zel'dovich	44
2.4.2. The Sivashinsky equation	44

Contents

2.4.3. Pole decomposition	45
2.5. Fractal descriptions of flame fronts	48
2.6. Turbulent combustion	50
2.6.1. Basic concepts of turbulence theory	51
2.6.2. Turbulent burning regimes and resulting length scales	52
2.6.3. Active turbulent combustion	54
2.7. Deflagration to detonation transition	54
3. Astrophysical background	57
3.1. Thermonuclear combustion in Type Ia Supernovae	57
3.1.1. Models for the explosion mechanism	57
3.1.2. Turbulent combustion in Type Ia supernova explosions	59
3.2. Hydrodynamical considerations	61
3.2.1. The equation of state for white dwarf matter	61
3.2.2. External forces: gravity	62
4. Numerical implementation	63
4.1. Fluid dynamics	64
4.1.1. Operator splitting	64
4.1.2. Discretization on a computational grid	65
4.1.3. Numerical solution of the Euler equations	65
4.1.4. Boundary conditions	68
4.1.5. Implementation of the hydrodynamics solver	69
4.2. Equation of state	69
4.3. Thermonuclear reactions	70
4.4. Flame model	70
4.4.1. The level-set technique	70
4.4.2. The G -equation	71
4.4.3. Re-initialization	72
4.5. Flame/flow coupling	72
4.5.1. Geometrical information	72
4.5.2. In-cell reconstruction	73
4.5.3. Flux-splitting	75
4.5.4. Treatment of the source terms	75
5. Results and discussion	79
5.1. Some verification tests of the implementation	79
5.2. Problems with the numerical implementation	82
5.3. Flame propagation into quiescent fuel	85
5.3.1. Passive vs. complete implementation	86
5.3.2. Simulation setup	87
5.3.3. General features of flame evolution	90
5.3.4. The linear regime of flame evolution	97

5.3.5.	The nonlinear regime of flame evolution	99
5.3.6.	Increase in flame surface and acceleration of the flame	99
5.3.7.	Influence of the initial flame shape and the boundary conditions	103
5.3.8.	Flame stability at different fuel densities	104
5.4.	Flame interaction with a vortical flow	109
5.4.1.	Simulation setup	109
5.4.2.	What can be expected?	111
5.4.3.	Simulation results	112
5.4.4.	A Parameter study	116
6.	Epilogue	127
6.1.	Conclusions	127
6.2.	Comparison with experiments	129
6.3.	Implications for SN Ia models	131
6.4.	Future work	132
A.	Derivation of the Sivashinsky equation for a hydrodynamical model of the flame	135
B.	Vectors of the general reactive flow equation	139
C.	Nomenclature	141
	Bibliography	145

1. Prologue

One evening, when, as usual, I was contemplating the heavenly dome whose face was so familiar to me, I saw with inexpressible astonishment a radiant star of extraordinary magnitude.

Struck with surprise, I could hardly believe my eyes. Its brightness was greater than that of Sirius, and Jupiter. It could only be compared with that of Venus. People gifted with good eyesight could see this star in daylight, even at noon.

— Tycho Brahe on the 1572 supernova encounter

Transient phenomena in the sky have attracted the attention of mankind for millennia and still today cosmic explosions pertain to the most fascinating objects of astrophysics. The observation of supernova explosions, which belong to the brightest astrophysical events, played an outstanding role in the history of astronomy. Ancient records provide observational data of astonishing accuracy, sometimes even allowing for the reconstruction of the light curve of historical supernovae (Stephenson & Green 2002, Green & Stephenson 2003). The dawn of modern European astronomy coincides with the systematic observation of two supernovae conducted by Tycho Brahe in 1572 (Brahe 1573) and by Johannes Kepler in 1604. The term *supernova* was introduced by Baade & Zwicky (1934) to distinguish these events from classical novae. Supernovae are astrophysical objects whose luminosity raises on timescales of a few days to weeks and then decreases over several years after reaching a peak luminosity up to $10^{42} - 10^{43} \text{ erg s}^{-1}$, equivalent to the luminosity of an entire galaxy. The overall energy release of supernova explosions amounts to 10^{51} to 10^{53} erg.

The observation of supernovae revealing Balmer lines in their near-maximum light spectra and others showing no signs of hydrogen led Minkowski (1941) to the suggestion of a classification of these events. The former class is termed Type II, while the latter is called Type I. Further spectroscopic and photometric features gave rise to a further sub-classification (e.g. Harkness & Wheeler 1990). This astronomical classification, however, does not reflect the astrophysical mechanism. Except for only one sub-class of Type I supernovae, namely the Type Ia events, all other types gain the explosion energy from the binding energy of a compact object that forms in the gravitational collapse of a massive star. This may occur after thermonuclear burning has ceased and the thermal pressure fails to stabilize it against collapse. Consequently, a Type II supernova gives rise to the formation of a neutron star or possibly even a black hole. In contrast to this scenario, Hoyle

1. Prologue

& Fowler (1960) suggested that Type Ia supernovae (abbreviated frequently as SN Ia in this text) originate from the thermonuclear explosion of a degenerate compact object, a white dwarf star. No compact object as a remnant of a SN Ia can be expected from this scenario. The observable light curve is believed to be powered by the decay energy of radioactive ^{56}Ni produced in the explosion (Truran et al. 1967, Colgate & McKee 1969). These assumptions define the astrophysical picture of SN Ia which is generally agreed on.

In the present work we shall investigate some aspects of the thermonuclear explosion mechanism of the white dwarf star.

1.1. Observational facts on Type Ia supernovae

The classification of SN Ia is based on spectroscopic features. Besides the absence of hydrogen absorption lines in the spectra defining them as Type I supernovae, the subclass Ia is characterized by the presence of strong silicon lines in the early and maximum light spectra.

One of the most intriguing features of Type Ia Supernovae is that most of them form a class of objects that is homogeneous in spectra, photometry, and absolute magnitude to a remarkable degree. These supernovae are frequently called “Branch normals” after the definition suggested by Branch et al. (1993). A prominent example is supernova SN 1994D. Nevertheless, even within this class detailed observations revealed subtle differences. However, a number of peculiar objects has been observed deviating considerably from Branch normals in their properties. We mention here in particular super-luminous (“1991T-like”) and sub-luminous (“1991bg-like”) objects. The peculiarity rate is not well-determined yet. Branch et al. (1993) estimate 15 % of all observed SNe Ia diverging from Branch normal type while recent observations suggest an even higher fraction of peculiar objects (Li et al. 2000).

A review on observational data is given by Leibundgut (2000). We will summarize here only the aspects that are most important for theoretical modeling and thereby neglect peculiarities.

Type Ia supernova rates

SN Ia frequencies carry important information on their progenitor systems and the explosion mechanism. However, the determination of reliable rates remains difficult. Cappellaro et al. (1997) report SN Ia rates as low as 1 event every 500 to 600 years for a galaxy with $10^{10} L_{B_{\odot}}$ (blue unit solar luminosity) assuming a Hubble constant of $65 \text{ km s}^{-1} \text{ Mpc}^{-1}$. In contrast to other supernova types, SN Ia occur in late and early type galaxies, but in the latter the frequency appears to be lower. They also show preference for star forming galaxies and spiral arms.

Spectral features

Apart from the absence of Hydrogen lines in the spectra of SN Ia, no Helium has been detected for most objects either. Near maximum light the spectra are dominated by P-Cygni lines of intermediate-mass elements, such as Si, Ca, Mg, and O, corresponding to the outer layers of the ejecta. Different expansion velocities for different spectra point to a layered structure of the outer shell. Typical velocities observed in the lines are between 1×10^9 and 1.5×10^9 cm s⁻¹. Low-ionization lines of Ni, Fe, and Co are present and increase after the peak, when the photosphere reaches the inner regions. One month after maximum the supernova enters the so-called nebular phase. Here the spectrum is dominated by forbidden FeII, FeIII, and CoIII lines¹.

Presently, efforts are taken to acquire a larger sample of UV and IR spectra. No appreciable polarization has been detected so far except for one object (Kasen et al. 2003, Wang et al. 2003). Attempts to detect γ -rays from the nuclear decay have not been successful with one exception (Diehl & Timmes 1998). Neither X-ray nor radio detections have been reported for SNe Ia.

Photometry

Light curves are taken with several filters. The first phase shows a rapid raise in luminosity at a timescale of about 20 days. Maxima appear at different times in different bands revealing a rapid color evolution at peak luminosity. In the *I* band and redder, most SN Ia show a second peak around 25 days after maximum. In the bluer bands a decline in luminosity of about 3 magnitudes in the weeks after maximum is observed. Finally, the SN enters an exponential decline of about one magnitude per month. From observations in separate bands, bolometric light curves can be constructed (e.g. Contardo et al. 2000). At maximum the luminosity reaches $M_B \approx M_V \approx -19.3$ mag (Riess et al. 1999) and $\log L_{\text{bol}} \approx 10^{43}$ erg s⁻¹ (Contardo et al. 2000).

Despite of the overall homogeneity of the SN Ia class, there exist small deviations in the peak luminosity even among Branch normal SNe. However, it has been noted that correlation between the peak magnitude and the decline rate of the light curve exists (Hamuy et al. 1996). The more luminous the supernovae, the broader is the light curve. Correlations can also be found between other observable features (e.g. Branch 1998). The class of SN Ia seems to be representable as a one-parameter sequence. Furthermore, the luminosity seems to depend on the environment. SN Ia in early type galaxies are generally fainter than in late types but the correlation between the light curve shape and the maximum luminosity still holds.

¹For a recent detailed survey of spectral features in the optical we refer to Filippenko (1997).

1.2. Astrophysical implications

1.2.1. Conclusions from the observations

From the observations the energetics of a SN Ia explosion can be inferred. Following the idea that the light curve is powered by the decay of ^{56}Ni over ^{56}Co to stable ^{56}Fe , measurement of the nickel mass would be a tool to test the explosion model. One way is to determine the bolometric peak luminosity and to apply “Arnett’s law” (Arnett 1982, Arnett et al. 1985). It states that the energy released at the surface at maximum luminosity is equal to the energy injected by nuclear decay at the bottom of the ejecta, the reason being that the atmosphere is turning optically thin at this point. Note, however, that this assumption does not generally apply if multi-dimensional effects play a significant role. The nickel masses for a number of objects were derived from the peak bolometric luminosity by Contardo et al. (2000) for a number of objects and lie typically around $\sim 0.6M_{\odot}$ for normal supernovae with a significant scatter.

1.2.2. Constraints for the astrophysical models

Several constraints for theoretical models result from the observations summarized above (cf. Hillebrandt & Niemeyer 2000). Obviously, the overall homogeneity of normal SNe Ia requires robustness of the explosion mechanism and does not allow dependence on fine-tuning of model parameters or initial conditions. A powerful explosion should result from the model, i.e. produce sufficient amounts of ^{56}Ni and high-velocity intermediate mass elements in the outer layers. In addition, the model should contain at least one parameter accounting for the intrinsic variability in explosion strength. The model should give rise to that parameter in a natural way. Moreover, the parameter has to be correlated with the progenitor system in order to explain the observed variations as a function of the host stellar population.

Some of these constraints apply directly to the explosion mechanism. Since the theoretical basis of the explosion will be established in Chapter 2, we will postpone that discussion to Section 3.1.1 and envisage here the consequences for the progenitor systems only.

1.2.3. Possible progenitor scenarios

The identification of the SN Ia progenitor is probably still one of the most uncertain components of the model. Nevertheless, from observations the following conclusions can be drawn: The occurrence of SNe Ia in old stellar population is a hint to relatively low-mass stars as progenitors. The spectral features point to a thermonuclear explosion of a rather compact object. The absence of hydrogen and to the greatest extent helium imply that the progenitor must have lost its envelope and the amount of circumstellar material is small. The failure to detect radio or X-ray emission from SN Ia disfavor a connection with a neutron star or a black hole.

These arguments leave low-mass electron-degenerate remnants of stellar evolution, so-called *white dwarfs* (WDs) as possible progenitor candidates. A single WD, however is

1.2. Astrophysical implications

an inert object and any dynamics necessary to trigger the explosion is missing. Therefore, a binary system with mass transfer onto a WD provides a promising progenitor scenario. Three chemical compositions of WDs come into consideration: WDs composed of helium, of carbon and oxygen (C+O WDs in the following), and of oxygen, neon and magnesium (O-Ne-Mg). The first composition will always produce nearly pure nickel when incinerated and is therefore not consistent with the observation of intermediate-mass elements in the spectra. Although O-Ne-Mg WDs show the tendency to collapse rather than to explode when ignited, they cannot be completely ruled out as a possible progenitor at least for some peculiar supernovae. However, there is general agreement that the majority of normal SNe Ia originates from thermonuclear explosions of C+O WDs, which we will focus on throughout this work.

The dynamics can be introduced by different scenarios: Depending on the nature of the binary companion of the WD, the models are called “single degenerate” if the companion is a main sequence star or a giant or “double degenerate” if the system consists of two WDs. For the first case, two classes of models are discerned. If the WD accretes matter until it reaches a limiting mass of $\sim 1.4M_{\odot}$, electron-degeneracy pressure cannot compensate gravity anymore. This mass is called Chandrasekhar mass M_{Ch} . When the WD reaches this mass, its central density increases rapidly while its heat capacity decreases. For masses too high, the WD will collapse to a neutron star, while otherwise the strongly temperature dependent thermonuclear reaction rates increase and a thermonuclear runaway is possible.

These so-called *Chandrasekhar-mass models* are particularly appealing, because the Chandrasekhar-mass limit provides a natural way to explain the homogeneity of SNe Ia. Hence they are the most promising scenario for Branch-normal SNe and will serve as the background for the studies presented in this work. However, the parameter space that allows the formation of a M_{Ch} progenitor is extremely narrow (cf. Figure 1.1) and observations enabling an estimation of the frequency of potential candidates are lacking. Usually, Supersoft X-ray sources are associated with binary systems capable of evolving toward a SN Ia (e.g. Livio 1996).

Sub-Chandrasekhar-mass models form the other single degenerate scenario. Here a WD below M_{Ch} accretes helium from the companion until a shell of $\sim 0.3M_{\odot}$ covers the C+O core. Reaching this mass, the helium will ignite near the interface and from a detonation wave. This detonation can then trigger C/O fusion in the WD. Whether or not this will in fact happen is not yet answered as well as the question at which location in the WD fusion will start eventually (Woosley & Weaver 1994, Livne & Arnett 1995, Benz 1997). The spectra produced by sub-Chandrasekhar-mass models are, however, not in good agreement with observations.

Double-degenerate scenarios were proposed by Webbink (1984) and Iben & Tutukov (1984). Numerical simulations show, that the less massive WD will be torn into a disk around its more massive companion (Benz et al. 1990, Mochkovitch & et al. 1997). At the boundary between core and disk thermonuclear reaction starts and propagates inward by incinerating the star into O-Ne-Mg (Nomoto & Iben 1985, Saio & Nomoto 1985). The resulting object collapses to a neutron star. It appears unlikely that this model can account for the normal SNe Ia.

1. Prologue

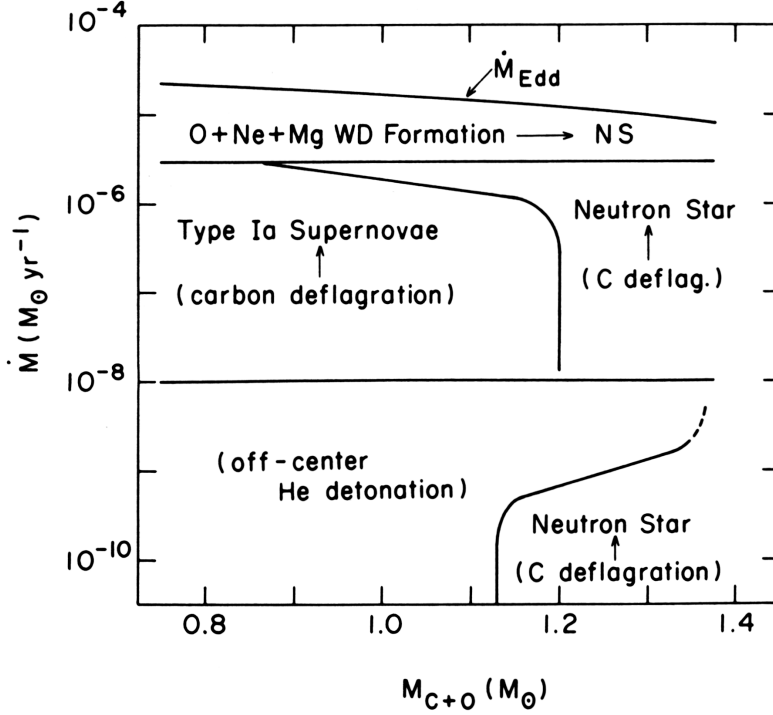


Figure 1.1.: The final fate of an accreting C+O WD expected depending on its initial mass M_{C+O} and accretion rate \dot{M} (from [Nomoto & Kondo 1991](#)).

The sub-Chandrasekhar-mass and the double-degenerate models both share the advantage that these systems are observed in sufficiently large numbers. However, in contrast to the M_{Ch} -models the homogeneity of the SNe Ia is not naturally inherent in both scenarios.

1.2.4. Pre-ignition evolution

The evolution toward ignition of the thermonuclear flame is one of the crucial points of the model. It determines the initial conditions for the explosion models. [Niemeyer et al. \(1996\)](#), [Reinecke et al. \(1999a\)](#), [Reinecke et al. \(2002b\)](#), and [Hillebrandt et al. \(2003\)](#) point out the sensitivity of the explosion energy (and eventually the nucleosynthetic yields) to possible off-center and multi-spot ignitions. However, the ignition conditions are not well-determined yet since numerical simulation of the pre-ignition phase is hampered by several factors, mainly the inherent multi-dimensionality and the wide range of timescales involved.

A review of the phase until flame ignition in M_{Ch} - models is given by [Hillebrandt & Niemeyer \(2000\)](#). As the white dwarf approaches the Chandrasekhar mass, two competing processes govern the energy budget near the core. These are plasmon neutrino losses and compressional heating. Above a central density of $\sim 2 \times 10^9 \text{ g cm}^{-3}$ the former become strongly suppressed ([Woosley & Weaver 1986](#)) while electron screening enhances the nu-

clear reactions. The core region enters the so-called “smoldering phase” marking the beginning of the thermonuclear runaway. Smoldering proceeds over about 1000 years. Convection due to internal heating takes place with progressively smaller turnover timescales. On the other hand, the time scale for thermonuclear burning drops even faster due to the strong temperature dependence of the reaction rates. A further complication is introduced by the action of the convective URCA process (introduced in this context by Paczyński 1972). However its effect on the evolution is discussed controversially. At a temperature of $T \approx 7 \times 10^8$ K the timescales of convection and nuclear reaction become comparable and the core enters the regime of strong reactive convection. At $T \approx 1.5 \times 10^9$ K the burning timescale becomes so small compared to the convective timescale, that a new equilibrium between energy generation and transport (now thermal conduction by degenerate electrons) establishes at much smaller length scales of $l \approx 10^{-4}$ cm. This marks the birth of a flame. A crude model of the pre-ignition phase by Garcia-Senz & Woosley (1995) suggests that the flame may ignite at the surface of burning bubbles that can rise some hundred kilometers from the center, giving support to the idea of off-center multi-spot ignition. On contrast, Höflich & Stein (2002) report on no indication of an off-center ignition. Instead, they claim that the flame starts out in a carbon-depleted centered region and find convective velocities that greatly exceed the expected flame propagation speed.

1.2.5. Astrophysical relevance of Type Ia supernovae

Type Ia supernovae have strong influence on their environment. Moreover, they can be used as tools for astrophysical and cosmological measurements.

Leibundgut (2000) refers to the following aspects illustrating the significance of SNe Ia: SN Ia are believed to be the main source of iron in the universe. The heating of the interstellar medium depends on the SN Ia rate of the corresponding galaxy. SNe Ia as explosions of WDs in binary systems can provide information on the binary fraction of stars and the evolution of binary systems in our Galaxy and as a function of look back time. They also play (together with other SN types) an important role during early galaxy formation and may influence the star formation process. Furthermore, they have been suggested as being responsible for substantial loss of material from galaxies. Note, that the suggestion of SNe Ia as significant source of metallicity sets a further constraint to the astrophysical models by requiring the nucleosynthesis to produce approximately solar isotopic abundances.

Cosmological distance measurements

The most spectacular application of Type Ia supernovae is certainly their use as cosmological distance indicators. Though variations in peak luminosity observed in nearby SNe confuted early claims that SNe Ia be “standard candles” (i.e. possess always exactly the same maximum brightness), the correlation between the light curve shape and the peak luminosity provides a handy tool to “standardize” them. Today it is agreed on the fact that SNe Ia are excellent distance indicators at high redshifts, owing to their enormous bright-

1. Prologue

ness. However, they still depend on the calibration of the nearby sample using Cepheid distances.

The most surprising result of cosmological SN Ia distance measurements is that supernovae at high redshifts appear to be dimmer than expected for a universe with $\Omega_\Lambda = 0$. From this, two independent research groups (Riess et al. 1998, Perlmutter et al. 1999) draw the conclusion that the universe is acceleratingly expanding. A possible interpretation is, that the supernova data (together with measurements of the Cosmic Microwave Background radiation, CMB) imply that we live in a universe dominated by “dark energy”. The cosmological parameters are determined by $\Omega_m = 0.3$ and $\Omega_\Lambda = 0.7$. A recent analysis of the presently available data from SN Ia measurements is provided by Tonry et al. (2003).

Of course, one could think of other explanations for the dimming of distant supernovae. Possible explanations are absorption by “grey dust”, attenuation by gravitational lensing, or evolutionary effects of SNe Ia depending for instance on the different metallicity of progenitors. These possibilities are reviewed by Leibundgut (2001). While the first two effects have to be investigated by astronomers, the study of a possible evolution of SNe Ia is a challenge to theoretical models and a motivation for currently ongoing efforts to improve numerical SN Ia simulations.

Another worrying fact is that the relation between light curve shape and peak luminosity, which forms the foundation of the application of SNe Ia as distance indicators, is of pure phenomenological nature and lacks theoretical reasoning so far. Moreover, the individual research groups apply different correction methods (see Leibundgut (2000) for a review). Drell et al. (2000) and Leibundgut (2000) point out differences between those corrections, although all corrections lead to a considerable improvement of the data in the nearby Hubble diagram.

These arguments call attention to the importance of a profound theoretical understanding of the SN Ia explosion mechanism as well as the progenitor scenario and the radiation transport.

1.3. Current status of Type Ia supernova research

To embed the present work in the currently ongoing investigation of SN Ia events, a brief overview of the current status of research shall be given in the following.² In doing so we will restrict ourselves to models of the explosion mechanism in the single degenerate M_{Ch} -scenario. We will omit the ongoing investigation of progenitor models and the light curve and spectra modeling. For a broader review we refer to Hillebrandt & Niemeyer (2000).

The ultimate goal of SN Ia models is the restriction to only basic physical principles as input, thereby reducing the number of free parameters. This will allow to deduce clear statements on the validation of cosmological interpretations of the distance measurements

²It is natural that some of the terms used in this section cannot be introduced in detail here and we refer to Chapters 2 and 3 for an exact description of these.

1.3. Current status of Type Ia supernova research

and provide insight into the (possibly substantial) contribution of SNe Ia to the nucleosynthetic evolution of the universe.

As will be discussed in Chapters 2 and 3 in detail, thermonuclear burning in SNe Ia proceeds in a spatially confined region which propagates as a wave through the star. This phenomenon will be called “flame” henceforth. Hydrodynamically, two distinct modes of propagation of that flame are permitted: a supersonic *detonation* and a subsonic *deflagration*. The fundamental parameter of all SN Ia models is the velocity by which the flame propagates through the material, since it determines both the energy release and the nucleosynthetic yield of the explosion. In the detonation mode the flame speed is fairly well known. It is essentially the speed of sound in the fuel. Enough energy is released to power a SN Ia explosion, but the nucleosynthesis of models applying pure detonations is inconsistent with observed spectra. Therefore, the currently favored scenario is, that the flame propagates in the subsonic deflagration mode, at least initially. The so-called *laminar* flame velocity under conditions prevailing in a C+O WD has been determined by one-dimensional numerical models (Timmes & Woosley 1992). These fully resolve the inner structure of the flame and apply a realistic nuclear reaction network to model thermonuclear burning. In the deflagration mode, however, instabilities and turbulent effects have drastic impact on the flame speed giving rise to an effective flame propagation velocity exceeding the laminar value by far. This results from the fact that the increase in flame surface by turbulent wrinkling is associated with an increase in the total energy release rate by the burning.

Due to the lack of sufficient computational power, numerical models of the first decades of supernova investigations were restricted to one dimension. This assumption of spherical geometry fell short of providing a self-consistent value of the flame speed since it neglected the inherent multidimensional effects of turbulence. Thus, the flame speed was treated as a free parameter in these models and tuned in a way that the model would agree with observed spectra. A prominent example of these class of models is W7 by Nomoto et al. (1984), which is still widely used as input for spectra and light curve modeling. Although these models can provide some insight to the needs of a viable self-consistent SN Ia model, they have low predictive power. Other one-dimensional models achieved good agreement with observations by imposing a transition of the flame propagation mode from deflagration to detonation at an arbitrarily chosen instant. Since the parameters of the one-dimensional models can be tuned to fit the observations, we will refer to that class in the following as *empirical SN Ia models*.

Contrasting to these, another class of models attempts to describe SN Ia explosions in a self-consistent way. From these models one can hope to ultimately get insight into possible evolution effects of distant supernovae and to understand the origin of the peak luminosity–light curve shape correlation. This has become possible with increasing computational capacity in the 1990s that made multidimensional models possible. A self-consistent determination of the effective flame propagation velocity from turbulent effects came into reach. However, multidimensional simulations suffer from a serious obstacle. Owing to the vast range of relevant length scales involved in the problem, it is impossible to resolve the full SN Ia event here. Therefore the task has to be tackled in different approaches

1. Prologue

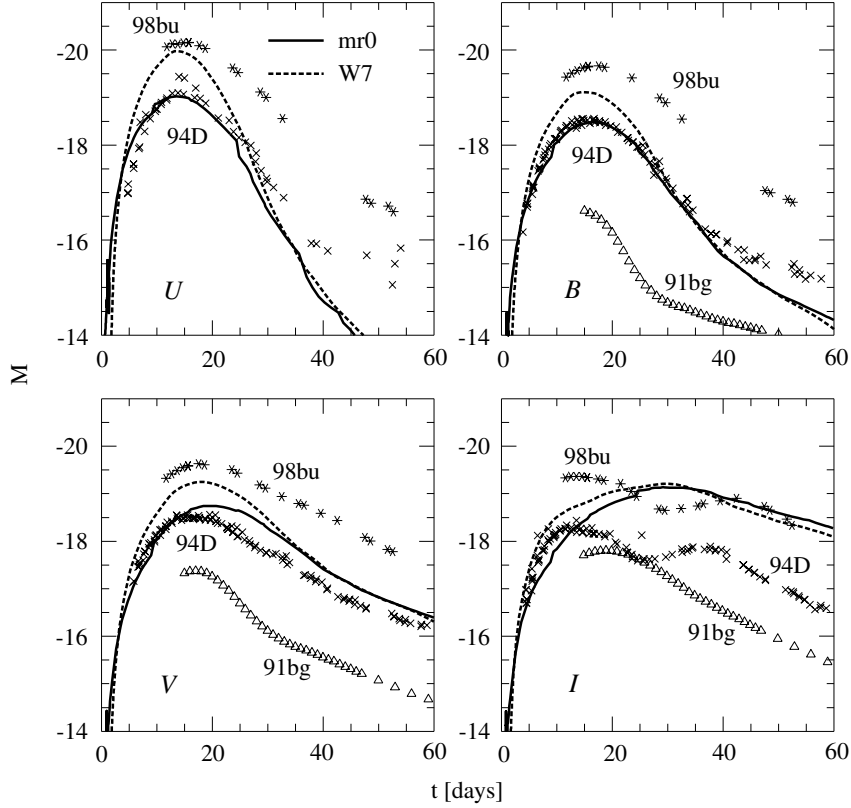


Figure 1.2.: Comparison of observed light curves in the U , B , V , and I filter bands with numerical models (one-dimensional simulation (W7, Nomoto et al. 1984) and a preliminary result from a three-dimensional simulation (mr0, Reinecke et al. 2002a)). From Sorokina & Blinnikov (2003).

to gain insight to various aspects of the explosion mechanism. Following Niemeyer & Hillebrandt (1997) these simulations can be classified in the following way: *Large scale calculations* (LSCs) try to model the explosion on scales of the stellar radius (for recent examples see Reinecke et al. 2002a, Gamezo et al. 2003). These, of course, have to rely on certain assumptions on the physics on small scales that are not numerically resolved. So-called sub-grid models supply information on the effects of turbulence on these scales on the flame. The underlying assumption is here, that turbulence is driven only from instabilities on large, numerically resolved scales. LSCs have been very successful in releasing enough energy to gravitationally unbind the star. However, the energy release and the nickel production are consistent only with weak SNe Ia so far. A further achievement is that light curves derived from these models agree amazingly well with observations (Sorokina & Blinnikov (2003), see also Figure 1.2). The deviation from observational data in the I filter originates from the method of the light curve calculation rather than from the explosion model.

The verification of the assumptions on the physics at unresolved scales made by LSCs is carried out by *small scale calculations* (SSCs) which perform simulations of the flame propagation in a small window in scale space in order to isolate the physical effects to be studied. The hope is to include the information gained here into LSCs. SSCs are subject of the present work. In particular, flame propagation in the so-called cellular regime will be investigated. These are performed on scales where the Landau-Darrieus instability (cf. Section 2.3.1) is expected to dominate flame propagation. A nonlinear stabilization mechanism (cf. Section 2.3.2) counteracts this instability and causes a cellular shape of the flame. The precursor of these studies are SSCs performed by Niemeyer & Hillebrandt (1995). They demonstrated for the first time that thermonuclear flames in WDs are indeed subject to the Landau-Darrieus instability, which was tested before only for chemical flames. However, their numerical implementation was not capable of entering the nonlinear regime of flame propagation. The authors reported on indications for a flame destabilization at low fuel densities.

A breakdown of the nonlinear stabilization of the flame could have dramatic impact on the flame propagation. Niemeyer & Woosley (1997) proposed the possibility that the flame would then produce turbulence on its own and thereby actively accelerate. This has been suggested as a mechanism for the transition of the flame propagation mode from deflagration to detonation.

1.4. Objectives of this work

As motivated in the previous section, the subject of this work is the study of flame propagation in the cellular regime. The astrophysical background is the “standard model” of Type Ia supernovae, i.e. the thermonuclear incineration of a C+O white dwarf star. In particular we refer to the Chandrasekhar-mass model and assume flame propagation in the deflagration mode. In the cellular regime (under conditions that apply to SN Ia explosions), flame propagation is dominated by two competing physical effects: the Landau-Darrieus instability and the nonlinear stabilization of the flame in a cellular pattern. The length scales at which these phenomena determine the flame evolution are around and below the so-called Gibson scale (see Section 3.1.2), where turbulent effects from large scale instabilities do not appreciably affect the flame propagation anymore. As will be discussed later, the Gibson scale depends on the density of the unburnt material and the turbulent scaling in the white dwarf, which is not established beyond doubt yet. Therefore its exact value is not well-known but lies orders of magnitude above the width of the internal flame structure. Thus, we arrange our small scale calculations at scales around 10^4 cm. This justifies the description of the flame as a sharp discontinuity in the state variables in our numerical simulations. We aim on the study of flame evolution in two spatial dimensions in this work. The main questions to be answered here are:

1. Does the cellular regime exist for thermonuclear flames in Type Ia supernovae? Although a number of previous studies assume that it does, so far no simulation with full treatment of the hydrodynamics has demonstrated that the flame here will stabi-

1. Prologue

lize in a cellular pattern. We know, however, from the simulations by Niemeyer & Hillebrandt (1995) that the burning front is subject to the Landau-Darrieus instability.

2. A more technical question is, what numerical model is appropriate to perform the studies? What accuracy of the flame representation is necessary to reproduce the predicted growth rate of perturbation due to the Landau-Darrieus instability (cf. Section 2.3.1) and eventually the cellular stabilization? The investigation of these questions provides information on the quality of the numerical flame models.
3. What is the exact shape of the flame in the cellular regime? How does it compare to available analytical approximations and results from chemical combustion experiments?
4. What flame acceleration results from the increase in flame surface?
5. Does the flame stabilize for all densities of the unburnt material? Niemeyer & Hillebrandt (1995) reported on the flame destabilization and subsequent turbulization at a fuel density of $5 \times 10^7 \text{ g cm}^{-3}$, which is low compared to the original density of the WD ($\sim 10^9 \text{ g cm}^{-3}$), i.e. it marks a late stage of the explosion when the star has already expanded considerably. Interestingly, this instant coincides with the favored choice of a deflagration-to-detonation transition from empirical SN Ia models. The possibility that the claimed flame destabilization can account for the underlying mechanism deserves thorough investigation.
6. Can the anticipated cellular structure of the flame be broken up due to interaction with a turbulent velocity field? This question is important since it appears to be a physically unrealistic scenario that the flame propagates into quiescent fuel. Relics from pre-ignition convection and from the turbulent cascade are sources of velocity fluctuations.
7. What will be the flame evolution after a possible breakdown of stabilization? Will the flame produce additional turbulence which could lead to a feedback in which the flame would actively accelerate?

These questions condense in two yet uninvestigated aspects of the current large scale supernova models. The first concerns the contribution to flame acceleration from scales where flame propagation proceeds in the cellular regime. The second addresses the possibility that physical effects at these scales could eventually account for the mechanism of a deflagration-to-detonation transition, which would include new pieces of physics into the large scale deflagration models for SNe Ia.

1.5. Organization of the thesis

After the introduction shed some light on the general framework and some physical considerations that play a role in our study, we will provide the theoretical background in Chapter 2 that enables us to synthesize the astrophysical picture (Chapter 3) of the problem we aim to answer. We will also review some analytical considerations which will be necessary to evaluate the later results of our numerical simulations. Some of the concepts loosely mentioned in the present chapter will be introduced in a more precise way in Chapter 3. Both the theoretical foundation and the astrophysical scenario help us to establish a numerical model that meets the requirements to answer the questions stated in Section 1.4. Chapter 5 presents and discusses the results from our simulations after some tests to verify the numerical model have been performed. Conclusions for Type Ia supernova models are drawn in Chapter 6 where also a comparison of our simulations with experimental results will be discussed. Finally, possible directions for further work will be pointed out.

2. Theoretical Considerations

The theory of combustion occupies a unique place in the mechanics and physics of continuous media because of the number of striking peculiarities.

— Ya. B. Zel'dovich (1980)

In this chapter some of the basic theoretical concepts shall be introduced that will be used later to build a model of thermonuclear flame propagation in SN Ia explosions. Furthermore, theoretical predictions shall be reviewed, that will be compared with the results from the numerical simulations.

2.1. Reactive fluid dynamics

In this section we will summarize the hydrodynamics that forms the foundation of our numerical modeling. We will present the basic equations that govern our physical system. The treatment of the white dwarf matter with concepts of hydrodynamics is based on the so-called continuum assumption. We describe it as a fluid, which is justified because of its negligible resistance to shear. In general, the matter consists of individual particles (molecules, atoms, elementary particles ...). However, the equations of hydrodynamics do not solve for the behavior of these individual particles but instead assume that the medium is a continuous, macroscopic fluid. This assumption incorporates statistical averaging processes over inter-particle processes.

The adopted hydrodynamic picture evidently depends on the spatial scale range on which the physical effects shall be modeled. The application of concepts of hydrodynamics throughout this work implicates a restriction to length scales much larger than the mean free path of particles composing the matter. At the same time, continuity of the matter premises scales on which quantities defined by statistical averaging like mass density ρ and temperature T do not change noticeably. In this spirit “fluid elements” contain certain amounts of matter and are not to be confused with individual particles. Furthermore, we require the matter contained in a fluid element to be in thermodynamical equilibrium which allows the complete description of its state with a basic set of thermodynamical quantities.

The system under consideration is appropriately described by the reactive flow equations. These equations represent physical effects originating from the nuclear, atomic, and molecular nature of matter in an averaged way, as well as collective phenomena. Diffusive transport and chemical or nuclear reactions fall into the first class while convection and wavelike properties (that are contained implicitly in the equation set) belong to the second class.

2. Theoretical Considerations

2.1.1. General form of a balance equation

The equations of hydrodynamics can be derived from basic principles of statistical physics (derivation of the Boltzmann equation from the Liouville equation making use of the Born-Bogoljubov-Green-Kirkwood-Yvon (BBGKY) hierarchy and calculating the moments of the Boltzmann equation) or in the spirit of a theory of continua. We will briefly discuss here the latter since it is more instructive for the numerical methods we are going to apply in Chapter 4. The derivation can be found in many textbooks on hydrodynamics or thermodynamics (e.g. Kluge & Neugebauer 1994)

Consider an extensive quantity A in a volume V that is fixed in space. The amount of A can be changed only due to creation or destruction d_s of A inside V , i.e. there is a source or sink of A inside V , or due to flow d_f of A over the boundary ∂V of the volume:

$$\frac{dA}{dt} = \frac{d_f A}{dt} + \frac{d_s A}{dt} \quad (2.1)$$

This is the integral form of a balance equation. Deriving the differential form of it makes use of the representation of A with help of its density $a(\mathbf{x}, t)$:

$$A = \int_V a(\mathbf{x}, t) dV. \quad (2.2)$$

The amount of A flowing over ∂V per unit time can be written as

$$\frac{d_f A}{dt} = - \oint_{\partial V} \mathbf{j}_a(\mathbf{x}, t) d\mathbf{f}, \quad (2.3)$$

where $d\mathbf{f}$ denotes the surface element pointing toward the exterior of V and \mathbf{j}_a stands for the flux density of A . The production (or depletion) of A in V can be formulated using the production density $s(a)$:

$$\frac{d_s A}{dt} = \int_V s(a) dV. \quad (2.4)$$

Making use of the divergence theorem the above equations yield

$$\frac{d}{dt} \int_V a(\mathbf{x}, t) dV = \int_V \frac{\partial}{\partial t} a(\mathbf{x}, t) dV = \int_V \{-\nabla \cdot \mathbf{j}_a + s(a)\} dV. \quad (2.5)$$

Since the volume can be chosen arbitrarily, we end up with the differential form of the balance equation

$$\frac{\partial a}{\partial t} = -\nabla \cdot \mathbf{j}_a + s(a). \quad (2.6)$$

We will now apply this equation to conserved quantities that characterize our hydrodynamical system.

2.1.2. The Euler equations

A simplified set of hydrodynamical equations is obtained when reaction and diffusive transport phenomena are neglected. This set of equations describes the dynamics of an ideal fluid and is based on three physical principles: the conservation of mass, momentum, and energy. The equations represent a balance between the convective transport terms and source terms.

The problem of thermonuclear combustion in SNe Ia is of non-relativistic nature. Therefore, mass and energy are conserved separately. The mass conservation equation reads

$$\frac{\partial \rho}{\partial t} = -\nabla \cdot (\rho \mathbf{v}). \quad (2.7)$$

Momentum conservation yields

$$\frac{\partial \rho \mathbf{v}}{\partial t} = -\nabla \cdot (\rho \mathbf{v} \mathbf{v}) - \nabla p + \rho \mathbf{f} \quad (2.8)$$

with pressure p . Combining equation (2.8) with (2.7) gives the so-called *Euler equation*¹:

$$\frac{\partial \mathbf{v}}{\partial t} = -(\mathbf{v} \nabla) \cdot \mathbf{v} - \frac{\nabla p}{\rho} + \mathbf{f}, \quad (2.9)$$

where \mathbf{f} denotes the specific external force acting on the system. Finally, energy conservation leads to

$$\frac{\partial \rho e_{\text{tot}}}{\partial t} = -\nabla \cdot (\rho e_{\text{tot}} \mathbf{v}) - \nabla \cdot (p \mathbf{v}) + \rho \mathbf{v} \cdot \mathbf{f}. \quad (2.10)$$

Incorporation of (chemical or nuclear) reactions requires at least an additional source term ρS in the energy balance equation (2.10)

$$\frac{\partial \rho e_{\text{tot}}}{\partial t} = -\nabla \cdot (\rho e_{\text{tot}} \mathbf{v}) - \nabla \cdot (p \mathbf{v}) + \rho \mathbf{v} \cdot \mathbf{f} + \rho S, \quad (2.11)$$

which depends on the reaction rates ω of the species ($i = 1 \dots N$), and the extension of the set of equations with the balance of species:

$$\frac{\partial \rho X_i}{\partial t} = -\nabla \cdot (\rho X_i \mathbf{v}) + \rho \omega_{X_i} \quad i = 1 \dots N. \quad (2.12)$$

Here, X_i denotes the mass fraction of species i , defined as

$$X_i = \frac{n_i A_i}{\sum_j n_j A_j}, \quad (2.13)$$

with n and A denoting the number density and the atomic mass, respectively. For simplicity we included only a single one-step reaction. N is the number of species contained in the reacting mixture. This overdetermines the system, since the sum of all equations (2.12) is

¹but note that the whole equation set is also frequently referred to as Euler's equations

2. Theoretical Considerations

equivalent to mass conservation (2.7) and yields the constraint for the species conversion rates

$$\sum_{i=1}^N \rho \omega_{X_i} = 0.$$

Thus, either mass conservation or one of the species equations is redundant. This is usually overcome by dropping one of the latter and letting N denote the total number of species minus one.

2.1.3. The Navier-Stokes equations

The Euler equations describe the dynamics of ideal fluids. For SN Ia events, however, it is (at least from a theoretical point of view) crucial to include effects like internal friction and diffusive transport since these effects dominate the fluid dynamics on smallest scales and are responsible for flame propagation. To include the effects of viscosity originating from internal friction an extension to the momentum (2.8) and energy balance equations (2.11) must be made. This is achieved by generalizing the pressure scalar p to a pressure tensor $\mathbf{\Pi}$:

$$\mathbf{\Pi} \equiv p \mathbf{I} + \boldsymbol{\tau}, \quad (2.14)$$

where the viscous stress tensor $\boldsymbol{\tau}$ is defined as

$$\boldsymbol{\tau} \equiv -\mu (\boldsymbol{\nabla} \mathbf{v} + (\boldsymbol{\nabla} \mathbf{v})^T) + \left(\frac{2}{3} \mu - \kappa \right) (\boldsymbol{\nabla} \cdot \mathbf{v}) \mathbf{I}. \quad (2.15)$$

Here, the coefficients of bulk and shear viscosity are denoted with κ and μ , respectively. Momentum balance now takes the form

$$\frac{\partial \rho \mathbf{v}}{\partial t} = -\boldsymbol{\nabla} \cdot (\rho \mathbf{v} \mathbf{v}) - \boldsymbol{\nabla} \cdot \mathbf{\Pi} + \rho \mathbf{f}, \quad (2.16)$$

which is called *Navier-Stokes equation*, and energy balance now reads

$$\frac{\partial \rho e_{\text{tot}}}{\partial t} = -\boldsymbol{\nabla} \cdot (\rho e_{\text{tot}} \mathbf{v}) - \boldsymbol{\nabla} \cdot (\mathbf{v} \mathbf{\Pi}) + \rho \mathbf{v} \cdot \mathbf{f} + \rho S. \quad (2.17)$$

2.1.4. General reactive flow equations

The Navier-Stokes equations are still not sufficient to describe combustion processes. For deflagrations for instance, the combustion wave is mediated by heat conduction and diffusion of chemical species. To incorporate these effects into the system of equations it is necessary to take into account additional terms in species and energy balance. The divergence of the heat flux vector \mathbf{q}

$$\mathbf{q} = -\sigma \boldsymbol{\nabla} T + \rho \sum_{i=1}^N h_i \mathbf{v}_i^D X_i, \quad (2.18)$$

2.1. Reactive fluid dynamics

where σ , h_i , and \mathbf{v}_i^D denote thermal conductivity, enthalpy, and diffusion velocity of species i , respectively, is subtracted from the right hand side of equation (2.17). The balance of species equation (2.12) is completed with the additional term describing the species diffusion

$$-\nabla \cdot (\rho \mathbf{v}_i^D X_i) \quad (2.19)$$

on the right hand side, while in the energy balance equation the term

$$\rho \sum_{i=1}^N X_i \mathbf{v}_i^D \cdot \mathbf{f}_i$$

must be added, where the \mathbf{f}_i denote the external forces per unit mass acting on species i . The system under consideration in this work is therefore described by the following set of equations:

- mass conservation

$$\frac{\partial \rho}{\partial t} = -\nabla \cdot (\rho \mathbf{v}). \quad (2.20)$$

- momentum balance

$$\frac{\partial \rho \mathbf{v}}{\partial t} = -\nabla \cdot (\rho \mathbf{v} \mathbf{v}) - \nabla \cdot \mathbf{\Pi} + \rho \mathbf{f} \quad (2.21)$$

- species balance

$$\frac{\partial \rho X_i}{\partial t} = -\nabla \cdot (\rho X_i \mathbf{v}) - \nabla \cdot (\rho \mathbf{v}_i^D X_i) + \rho \omega_{X_i} \quad i = 1 \dots N, \quad (2.22)$$

- energy balance

$$\frac{\partial \rho e_{\text{tot}}}{\partial t} = -\nabla \cdot (\rho e_{\text{tot}} \mathbf{v}) - \nabla \cdot (\mathbf{v} \mathbf{\Pi}) + \rho \mathbf{v} \cdot \mathbf{f} + \rho \sum_{i=1}^N X_i \mathbf{v}_i^D \cdot \mathbf{f}_i - \nabla \cdot \mathbf{q} + \rho S \quad (2.23)$$

Certainly, the terms included in these equations do not account for all physical effects that could be related to a combustion process. We neglect, for instance, radiative heat flux for reasons given by Timmes & Woosley (1992). The balance equations given above have to be completed by a set of auxiliary relations. The equation of state relates pressure to density, internal energy ($e_{\text{int}} = e_{\text{tot}} - \mathbf{v}^2/2$), and composition:

$$p = f_{\text{EOS}}(\rho, e_{\text{int}}, X_i). \quad (2.24)$$

Additionally one has to supply an expression for the diffusion velocities, for instance Fick's law² (given the conditions deviate only slightly from equilibrium) for the diffusion flux \mathbf{j}_i of species i ,

$$\mathbf{j}_i = \rho \mathbf{v}_i^D X_i = -\rho \sum_{k=1}^N D_{ik} \nabla X_k, \quad (2.25)$$

²This is certainly not a very elaborate model for the transport properties, since diffusion could respond also to pressure and temperature gradients as well as external forces. A multicomponent diffusion equation taking these effects into account can be found in (Chapman & Cowling 1960).

2. Theoretical Considerations

where D_{ik} denotes the binary diffusion coefficient for species i and k . The source terms in the species and energy equation depend on density, temperature, and composition as

$$\omega_{X_i} = \omega_{X_i}(\rho, T, X_i) \quad (2.26)$$

$$S = S(\omega_{X_i}) \quad (2.27)$$

2.1.5. Nondimensional representation of the general reactive flow equations

Consider two systems governed by the reacting flow equations that differ in size, composition and other conditions. In some special cases it is nevertheless possible that the two different systems show a similar behavior. This fact is extensively used in experimental studies of fluid mechanical processes with help of down-scaled models. It turns out that the condition for the similarity in the flow properties is that certain ratios of parameters be comparable. These ratios characterize the hydrodynamical flow and the combustion processes occurring in a system. They are obtained when flow equations are written in a dimensionless form by dividing the dimensional quantities ($\mathbf{x}, t, \rho, p \dots$) by some reference values. The equations then contain coefficients in form of ratios of dimensional parameters which are given special names according to Table 2.1. The combination of these *dimensionless numbers* characterizes universal solutions of the equations. In this way a universal formulation of the reactive flow equation system is possible. Of particular interest is the fact that the order of magnitude of a specific dimensionless number is a key to the relevance of the corresponding term in the equations and tells one which physical processes dominate the dynamics of the system.

As an example, we write the dimensional parameters occurring in the mass conservation equation (2.20) as

$$\rho = \rho_{\text{ref}} \rho^* \quad t = t_{\text{ref}} t^* \quad x_i = l_{\text{ref}} x_i^* \quad v_i = v_{\text{ref}} v_i^*, \quad (2.28)$$

where the dimensionless quantities are indexed with $*$ and the variables with index “ref” are the (dimensional) reference values. Writing the mass equation using (2.28) one ends up with

$$\frac{l_{\text{ref}}}{t_{\text{ref}} v_{\text{ref}}} \frac{\partial \rho^*}{\partial t^*} + \frac{\partial \rho^* v_i^*}{\partial x_i^*} = 0. \quad (2.29)$$

The ratio of reference values in the first term defines the *Strouhal number*³ Sr . It compares the characteristic time scale of the system to the convective timescale $l_{\text{ref}}/v_{\text{ref}}$. Often it is convenient to choose the convective timescale as reference setting $Sr = 1$. Proceeding in the way outlined above with the other equations of the system yields:

- dimensionless momentum balance

$$\frac{1}{Sr} \frac{\partial \rho^* \mathbf{v}^*}{\partial t^*} = -\nabla^* \cdot (\rho^* \mathbf{v}^* \mathbf{v}^*) - \frac{1}{Ma^2} \nabla^* p^* + \frac{\rho^* \mathbf{f}^*}{Fr} - \frac{1}{Re} \nabla^* \cdot \boldsymbol{\tau}^* \quad (2.30)$$

³Sometimes a dimensionless number characterizing oscillating properties of the flow is also termed “Strouhal number”. This deviates from the definition used here.

Symbol	Name	Definition	Significance
Da_1	(first) Damköhler number	$t_{\text{flow}}/t_{\text{reaction}}$	chemical reaction rate / convective transport rate
Fr	Froude number	$v_{\text{ref}}^2/l_{\text{ref}}a_{\text{ref}}$	internal forces / external forces (a denotes acceleration caused by these)
Le_i	Lewis number	$\sigma/(\rho_{\text{ref}}D_i c_p)$	thermal conduction / diffusive energy transport
Ma	Mach number	v_{ref}/c_s	magnitude of compressibility effects
Pe	Peclet number	$Re Pr$	convective heat transport / thermal conduction
Pr	Prandtl number	$\mu c_p/\sigma$	momentum transport / thermal conduction
Re	Reynolds number	$l_{\text{ref}}v_{\text{ref}}\rho_{\text{ref}}/\mu$	inertial forces / viscous forces
Sc_i	Schmidt number	$\mu/(\rho_{\text{ref}}D_i)$	momentum diffusion / mass diffusion
Sr	Strouhal number	$v_{\text{ref}}t_{\text{ref}}/l_{\text{ref}}$	timescale of convective transport / reference timescale

Table 2.1.: Similarity numbers

- dimensionless species balance

$$\begin{aligned} \frac{1}{Sr} \frac{\partial \rho^* X_i^*}{\partial t^*} = & -\nabla^* \cdot (\rho^* X_i^* \mathbf{v}^*) \\ & + Da_1 \rho^* \omega_{X_i}^* - \frac{1}{Sc_i Re} \nabla^* \cdot (\rho^* \mathbf{v}_i^{*D} X_i^*) \quad i = 1 \dots N, \end{aligned} \quad (2.31)$$

- dimensionless energy balance

$$\begin{aligned} \frac{1}{Sr} \frac{\partial \rho^* e_{\text{tot}}^*}{\partial t^*} = & -\nabla^* \cdot ([\rho^* e_{\text{tot}}^* + p^*] \mathbf{v}^*) - \frac{Ma^2}{Re} \nabla^* \cdot (\mathbf{v}^* \boldsymbol{\tau}^*) \\ & + \frac{Ma^2}{Fr} \left(\rho^* \mathbf{v}^* \cdot \mathbf{f}^* - \rho^* \sum_{i=1}^N X_i^* \mathbf{v}_i^{*D} \cdot \mathbf{f}_i^* \right) + \frac{1}{Re Pr} \nabla^* \cdot (\sigma \nabla^* T) \\ & - \frac{1}{Re Pr} \nabla^* \cdot \left(\rho^* \sum_{i=1}^N \frac{1}{Le_i} h_i^* \mathbf{v}_i^{*D} X_i^* \right) + \rho^* S^* \end{aligned} \quad (2.32)$$

These equations are obtained by setting

$$p_{\text{ref}} \equiv c_s^2 \rho_{\text{ref}}, \quad v_{i\text{ref}}^D \equiv \frac{D_i}{l_{\text{ref}}}, \quad e_{\text{tot,ref}} \equiv \frac{p_{\text{ref}}}{\rho_{\text{ref}}}, \quad T_{\text{ref}} \equiv \frac{e_{\text{tot,ref}}}{c_p}, \quad (2.33)$$

$$h_{\text{ref}} \equiv e_{\text{tot,ref}}, \quad \text{and} \quad S_{\text{ref}} \equiv \frac{e_{\text{tot,ref}} v_{\text{ref}}}{l_{\text{ref}}}. \quad (2.34)$$

Here, c_s and c_p denote the sound speed in the material and the specific heat at constant pressure, respectively. The definitions of the similarity numbers applied here are given in Table 2.1.

2.1.6. Source terms for nuclear reactions

In astrophysical systems, a number of different coupled reactions usually has to be taken into account. Thermonuclear burning in C+O white dwarf matter is dominated by the

2. Theoretical Considerations

heavy ion reactions $^{12}\text{C}+^{12}\text{C}$, $^{12}\text{C}+^{16}\text{O}$, and $^{16}\text{O}+^{16}\text{O}$, since they have a high Coulomb barrier and thus the ignition temperature is high. The reaction after the heavy ion reactions up to ^{56}Ni are α -reactions exhibiting a much smaller Coulomb barrier and are thus much faster. Hence, the reaction rate is governed by the initial heavy-ion reaction (for the rate of the $^{12}\text{C}+^{12}\text{C}$ see [Caughlan & Fowler 1988](#)).

Introducing the specific abundance Y_i as

$$Y_i = \frac{X_i}{A_i} = \frac{n_i}{\sum_j n_j A_j} \quad (2.35)$$

as the ratio of the number of nuclei of species i to the total number of nuclei in the system, the following equation describing the change in Y_i due to reactions up to three-body interactions can be established (e.g. [Müller 1998](#)):

$$\begin{aligned} \dot{Y}_i = & \sum_j c_i(j) \lambda_j Y_j \\ & + \sum_{j,k} c_i(j,k) \left(\sum_a n_a A_a \right) \langle jk \rangle Y_j Y_k \\ & + \sum_{j,k,l} c_i(j,k,l) \left(\sum_a n_a A_a \right)^2 \langle jkl \rangle Y_j Y_k Y_l. \end{aligned} \quad (2.36)$$

The first term on the right hand side describes changes due to β -decays and electron captures or photo-disintegrations, the second and third describe two-body and three-body reactions. Accordingly, λ_i denotes the weak interaction rate, and $\langle jk \rangle$ and $\langle i, j, k \rangle$ are the thermally averaged products of cross sections and relative velocities in the center of mass system for the two-body and three-body interactions. The coefficients c_i abbreviate

$$c_i(j) = \pm N_i, \quad c_i(j,k) = \pm \frac{N_i}{N_j! N_k!}, \quad \text{and} \quad c_i(j,k,l) = \pm \frac{N_i}{N_j! N_k! N_l!}. \quad (2.37)$$

The signs indicate production (+) or destruction (−) of nucleus i . The rate terms usually contain second and higher orders of the abundances sought and equations (2.36) thus state a set of coupled ordinary nonlinear differential equations, called a *nuclear reaction network*.

2.2. Combustion theory

Combustion takes place under various circumstances in nature and technology. All these processes are subject to fluid dynamics combined with some sort of reactions resulting in species conversion and release of thermal energy. In principle, they can be described by a set of equations similar to that introduced in the previous section. The particular conditions of these processes are reflected in the relevance of corresponding terms in the equations characterized by the magnitude of dimensionless numbers.

The main subcategories of combustion phenomena are discriminated by the state in which the fuel for the reaction is available. One can imagine realizations where all ingredients necessary for the reaction to take place are contained in the fuel mixture (“*premixed flames*”) and situations where the reaction can only take place in regions where the ingredients encounter due to diffusion processes (“*nonpremixed flames*” or “*diffusion flames*”). In the context of Type Ia supernovae (like in all combustion processes on the basis of thermonuclear reactions) only the former case is relevant. An analogous case in technology would be the combustion in an injection car engine. We will restrict the following considerations to premixed flames.

2.2.1. The discontinuity approximation of burning fronts and modes of propagation

The burning reactions release energy and heat the burnt material resulting in an increase of temperature across the burning front. For common equations of state of gases the increase in temperature causes a decrease in density. In case of thermonuclear burning in white dwarfs this statement holds true. The fuel consists of material containing a degenerate electron gas. Since the degeneracy of the relativistic electron gas is partly lifted in the burnt matter, the temperature increase across the reaction zone yields a decrease in density.

Thus, if the scales under consideration are much larger than the width of the reaction zone, it is well justified to simplify the burning front to a moving discontinuity in the state variables. This is the simplest model of a flame, which, however, neglects completely its internal structure. It only provides a description of the hydrodynamical states in front of and behind the flame. All physical processes that actually govern the flame propagation, the reaction kinetics and the transport processes inside the thin flame structure are ignored. Nevertheless, even in this strongly simplified picture it is possible to derive conditions for the pre-front and post-front states from conservation laws across the flame sheet.

The Euler equations of fluid dynamics admit the formulation of certain jump conditions for the state variables on the basis of continuity in all flux densities of conserved quantities across the front. The derivation is done most conveniently in the rest frame of the front. Here, the velocities v_u and v_b represent the fluid velocities relative to the front in the unburnt and burnt material, respectively. The velocity v_u in the chosen frame of reference will be used as a definition of the propagation velocity of the simplified flame⁴. Integration of

⁴It will later be identified with the laminar burning velocity s_l .

2. Theoretical Considerations

equations (2.7), (2.8), and (2.10) over some arbitrary volume containing part of the front yield

$$\rho_u \mathbf{v}_u \mathbf{n} = \rho_b \mathbf{v}_b \mathbf{n} \quad (2.38)$$

$$p_u \mathbf{n} + \rho_u v_u (v_u \mathbf{n}) = p_b \mathbf{n} + \rho_b v_b (v_b \mathbf{n}) \quad (2.39)$$

$$\rho_u e_{\text{tot},u} \mathbf{v}_u \mathbf{n} + p_u \mathbf{v}_u \mathbf{n} = \rho_b e_{\text{tot},b} \mathbf{v}_b \mathbf{n} + p_b \mathbf{v}_b \mathbf{n}, \quad (2.40)$$

where \mathbf{n} is the normal vector to the front, without loss of generality defined as pointing toward the fuel region. The quantities in the region of unburnt and burnt material are denoted with the indices u and b , respectively. Equation 2.40 can be reformulated making use of the specific enthalpy $h = (e_{\text{int}} + p)/\rho$:

$$\rho_u \mathbf{v}_u \mathbf{n} \left(\frac{v_u^2}{2} + h_u \right) = \rho_b \mathbf{v}_b \mathbf{n} \left(\frac{v_b^2}{2} + h_b \right). \quad (2.41)$$

Without loss of generality we may assume that the boundary of the domain of integration is chosen in a way, that the normal vector of its interface is parallel to the normal vector of the front. Now we can split the velocity on both sides of the front into a component $v_n \mathbf{n}$ normal and a component \mathbf{v}_t tangential to it:

$$\mathbf{v} = v_n \mathbf{n} + \mathbf{v}_t; \quad v_n = \mathbf{v} \mathbf{n}, \quad \mathbf{v}_t = \mathbf{v} - v_n \mathbf{n}. \quad (2.42)$$

Thus, momentum conservation over the front yields

$$p_u + \rho_u v_{u,n}^2 = p_b + \rho_b v_{b,n}^2, \quad (2.43)$$

$$\rho_u v_{u,n} \mathbf{v}_{u,t} = \rho_b v_{b,n} \mathbf{v}_{b,t}. \quad (2.44)$$

Combination of equations (2.38)

$$\rho_u v_{u,n} = \rho_b v_{b,n} \quad (2.45)$$

and (2.44) leads to continuity of the tangential velocity component over the front

$$\mathbf{v}_{u,t} = \mathbf{v}_{b,t}, \quad (2.46)$$

provided the mass flux over it is non-vanishing, which is actually the case for reaction fronts. Hence, combustion front discontinuities fall into the class of shock waves. Finally, energy conservation over the discontinuity gives

$$\frac{v_{u,n}^2}{2} + e_{\text{int},u} + p_u V_u + \Delta h_0 = \frac{v_{b,n}^2}{2} + e_{\text{int},b} + p_b V_b, \quad (2.47)$$

where $V := 1/\rho$ denotes the specific volume.

Equations (2.45), (2.43), (2.46), and (2.47) are known as the *Rankine-Hugoniot jump conditions*. The connection between the states (p, V) of unburnt and burnt material is

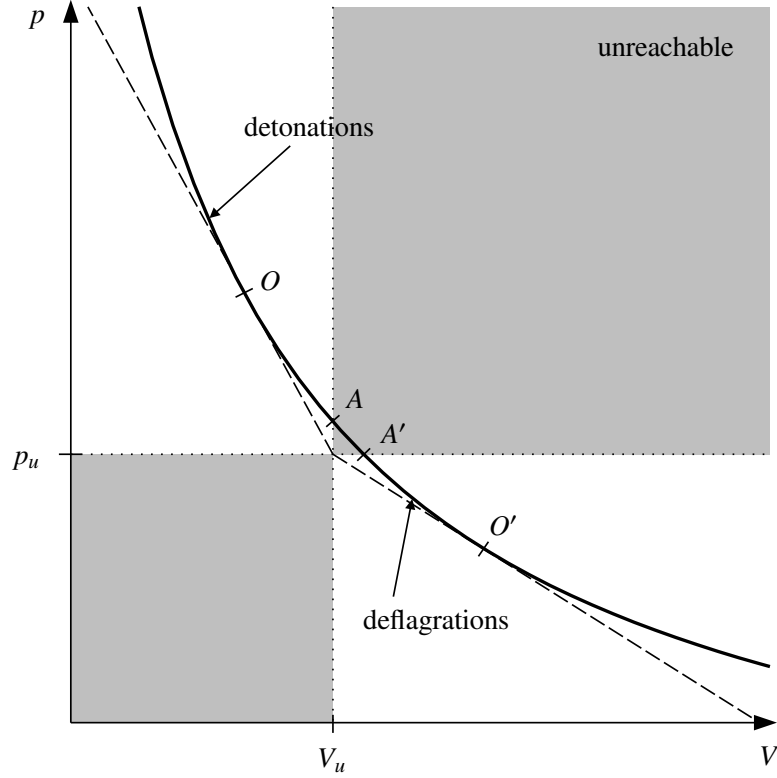


Figure 2.1.: Relation between unburnt (V_u, p_u) and burnt (V_b, p_b) states.

found by combining equations (2.45) and (2.43). The square of the mass flux on both sides of the front is then given by

$$\dot{j}_m^2 = (\rho_u v_{u,n})^2 = (\rho_b v_{b,n})^2 = \frac{p_u - p_b}{V_b - V_u}. \quad (2.48)$$

This is the so-called *Rayleigh criterion*. Elimination of the velocities in (2.47) using (2.48) leads to

$$e_{\text{int},u} - e_{\text{int},b} = \Delta h_0 - \frac{p_u + p_b}{2}(V_b - V_u), \quad (2.49)$$

defining the *Hugoniot curve*.

Using the Hugoniot curve and the Rayleigh criterion, conditions for burnt states can be derived for given unburnt states. This is illustrated in Figure 2.1 assuming an ideal gas equation of state. The state of the burnt material must lie on the Hugoniot curve (sometimes also called detonation adiabetic). Because of the Rayleigh criterion (2.48), the unburnt and the resulting burnt state are connected by a straight line, the slope of which corresponds to the square of the mass flux density over the front. This excludes the part AA' of the Hugoniot curve from the range of possible final states, because for states of the burnt material in this range the mass flux density would be imaginary. Constructing the tangentials on the Hugoniot curve starting from (V_u, p_u) , four regions of possible final

2. Theoretical Considerations

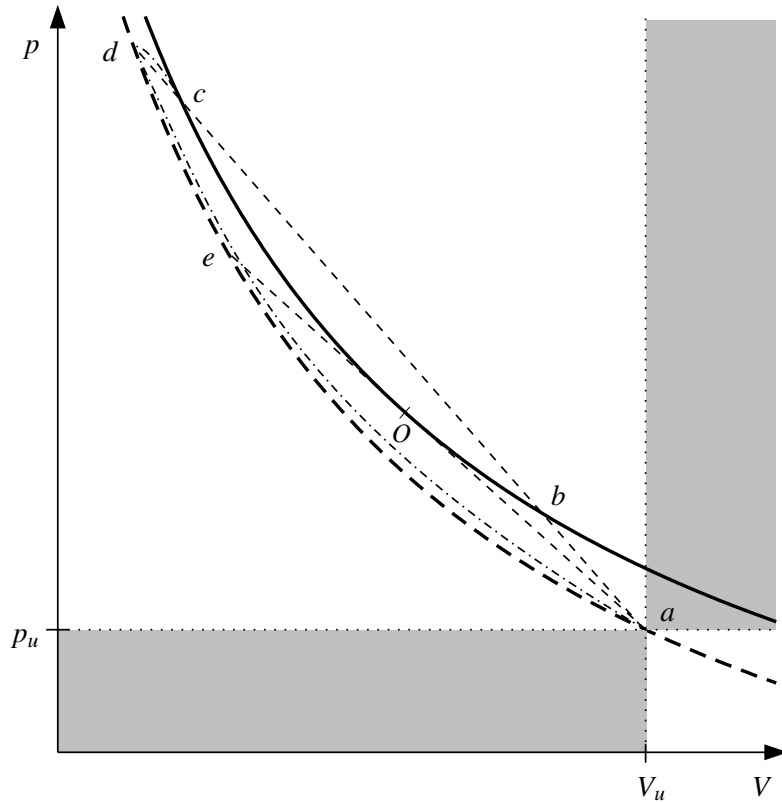


Figure 2.2.: Close-up of the detonation branch, following Liñan & Williams (1993) and Landau & Lifshitz (1959).

states emerge: the parts of the Hugoniot curve above A and below A' , each separated again into two sub-regions by O and O' , respectively. The significance of these regions will be explained in the following.

Figure 2.2 shows a close-up of the Hugoniot curve above A' . The bold dashed curve corresponds to the ordinary shock adiabat for the unburnt state, while the solid curve is the Hugoniot. Thus, the former does not take into account reaction from the unburnt state to the burnt states and passes through the initial state (V_u, p_u) . The possible final states (V_b, p_b) must lie on the Hugoniot curve and are connected to the state of the fuel by the Rayleigh lines (shown as light dashed lines, e.g. ac). By virtue of equation (2.48), the slopes of these lines correspond to the velocity of the unburnt material v_u . Contrary to that, the slopes of the tangents to the dashed curve measure the sound speed in the unburnt material $c_{s,u}$. The smallest possible slope of a Rayleigh-line is the one of the tangential aOe to the Hugoniot curve. It is evident, that above A the velocity of the flame with respect to the fuel is supersonic ($v_u > c_{s,u}$). Combustion processes terminating on this branch of the Hugoniot curve are termed *detonations*.

Starting from p_u, V_u , we now construct the tangential on the Hugoniot in O . The mass

flux corresponding to that Rayleigh line has to satisfy the condition

$$\frac{d(j_m^2)}{dp_b} = 0. \quad (2.50)$$

It can be shown (see Landau & Lifshitz 1959) that this implies $v_b = c_{s,b}$ in O . Furthermore,

$$\frac{d}{dp_b} \left(\frac{v_b^2}{c_{s,b}^2} \right) = -\frac{d}{dp_b} \left[j_m^2 \left(\frac{\partial V_b}{\partial p_b} \right)_{s_b} \right] = -j_m^2 \left(\frac{\partial^2 V_b}{\partial p_b^2} \right)_{s_b}, \quad (2.51)$$

where s_b denotes the entropy density of the burnt material, holds. Assuming an adiabatic compressibility consistent with

$$\left(\frac{\partial^2 V}{\partial p^2} \right)_{s_b} > 0 \quad (2.52)$$

(which is the case for most materials), we conclude that the relation

$$\frac{d}{dp_b} \left(\frac{v_b}{c_{s,b}} \right) < 0 \quad (2.53)$$

applies in O . The considerations outlined above can be performed in a similar way for the lower branch of the Hugoniot. The results can be summarized as follows:

above	O :	$v_u > c_{s,u}$,	$v_b < c_{s,b}$,	“strong detonations”
in	O :	$v_u > c_{s,u}$,	$v_b = c_{s,b}$,	“upper Chapman-Jouguet point”
segment	AO :	$v_u > c_{s,u}$,	$v_b > c_{s,b}$,	“weak detonations”
segment	$A'O'$:	$v_u < c_{s,u}$,	$v_b < c_{s,b}$,	“weak deflagrations”
in	O' :	$v_u < c_{s,u}$,	$v_b = c_{s,b}$,	“lower Chapman-Jouguet point”
below	O' :	$v_u < c_{s,u}$,	$v_b > c_{s,b}$,	“strong deflagrations”

For reasons given in Landau & Lifshitz (1959), the region below O' represents an unstable wave and the corresponding combustion regime can not be realized. Detonations mostly proceed in the upper Chapman-Jouguet point. Strong and in particular weak detonations require special experimental arrangements.

2.2.2. Internal structure of detonation and deflagration waves

The classification of combustion processes given in the last subsection refers only to conditions that are derived from the conservation laws across the flame front described as a discontinuity. This picture is, however, oversimplified because it assumes that the reaction proceeds to completion instantaneously.

We will now briefly review⁵ the internal structure of a deflagration and a detonation wave. The latter can be understood as a trajectory in the pressure-volume plane. Return to Figure 2.2, which shows the detonation branch of the Hugoniot curve and consider for

⁵The discussion proceeds closely to Liñan & Williams (1993) and Landau & Lifshitz (1959).

2. Theoretical Considerations

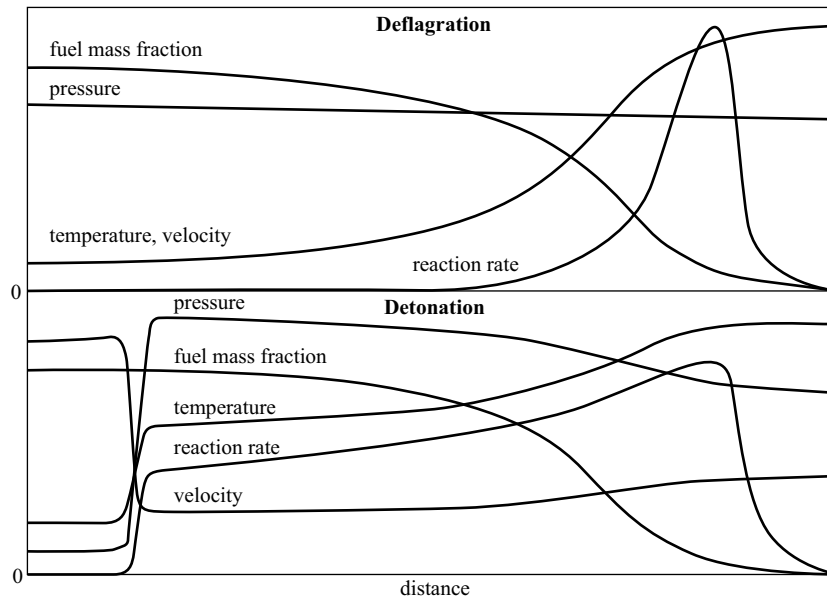


Figure 2.3.: Internal structure of a deflagration wave (top) and a detonation wave (bottom). Adopted from Liñan & Williams (1993).

example the detonation represented by the final state $(V_b, p_v) = c$. Then we can follow the change of state within the finite internal structure of the detonation wave. The front of that wave is actually a shock wave, which heats and compresses the gas to state d following the path of the shock adiabat aed . Point d is known as the *von Neumann spike*. The reaction inside the detonation wave corresponds to the transition along line dc . The heat release of the reaction causes subsequent expansion and pressure decline of the gas until the final state c on the Hugoniot curve is reached. A more realistic path of the change of state deviates from both the Hugoniot and the Rayleigh lines (dashed-dotted line in Figure 2.2). This is due to the fact that strong shocks are only a few molecular mean-free-paths in thickness and an exact treatment must therefore apply kinetic theory rather than use continuum equations.

The theory underlying the concept of the detonation structure was developed independently by Zel'dovich (1940), von Neumann (1942), and Döring (1943) and is usually called “ZND theory”. It is schematically illustrated in Figure 2.3. In case of detonations, burning is mediated by a shock wave that heats the unburnt material. For gaseous mixtures, across that shock pressure and temperature increase, velocity decreases and the chemical composition remains unchanged, because the shock is too thin to cause enough collisions. Reactions then take place in a zone downstream from the shock. In the subsonic flow behind the shock, heat release from the reactions causes the pressure to decrease and velocity and temperature to increase. The reaction typically starts out slowly in a so-called induction zone and then proceeds more rapidly.

In contrast to the detonation mechanism, flame propagation in the deflagration mode is

2.2. Combustion theory

mediated by transport processes, i.e. thermal conduction and diffusion. One of the earliest descriptions of flames in the deflagration mode, usually called *laminar flames*, goes back to Mikhel'son (1889). Here, the pressure over the flame, as well as the specific heat c_p of the mixture, are taken to be constant. Thus, the energy per unit mass added to the mixture is

$$e_0 = c_p(T_b - T_u). \quad (2.54)$$

With l_f denoting the thickness of the flame and w standing for the conversion rate (mass per unit volume per unit time) due to the reaction, the chemical energy released per unit area per unit time reads $e_0 w l_f$. This produces upstream conduction of energy from the hot ashes to the cold fuel:

$$e_0 w l_f = \sigma(T_b - T_u)/l_f \quad (2.55)$$

Substituting (2.54) into (2.55) yields

$$l_f = \sqrt{\frac{\sigma}{c_p w}} \quad (2.56)$$

for the flame thickness. The laminar burning velocity of the flame, s_l , sets the mass of fuel converted per unit flame area per unit time to

$$\rho_u s_l = w l_f. \quad (2.57)$$

Thus, according to Mikhel'son,

$$s_l = \frac{1}{\rho_u} \sqrt{\frac{w \sigma}{c_p}}. \quad (2.58)$$

These are, however, only crude estimates for the flame thickness and the laminar burning velocity. The structure of a laminar deflagration flame according to Mikhel'son is schematically given in Figure 2.4. For a one-step Arrhenius reaction of n -th order, the conversion rate is

$$w \propto X_{\text{fuel}}^n e^{-E_A/(\mathcal{R}T)}. \quad (2.59)$$

Here, E_A and \mathcal{R} denote the activation energy of the reaction and the universal gas constant, respectively. Typical values for E_A/\mathcal{R} are very large compared with temperatures within the flame. Therefore, the reaction is strongly temperature-dependent. This dependency is estimated by the *Zel'dovich number*

$$\beta = E_A \frac{T_b - T_u}{\mathcal{R}T_b^2}. \quad (2.60)$$

For a large Zel'dovich number the reaction rate throughout most parts of the flame is negligible and appreciable reaction takes place only at the hot end of the flame, in a region l_f/β , called the *reaction zone*. The part upstream of the reaction zone is termed *convective-diffusive zone* or *preheat zone*. This new model, which is depicted in Figure 2.4, revises the balance (2.55) to

$$e_0 w l_f / \beta = \sigma(T_* - T_u)/l_f \approx \sigma(T_b - T_u)/l_f, \quad (2.61)$$

2. Theoretical Considerations

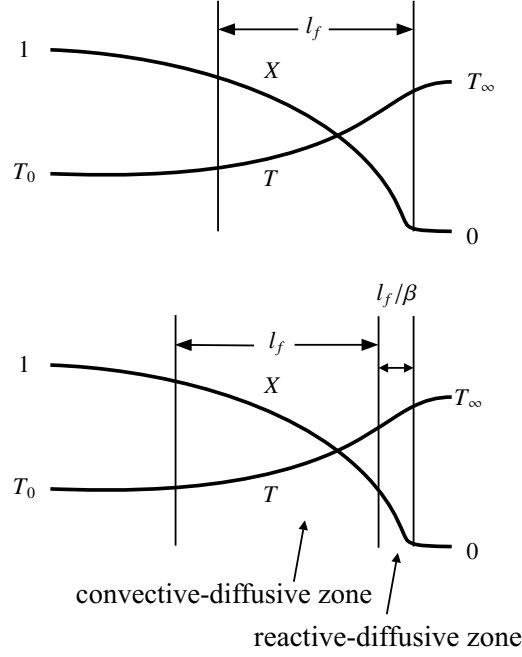


Figure 2.4.: Internal structure of a premixed laminar flame according to Mikhel'son (top) and the refined model (bottom). Adopted from Liñan & Williams (1993).

where T_* denotes the value of the temperature at the boundary between the preheat zone and the reaction zone. Equivalently, (2.57) becomes

$$\rho_u s_l = w l_f / \beta \quad (2.62)$$

and the flame thickness and the burning velocity now read

$$l_f = \sqrt{\frac{\sigma \beta}{c_p w}} \quad (2.63)$$

and

$$s_l = \frac{1}{\rho_u} \sqrt{\frac{w \sigma}{c_p \beta}}, \quad (2.64)$$

respectively.

2.2.3. Laminar flames

The mathematically correct description of laminar flames is obtained from the general reactive flow equations (2.20)–(2.23). The simplest nontrivial solution of those are planar laminar flames found by assuming translational symmetry in two dimensions and looking for stationary solutions in the remaining direction denoted by x . We will additionally

neglect external forces. In terms of the dimensionless formulation stationarity is expressed by setting $Sr \rightarrow \infty$. Together with (2.29) this gives $\rho v = \text{constant}$. Equation (2.31) becomes

$$\rho^* s_l^* \frac{\partial X_i^*}{\partial x^*} = -\frac{1}{Sc_i Re} \frac{\partial}{\partial x^*} (\rho^* v_i^{*D} X_i^*) + Da_1 \rho^* \omega_{X_i}^*, \quad i = 1 \dots N, \quad (2.65)$$

and (2.32) gives

$$\begin{aligned} \rho^* s_l^* \frac{\partial e_{\text{tot}}^*}{\partial x^*} = & -\frac{\partial p^* s_l^*}{\partial x^*} - \frac{Ma^2}{Re} \frac{\partial}{\partial x^*} (s_l^* \tau^*) + \frac{1}{Re Pr} \frac{\partial}{\partial x^*} \left(\sigma \frac{\partial}{\partial x^*} T \right) \\ & - \frac{1}{Re Pr} \frac{\partial}{\partial x^*} \left(\rho^* \sum_{i=1}^N \frac{1}{Le_i} h_i^* v_i^{*D} X_i^* \right) + \rho^* S^*. \end{aligned} \quad (2.66)$$

Choosing boundary conditions for X^* and e_{tot}^* at $x^* = \pm\infty$, i.e. burnt and unburnt states, (2.65) and (2.66) establish a system of ordinary differential equations with the laminar flame velocity s_l being an unknown eigenvalue.

2.2.4. Phenomenological description according to Markstein

A flame description that goes one step beyond the discontinuity approximation of Section 2.2.1 was suggested by Markstein (1951). The simplicity of the approach in the discontinuity approximation is retained by restricting the model to length scales far above the flame thickness. Therefore this flame description applies to cases in which the flame is wrinkled by perturbations much larger than the flame thickness, which leads to a bending of the reaction zone without affecting its internal structure. The phenomenological ansatz made by Markstein (1951) models the burning speed of the flame as being curvature-dependent:

$$s_M = s_l(1 - l_M \kappa), \quad (2.67)$$

where κ denotes the curvature of the flame front and l_M is a phenomenological parameter, called *Markstein length*, which is of the order of the flame width. This assumption on the flame propagation velocity prevents the burning front from forming apices with infinite curvature, which are inconsistent with the picture of a finite inner structure of the flame. A numerical approach to determine values of l_M for astrophysical thermonuclear flames was given by Dursi et al. (2003).

2.2.5. Thermonuclear deflagration in C+O white dwarf matter

The transport processes in white dwarf matter are dominated by the electron gas. This is due to the high degeneracy of the material. The Fermi energy E_F of the electron gas is about 1 MeV while the thermal energy is $k_B T \sim 10$ keV. Electron states below $E_F - k_B T$ are occupied limiting the final states for scattering processes to high velocities. Therefore the mean free path of the electrons is much larger than that for the baryons.

2. Theoretical Considerations

Following [Timmes & Woosley \(1992\)](#) we estimate the relevant similarity numbers for white dwarf matter. Typical values for the shear viscosity and the diffusion coefficients are ([Nandkumar & Pethick 1984](#), [Paquette et al. 1986](#)) $\mu \sim 10^9 \text{ g cm}^{-1} \text{ s}^{-1}$ and $D \sim 10^{-4} \text{ cm}^2 \text{ s}^{-1}$. Thermal conductivity σ is composed of contributions from radiative and conductive transport processes:

$$\sigma \propto \left(\frac{1}{\kappa_{\text{rad}}} + \frac{1}{\kappa_{\text{cond}}} \right), \quad (2.68)$$

where κ_{rad} and κ_{cond} denote the opacities. [Timmes & Woosley \(1992\)](#) argue, that the radiative opacity has much higher values than the conductive opacity. As an example they give values of the opacities of $\kappa_{\text{rad}} \sim 5 \times 10^{-2} \text{ cm}^2 \text{ g}^{-1}$ and $\kappa_{\text{cond}} \sim 1.5 \times 10^{-4} \text{ cm}^2 \text{ g}^{-1}$ under the conditions $\rho = 6 \times 10^9 \text{ g cm}^3$ and $T = 4 \times 10^9 \text{ K}$, assuming the composition $X(\text{C}) = X(\text{O}) = 0.5$. Thus, σ is dominated by conductive processes due to the electrons and its value is given with $\sigma \sim 10^{19} \text{ erg cm}^{-1} \text{ K}^{-1} \text{ s}^{-1}$ ([Timmes & Woosley 1992](#)).

This yields for the Lewis and Prandtl numbers:

$$Le = \frac{\sigma}{\rho D c_p} \sim 10^7 \quad (2.69)$$

and

$$Pr = \frac{\mu c_p}{\sigma} \sim 10^{-3}, \quad (2.70)$$

characterizing one of the main differences between thermonuclear flames in degenerate matter and chemical flames, where usually $Le \sim 1$.

The basic objective in the investigation of laminar thermonuclear flames is to determine their fundamental properties, such as the burning velocity and the flame width. This can be achieved in a one-dimensional flame model. The most general way of these studies is to solve concurrently for the hydrodynamics, nuclear kinetics, and transport properties.

In this spirit, [Timmes & Woosley \(1992\)](#) set up a numerical simulation based on the equations for the general reactive flow (2.20)–(2.23), neglecting the bulk viscosity. To a good approximation they set Le to infinity and Pr to zero, i.e. the ionic diffusion velocities and the shear viscosity are neglected, leading to a substantial simplification of (2.20)–(2.23) and (2.18). Additionally, (2.26) and (2.27) have to be specified. The net reaction rates for the i -th isotope for all reactions of the form $i(j, k)l$ are given by

$$\rho \omega_{X_i} = \frac{1}{A_i} \sum_{j,k} -\lambda_{j,k}(i) \frac{X_j X_k}{A_j A_k} + \lambda_{k,j}(l) \frac{X_l X_k}{A_l A_k}, \quad (2.71)$$

with λ_{jk} and λ_{kj} denoting the forward and reverse reaction rates, respectively. With B_i standing for the nuclear binding energy of the i -th isotope, the nuclear energy generation rate \dot{S} is related to the net reaction rates \dot{R}_i ($\dot{R}_i A_i = \rho \omega_{X_i}$) by

$$\dot{S} = N_A \sum_{j=1}^N \frac{1}{A_j} \dot{R}_j B_j. \quad (2.72)$$

Timmes & Woosley (1992) solve the above equations by applying a 19 isotope nuclear reaction network that couples 80 reaction rates. They claim that

$$s_l = 92.0 \times 10^5 \left(\frac{\rho_u}{2 \times 10^9} \right)^{0.805} \left[\frac{X(^{12}\text{C})}{0.5} \right]^{0.889} \text{ cm s}^{-1} \quad (2.73)$$

fits the computed values for laminar flame speeds in C+O white dwarf matter to about 10% in the density range $10^7 \text{ g cm}^{-3} \leq \rho_u \leq 10^{10} \text{ g cm}^{-3}$. We note, however, that the discrepancy between this fit and the data from numerical simulations given by Timmes & Woosley (1992) can be larger than that (in particular toward low fuel densities and for fuel compositions deviating from $X(^{12}\text{C}) = X(^{16}\text{O}) = 0.5$).

A further method is, to assume the existence of a steady flame propagation into the unburnt material with a constant velocity s_l (see Section 2.2.3). Its value now can be determined from the eigenvalue problem (2.65), (2.66) together with an appropriate choice of boundary values for the composition and total energy at $x = \pm\infty$. This, however, involves the difficulty of specifying the total energy of the burnt material which is not a priori known. Nevertheless, it is possible to approximate s_l numerically by means of a “trial-and-error”-method using properties of the integral curve that joins the boundary values (Zel’dovich et al. 1980a, Khokhlov et al. 1997).

2.3. Flame instabilities

Fluid motions generally feature various instabilities depending on the physical and geometrical context. These instabilities play a crucial role in various astrophysical phenomena. In particular, many of the instabilities occur in the context of flame propagation. Those are of eminent importance in Type Ia supernova models. In the following, three instabilities that dominate the flame propagation on different scales in the supernova explosion, namely the Rayleigh-Taylor, the Kelvin-Helmholtz, and the Landau-Darrieus instabilities, shall be reviewed. The first two instabilities occur in many fields of hydrodynamics, whereas the Landau-Darrieus instability is specific to the propagation of burning fronts.

There exist, of course other instabilities of flames, such as the so-called diffusional-thermal instability. This instability is, however, not relevant to the propagation of thermonuclear flames in degenerate matter. It results from the competing effects of enhanced heat loss and enhanced accumulation of fuel due to diffusion at bulges of the flame front. The former decreases the temperature in the reaction sheet and therefore reduces the reaction rate, while the latter increases the reaction rate. The growth rate of the perturbation amplitude is given by Barenblatt et al. (1962) as

$$\omega_{td} = \lambda \left[\frac{1}{2} \beta (1 - Le) \right] k^2 \quad (2.74)$$

(for the definition of β see equation (2.60)) Thus, for $Le < 1$ thermal-diffusive effects exert a stabilizing action on the flame. This is the case in Type Ia supernova explosions, where $Le \sim 10^7$ (see Section 2.2.5).

2. Theoretical Considerations

2.3.1. Linear stability analysis

In the following, the linear stability of three different simplified configurations, characterizing the Landau-Darrieus, the Rayleigh-Taylor, and the Kelvin-Helmholtz-instability, respectively, shall be discussed. Here one starts out with a system in equilibrium and perturbs the relevant variables slightly using plane waves. Because the perturbations are small, all relevant equations can be linearized in terms of the perturbed quantities. The resulting linearized system of equations is then solved making use of an ansatz in the form $\exp(i\mathbf{k} \cdot \mathbf{x} + \omega t)$. The result of the linear stability analysis is a dispersion relation between the growth rate ω and the wavenumber k of the perturbation. If ω contains a positive real part, then the perturbation will grow exponentially with time and the system is unstable.

The Landau-Darrieus instability

Landau (1944) and Darrieus (1938) independently discovered the surprising fact that the propagation of a laminar flame in the discontinuity approximation is actually unstable. This instability is of pure hydrodynamical origin and is known as the *Landau-Darrieus instability*⁶, abbreviated as LD instability hereafter, sometimes also called *hydrodynamic instability*. It is universal and applies to all scales that are adequately described by in the discontinuity picture.

Under the assumption that this condition is satisfied, the linear stability analysis given by Landau (1944) and Landau & Lifshitz (1959) shall be followed here. For simplicity the flow is considered as non-viscous. The low Mach number of deflagration phenomena additionally justifies the assumption of incompressible fluids. Consider a small part of the flame front which may be regarded as a plane. Without loss of generality, the coordinate system is chosen to be detached to the front, so that the flame is in rest to it. The plane of the flame front is spanned in y and z direction and the unperturbed motion of the fuel and ashes is stationary with the velocity vector \mathbf{v} coinciding with the positive x direction (i.e. $v_y = 0$). Let the region $x > 0$ contain the unburnt material. Here, the quantities will be indexed by u while the burnt material in $x < 0$ is labeled by the index b in the relevant quantities. Suppose now that a small perturbation \mathbf{v}' is superimposed to the unperturbed constant motion, so that this perturbation is periodic with respect to time and y -coordinate. From continuity (2.7) and Euler's equation (2.9), it follows for the perturbation to leading order that

$$\frac{\partial v'_x}{\partial x} + \frac{\partial v'_y}{\partial y} = 0; \quad (2.75)$$

$$\frac{\partial v'_x}{\partial t} + v_x \frac{\partial v'_x}{\partial x} = -\frac{1}{\rho} \frac{\partial p'}{\partial x}; \quad \frac{\partial v'_y}{\partial t} + v_x \frac{\partial v'_y}{\partial x} = -\frac{1}{\rho} \frac{\partial p'}{\partial y}, \quad (2.76)$$

with v_x representing $v_{u,x}$ or $v_{b,x}$ and ρ denoting ρ_u or ρ_b , according to the region for which the equations are written. Note, that $v_{u,x} = s_l$ for the chosen frame of reference. Differentiating the first equation of (2.76) with respect to x and the second with respect to y , one

⁶or *Darrieus-Landau* instability, depending on the country of origin of the respective publication

obtains by adding both resulting expressions

$$\frac{\partial^2 p'}{\partial x^2} + \frac{\partial^2 p'}{\partial y^2} = 0. \quad (2.77)$$

The jump conditions over the front discontinuity (see Section 2.2.1) have to be satisfied. Let $\xi(y, t)$ be a small displacement of the front in x direction due to the perturbation. Then the component of the fluid velocity tangential to the flame front consists of two contributions: the projection of \mathbf{v}' on the surface, which, in first approximation, equals v'_y , and the projection of the unperturbed velocity v_x , which is $v_x \partial \xi / \partial y$. Continuity of the tangential velocity component (2.46) thus reads

$$v'_{u,y} + s_l \frac{\partial \xi}{\partial y} = v'_{b,y} + v_{b,x} \frac{\partial \xi}{\partial y}. \quad (2.78)$$

It will additionally be assumed that the small perturbation leaves the propagation velocity of the discontinuity unchanged. This condition cannot be derived from conservation laws and is posed artificially here. In the adopted coordinate system this is equivalent to the condition that variations in the relative velocities of the fluid and the discontinuity be zero, i.e.

$$v'_{u,x} = v'_{b,x} = \frac{\partial \xi}{\partial t}. \quad (2.79)$$

Finally, it is stipulated that

$$p'_u = p'_b. \quad (2.80)$$

Looking for a solution of equations (2.75)–(2.77) for $x < 0$ (burnt material) in which p' , v'_x , and v'_y are proportional to the factor $\exp\{iky + \omega t\}$, one finds

$$\left. \begin{aligned} v'_{b,x} &= A e^{iky+kx+\omega t}, & v'_{b,y} &= iA e^{iky+kx+\omega t} \\ p'_b &= A \rho_b \left(\frac{\omega}{k} - s_l \right) e^{iky+kx+\omega t} \end{aligned} \right\} \quad (2.81)$$

Setting $p' = 0$, equations (2.76) yield another solution with the same dependency on y and t of the form $\text{const} \cdot \exp\{iky + \omega t\}$. The right hand side of Euler's equations (2.76) vanishes and the resulting homogeneous system has a solution in which

$$v'_x, v'_y \propto \exp \left\{ iky + \omega t - \frac{\omega}{v_x} x \right\}. \quad (2.82)$$

It is sufficient to consider this solution only in the unburnt region ($x > 0$) because the aim is to determine whether frequencies ω can exist having positive real parts. For such frequencies, however, the factor $\exp\{-\omega x/v\}$ increases without limit with $|x|$ for $x < 0$. Thus a solution of this form is not possible in the region of the burnt fluid.

Choosing appropriate constant coefficients, a solution for $x > 0$ of the form

$$\left. \begin{aligned} v'_{u,x} &= B e^{iky-kx+\omega t} + C e^{iky+\omega t-\omega x/v_{u,x}}, \\ v'_{u,y} &= -iB e^{iky-kx+\omega t} - \frac{i\omega}{kv_{u,x}} C e^{iky-i\omega t+i\omega x/v_{u,x}}, \\ p'_u &= -B \rho_u \left(v_{u,x} - \frac{\omega}{k} \right) e^{iky-kx+\omega t} \end{aligned} \right\} \quad (2.83)$$

2. Theoretical Considerations

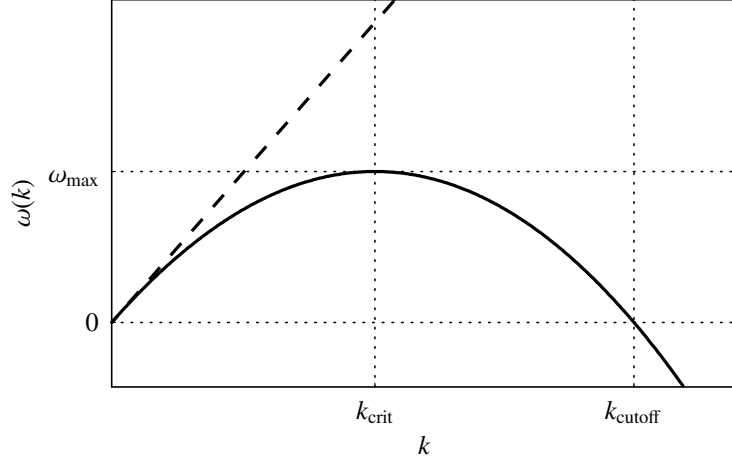


Figure 2.5.: Dispersion relation between ω and k for the Landau-Darrieus-instability according to (2.86) – dashed line and modified according to Markstein's burning law (2.87) – solid line.

is sought for. By putting

$$\xi = D e^{iky + \omega t}, \quad (2.84)$$

and substituting all obtained expressions into the conditions (2.78)–(2.80), four homogeneous equations for the coefficients A , B , C , and D emerge. These yield (making use of $\rho_u s_l = \rho_b v_b$) the following compatibility condition:

$$\omega^2(s_l + v_b) + 2\omega k s_l v_b + k^2 s_l v_b (s_l - v_b) = 0. \quad (2.85)$$

For $s_l > v_b$ this equation has either two real roots or two conjugate complex roots with $\Re \omega < 0$ and the flow is stable. On contrast, if $s_l < v_b$ (and $\rho_u > \rho_b$ correspondingly), both roots of equation (2.85) are real, with one of them positive, resulting in the dispersion relation (in the following frequently referred to as *Landau's dispersion relation*)

$$\omega_{LD} = k s_l \frac{\mu}{1 + \mu} \left(\sqrt{1 + \mu - \frac{1}{\mu}} - 1 \right), \quad (2.86)$$

with $\mu = \rho_u / \rho_b$. Thus the flow is unstable. Note, that this is just the case for a burning front since the density of the products is always smaller compared with that of the unburnt fluid due to the heating during the combustion.

The fact that $\Im \omega = 0$ means that the wave does not propagate along the front but is amplified as a standing wave. For fixed k the slope increases with larger μ . The instability occurs on all wavelengths of the perturbation, while the increment of the amplification grows with k . Here it shall be stressed, that the given derivation, which treats the front as a geometrical surface, is valid only if the wavelength of the perturbation is large in comparison to the flame thickness $kl_f \ll 1$. Thus, the model breaks down for high perturbation wavenumbers.

2.3. Flame instabilities

The finite flame thickness is expected to exert a stabilizing effect at perturbation wavelengths comparable to the flame width. This can be modeled in terms of Markstein's approach (Section 2.2.4) deviating from the assumption that led to equation (2.79). A derivation similar to that carried out above (see Markstein (1951) for details) with the burning velocity modeled according to (2.67) yields the modified dispersion relation

$$\omega_M = ks_l \frac{\mu}{1 + \mu} \left\{ \sqrt{1 + \mu - \frac{1}{\mu} + k^2 l_M^2 - 2kl_M \mu - (1 + kl_M)} \right\}, \quad (2.87)$$

which is plotted in Figure 2.5. This dispersion relation introduces two scales to the system. One is the perturbation wavelength λ_{crit} which grows fastest and the other is the cutoff scale below which perturbations are not amplified anymore. From (2.87) the cutoff scale is found to be

$$\lambda_{\text{cutoff}} = 4\pi l_M \frac{\mu}{\mu - 1}. \quad (2.88)$$

The cumbersome expression for λ_{crit} shall not be given explicitly here.

While for the two other instabilities to be discussed in the following the mechanism may be clear from physical intuition, it seems appropriate to provide a more descriptive interpretation of the mechanism that causes the LD instability.

The origin of the instability is the refraction of the streamlines of the flow on the density change over the flame (approximated as a discontinuity). The fluid velocity component tangential to the flame front is steady and mass conservation leads to a discontinuity in the normal velocity component. Consider a flame front that is perturbed from an originally planar shape (see Figure 2.6). Mass flux conservation leads to a broadening of the flow tubes in the vicinity of a bulge of the perturbation. Thus the local fluid velocity is lower than the fluid velocity at $\pm\infty$. Therefore the burning velocity s_l of the flame is higher than the corresponding local fluid velocity and this leads to an increment of the bulge. The opposite holds for recesses of the perturbed front. In this way the perturbation keeps growing.

The Rayleigh-Taylor instability

The *Rayleigh-Taylor (RT) instability* or *buoyancy instability* is caused by the stratification of fluids of different densities inversely to the gravitational field. Consider the most simple case of two different non-viscous, incompressible fluids of densities ρ_1 and ρ_2 resting on top of each other with a gravitational field acting downwards. Now choose a coordinate system in which the x - y plane coincides with the equilibrium surface separating both fluids, while the z axis points upwards.

Proceeding similar to the last section (see also Chandrasekhar 1961), one applies a small

2. Theoretical Considerations

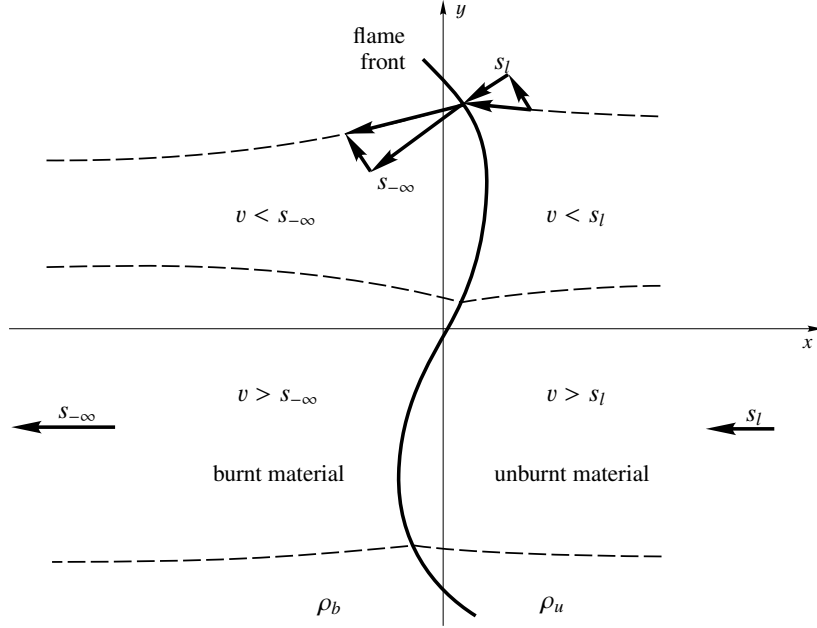


Figure 2.6.: Schematic illustration of the mechanism of the Landau-Darrieus-instability (adopted from Liñan & Williams 1993)

perturbation to the equilibrium configuration, yielding

$$\rho \frac{\partial}{\partial t} v'_x = -\frac{\partial}{\partial x} p', \quad \rho \frac{\partial}{\partial t} v'_z = -\frac{\partial}{\partial z} p' - g\rho', \quad (2.89)$$

$$\frac{\partial v'_x}{\partial x} = -\frac{\partial v'_z}{\partial z} \quad (2.90)$$

$$\frac{\partial}{\partial t} \rho' = -v'_z \frac{\partial}{\partial z} \rho', \quad (2.91)$$

from Euler's equation (2.9), incompressibility condition, and mass continuity (2.7), respectively. The gravitational acceleration is denoted by g . Again, it is assumed that the perturbations be proportional to $\exp\{ikx + \omega t\}$. Substituting this into (2.89)–(2.91) one obtains the equation

$$\frac{\partial}{\partial z} \left(\rho \frac{\partial}{\partial z} v'_z \right) = k^2 \rho v'_z - \frac{k^2}{\omega^2} g v'_z \frac{\partial}{\partial z} \rho'. \quad (2.92)$$

Integration over a volume containing a part of the interface of the two fluids yields

$$\rho_1 \frac{\partial}{\partial z} v'_{1,z} - \rho_2 \frac{\partial}{\partial z} v'_{2,z} = -\frac{k^2}{\omega^2} g v'_{z,12} (\rho_1 - \rho_2), \quad (2.93)$$

where $v'_{z,12}$ denotes the value of the velocity at the interface. Treating the fluids separately, one finds from (2.92)

$$\left(\frac{\partial^2}{\partial z^2} - k^2 \right) v'_z = 0, \quad (2.94)$$

which is solved by the ansatz

$$v'_z = Ae^{kz} + Be^{-kz}. \quad (2.95)$$

For v'_z to be continuous over the interface,

$$v'_{1,z} = Ae^{kz} \quad (z < 0) \quad \text{and} \quad v'_{2,z} = Ae^{-kz} \quad (z > 0) \quad (2.96)$$

must hold. Inserting these expressions into (2.93) gives the result

$$\omega_{\text{RT}} = \sqrt{gk \frac{\rho_1 - \rho_2}{\rho_1 + \rho_2}}. \quad (2.97)$$

Thus, in case of $\rho_2 > \rho_1$ the configuration is unstable.

The Kelvin-Helmholtz instability

Another instability of fluid motion is the *Kelvin-Helmholtz (KH) instability* or *shear instability*. It occurs on the interface of two fluids moving with different velocities. This interface marks a tangential discontinuity. Again, following Landau & Lifshitz (1959), consider an incompressible medium and a small part of the discontinuity, which can be regarded as plane. Without loss of generality, choose a coordinate system comoving with one of the fluids. The other fluid moves then with the velocity \mathbf{v} , which defines the x -direction of the coordinate system. Fluid 1 with velocity $v_{1,x}$ is located at positive z and fluid 2 (resting in the chosen frame of reference) at negative z . The derivation proceeds analogous to those given above. A perturbation proportional to $\exp\{ikx + \omega t\}$ is applied to the relevant quantities as well as to the coordinates of the interface itself. Equations similar to (2.75)–(2.77) describe the system. The displacement of the discontinuity surface in z -direction due to the perturbation is denoted by $\zeta = \zeta(x, t)$ and the velocity of the movement of the surface at fixed x is given by $\partial\zeta/\partial t$. Since this velocity equals the velocity component of the fluid motion normal to the discontinuity surface, the condition

$$\frac{\partial\zeta}{\partial t} = v'_z - v_{1,x} \frac{\partial\zeta}{\partial x} \quad (2.98)$$

must hold (v'_z being the value at the surface). An ansatz for the pressure perturbation in the form

$$p' = f(z)e^{ikx + \omega t} \quad (2.99)$$

yields from the analog of equation (2.77)

$$\frac{\partial^2 f}{\partial z^2} - k^2 f = 0 \quad (2.100)$$

Therefore the pressure on side 1 (positive z) becomes

$$p'_1 = \text{const} \cdot e^{ikx + \omega t} e^{-kz}. \quad (2.101)$$

2. Theoretical Considerations

Setting the displacement ζ proportional to $\exp\{ikx + \omega t\}$, equations (2.98), (2.100) and the analog to (2.75) give

$$p'_1 = -\zeta \frac{\rho_1(\omega + ikv_{1,x})^2}{k}. \quad (2.102)$$

and on side 2 ($v = 0$)

$$p'_2 = -\zeta \frac{\rho_1 \omega^2}{k}. \quad (2.103)$$

The condition that the pressure on both sides of the interface be equal yields

$$\omega_{\text{KH}} = kv_{1,x} \frac{-i\rho_1 \pm \sqrt{\rho_1 \rho_2}}{\rho_1 + \rho_2}. \quad (2.104)$$

Owing to the existence of a positive real part in ω_{KH} , the system is unstable with respect to small perturbations. The growth rate of the perturbation increases with its wavenumber. Thus, small-scale perturbations are not suppressed in this idealized model. In real flows a shear layer of finite thickness will develop instead of the discontinuity due to finite viscosity. This will prevent small-scale perturbations from growing.

2.3.2. Corollaries from the flame instabilities

In this section, some consequences from the flame instabilities discussed in the preceding section shall be drawn, keeping in mind the situation of SN Ia explosions. After having revealed the instabilities in the linear approximation, the question arises what flame structure and flow field would establish as result of these instabilities?

The structure of the flame front is of particular interest, since one of the fundamental tasks in order to model SN Ia explosions is to determine the effective flame propagation velocity. Consider the simplified case of a flame front advancing with the constant laminar burning speed s_l independently of the flame shape. Comparing the flame propagation velocity of a planar laminar flame with the surface area A_0 to the effective speed v_{eff} of the mean position of a flame wrinkled due to instabilities (surface area $A' > A_0$) yields

$$v_{\text{eff}} = s_l \frac{A'}{A_0}. \quad (2.105)$$

The flame thus accelerates with increasing surface area. Therefore the task to determine the effective flame propagation velocity reduces to the determination of the increase in flame surface area. One has to describe the rate of that increase and to find out, whether there exists a limiting steady state of the flame structure.

Effects of the Rayleigh-Taylor and the Kelvin-Helmholtz instabilities

As discussed in the previous section, departing from the idealized models, the LD and KH instabilities will be suppressed for small wavelength perturbations. Is there a similar effect for the RT instability?

2.3. Flame instabilities

Consider the situation that occurs in SNe Ia. Here, the flame front will be RT unstable because the ashes of the thermonuclear reaction have lower density than the fuel, as argued in Section 2.2.1. As the flame is ignited near the center of the WD and propagates outward, the density stratification due to the nuclear burning is inverse to the gravitational field. Now, if the RT instability acts on the propagating burning front, it is clear that it can have effect only in the case that the timescale of its growth is larger than time for the flame to cross the length scale of the perturbation. Therefore, there exists a minimum length scale capable of deforming the flame front (Timmes & Woosley 1992):

$$\lambda_{\min} = s_l \tau_{\text{RT}}(\lambda_{\min}) \quad (2.106)$$

The time scale of the RT instability is given by

$$\tau_{\text{RT}}^2 = \omega_{\text{RT}}^{-2} = \frac{\lambda}{2\pi} \left(g \frac{\rho_u - \rho_b}{\rho_u + \rho_b} \right), \quad (2.107)$$

according to (2.97). Hence,

$$\lambda_{\min} = \frac{s_l^2}{2\pi} \left(g \frac{\rho_u - \rho_b}{\rho_u + \rho_b} \right). \quad (2.108)$$

What flow field is caused by the RT instability? In Section 2.3.1 only the linearized behavior of the flame front under the influence of instabilities was investigated. Yet the flow field will very soon be dominated by nonlinear effects. This results in large rising bubbles of light burnt material with fingers (in two dimensions) or sheets (in three dimensions) of dense fuel sinking down in between. The preference of large structures as a result of the RT instability originates from the tendency of initially smaller bubbles to merge into larger ones while rising. For the situation in SN Ia explosions this has been simulated by Reinecke et al. (1999a, 2002a,b,c), and Gamezo et al. (2003).

The general picture of a flow field dominated by the KH instability is that in the vicinity of the tangential discontinuity vortices will develop in the nonlinear regime. However, for the KH instability to occur, a tangential discontinuity is necessary. This kind of discontinuity requires the mass flux across the surface of discontinuity to vanish (see Section 2.2.1). This is, however, not the case for burning fronts, where finite mass flux across the discontinuity stabilizes the flame against the KH instability. Nevertheless the situation changes if the flow field around a burning RT-bubble is dominated by buoyant acceleration. Here, the mass flux can become negligibly small compared with the tangential velocity components (Niemeyer 1995). This system can be regarded as being similar to the situation of a tangential shear flow in a viscous fluid. Here, the mass flux across the surface does not vanish either, because of microscopic transport and this leads to a shear layer of finite thickness. The question of the stability of this modified configuration was addressed in a numerical simulation by Niemeyer (1995) and Niemeyer & Hillebrandt (1997). The authors found that the flames become unstable when the shear velocities reach the laminar burning velocities of the flame fronts.

Summarizing the effects of the RT and the KH instabilities for the situation in SN Ia explosions, one finds, that rising bubbles of light burnt material will develop surrounded

2. Theoretical Considerations

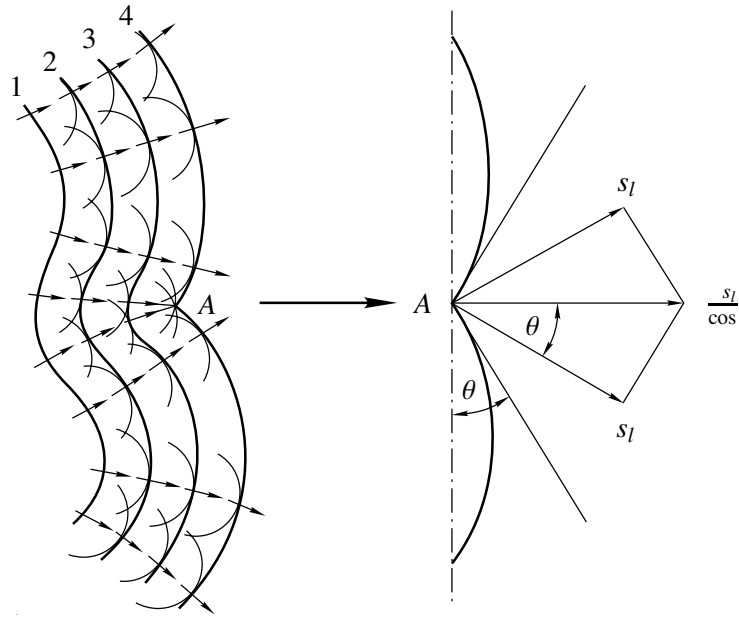


Figure 2.7.: Nonlinear effect stabilizing the flame front (adopted from Zel'dovich et al. 1980a).

by sinking dense fuel. At the interfaces strong shear flows cause the development of a vortical flow field.

The Landau-Darrieus instability: cellular stabilization

The reason why the LD instability has been ignored in all large scale SN Ia models so far is that there exists a nonlinear stabilization mechanism which limits the perturbation growth. Figure 2.7 illustrates this effect. Following Zel'dovich (1966), it can be explained in terms of geometrical considerations. The reason for the growth of the LD instability is a multi-dimensional motion of the fluid as described in Section 2.3.1. Suppose that one would shut off this fluid motion ceasing the development of the hydrodynamic instability. The self-propagation of an initially sinusoidally perturbed flame due to burning is now followed by means of Huygens' principle, that is one constructs circles of the radius $s_l \Delta t$ around each point of the front and determines the front position at $t + \Delta t$ by their envelope (see Figure 2.7, left hand side). This procedure changes the original shape of the flame. Convex regions grow while concave ones diminish. Finally, a cusp forms at the interfaces of neighboring cells (point A). Here Huygens' principle breaks down and the flame propagation enters the nonlinear regime. The propagation velocity at the cusp exceeds s_l :

$$v_{\text{cusp}} = \frac{s_l}{\cos \theta}, \quad (2.109)$$

which can be inferred from the simple vector addition illustrated at the right hand side of Figure 2.7. This effect causes a decrease of the perturbation amplitude \hat{x} which balances its increase due to the LD instability. This leads to a stabilization of the flame in a cellular shape which has been observed in experiments.

It is now straight forward to derive the steady state amplitude, which will attune as a result of the competing effects. The reduction of the perturbation amplitude due to the increased velocity of the cusps reads

$$\left(\frac{d\hat{x}}{dt}\right)_- = s_l \left(1 - \frac{1}{\cos\theta}\right). \quad (2.110)$$

Prescribing the shape of the cells as parabolae leads in case of small θ to

$$\tan\theta = \frac{4\hat{x}}{\lambda} = \frac{2\hat{x}k}{\pi} \approx \theta, \quad (2.111)$$

with λ and k denoting the wavelength and wavenumber of the perturbation, respectively. Equation (2.110) then gives

$$\left(\frac{d\hat{x}}{dt}\right)_- = -\frac{2}{\pi^2}k^2s_l\hat{x}^2. \quad (2.112)$$

Combining this expression with the result from Landau's linear stability analysis (see equation (2.86)) yields

$$\frac{d\hat{x}}{dt} = \omega_{LD}\hat{x} - \frac{2}{\pi^2}k^2s_l\hat{x}^2. \quad (2.113)$$

The quadratic damping term was not included in the linear stability analysis of Section 2.3.1. It accounts for the stabilization of the flame in a cellular pattern with the stationary amplitude

$$\hat{x}_s = \frac{\omega_{LD}\pi^2}{2k^2s_l} \quad (2.114)$$

The assumption of a parabolic cell structure allows an estimation of the effective flame propagation velocity in the cellular regime (Zel'dovich et al. 1980b). The line integral over a cell of stationary amplitude yields

$$L = \frac{\lambda}{2} \left\{ \sqrt{1 + \left(\frac{4\hat{x}_s}{\lambda}\right)^2} + \frac{1}{4\hat{x}_s} \sinh^{-1}\left(\frac{4\hat{x}_s}{\lambda}\right) \right\}. \quad (2.115)$$

Equation (2.105) now gives

$$\frac{v_{\text{cell}}}{s_l} = \frac{L}{\lambda} := 1 + \epsilon. \quad (2.116)$$

Using Landau's dispersion relation (2.86), Zel'dovich et al. (1980b) estimates the velocity increment ϵ of a cellularly shaped flame compared to a planar flame from equations (2.115) and (2.114) as

$$\epsilon = \frac{\pi^2}{24} \left(1 - \frac{1}{\mu}\right)^2. \quad (2.117)$$

2. Theoretical Considerations

This result has been applied to the conditions of SN Ia explosions by [Khokhlov \(1995\)](#). Note, however that the above relations for the amplitude and propagation velocity of the steady cellular flame can only give a rough estimate, since the approach taken here does not allow for treatment of the full nonlinear problem. An approach that is capable of doing so will be discussed in Section [2.4.2](#).

2.4. Analytical studies of nonlinear flame propagation

In this section we will review some analytical approaches to model the propagation of flame fronts, which in certain approximations give insight to the nonlinear stage of evolution. This is of interest for the present study because it sheds light on the roots of phenomena that will later be observed in our numerical investigations of the full problem. Some of the features of these simulations will be explained referring to analytical and semianalytical results based on the concepts introduced in the following. Two of them shall be briefly described in the following. Both reach the conclusion that the flame shows a preference to stabilize in a long-wavelength pattern, which may considerably exceed the wavelength λ_{crit} , that should be fastest growing according to Section [2.3.1](#). At first glance this may seem surprising, but is observed in experiments with chemical flames.

2.4.1. Stability analysis after Zel'dovich

[Zel'dovich et al. \(1980b\)](#) investigate the propagation of curved flames in cylindrical tubes. They point out, that this problem is closely related to the cellular flame propagation, the tube walls acting similar to the cusps of the flame front. The study of the flame stability in this paper is particularly interesting for us.

[Zel'dovich et al. \(1980b\)](#) describe the flame as a hydrodynamic discontinuity and assume a potential flow field upstream of it. The authors derive a flame structure that resembles a one-cell pattern filling the tube and is convex to the fuel. Analyzing the flow ahead of the flame front, they find that there exists a tangential velocity along the flame that increases from the flame tip to the tube walls. Due to this phenomenon, short-wavelength perturbations are advected toward the walls where they will be absorbed. In order to guarantee stability of the flame propagation this has to happen faster than the LD growth time. Another point that has to be taken into consideration is that a velocity gradient along the flame front introduces a stretch of the perturbation wavelength that modifies its growth rate. The combination of effects is analyzed by [Zel'dovich et al. \(1980b\)](#) in a WKB-like⁷ approach. They derive a criterion for stability relating the (finite) initial perturbation to the tube radius.

⁷semi-classical technique in quantum mechanics, developed by and named after Wenzel, Kramers, and Brillouin (see standard textbooks of quantum mechanics)

2.4.2. The Sivashinsky equation

In his analysis [Sivashinsky \(1977\)](#) derived an asymptotic nonlinear integrodifferential equation. It captures the flame evolution for the case of a potential flow ahead of the front in the limit of weak thermal expansion. Two asymptotic cases were investigated: the flame being dominated by the hydrodynamic instability or by diffusional and thermal effects, respectively. The chemistry inside the flame was modeled by a one-step reaction taking place in a narrow reaction zone. The flame model comprised the diffusion equation for the concentration of the component limiting the reaction, the heat conduction equation and the Navier-Stokes-equations (see Section 2.1.3) together with boundary conditions of constant temperatures and concentrations far ahead and beyond the flame front. The flow was assumed to be incompressible.

Appendix A provides the derivation of the Sivashinsky equation following the simplified case presented by [Sivashinsky & Calvin \(1987\)](#). This approach focuses on the description of the hydrodynamic instability and neglects diffusional and thermal effects. The perturbed flame front is parametrized by

$$x = \phi(y, t). \quad (2.118)$$

[Sivashinsky & Calvin \(1987\)](#) derive the evolution equation for ϕ ,

$$\phi_t + \frac{1}{2}\phi_y^2 = \frac{\gamma}{2}I\{\phi\}, \quad (2.119)$$

where $I\{\cdot\}$ represents a linear singular nonlocal operator defined by (A.42). It is responsible for the LD instability.

Equation (2.119) is a simplified version of the original Sivashinsky equation. A more general derivation (see [Sivashinsky 1977](#)) does not imply the condition (A.2) of a constant propagation velocity of the flame with respect to the ashes. The resulting Sivashinsky⁸ equation includes a term that describes a Markstein-like propagation behavior (cf. Section 2.2.4) of the flame front:

$$\phi_t + \frac{1}{2}\phi_y^2 = \frac{\gamma}{2}I\{\phi\} + l_M\phi_{yy}. \quad (2.120)$$

[Sivashinsky \(1977\)](#) derives an even more generalized equation that apart from the hydrodynamic (LD) instability also reproduces effects of the thermal-diffusional instability⁹. We wish to emphasize here, that the Sivashinsky equation relies on the assumption of a potential flow ahead of the front and describes the flame evolution in the limit of small γ . It also assumes that the perturbation of the flame front from a planar shape is weak.

A number of modifications of the original Sivashinsky have been proposed in literature. These models it have been widely applied in studies of the flame propagation. It is not our intention to provide a comprehensive list of references here and we thus refer to [Sivashinsky \(1983\)](#), [Gutman & Sivashinsky \(1990\)](#), [Filyand et al. \(1994\)](#), [Rahibe et al. \(1995\)](#),

⁸sometimes also called *Michelson-Sivashinsky*-equation

⁹This variant includes a ϕ_{yyyy} -term and the equation neglecting the hydrodynamical instability (by omitting the integral term) is frequently called *Kuramoto-Sivashinsky* equation

2. Theoretical Considerations

Boury & Joulin (2002), and references therein. Frankel (1990) introduces a significant improvement by an approximative equation which is not restricted to the limit of weak perturbations anymore. One possibility to infer the flame evolution from these equations is via numerical integrations (e.g. Gutman & Sivashinsky 1990). We will refer to this approach as “semianalytical” studies of flame propagation. The above equations also have been applied to the supernova problem (e.g. Blinnikov & Sasorov 1996).

2.4.3. Pole decomposition

A rather exceptional property¹⁰ of the Sivashinsky equation is, that it admits a pole-decomposition (Thual et al. 1985). This reduces the original partial differential equation to a finite set of ordinary differential equations describing the motion of the poles in the spatial derivative of ϕ in the complex plane. This provides another possibility to determine flame evolution from the Sivashinsky equation.

Differentiating (2.120) with respect to y yields

$$u_t + u\partial_y u = \Lambda u + l_M \partial_y^2 u, \quad (2.121)$$

where $u = \partial_y \phi$ following the notation of Thual et al. (1985). This equation has solutions of the form

$$u(y, t) = -2l_M \sum_{\alpha=1}^{2N} \frac{1}{y - z_\alpha(t)}, \quad (2.122)$$

corresponding to the slope of the flame front. The z_α ($\alpha = 1, 2, \dots, 2N$) denote poles in the complex plane coming in complex conjugate pairs. They move according to

$$\dot{z}_\alpha = -2l_M \sum_{\beta \neq \alpha} \frac{1}{z_\alpha - z_\beta} - i \operatorname{sign} \{\Im(z_\alpha)\}. \quad (2.123)$$

A proof that (2.122) and (2.123) satisfy (2.120) is given by Thual et al. (1985). The only constraint is that they must occur in complex conjugate pairs. Otherwise, they may be arbitrarily numerous. Their number is a constant of motion and given by the initial conditions. A mechanism for the creation of poles at later times is controversial. Solutions of (2.120) can thus be found in the form

$$\phi(y, t) = -2l_M \sum_{\alpha=1}^{2N} \log\{y - z_\alpha(t)\}. \quad (2.124)$$

Assuming 2π spatial periodicity makes it sufficient to consider only poles with real parts between $-\pi$ and π . Instead of equations (2.122) and (2.123) now

$$u(y, t) = -l_M \sum_{\alpha=1}^{2N} \cot\left(\frac{y - z_\alpha}{2}\right) \quad (2.125)$$

¹⁰shared only by very few other equations, like the Burgers, the Benjamin-Ono and the Korteweg-de Vries equations

2.4. Analytical studies of nonlinear flame propagation

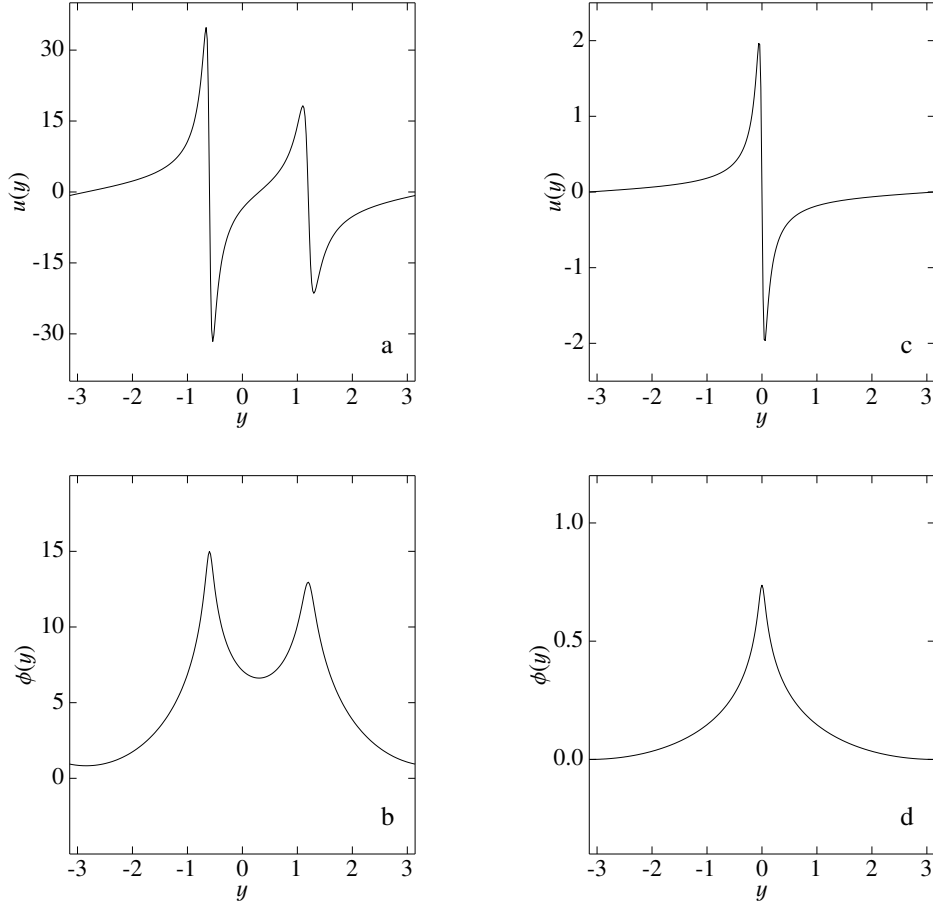


Figure 2.8.: (a),(b) example of a solution to the Sivashinsky equation with $l_M = 1$ and four poles as two complex conjugate pairs located at $(-0.6 + 0.06i)$ and conjugate complex; $(1.2 + 0.1i)$ and conjugate complex. (c) shows the slope and (d) the corresponding structure of the flame front for a two complex conjugate poles solution with $l_M = 0.05$ and $a = 0$. In all examples 2π spatial periodicity is applied.

and

$$\dot{z}_\alpha = -l_M \sum_{\beta \neq \alpha} \cot\left(\frac{z_\alpha - z_\beta}{2}\right) - i \operatorname{sign}(\Im(z_\alpha)) \quad (2.126)$$

are used. Thus solutions of (2.120) for spatially periodic perturbations read

$$\phi(y, t) = -2l_M \sum_{\alpha=1}^{2N} \log \left\{ \sin \left(\frac{y - z_\alpha}{2} \right) \right\}. \quad (2.127)$$

An example with two complex conjugate pairs of poles is plotted in Figure 2.8(a),(b).

2. Theoretical Considerations

The existence of a pole-decomposition allows to study the continuous non-linear problem in terms of a discrete N-body problem for movable singularities. For the simplest dynamical situation, i.e. two complex conjugate poles at the locations $z(t) = a(t) + ib(t)$ and $z^*(t) = a(t) - ib(t)$, it is easily seen from equation (2.126) that $a = \text{const}$ for both the non-periodic and the periodic case and the stable equilibrium configuration is $b_{\text{eq}} = l_M$ for the non-periodic and $b_{\text{eq}} = \tanh^{-1} l_M$ for the periodic situation. Figures 2.8(c) and (d) show the slope and the structure of the flame front for a two-pole equilibrium solution. Note that Figures 2.8(a),(b) do not correspond to an equilibrium configuration.

From the study of the interaction of two poles Thual et al. (1985) show that poles have the tendency to attract each other horizontally (in the real direction of the complex plane) and to repel each other vertically. Additionally, they exhibit a drift toward the real axis. Studies for N poles confirm that steady state solutions with all poles aligned parallel to the imaginary axis exist. A steady state solution in case of multiple poles is a solution of the simultaneous equations $\dot{z}_\alpha = 0, \alpha = 1 \dots 2N$. In the spatially periodic case Thual et al. (1985) derive a criterion which restricts the maximum number of poles for a steady state solution depending on l_M .

Thual et al. (1985) perform a transition from discrete dynamics to a continuous approximation at large N . They find that the poles show the tendency to concentrate near the real axis. This phenomenon is termed *pole condensation*. The concentration proceeds without limit for the non-periodic case and $N \rightarrow \infty$. In the periodic case, however, the maximum number of N is restricted and the cusp forming here will always be rounded for finite l_M , since the innermost pole will still have a finite distance from the real axis.

Concluding, we note that the pole dynamics resembles the picture of flame front evolution in Zel'dovich's reasoning (Section 2.4.1). The tendency of the poles to align parallel to the imaginary axis corresponds to the advection of perturbations toward the cusp.

2.5. Fractal descriptions of flame fronts

As discussed in the preceding sections, instabilities lead to a complex spatial flame structure. The relation of the effective flame propagation to the surface area of the wrinkled flame front (equation (2.105)) thus gave rise to attempts of capturing the flame geometry in a fractal description. In connection to the supernova problem this idea was put forward by Woosley (1990) who suggested a fractal model for the RT unstable burning front.

The numerical studies that will be presented in this work focus on scales, where the LD instability is the dominant effect. Therefore we will concentrate on a fractal description of the cellular burning regime. This topic has been addressed by Blinnikov & Sasorov (1996), Niemeyer (1995), and Niemeyer & Woosley (1997).

Fundamental to these approaches is the assumption of the formation of a hierarchy of cellular structures as a result of the nonlinear stabilization of the LD-unstable burning front. The mechanism that accounts for the build-up of the hierarchy is the superposition of a cellular structure by cells of shorter wavelength in an overall planar flame geometry or repeated cell-splitting in a spherically expanding flame. This idea is supported by exper-

imental observations and also by numerical integrations of the Sivashinsky equation (e.g. Gutman & Sivashinsky 1990, Filyand et al. (1994), and Blinnikov & Sasorov (1996)). However, the origin of the cell-splitting is controversial. In the pole decomposition approach, the number of complex poles is a constant of motion and thus the repeated cell splitting phenomenon appears to be non-generic in the class of pole-decomposable solutions as argued by Joulin (1989, 1994). Here, numerical noise in the simulations applying the Sivashinsky equation is suggested to account for the phenomenon, while Rahibe et al. (1995) suggest that solutions built with a fixed number of poles are not stable solutions of the Sivashinsky equation (in its modified version that accounts for flame expansion). This controversy, however, is not relevant for the reasoning of a fractal flame model for cellular flames in SN Ia explosions, since physical noise is expected to be present here, which can account for cell splitting anyway.

The foundation of the fractal models is the notion that a flame in a certain range of length scales can be considered as an irregular surface whose statistical properties change in a self-similar way. Self-similarity can be defined in the following way: Let A denote a surface area. Then \bar{A}_l denotes the surface area smoothed on a length scale l by filtering out all scales below l (by convolution with an appropriate low-pass filter). Consider the flame surface \bar{A}_{l_0} smoothed at l_0 and make a transition in the length scale $l' = bl_0$, $b \in \mathbb{R}$. Self-similarity then states

$$\bar{A}_{l'} = \bar{A}_{l_0} f(b), \quad (2.128)$$

$f(b)$ being a function independent of l_0 . The constraint $f(b)f(c) = f(bc)$ implies power law dependence of f . A scale range in that this similarity holds is then called similarity range. Sets $S(D)$ in n spatial dimensions whose $(n - 1)$ -dimensional surface scales self-similarly

$$\bar{A}_l \propto l^\beta \quad \rightsquigarrow \quad f(b) \propto b^\beta \quad (2.129)$$

are termed *fractals* Mandelbrot (1983). The fractal dimension D of the surface is then defined as

$$D = n - 1 + \beta, \quad (2.130)$$

where β denotes the so-called fractal excess. Consider the case of a flame front in two-dimensional space. Then the fractal dimension of the one-dimensional flame surface reads

$$D_{1d} = 1 + \beta. \quad (2.131)$$

Blinnikov & Sasorov (1996) proved analytically that a flame modeled by the Frankel equation¹¹ (Frankel 1990) obeys

$$\beta = D_0(1 - 1/\mu)^2. \quad (2.132)$$

By means of numerical simulations applying the Frankel equation, they determined $D_0 \approx 0.3$ within an error of about 50%.

¹¹That means, this model for a flame is valid only in the limit of weak thermal expansion. The authors also showed that the fractal excess β is rigorously zero for a flame modeled by the Sivashinsky equation, i.e. equation does not produce a fractal flame surface.

2. Theoretical Considerations

Niemeyer & Woosley (1997) and Niemeyer (1995) take a simplified approach and describe the flame front as a hierarchy of cells at all length scales above a critical scale l_{\min} of the order of the Markstein length. The effective front propagation speed v_i on each scale l_i is then related to the scale $l_{i-1} < l_i$ by

$$v_i = v_{i-1} + \epsilon v_i, \quad (2.133)$$

with the velocity increment defined by equation (2.117). Taking the continuum limit and assuming cell splitting to occur after a spatial dilatation interval of S gives

$$v_{\text{eff}} \approx s_l \left(\frac{l}{l_{\min}} \right)^{\epsilon / \ln S}, \quad (2.134)$$

which yields

$$\beta = \frac{\epsilon}{\ln S}. \quad (2.135)$$

This agrees with (2.132) in the functional dependence on $(1 - 1/\mu)^2$. The parameter S , however is not fixed by this model. It can be estimated by comparison with the simulation result of Blinnikov & Sasorov (1996) to $S \approx 4$.

2.6. Turbulent combustion

As has been pointed out in literature many times and recently has been confirmed by large scale supernova simulations (Reinecke et al. 2002b, Gamezo et al. 2003), turbulent combustion is the key to deflagration models of SN Ia. After introducing some basic concepts to describe turbulent flows, we will give an overview of the effects of turbulence on flame propagation. Since the fluid velocities in SN Ia explosions are mostly well below sound speed, we will restrict the discussion to turbulence in incompressible flows, i.e. $\nabla \cdot \mathbf{v} = 0$. Thus, neglecting external forces, the Navier-Stokes equation (2.16) takes the form

$$\frac{\partial \rho \mathbf{v}}{\partial t} = -\nabla \cdot (\rho \mathbf{v} \mathbf{v}) - \nabla p + \mu \Delta \mathbf{v}, \quad (2.136)$$

or in nondimensional notation¹²

$$\frac{1}{Sr} \frac{\partial \rho^* \mathbf{v}^*}{\partial t^*} = -\nabla^* \cdot (\rho^* \mathbf{v}^* \mathbf{v}^*) - \nabla^* p^* - \frac{1}{Re} \mu \Delta^* \mathbf{v}^* \quad (2.137)$$

¹²In principle, one could derive this equation from taking the limit $Ma \rightarrow 0$ of equation (2.30), but obviously, that equation then gets singular in the second term on the right hand side. Thus, the common procedure is to expand the quantities in a series of the Mach number and to analyze the equations for powers of Ma separately. Making (2.136) nondimensional applying the procedure from Section 2.1.5 does not involve the Mach number anymore, since the incompressible limit corresponds to infinite sound speed, which then cannot serve as a reference velocity anymore. Thus the reference pressure to make the second term of (2.136) dimensionless is chosen such, that it cancels out with $\rho_{\text{ref}} v_{\text{ref}}$ from the kinematic term.

The only relevant characteristic dimensionless quantity here (choosing $Sr = 1$ as discussed in Section 2.1.5) is the *Reynolds number*¹³

$$Re(l) = \frac{\rho l v(l)}{\mu}. \quad (2.138)$$

It compares inertial forces to the viscous forces at a given reference length scale. Thus, different flows show the same features as long as the Reynolds number is unchanged. Consider the Reynolds number at the integral scale $Re(L)$, where L is defined by the boundary conditions of the problem. A large number of experiments revealed distinct regimes of flow characteristics depending on $Re(L)$. In case of small Reynolds numbers $Re \lesssim 10$ (that is, the impact of the advection term is still balanced by the viscous term in the Navier-Stokes equation), the flow is stationary and laminar. For higher Reynolds numbers the advection term becomes more and more dominant. The flow adopts a quasi-stationary pattern and for $Re \gtrsim 200$ it develops spatially and temporally chaotic fluctuations. This is called fully developed turbulence and we will assume the flow to be in that state in the following paragraphs and simply refer to it as “turbulence”.

2.6.1. Basic concepts of turbulence theory

In our discussion of turbulence we will restrict ourselves to a heuristic approach instead of a more rigorous statistical description. It is founded on the concept of a *turbulent cascade* introduced by Richardson (1922). The basic element of this cascade is the *turbulent eddy*¹⁴. Turbulent eddies are produced by large scale instabilities at the integral scale L (in case of SN Ia explosions the RT and KH instabilities) and become themselves unstable. Thus they decay into successively smaller eddies of lower rotation velocity $v(l)$ forming a cascade in spatial scale space¹⁵. Since the Reynolds number is scale-dependent and decreases with smaller scales, viscosity effects become dominant at a certain scale and the turbulent eddies are dissipated into heat. The corresponding scale is termed dissipation scale or *Kolmogorov scale* l_K . Clearly, a single energy input and dissipation scale is an idealized concept. However, if both scales are separated well enough, then one can expect a scale range in between where a constant amount of kinetic energy ϵ is gradually transported from larger to smaller eddies. This amount should be equal to the energy input and the energy dissipation. Otherwise energy would pile up or disappear at a certain scale, which would be unphysical. The described scale range is called *inertial range*,

$$l_K \ll l \ll L, \quad (2.139)$$

and here turbulence can be expected to be isotropic and inviscid.

¹³The scale-dependent Reynolds number defined by (2.138) is sometimes also called *turbulent Reynolds number*.

¹⁴A precise definition of an “eddy” is lacking; it is meant to be a turbulent motion localized within a region of a specific size.

¹⁵A more exact formulation would define the reference velocity $v(l)$ in (2.138) as the statistical velocity fluctuation $v'(l)$ at scale l .

2. Theoretical Considerations

Kolmogorov (1941) formulated this model in a more quantitative way. He based his considerations on three hypotheses: on local isotropy, on a universal form of the statistics of the small scale motions, and on similarity of intermediate-scale turbulent motions. We will not follow this approach in detail here and refer to Pope (2000) for further reading. Nevertheless, some of the consequences of Kolmogorov's hypotheses shall be summarized in the following.

Starting from the notion that the properties of the flow in the inertial range are completely determined by the quantities ρ , l , and $v(l)$, one finds that the only combination of these possessing the dimension of a rate of specific energy [erg g⁻¹ s⁻¹] is (Landau & Lifshitz 1959)

$$\epsilon \propto \frac{v(l)^3}{l}. \quad (2.140)$$

yielding

$$v(l) = v(L) \left(\frac{l}{L} \right)^{1/3}. \quad (2.141)$$

Inserting (2.141) into (2.138) one obtains

$$Re(l) = \frac{\rho v(l) l^{4/3}}{\mu L^{1/3}} = Re(L) \left(\frac{l}{L} \right)^{4/3}. \quad (2.142)$$

It is clear that the dissipation of turbulent kinetic energy takes place at scales l_K where viscous effects become dominant, i.e. $Re(l_K) \sim 1$. Thus

$$l_K \sim \frac{L}{Re^{3/4}}. \quad (2.143)$$

The spectrum of the turbulent kinetic energy in the inertial range can be derived giving (Pope 2000)

$$E(k) = C \epsilon^{2/3} k^{-5/3}, \quad (2.144)$$

where $k = 2\pi/l$ denotes the wavenumber of the turbulent eddy of size l and C is a universal constant.

In the discussion so far, we neglected external forces. However, on large scales gravity is relevant for the SN Ia problem and the presence of a gravitational field can modify the turbulent scaling. According to Bolgiano (1959) and Obukhov (1959) velocity fluctuations then follow the relation

$$v(l) \propto l^{5/3}. \quad (2.145)$$

The effects of this modifications on supernova explosion models are discussed by Niemeyer & Kerstein (1997a,b).

2.6.2. Turbulent burning regimes and resulting length scales

The most important question regarding turbulence with respect to the subject of this work is: How does turbulence interact with combustion? The theory of turbulent combustion

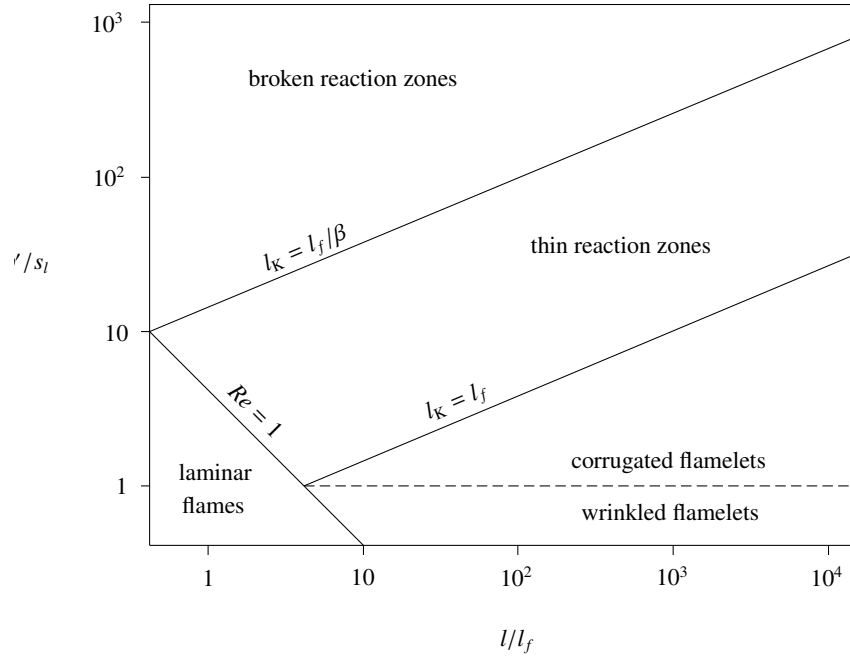


Figure 2.9.: Regimes of premixed turbulent combustion (following Peters 1999).

stems mainly from applications of chemical flames. Here one distinguishes between premixed and non-premixed turbulent combustion. Of course, a mixture of reactants is not required in thermonuclear reactions as in SN Ia. Here, combustion is consequently similar to premixed combustion, which will be discussed henceforth.

Turbulence alone is a complex field and combustion processes add even more complications. Therefore the theory of turbulent combustion is still under continuous development and only a fraction of phenomena can be regarded as being well understood. One of the most important notions in this subject is probably, that turbulent combustion takes place in distinct regimes, which are accessible by different methods of theoretical modeling. One way of classification is to relate the turbulent velocity fluctuations (normalized to the laminar burning velocity) to the corresponding length scale (normalized to the flame width). A diagram of this classification was introduced by Borghi (1985) and Peters (1986) and is shown in Figure 2.9. The transition regions between the regimes are determined here by comparing the velocity of turbulent eddies at certain scales characteristic to the flame to the laminar burning velocity. As long as the turbulent eddies of a given size are much slower than the laminar burning velocity, the flame will burn through the eddies before they can affect its structure. The corresponding regime is called *wrinkled flamelet regime*. The turbulent flow bends the flame slightly on scales large compared to the flame width

2. Theoretical Considerations

and thereby increases the flame surface (and thus the total energy release rate according to equation (2.105)). However, it does not affect the inner structure of the flame (and thus microscopically the flame velocity remains s_l). This changes in the *corrugated flamelet regime*, where the turbulent eddies now noticeably alter the shape of the flame, but still leave its inner structure unaffected. The transition scale l_{Gibs} between the regimes is defined by comparing the eddy turnover time to the flame crossing time at that length:

$$\tau_{\text{eddy}}(l_{\text{Gibs}}) = \tau_{\text{flame}}(l_{\text{Gibs}}), \quad (2.146)$$

yielding

$$v(l_{\text{Gibs}}) = s_l. \quad (2.147)$$

The scale l_{Gibs} is identified with the *Gibson scale* (Peters 1986). If the Kolmogorov scale of the turbulent flow becomes smaller than the thermal width of the flame, then turbulent motion starts to modify the structure of the preheat zone and the flame enters the *thin reaction zone* regime. Eddies are now able to distribute burning material and to disrupt the closed flame front. Therefore, the region $l_K < l_f$ is also termed *distributed burning regime*. At an even smaller Kolmogorov scale the turbulent eddies finally start to dominate the structure of the reaction zone (l_f/β , see Section 2.2.2). The corresponding regime is that of broken reaction zones which ultimately turns into the so-called well-stirred reactor. Except for the flamelet regimes all other turbulent burning modes modify the inner structure of the flame, whose propagation velocity then deviates from s_l accordingly.

We would like to emphasize at this point, that the above classification and in particular the transition regions only apply to chemical combustion processes. Here, the Prandtl number is $Pr \sim 1$. This is not true for the situation in SN Ia explosions, where $Pr \sim 10^{-3}$ (cf. Section 2.2.5). The possible changes have been investigated by Niemeyer & Kerstein (1997a). The authors point out that the transition between the flamelet and the thin reaction zones regimes may shift toward stronger turbulent fluctuations for lower Prandtl numbers.

2.6.3. Active turbulent combustion

The consideration in the preceding section neglected any feedback of burning on the turbulent flow. However, it may be true that the expansion of the burnt material inside the flame significantly increases the strength of turbulent fluctuations. As Niemeyer & Woosley (1997) point out, the efficiency of such a feedback mechanism need not be large in order to have substantial impact on the supernova model. Following from the fact that thermal expansion behind the flame is the origin of the LD instability, one could conclude, that the resulting stabilization of the flame in a cellular pattern will prevent a feedback between burning and turbulence. However, it is not known what will happen if the cellular stabilization breaks down. This can possibly occur due to the turbulent cascade from above. Niemeyer & Woosley (1997) predict a flame structure that still resembles a cellular pattern but now in a random orientation that inhibits self-stabilization. They assume in a first approximation that this effect is most efficient on the scale of the expanding regions themselves and does not significantly couple to turbulent velocities on other scales. It thus

2.7. Deflagration to detonation transition

affects only the fluctuation amplitudes and not the spectrum. The simplest case is then a constant scale-independent growth rate, that is a function of the expansion parameter only, leading to an exponential growth of the turbulent velocity fluctuations.

The conjecture of a feedback mechanism attempts to reason a possible production of turbulence by the flame itself and was thus termed “*active turbulent combustion*” (ATC) by Niemeyer & Woosley (1997). The idea is supported by Kerstein (1996) in a study addressing the evolution of a flame that is missing any stabilization mechanism. Taking into account the two-way interaction between the turbulent burning velocity of the flame and the turbulent velocity fluctuations ahead of it, the author concludes that such a flame model does not admit a statistically steady propagation resulting in an increase of the turbulent flame speed until finite Mach-number effects predominate. Kerstein (1996) argues that this runaway is caused either by a self-acceleration mechanism or by a purely statistical effect and predicts a power law growth of the turbulent burning velocity. The growth exponent is sensitive to the details of the flame dynamics and strongly configuration-dependent and therefore remains undetermined in that study.

2.7. Deflagration to detonation transition

In Section 2.2.1 we showed that the conservation laws admit two distinct modes of the propagation of a flame, the subsonic deflagration mode and the supersonic detonation mode. These modes are also different in the mechanism of flame mediation: microphysical transport processes on the one hand and shock waves on the other. Here arises the question, whether or not a transition from one mode into the other is possible and what mechanisms can account for it.

In fact, *deflagration to detonation transitions* (DDTs) are observed in experiments with terrestrial flames. Here, however, it appears that mostly interaction with obstacles in the combustion chamber or the walls of it (e.g. Shchelkin 1940) account for the transition. These effects do, of course, not apply to astrophysical explosions. In general, the physics of the DDT is not well understood.

Nevertheless, mechanisms providing a DDT in the context of SN Ia explosions have been suggested in literature (for a discussion of those see Niemeyer 1999). Assume that the turbulization of the flame proceeds passively by the turbulent eddy cascade evoked by large-scale instabilities. Then the creation of a pressure spike that turns into a detonation can only be achieved by burning a critical volume of fuel in sound-crossing time (or less). Augmentation of the flame surface by turbulent wrinkling (captured for instance in a fractal model of the flame) is unlikely to allow for this, since in the flamelet regime the flame acceleration is determined by the turbulent velocity fluctuations. These, however, cannot exceed sound speed in standard SN Ia explosion models (Niemeyer & Woosley 1997).

Thus, a mechanism that is often proposed to account for a possible DDT in SNe Ia is the induction time gradient mechanism (Zel'dovich et al. 1970). It was applied to the supernova problem by Blinnikov & Khokhlov (1986) and later re-examined by Khokhlov et al. (1997). This mechanism is based on the pre-conditioning of the temperature gradient

2. Theoretical Considerations

in a sufficiently large volume. The combustion wave moving along this volume may then build up a pressure wave that turns into a detonation. However, [Niemeyer \(1999\)](#) argues that the preconditioning of a smooth temperature gradient in large volumes is very unlikely to be achievable in SN Ia explosions. As an alternative route for a DDT he suggests acceleration of the flame propagation via active turbulent combustion.

3. Astrophysical background

After the introduction of the physical fundamentals in the last chapter we now turn to the synthesis of the astrophysical model of Type Ia Supernova explosions focusing on the aspects relevant to the objective of this work. Here we will apply the concepts described in the previous chapter and infer constraints on the numerical implementation of this model that will be subject of the next chapter. The astrophysical model that sets the framework for our study has already been discussed briefly in Chapter 1. We will now assemble the theory summarized in the preceding chapter into this model.

3.1. Thermonuclear combustion in Type Ia Supernovae

3.1.1. Models for the explosion mechanism

In our work, we focus on Chandrasekhar-mass models for SN Ia. Despite the general agreement that C+O white dwarfs are promising progenitors for SNe Ia, the details of the explosion mechanism is still controversial. At $T \sim 10^{10}$ K the carbon burning reaction rate scales as $\dot{S} \sim T^{12}$ (Hansen & Kawaler 1994). This confines the reaction to very thin layers and gives rise to the formation of a flame. The fundamental question in models of the explosion is, how does the flame propagate through the star? We will now give a brief overview over the various mechanisms that have been proposed leading to the problem we address in our study.

- *The detonation model* was first applied in a numerical simulation by Arnett (1969). A spherically symmetric detonation wave was initiated near the center of the WD and propagated outward. Criteria for the spontaneous formation of a detonation wave have been investigated by Blinnikov & Khokhlov (1986) and Woosley (1990). They reach the conclusion, that a detonation can initiate for certain prerequisites. A prompt detonation as explosion model produces enough energy required for a SN Ia event. However, ahead of a supersonic detonation wave the fuel cannot expand and is therefore incinerated at the high densities of an equilibrium white dwarf. This results in the almost complete conversion of the material in nickel-peaked nuclear statistical equilibrium (Arnett 1969), which is in conflict with the intermediate mass elements observed in SN Ia spectra. These nucleosynthetic problems and uncertainties on the possibility of the initiation of the detonation wave rule out a pure detonation scenario as a standard model for SN Ia explosions.
- *The deflagration model* assumes the flame propagating in the subsonic deflagration mode. As explained in Section 2.2.2, the laminar burning speed of the deflagration

3. Astrophysical background

flame is determined by microphysical transport processes. For conditions of carbon burning in C+O WDs it is highly subsonic (Timmes & Woosley 1992) and therefore the flame propagates far too slowly to explain SN Ia explosions. The expansion of the star will then quench burning before the WD gets unbound. On the other hand, this model can cure the problem of nucleosynthesis, since rarefaction waves can travel ahead of the flame with sound speed and lower the fuel density prior to burning. Thus the material can partly be processed to intermediate mass elements.

This model undergoes a significant improvement when multidimensional effects are taken into account. Since the deflagration front is unstable (cf. Section 2.3), turbulent effects will increase the effective propagation velocity of the flame. This has been incorporated as a free parameter in one-dimensional models leading to reasonable results both regarding the energy release of the explosion and the produced spectra. Recent three-dimensional numerical simulations (Reinecke et al. 2002b, Gamezo et al. 2003) that self-consistently model turbulent effects confirmed that the star can successfully be unbound in that way.

- *The delayed detonation (DD) model* conjoins the advantages of the deflagration and the detonation models. It was put forward by Ivanova et al. (1974), Khokhlov (1991), and Woosley & Weaver (1994). Burning starts out in the slow deflagration mode and the star can pre-expand. When the flame reaches fuel of a certain transition density ρ_{tr} , flame propagation turns into a detonation and burns the star until the flame is quenched at low densities. This detonation is an easy way to explain the energy release necessary for a SN Ia explosion. The important notion in this model is that a detonation at low fuel densities can lead to only partial burning and is therefore capable to generate intermediate mass elements. Another possible advantage of this model derives from a problem of current three-dimensional implementations of the deflagration model. The Rayleigh-Taylor bubbles being the origin of the turbulent flame acceleration cause considerable amounts of unburnt C+O matter to remain in “fingers” near the center of the star, which are eventually in conflict with spectral SN Ia observations. A detonation wave initiated at later stages of the evolution could be capable to burning out those fingers and to process the unburnt material.

The main disadvantage of the DD model is that the transition density is an artificially introduced parameter. The mechanism of a possible DDT is completely unclear yet (if there exists one at all, cf. Niemeyer 1999) and thus the exact value of ρ_{tr} is unknown, although phenomenological models suggest $\rho_{\text{tr}} \sim 1 \times 10^7 \text{ g cm}^{-3}$ (Höflich & Khokhlov 1996, Iwamoto et al. 1999).

- *The pulsational delayed detonation (PDD) model* (Arnett & Livne 1994a,b) is similar to the DD model in the sense that it combines an initial deflagration with a later detonation. The flame is assumed to propagate in the initial deflagration phase with its laminar burning speed and pre-expands the star. Due to the slow flame velocity, the burning front stalls and fails to unbind the star. The WD then re-contracts giving the interface between burnt and unburnt material enough time to mix and to become

3.1. Thermonuclear combustion in Type Ia Supernovae

nearly isothermal. Compressional heating finally triggers a detonation at densities that are lower than that prior to the first expansion phase. Höflich & Khokhlov (1996) employ this scenario in a phenomenological one-dimensional model and conclude that it may account for sub-luminous SN Ia. However, the assumption that the flame propagates with the pure laminar burning velocity in the deflagration phase seems unrealistic, because of the flame instabilities and the resulting turbulent flame acceleration. Recent multidimensional deflagration models (Reinecke et al. 2002b) demonstrated that taking into account these effects, the star will get unbound and not recontract.

The studies in this work apply to the deflagration model and possibly to the DD model. We will study the flame evolution in the deflagration mode on scales, where the flame propagates in a cellular pattern. This burning regime is yet unexplored by full hydrodynamical simulations. It could modify the effective flame propagation velocity and eventually (as suggested by Niemeyer & Woosley 1997) provide some insight into possible DDT mechanisms.

3.1.2. Turbulent combustion in Type Ia supernova explosions

The flame instabilities that play an important role in the SN Ia problem and their effects on the flow and the flame shape in SN Ia explosions have been discussed in Section 2.3. On large scales, the RT and KH instabilities predominate and lead to the development of a turbulent cascade.

The fact that turbulent effects will be present can be easily understood from estimating the Reynolds number around a RT bubble. With the typical size of a RT bubble of $L \sim 10^7$ cm, its characteristic shear velocity of $\sim 10^7$ cm s⁻¹, $\mu \sim 1$ cm² s⁻¹ (cf. Section 2.2.5), and $\rho \sim 10^9$ g cm⁻³, one obtains $Re(L) \sim 10^{14}$ and can thus expect pronounced turbulent effects. According to equation (2.143) this yields the Kolmogorov scale $l_K \sim 10^{-3}$ cm. The large scale space in between the integral length scale L and l_K allows a turbulent cascade to build up.

Consequently, thermonuclear burning in SN Ia explosions is subject to turbulent combustion. Classification of the turbulent combustion in SN Ia yields burning in the flamelet regime for fuel densities $\gtrsim 10^7$ g cm⁻³, and transition to distributed burning (thin reaction zones regime) below.

A relevant scale to classify the burning regime is the Gibson scale¹, defined by (2.147). This scale is, however, afflicted with considerable uncertainties. Firstly, the fitting formula by Timmes & Woosley (1992) for the laminar burning velocity s_l does not as well agree with the simulation data as the authors claim. Nevertheless, we applied this expression for s_l in our simulations. Because of the power law dependence of l_{Gibs} on s_l this may cause large discrepancies. Secondly, the power law exponent is dependent on the scaling relation

¹Note, that we use a slightly generalized notion of this term which was originally introduced in connection with Kolmogorov scaling. In this work, the ‘‘Gibson scale’’ is defined solely by equation (2.147) with no presumed scaling.

3. Astrophysical background

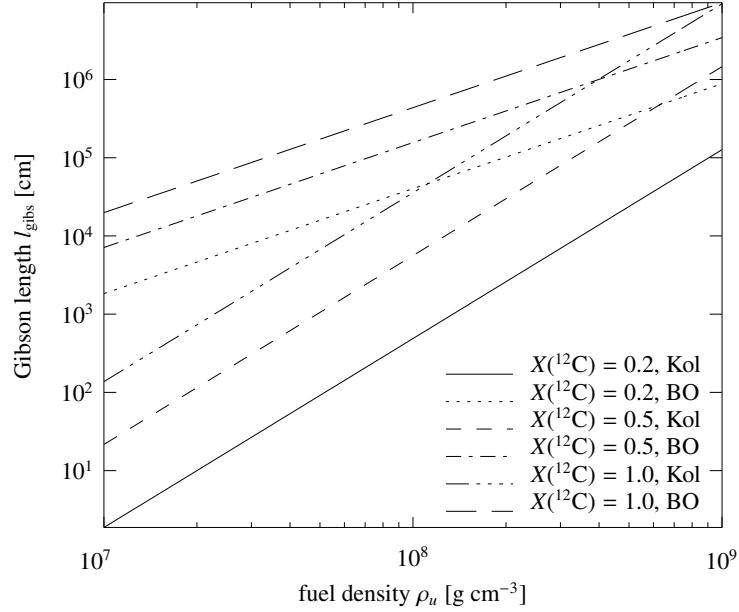


Figure 3.1.: Gibson length as function of fuel density for various compositions $X(^{12}\text{C})$, $X(^{16}\text{O}) = 1.0 - X(^{12}\text{C})$, assuming Kolmogorov (Kol) or Bolgiano–Obukhov (BO) scaling.

of the eddy cascade. For Kolmogorov scaling one obtains from (2.147)

$$l_{\text{Gibs}} = L \left(\frac{s_l}{v(L)} \right)^3 \quad (3.1)$$

and Bolgiano–Obukhov scaling gives

$$l_{\text{Gibs}} = L \left(\frac{s_l}{v(L)} \right)^{5/3}. \quad (3.2)$$

Figure 3.1 displays the Gibson length for Kolmogorov and Bolgiano–Obukhov scaling for different fuel compositions, assuming the Timmes & Woosley (1992) fit for s_l to be correct in the density range of consideration. Despite the obvious uncertainties we will assume throughout our astrophysical and numerical modeling that the Gibson scale is well above the thermal width of the flame and burning therefore takes place in the flamelet regime. We shall arrange the computational domains in our simulations in a way that effects on scales around 10^4 cm can be explored. Since simulations at these scales do not resolve the inner structure of the flame, we will develop numerical techniques that treat the flame in the discontinuity approximation (see Chapter 4).

3.2. Hydrodynamical considerations

3.2.1. The equation of state for white dwarf matter

White dwarfs are the relics of stars that have ceased nuclear burning and are therefore not supported against gravitational collapse by thermal pressure anymore. By contracting from their former size they reach extremely high densities defining them as part of the class of compact objects besides neutron stars and black holes. The interior of a WD resembles a very dense solid with an ion lattice surrounded degenerate electrons. These provide the cold degenerate fermion pressure that supports the WD against further contraction.

The mass of a WD is limited by the Chandrasekhar mass to be less than $\sim 1.4M_{\odot}$. Typical parameters are (Balberg & Shapiro 2000) a radius of $\sim 5 \times 10^8$ cm, a mean density of $\sim 10^7$ g cm $^{-3}$, and a mean pressure of $\sim 10^{24}$ dyne cm $^{-2}$. Since $\mathcal{G}M/Rc^2 \sim 10^{-4}$, general relativistic effects are not relevant to our model. Temperatures of the white dwarf depend on its pre-ignition evolution and age but are below $\sim 10^9$ K.

The equation of state of white dwarf matter is governed by the electron gas. Further contributions come from the photon gas, the nuclei, and—at high densities—from electron positron pair creation. We will neglect solidification effects, allowing the treatment of the nuclei as an ideal gas. Corrections due to Coulomb interaction between electrons and baryons are only marginal and thus will be neglected here. This leads to the following constituents of the equation of state:

- The *electrons* are both degenerate and relativistic to a degree that depends on the Fermi energy E_F and the temperature. The degeneracy is partially lifted in the burning products due to the higher temperature. Defining the relativistic Fermi integrals as

$$F_k(\eta, \beta) = \int_0^{\infty} \frac{x^k (1 + \frac{1}{2}\beta x)^{1/2}}{e^{-\eta+x} + 1} dx, \quad k > -1, \quad (3.3)$$

energy and pressure of the electron gas are given by

$$e_e = \frac{8\pi\sqrt{2}}{h^3} m_e^4 c^5 \beta^{5/2} [F_{3/2}(\eta, \beta) + \beta F_{5/2}(\eta, \beta)] \quad (3.4)$$

$$p_e = \frac{16\pi\sqrt{2}}{3h^3} m_e^3 c^5 \beta^{3/2} \left[F_{3/2}(\eta, \beta) + \frac{1}{2}\beta F_{5/2}(\eta, \beta) \right], \quad (3.5)$$

where the parameters

$$\eta = \frac{E_F}{k_B T} \quad \text{and} \quad \beta = \frac{k_B T}{m_e c^2} \quad (3.6)$$

characterize the degrees of degeneracy and the effects of relativity, respectively. Here, c denotes the vacuum speed of light.

- The *nuclei* are entirely ionized owing to the high prevailing temperatures and pressures. The high densities under consideration justify the assumption of thermal equi-

3. Astrophysical background

librium between electron gas and nuclei. This allows the unique definition of a temperature. Thus, the nuclei are described in a good approximation by the Maxwell-Boltzmann statistics yielding

$$e_n = \frac{3}{2} \mathcal{R} T \rho \sum_i \frac{X_i}{A_i}, \quad (3.7)$$

$$p_n = \frac{2}{3} e_n. \quad (3.8)$$

- The contribution of the *photons* is assumed to follow a local black-body spectrum and are obtained from the Stefan-Boltzmann law:

$$e_\gamma = \frac{4 \sigma_{\text{SB}}}{c} T^4, \quad (3.9)$$

$$p_\gamma = \frac{e_\gamma}{3}, \quad (3.10)$$

with σ_{SB} denoting the Stefan-Boltzmann constant.

- *Electron-positron pair creation* may occur if the photon energy exceeds $2m_e c^2$ and corresponding cells in phase space of the electrons are unoccupied. This effect is noticeable in the hot ashes. The contributions of the electrons and positrons follow equations (3.4) and (3.5) with the modified Fermi integrals (Cox & Giuli 1968)

$$\mathcal{F}_k(\eta, \beta) = \left[F_k(\eta, \beta) + F_k\left(-\eta - \frac{2}{\beta}, \beta\right) \right]. \quad (3.11)$$

Neutronization may occur in the reaction products (Nomoto & Kondo 1991, Brachwitz et al. 2000), but this effect will not be taken into account here.

3.2.2. External forces: gravity

Obviously, the self-gravity of the white dwarf star introduces an external force to the hydrodynamical equations (cf. Section 2.1):

$$\mathbf{f} = -\nabla\Phi, \quad (3.12)$$

where Φ is the gravitational potential. As stated in Section 3.2.1 it is well-justified to apply the Newtonian limit, where Φ is given by Poisson's equation $\Delta\Phi = 4\pi\mathcal{G}\rho$. The numerical solution of this elliptic partial differential equation introduces some complications especially in parallel computational code designs (cf. Reinecke 2001). However, we concentrate on scales where gravitational effects are negligible and will therefore neglect external forces in the following.

4. Numerical implementation

In principle, a full numerical implementation of a system describing the propagation of a thermonuclear flame in white dwarf matter would require to solve concurrently for the hydrodynamics (Section 2.1.4), nuclear kinetics (Section 2.1.6), and transport properties together with an appropriate equation of state (Section 3.2.1). In one dimension, this has been done by Timmes & Woosley (1992) and currently efforts are taken to perform such simulations in more than one dimension (Fryxell et al. 2000). In principle, this task is feasible with today's computer power, although simulations of this kind will not be able to reach the global scales of the white dwarf.

The reason for this is the vast range of relevant length scales involved in the Type Ia supernova explosion problem. From the scales of the white dwarf star (radius $\sim 5 \times 10^8$ cm) and the integral scales of turbulence due to the RT instability ($\sim 10^7$ cm) down to the scales of the inner structure of the thermonuclear flame it spans about 10–11 orders of magnitude. Clearly, there is no hope to be able to resolve the full scale space in numerical simulations in foreseeable future.

Thus, one has to apply approximations in order to be able to perform flame simulations on scales of the white dwarf star (LSCs, see Section 1.3) or on intermediate scales, such as the Gibson scale, which we will tackle in this work. A model that is physically rigorous at these scales is the discontinuity approximation for the flame (Section 2.2.1).

The general reactive flow equations (see Section 2.1.4) incorporate the hydrodynamics as well as microphysical transport phenomena that determine the internal flame structure and are responsible for flame mediation. The discontinuity approximation does not resolve the inner structure of the flame front. Hence, the laminar flame velocity s_l is not intrinsically given, but must be provided as an external parameter. In that sense, flame propagation is now decoupled from the remaining parts of the flow equations and can be treated separately in the numerical scheme. This results in an operator splitting.

Apart from the microphysical phenomena, there still remains complex interplay between flame propagation and hydrodynamics. The density contrast across the flame affects the flow field and the flame in turn is advected by the flow. These effects have to be modeled by an appropriate way of flame/flow coupling.

Our numerical implementation of the thermonuclear combustion model is based on methods described by Reinecke et al. (1999b), but differs in the treatment of the flame/flow coupling, which turns out to be essential for the present study (cf. Section 5.3.1).

In this chapter, the numerical models applied in the simulation of thermonuclear burning fronts in SN Ia shall be introduced, starting with the hydrodynamical model. After discussing the implementation of the equation of state and the thermonuclear reactions, the flame model and the flame/flow coupling method shall be described.

4. Numerical implementation

4.1. Fluid dynamics

The general equations of reactive fluid dynamics (2.20)–(2.23) state an inhomogeneous system of nonlinear partial differential equations in Eulerian formulation that have to be solved numerically. In terms of mathematical classification they are a mixed system containing hyperbolic and parabolic contributions, namely the advection terms and the diffusion terms, respectively.

As mentioned before, we will treat flame propagation and hydrodynamics of the flow separately. The former will be numerically modeled in a parametrized way, neglecting the underlying microphysical mechanisms (see Section 4.4). This gives more flexibility in the choice of scales which will be investigated in this study and is a necessary prerequisite¹ for the large-scale simulations of SN Ia explosions performed by Reinecke et al. (2002a). The treatment of the hydrodynamics part will be discussed in the following paragraphs. First we note, that the discretization on an Eulerian grid introduces a considerable simplification of the hydrodynamics equations. Since viscous effects are expected to become relevant on scales smaller than the numerical resolution reached in our simulations, it is sufficient to employ the (physically) simpler Euler equations (cf. Section 2.1.2) rather than the complete Navier-Stokes (cf. Section 2.1.3) equations to model the fluid flow. The error introduced by the discretization outweighs the error resulting from the omission of the viscosity terms substantially.

4.1.1. Operator splitting

The general reactive flow equations (2.20)–(2.23) can be written as a vector equation:

$$\frac{\partial}{\partial t} \mathbf{U} + \frac{\partial}{\partial x} \mathbf{I} + \frac{\partial}{\partial y} \mathbf{J} + \frac{\partial}{\partial z} \mathbf{K} = \frac{\partial}{\partial x} \mathbf{L} + \frac{\partial}{\partial y} \mathbf{M} + \frac{\partial}{\partial z} \mathbf{N} + \mathbf{Q}. \quad (4.1)$$

The vectors in that equation are given in Appendix B on page 139. We neglect external forces, since these are not relevant to the situation that will be simulated. The vectors on the left hand side of equation (4.1) correspond to the hyperbolic Euler equations (cf. Section 2.1.2), while the flame microphysics is governed by the terms on the right hand side of it.

Following the strategy proposed by Strang (1968), an operator splitting is applied, which allows subsequent treatment of the Euler equations and the flame propagation. Additionally, the terms are splitted in direction. Provided the change of the state vector \mathbf{U} during a time step is small, the operator splitting ansatz provides a reasonable approximation to the solution of the vector equation (4.1), though this method is mathematically not rigorous.

In this section, the methods which are used to solve the first part of the problem, namely the Euler equations,

$$\frac{\partial}{\partial t} \mathbf{U} + \frac{\partial}{\partial x} \mathbf{I} + \frac{\partial}{\partial y} \mathbf{J} + \frac{\partial}{\partial z} \mathbf{K} = 0 \quad (4.2)$$

¹Another approach, put forward by Khokhlov (1993), Gamezo et al. (2003), is to artificially broaden the inner structure of the flame so that it can be resolved in large scale calculation. This is achieved by modification of the diffusion coefficients and the reaction rates. This method is frequently called *reaction-diffusion approach*.

shall be discussed.

4.1.2. Discretization on a computational grid

In our numerical implementation, the Euler equations are discretized on an equidistant regular Cartesian grid. The computational domain is therefore divided into computational cells of quadratic shape with the conserved quantities defined at the cell centers. These represent the mean value of the surrounding cell. We employ explicit discretization.

Consider a the density of a conserved quantity a . Its numerical discretization in one spatial dimension will be denoted by

$$a_i^n \approx a(x_i, t_n) \quad (4.3)$$

in the following.

4.1.3. Numerical solution of the Euler equations

Numerical fluid dynamics distinguishes various strategies to solve the underlying hyperbolic system of partial differential equations. General strategies are classified into *finite-difference* and *finite-volume methods*. A brief review of the fundamental ideas will be given here, following in parts [LeVeque \(1998\)](#), where further details can be found. The foundation of our numerical implementation is a finite-volume approach, which is applied in the solution of the Euler equations. Moreover, it forms the basis of the specific method of flame/flow coupling that shall be used.

Finite-difference methods

Finite-difference methods are based on the balance equations in differential form, such as (2.6). The derivatives in those equations are replaced by difference quotients and the system is then evolved in time iteratively. Finite-difference methods in this basic implementation share severe disadvantages. Due to inevitable discretization errors the schemes are locally non-conservative, i.e. the integral value of the conserved quantities (mass, momentum, and energy) changes. Because the balance equations in their differential form allow only for continuous solutions, finite-difference techniques are incapable of resolving discontinuities, such as shock waves. These are smeared out and thus require rather high resolutions.

Finite-volume methods

Finite-volume methods on the other hand are based on the integral formulation of the balance equations (2.1). These schemes do not directly compute the changes in the conserved quantities that are defined in the centers of the computational cells, but rather determine the fluxes of mass, momentum, and energy across the interfaces between individual cells in a certain time interval followed by a corresponding update of the cell mean values. This

4. Numerical implementation

approach guarantees the exact balance of gains and losses in each cell and the scheme is thus conservative by construction. Although finite-volume schemes are numerically much more expensive than simple Taylor-expansion based finite-difference methods, they require much less resolution in order to reach the same accuracy and therefore are much more efficient—especially in multi-dimensional simulations.

While in finite-difference methods a_i^n is regarded as an approximation to a single value $a(x_i, t_n)$, finite-volume methods view this expression as an average value of $a(x_i, t_n)$ over some interval Δx (“grid cell”). Splitting the domain into N intervals

$$\mathcal{V}_i = [x_{i-1/2}, x_{i+1/2}],$$

where the integer indices denote centers of the interval and half-valued indices its boundaries in the following, yields

$$a_i^n \approx \frac{1}{\Delta x} \int_{\mathcal{V}_i} a(x, t_n) dx. \quad (4.4)$$

Conservativity of the scheme (with exception of the boundaries of the domain) is achieved by applying the integral form of the conservation law (2.5) to each grid cell:

$$\begin{aligned} \frac{1}{\Delta x} \int_{\mathcal{V}_i} a(x, t_{n+1}) dx &= \frac{1}{\Delta x} \int_{\mathcal{V}_i} a(x, t_n) dx \\ &\quad - \frac{1}{\Delta x} \left[\int_{t_n}^{t_{n+1}} j(a(x_{i-1/2}, t)) dt - \int_{t_n}^{t_{n+1}} j(a(x_{i+1/2}, t)) dt \right] \end{aligned} \quad (4.5)$$

In general, the quantities $a(x_{i-1/2}, t)$ and $a(x_{i+1/2}, t)$ along the cell edges vary with time and it is thus impossible to evaluate the corresponding fluxes $j(a(x_{i-1/2}, t))$ and $j(a(x_{i+1/2}, t))$ exactly. Nevertheless, (4.5) suggests that a conservative numerical scheme should follow the ansatz

$$a_i^{n+1} = a_i^n - \frac{\Delta t}{\Delta x} (F_{i+1/2}^n - F_{i-1/2}^n)$$

where $F_{i+1/2}^n$ is a numerical approximation to the average flux along $x = x_{i+1/2}$:

$$F_{i+1/2}^n = \frac{1}{\Delta t} \int_{t_n}^{t_{n+1}} j(a(x_{i+1/2}, t)) dt. \quad (4.6)$$

Godunov’s method

The obstacle to be overcome in order to compute the hydrodynamical fluxes across the cell interfaces is that these depend on the values of the conserved quantities a_i^n that are defined at the cell centers. Thus, values from the cell centers have to be extrapolated to the cell boundaries by some means. Conceptually simplest is the approach suggested by **Godunov**

(1959). There, the mean values are extrapolated in a piecewise linear way, yielding the following piecewise constant approximation to $a(x, t_n)$:

$$a(x, t_n) \approx \tilde{a}^n(x, t_n) = a_i^n; \quad x \in \mathcal{V}_i.$$

This approximation forms discontinuities at the cell interfaces, which in turn define Riemann problems consisting of the conservation law for the quantity \tilde{a}^n

$$\frac{\partial}{\partial t} \tilde{a}^n + \frac{\partial}{\partial x} j_{\tilde{a}^n} = 0$$

together with the initial condition

$$\tilde{a}^n(x, t_n) = \begin{cases} a_i^n, & \text{if } x < x_{i+1/2} \\ a_{i+1}^n, & \text{if } x \geq x_{i+1/2}. \end{cases}$$

The key feature that is exploited in the scheme is the self-similarity of the solution to this Riemann problem, i.e. it is constant along rays $(x - x_{i+1/2})/t = \text{const}$. Let $a^*(a_i^n, a_{i+1}^n)$ denote the exact solution to the Riemann problem along the ray $x/t = 0$. Then the solution $\tilde{a}^n(x, t)$ to the conservation laws over the time interval $t \in [t_n, t_{n+1}]$ is

$$\tilde{a}^n(x_{i+1/2}, t) \equiv a^*(a_i^n, a_{i+1}^n), \quad (4.7)$$

provided the time step is small enough to prevent waves from the Riemann problem from traveling further than Δx . This solution is now inserted into (4.6) yielding the numerical fluxes of conserved quantities across the cell borders:

$$F_{i+1/2}^n = \frac{1}{\Delta t} \int_{t_n}^{t_{n+1}} j(\tilde{a}^n(x_{i+1/2}, t)) dt. \quad (4.8)$$

Thus, the main features of the Godunov scheme are that a shock-capturing property is inherent in the solver by construction and that the method is conservative. The main drawback is that it is rather diffusive compared to more elaborate finite-volume approaches.

Time-step determination

In the last paragraph, the condition was posed that the time step must be taken small enough so that there is no interaction of waves from neighboring Riemann problems with the states at the given interface. This is a special case of the CFL criterion (Courant et al. 1928). In general, this criterion states that a numerical method can be convergent only if its numerical domain of dependence contains the true domain of dependence of the partial differential equation, at least in the limit as Δt and Δx go to zero (cf. LeVeque 1998). If the method described in the last paragraph would end up with the explicit construction of the cell averages according to (4.4) from the solution of the Riemann problem, then this would mean that the time step must be taken small enough to prevent interaction of waves

4. Numerical implementation

from neighboring problems. However, using the flux formula (4.6) requires only constant values of the conserved quantities at the cell interfaces over the time step, which hence can be roughly twice as large:

$$\Delta t \leq \frac{\Delta x}{s_{\max}}, \quad (4.9)$$

where s_{\max} denotes the largest possible wave speed, i.e. in time step n it is given by the advection velocity v and the sound speed c_s :

$$s_{\max}^n = \max_i \{ |v_i^n| + c_{s,i}^n \}. \quad (4.10)$$

The CFL criterion is necessary but not sufficient for stability of the scheme. In order to ensure stability it is thus common practice to reduce the time step by a factor $C_{\text{CFL}} \in [0.2, 0.8]$.

Reconstruction scheme

Although it is conservative, the Godunov scheme has the severe drawback of being still rather diffusive compared to other methods. This is cured in so-called *high-resolution shock capturing methods*. The key to those methods is to reconstruct the boundary values of the Riemann problem from the cell averages in higher order. In case of Godunov's method, a piecewise constant reconstruction is applied yielding only first-order accuracy. A better alternative would be to implement a piecewise linear reconstruction instead. Even more sophisticated is the approach suggested by [Colella & Woodward \(1984\)](#). The mean values are interpolated by local parabolae constrained to be monotonic inside the cells. Accordingly, this scheme is called *Piecewise Parabolic Method* (PPM).

In order to avoid still possible oscillations at the discontinuities so-called slope-limiter and flux-limiter methods have been introduced (cf. [LeVeque 1998](#)). PPM comprises appropriate limiting.

Approximate Riemann solver

Exact Riemann solvers require the knowledge of the spectral decomposition of the system that is to be solved. If this is not available or numerically too expensive, one usually falls back on approximative Riemann solvers. Several of those have been proposed in literature, and in connection with PPM usually the efficient numerical method suggested by [Colella & Glaz \(1985\)](#) is applied.

4.1.4. Boundary conditions

Since numerical simulations are performed on a finite grid, it is necessary to prescribe certain boundary conditions at the edges of it. One way would be to develop a special treatment of the boundary cells, which have no neighbors in one direction and consequently cannot be updated in the manner described above. A simpler approach which is commonly applied in numerical schemes is to introduce "ghost cells" at the edges of the

computational grid and to update the edge cells in exactly the same way as all other cells. The contents of the ghost cells is set prior to each time step and is determined by the physical type of boundary that is to be set. The required number of ghost cells depends on the employed hydrodynamics solver and in particular on the reconstruction scheme.

- *Periodic boundary conditions* are easily imposed by mapping the contents of cells next to the opposite edge of the domain into the ghost cells. Suppose Q_0^n and Q_N^n represent the contents of the marginal cells at time n at opposite sides of the grid. Then Q_0^{n+1} is determined using the contents of the ghost cell Q_{-1}^n which is set to equal Q_N^n .
- *Reflecting boundary conditions* mimic a line of symmetry or a solid wall. These are enforced by simply mirroring the contents of near-edge cells into the ghost cells. Hence $Q_{-1}^n = Q_1^n$ in this case.
- *Outflow boundary conditions* are meant to ensure that no waves can enter from these edges of the domain. This can be achieved by extrapolating from near-edge cells into the ghost cells, thereby effectively computing the Riemann fluxes on the basis of the near-edge cells alone. The simplest approach is zero-order extrapolation: $Q_{-1}^n = Q_{-2}^n = \dots = Q_0^n$.
- *Inflow boundary conditions* will also be employed in our numerical simulations. Here the quantities in the ghost cells are artificially imposed with a velocity pointing toward the domain. In conjunction with outflow boundaries on the opposite side of the domain they provide a possibility to establish a computational grid that comoves with some object—in our particular case with the flame front.

4.1.5. Implementation of the hydrodynamics solver

In order to solve the Euler equations, we employ the PROMETHEUS implementation (Fryxell et al. 1989). It is based on the Piecewise Parabolic Method (PPM) suggested by Colella & Woodward (1984). However, the problems to be investigated in our numerical simulations are highly subsonic. Therefore, PPM is certainly not the most effective scheme available. A future implementation of alternative hydrodynamics solvers that are tailored to the specific situation, such as incompressible low Mach-number approximations, would be desirable.

To avoid multidimensional Riemann problems, directional splitting is applied in the two-dimensional simulations. Time steps for the integration are determined according to the CFL criterion with a time step reduction by a factor of $C_{\text{CFL}} = 0.8$.

4.2. Equation of state

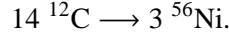
Since the calculation of the Fermi-integrals needed to determine the electron-contribution and the electron-positron pair creation is numerically too expensive to be carried out during

4. Numerical implementation

the simulation, these contributions are read off a recalculated table via bilinear interpolation. The table entries were located on a regular grid in the $(\log T, \log \rho)$ -plane and spanned ranges of $\log_{10} T [\text{K}] = [3; 11]$ and $\log_{10} \rho [\text{g cm}^{-3}] = [-5; 11]$ (Reinecke 2001).

4.3. Thermonuclear reactions

The thermonuclear burning considered in the presented simulation takes place at fuel densities above 10^7 g cm^{-3} and terminates in nuclear statistical equilibrium (NSE), which consists mainly of nickel. Because of the high computational costs of the implementation of a full nuclear reaction network (see Section 2.1.6) and due to the fact that our intention is the investigation of flame dynamics rather than a correct nucleosynthetic description of SNe Ia, we simplify the nuclear processes to an effective reaction (see also Steinmetz et al. 1992):



This yields a specific energy release of $q = 9.28667 \cdot 10^{17} \text{ erg g}^{-1}$ (Audi & Wapstra 1995). Consequently, we model the initial composition as being pure carbon.

4.4. Flame model

The method that is applied in our simulations to parameterize the flame propagation is based on the so-called level-set technique that was introduced by Osher & Sethian (1988).

As argued in Section 3.1.2, it is justified to treat the thermonuclear flame as a discontinuity in the state variables in simulations at scales we aim at. This picture does not resolve the inner structure of the flame and therefore the laminar burning velocity s_l has to be taken as a parameter from direct numerical simulations. We use the results by Timmes & Woosley (1992) (cf. Section 2.2.5, equation (2.73)).

For the purpose of describing the flame in this “burning front approach” the level-set technique is particularly well suited.

4.4.1. The level-set technique

The central idea of the level-set method is to associate the flame with a moving hypersurface $\Gamma(t)$, which is the zero level set of a function $G(\mathbf{x}, t)$:

$$\Gamma(t) := \{\mathbf{x} \mid G(\mathbf{x}, t) = 0\}. \quad (4.11)$$

In principle, there is no constraint on G away from the front and it thus could be chosen arbitrarily. However, it is convenient to prescribe G to be a signed distance function

$$|\nabla G| \equiv 1 \quad (4.12)$$

with respect to the flame front and with $G < 0$ in the unburnt material and $G > 0$ in the ashes. This is illustrated in Figure 4.1

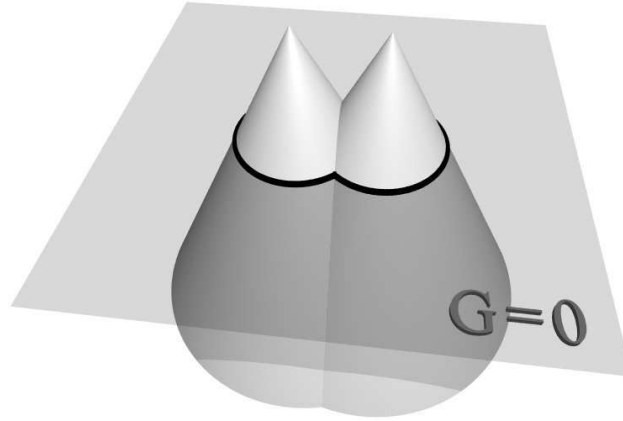


Figure 4.1. Illustration of the G -function according to equation (4.12). The zero level set of G (black curve) corresponds to the location of the flame front (courtesy of M. Reinecke).

4.4.2. The G -equation

Follow the path \mathbf{x}_P of a point P attached to the propagating front in Eulerian frame of reference. Its motion will obviously be determined by the advection due to fluid motion and propagation due to burning of the front:

$$\dot{\mathbf{x}}_P = \mathbf{v}_u + s_u \mathbf{n}, \quad (4.13)$$

where \mathbf{v}_u , s_u , and \mathbf{n} denote the fluid velocity in the fuel region, the flame propagation speed with respect to the unburnt material, and the normal vector to the front, respectively. The latter will be defined to point toward the unburnt material by

$$\mathbf{n} = -\frac{\nabla G}{|\nabla G|}, \quad (4.14)$$

which becomes possible by fixing G as in equation (4.12).

The value of G on the trajectory of such a point is zero by definition. Hence the total time derivative of G on the trajectory vanishes:

$$\frac{dG(\mathbf{x}_P)}{dt} = \frac{\partial G(\mathbf{x}_P)}{\partial t} + \nabla G(\mathbf{x}_P) \cdot \dot{\mathbf{x}}_P := 0. \quad (4.15)$$

This condition yields together with equations (4.13) and (4.14) the temporal evolution of G ,

$$\frac{\partial G}{\partial t} = -\nabla G(\mathbf{x}_P) \cdot \dot{\mathbf{x}}_P = -(\mathbf{v}_u + s_u \mathbf{n}) \cdot (-\mathbf{n} |\nabla G|) = (\mathbf{v}_u \mathbf{n} + s_u) |\nabla G| \quad (4.16)$$

for points located on the front. This equation is often termed the “ G -equation” in literature. It bears physical meaning only for points at the front, since s_u is undefined elsewhere.

To apply this formula to the region of fuel and ashes, the velocities have to be spread out from the front.

4. Numerical implementation

4.4.3. Re-initialization

Additional measures have to be taken in order to preserve the G -function's property of being a distance function (4.12). One way, according to Sussman et al. (1994), is to employ a pseudo time iteration of

$$\frac{\partial G}{\partial \tau} = \frac{G}{|G| + \epsilon} (1 - |\nabla G|), \quad (4.17)$$

until convergence to $|\nabla G| = 1$ is reached. Values used in our numerical implementation are $\Delta \tau \approx 0.1 \Delta x$ and $\epsilon \approx \Delta x$. Further measures (Reinecke et al. 1999b) have to be taken to prevent this algorithm from affecting the zero level set of G , since this would correspond to an unphysical shift of the flame front. Also topological changes of the flame require a correction of the G field. For a detailed discussion of these methods we refer to Reinecke (2001).

4.5. Flame/flow coupling

In the context of the finite-volume method we apply to discretize the hydrodynamics, the cells cut by the flame front (“mixed cells” in the following) contain a mixture of burnt and unburnt states. Therefore the quantity \mathbf{v}_u needed in (4.16) is not readily available. One strategy to circumvent this problem is the so-called “passive implementation” of the level-set method (Reinecke et al. 1999b). There it is assumed that the velocity jump is small compared to the laminar burning velocity and \mathbf{v}_u is approximated by the average flow velocity. An operator splitting approach for the time evolution of G (4.16) yields the advection term due to the fluid velocity in conservative form which is identical to the advection equation of a passive scalar. This part can be treated by the PROMETHEUS implementation of the PPM method. Front propagation, energy release, and species conversion due to burning are performed in an additional step.

The strategy we use is called “complete implementation” by Reinecke et al. (1999b). It was developed by Smiljanovski et al. (1997) and enables us to reconstruct the exact burnt and unburnt states in mixed cells. This allows accurate treatment of (4.16). The main advantage is that it now becomes possible to treat flows of burnt and unburnt material over cell boundaries separately. This prevents the flame front from smearing out over several cells as it does for the “passive implementation”. The flame front is resolved as a sharp discontinuity without any mesh refinement, which would lead to very small CFL timesteps. The “complete implementation” consisting of in-cell reconstruction and flux-splitting schemes will be reviewed in the following paragraphs. The description focusses on two-dimensional simulations.

4.5.1. Geometrical information

A prerequisite of the in-cell reconstruction and flux-splitting schemes is the knowledge of geometrical quantities, such as the front normal \mathbf{n} , the unburnt volume fraction of mixed

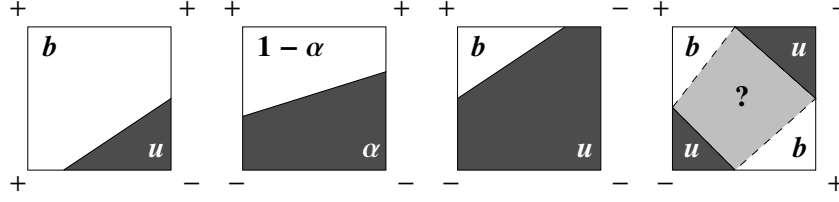


Figure 4.2.: Determination of α in mixed cells. The signs on the cell corners denote the sign of G at these locations (adopted from Reinecke et al. 1999b).

cell, and the unburnt fraction of the interface area between the cells. The normal vector of the flame front can be directly derived from the G field using equation (4.14).

Although not necessarily needed for the in-cell reconstruction, the level set method provides a convenient way to determine the curvature κ of the flame front (Sethian 1996):

$$\kappa = \nabla \cdot \mathbf{n} = \nabla \cdot \frac{\nabla G}{|\nabla G|} = \frac{G_{xx}G_y^2 - 2G_xG_yG_{xy} + G_{yy}G_x^2}{(G_x^2 + G_y^2)^{3/2}}. \quad (4.18)$$

This quantity is eventually used in a burning law according to Markstein (1951) (cf. Section 2.2.4).

The unburnt volume fraction α of a cell is obtained from the intersections of the zero level set of the G -function with the cell interfaces. Connecting these intersection points with straight lines results in a piecewise linear approximation of the flame in the cells. Then, α is obtained by calculating the area behind the connecting line. This procedure is depicted in Figure 4.2. The rightmost sketch shows a situation, where the geometry is ambiguous. In these (fortunately rare) cases we choose that α of the two possibilities, which is closest to the value of the preceding time step.

4.5.2. In-cell reconstruction

With this geometrical information it is now possible to reconstruct the exact states of burnt and unburnt material in each mixed cell from the given average quantities. This is done by setting up a system of equations. The first three equations of that *reconstruction system of equations* describe the cell averages of the conserved quantities mass, momentum, and total energy as linear combinations of the unburnt and the burnt part of the cell:

$$\bar{\rho} = \alpha\rho_u + (1 - \alpha)\rho_b \quad (4.19)$$

$$\bar{\rho\mathbf{v}} = \alpha\rho_u\mathbf{v}_u + (1 - \alpha)\rho_b\mathbf{v}_b \quad (4.20)$$

$$\overline{\rho e_{\text{tot}}} = \alpha\rho_ue_{\text{tot},u} + (1 - \alpha)\rho_be_{\text{tot},b}. \quad (4.21)$$

Here, ρ stands for the mass density, $\rho\mathbf{v}$ for the momentum density, and ρe for the density of the total energy. Again, the indices u and b denote the unburnt and burnt quantities respectively.

4. Numerical implementation

In Section 2.2.1 we derived how continuity of mass flux density, momentum flux density, and energy flux density over the flame front yield the Rankine-Hugoniot jump conditions and the Rayleigh criterion. To incorporate the former into the equation system it is convenient to split the velocity vector into a normal part \mathbf{v}_n and a tangential part \mathbf{v}_t with respect to the front. Equation (4.20) then reads

$$\bar{\rho}\bar{v}_n = \alpha\rho_u v_{u,n} + (1 - \alpha)\rho_b v_{b,n} \quad (4.22)$$

and equation (2.46) gives

$$\bar{v}_t = v_{u,t} = v_{b,t}. \quad (4.23)$$

The Rayleigh (2.48) criterion and the Hugoniot jump condition (2.49) for the internal energy $e_{\text{int}} = e_{\text{tot}} - \mathbf{v}^2/2$ read

$$(\rho_u s_u)^2 = \frac{p_u - p_b}{V_b - V_u} \quad (4.24)$$

and

$$e_{\text{int},b} - e_{\text{int},u} = \Delta h_0 - \frac{1}{2}(p_b + p_u)(V_b - V_u). \quad (4.25)$$

The equation of state provides the pressures

$$p_u = p_{\text{EOS}}(\rho_u, e_{\text{int},u}, \mathbf{X}_u) \quad \text{and} \quad p_b = p_{\text{EOS}}(\rho_b, e_{\text{int},b}, \mathbf{X}_b), \quad (4.26)$$

where \mathbf{X} denotes the mass fractions of the species. In Section 2.2.1 we considered the rest frame of the flame front. Thus, $v_{u,n}$ and $v_{b,n}$ in equation (2.38) are of the same value as the laminar flame speed with respect to fuel and ashes, $s_u (= s_l$ according to our notation) and s_b , respectively, but they have opposite signs. This equation hence yields for the jump of normal velocities across the flame front at rest

$$s_b = s_l \frac{\rho_u}{\rho_b}. \quad (4.27)$$

For a moving flame Galilean invariance²

$$v_{u,n} - v_{b,n} = s_b - s_l \quad (4.28)$$

(taking into account the opposite signs of the fluid velocities and the burning speeds) yields

$$v_{b,n} - v_{u,n} = s_u \left(1 - \frac{\rho_u}{\rho_b} \right) \quad (4.29)$$

as a further equation of the system. Additionally, a burning rate law prescribing the laminar burning velocity (e.g. in terms of the front geometry) must be provided. The reconstruction system of equations consists of (4.19), (4.21), (4.22), (4.24), (4.25), (4.26), and (4.29).

²Note that $v_{u,n}$ and $v_{b,n}$ here correspond to the moving flame front and should rather be denoted as $v'_{u,n}$ and $v'_{b,n}$ in order to avoid confusion with the variables used in equation (2.38)

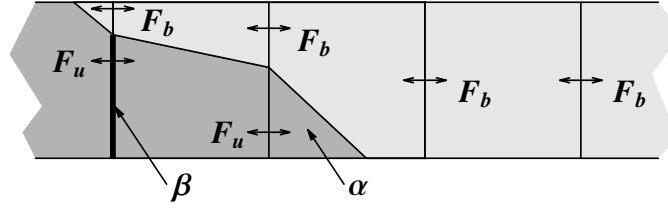


Figure 4.3.: Determination of the total flux over a cell interface as a linear combination of fluxes of burnt and unburnt material (adopted from Reinecke et al. 1999b).

Assuming the composition of the fuel and the ashes as known, we end up with eight equations for the unknown quantities $\rho_u, \rho_b, v_{n,u}, v_{n,b}, e_{i,u}, e_{i,b}, p_u,$ and p_b . Thus the nonlinear reconstruction system of equations is closed and can be solved iteratively.

To solve that system we reduce it to four equations in the unknown variables $\rho_u, \rho_b, e_u,$ and e_b and employ the MINPACK implementation (Moré et al. 1980) of Powell's hybrid scheme (Powell 1970).

4.5.3. Flux-splitting

In addition to the accurate treatment of the G -equation (4.16), the knowledge of the exact burnt and unburnt states allows for the separate handling of the numerical fluxes of burnt and unburnt material in the finite-volume hydrodynamics solver. Again, these fluxes are interpreted as linear combinations of two single fluxes: the flux resulting from the unburnt part of the cell F_u and the flux resulting from the burnt part F_b . Imagine a computational cell as composed of two volume parts containing fuel and ashes separately. Then the cell interface can be divided into a part β adjoining to fuel and a part $(1 - \beta)$ adjoining to ashes (see Figure 4.3). The fluxes F_u and F_b are being weighted with β and $(1 - \beta)$, respectively. Since the front usually moves over a time step, we take the time averages of the interface fractions, $\bar{\beta}$ for the unburnt cell part and $(1 - \bar{\beta})$ for the burnt cell part:

$$\bar{\beta} = \int_{t_n}^{t_{n+1}} \beta dt \quad (4.30)$$

The total flux \bar{F} of a conserved quantity over the cell interface is now given by

$$\bar{F} = \bar{\beta}F_u + (1 - \bar{\beta})F_b. \quad (4.31)$$

This flux-splitting procedure guarantees that the newly computed mixed state is consistent with the volume parts α and $(1 - \alpha)$ to be computed in the next time step. It also prevents the burning front from smearing out by assuring that for example in the situation depicted in Figure 4.3 no unburnt material flows over the third cell interface from the left.

4. Numerical implementation

4.5.4. Treatment of the source terms

So far, we have neglected that a flame generates source terms in species and energy, which have to be dealt with in addition. Taking into account the species source term $\omega_{X_{\text{fuel}}}$, the mass fraction evolution (2.22) reads

$$\frac{\partial}{\partial t}(\rho X_{\text{fuel}}) + \nabla \cdot (\rho X_{\text{fuel}} \mathbf{v}) = \rho \omega_{X_{\text{fuel}}}. \quad (4.32)$$

In a finite-volume approach employing directional splitting, the x -sweep is discretized as

$$(\rho X_{\text{fuel}})_{i,j,k}^{n+1} = (\rho X_{\text{fuel}})_{i,j,k}^n - \frac{\Delta t}{\Delta x} \left(F_{i+1/2,j,k}^{n+1/2}(\rho X_{\text{fuel}}) - F_{i-1/2,j,k}^{n+1/2}(\rho X_{\text{fuel}}) \right) - (\rho \omega_{X_{\text{fuel}}})_i^n \Delta t. \quad (4.33)$$

The numerical fluxes are determined according to Section 4.1.3. Now the task is to determine the species source term $\rho \omega_{X_{\text{fuel}}}$ which then enters the energy balance. Smiljanovski et al. (1997) introduce a method for an explicit evaluation of the term. Reinecke et al. (1999b) follow this approach. We summarize their implementation here to point out the difference to our implementation. The different treatment of the source terms may be part of the reason why Reinecke et al. (1999b) were not able to apply the complete implementation of the level set method to more complex problems, while it is successfully used in the present work. Reinecke et al. (1999b) perform the species and energy conversion steps after the in-cell reconstruction in mixed cells. Here, the amount of matter consumed over a time step reads

$$\Delta m = \int_{t_n}^{t_{n+1}} A s_l \rho_u dt, \quad (4.34)$$

where A denotes the flame surface in the cell. For the x -sweep in directional splitting this yields

$$\Delta m_x = \int_{t_n}^{t_{n+1}} n_x^2 A s_l \rho_u dt. \quad (4.35)$$

The square of the x -component of the flame normal results from projections of the flame surface and flame speed. The ratio of the projected flame surface and the cell interface in cell i is approximately given by $|\bar{\beta}_{i+1/2} - \bar{\beta}_{i-1/2}|$ resulting in the following expressions for the source terms for species and energy:

$$\Delta X_{\text{ashes},i} = \frac{\Delta t}{\Delta x_i} \frac{\rho_{u,i}}{\bar{\rho}_i} |s_{u,i} n_{x,i} (\bar{\beta}_{i+1/2} - \bar{\beta}_{i-1/2})| \quad (4.36)$$

$$\Delta X_{\text{fuel},i} = -\Delta X_{\text{ashes},i} \quad (4.37)$$

$$\Delta e_{\text{tot},i} = \Delta h_0 \Delta X_{\text{ashes},i}. \quad (4.38)$$

Schmidt (2001) points out that this method can raise severe complications, which may cause a failure of the reconstruction. The reason is that the species evolution is solved in a conservative way whereas the G -evolution is non-conservative. This leads eventually

to a discrepancy between the front shape represented by the zero level-set of G and the species field. In order to avoid these problems, [Schmidt \(2001\)](#) suggests an algorithm for an implicit evaluation of the reaction term with help of the G -function. He introduces a “predictor” of the energy in the hydrodynamics module which is then corrected after the reconstruction. We follow this suggestion in our implementation in a slightly modified version according to [Gröbl \(1999\)](#). The energy balance equation reads

$$\frac{\partial}{\partial t}(\rho e_{\text{tot}}) + \nabla \cdot (\mathbf{v}\rho e_{\text{tot}} + p) = -\Delta h_0 \rho \omega_{X_{\text{fuel}}} = -\Delta h_0 \left(\frac{\partial}{\partial t}(\rho X_{\text{fuel}}) + \nabla \cdot (\rho X_{\text{fuel}} \mathbf{v}) \right), \quad (4.39)$$

making use of equation (4.32). Its discretized form is

$$\begin{aligned} \frac{(\rho e_{\text{tot}})_{i,j,k}^{n+1} - (\rho e_{\text{tot}})_{i,j,k}^n}{\Delta t} + \frac{1}{\Delta x} \left(F_{i+1/2,j,k}^{n+1/2}(\rho e_{\text{tot}}) - F_{i-1/2,j,k}^{n+1/2}(\rho e_{\text{tot}}) \right) = \\ -\Delta h_0 \left(\frac{(\rho X_{\text{fuel}})_{i,j,k}^{n+1} - (\rho X_{\text{fuel}})_{i,j,k}^n}{\Delta t} + \frac{F_{i+1/2,j,k}^{n+1/2}(\rho X_{\text{fuel}}) - F_{i-1/2,j,k}^{n+1/2}(\rho X_{\text{fuel}})}{\Delta x} \right). \end{aligned} \quad (4.40)$$

Unless the source terms are evaluated, $(\rho X_{\text{fuel}})_{i,j,k}^{n+1}$ remains unknown and the energy evolution cannot be computed. However, it is possible to determine a predictor $(\rho e_{\text{tot}})_{i,j,k}^*$ by ignoring the source term:

$$\frac{(\rho e_{\text{tot}})_{i,j,k}^* - (\rho e_{\text{tot}})_{i,j,k}^n}{\Delta t} = -\frac{1}{\Delta x} \left(F_{i+1/2,j,k}^{n+1/2}(\rho e_{\text{tot}}) - F_{i-1/2,j,k}^{n+1/2}(\rho e_{\text{tot}}) \right). \quad (4.41)$$

After the reconstruction of burnt and unburnt states in the mixed cell, it can be corrected appropriately. [Schmidt \(2001\)](#) introduces a more general scheme for accomplishing this, but in our case the procedure reduces to a single step since we assume—in addition to complete fuel consumption—the unburnt material to consist entirely of fuel. Thus, $X_{\text{fuel},u} \equiv 1$, so that

$$(\rho X_{\text{fuel}})_{i,j,k}^{n+1} = (\alpha \rho_u X_{\text{fuel},u})_{i,j,k}^{n+1}, \quad (4.42)$$

which can easily be evaluated after reconstruction. The correction of the energy predictor then reads

$$\begin{aligned} (\rho e_{\text{tot}})_{i,j,k}^{n+1} = (\rho e_{\text{tot}})_{i,j,k}^* - \Delta h_0 \left(\frac{(\rho X_{\text{fuel}})_{i,j,k}^{n+1} - (\rho X_{\text{fuel}})_{i,j,k}^n}{\Delta t} \right. \\ \left. + \frac{F_{i+1/2,j,k}^{n+1/2}(\rho X_{\text{fuel}}) - F_{i-1/2,j,k}^{n+1/2}(\rho X_{\text{fuel}})}{\Delta x} \right). \end{aligned} \quad (4.43)$$

5. Results and discussion

In this chapter, results of the numerical simulations of flame evolution will be presented and discussed. It is organized in three parts, the first concerning tests to verify the numerical implementation, the second investigating the flame evolution for propagation into quiescent fuel, and the third discusses results of studies of the flame interaction with vortical fuel flows.

5.1. Some verification tests of the implementation

The appropriate tool for our investigation is the “complete implementation” of the level set scheme (see Section 4.5). The reason for this is that it provides an accurate coupling between the flame propagation and the flow field, which the “passive implementation” cannot afford. This statement will be supported by a simulation comparing the two algorithms (see Section 5.3.1).

Some verification tests of the “complete implementation” have already been performed by Smiljanovski et al. (1997) (who also validated the technique by comparison with the Russian RUT experiments) and Reinecke et al. (1999b). Our computer code is a direct successor of that developed by Reinecke et al. (1999b). Since parts of it have been changed in this work (e.g. new implementation of the method in FORTRAN 90, changes in the treatment of the source terms, parallelization), it seems appropriate to repeat some of the tests of the numerical implementation here. One has to keep in mind that the aim of this work, i.e. the investigation of the flame evolution, crucially depends on the accuracy of the methods used.

First of all, the propagation of a one-dimensional flame is investigated. Since a truly one-dimensional implementation of the flame propagation would require some changes in the code, we study a “pseudo one-dimensional” flame instead. That is, the computational domain has been set to the minimal extend in y -direction, namely 4 grid cells. Additionally, we impose reflecting boundaries in this direction. In x -direction, the domain of 15×10^3 cm was divided into 300 grid cells with a reflecting boundary to the left and an outflow condition to the right. The flame was placed initially at $x = 500$ cm. The fuel density was set to $\rho_u = 5 \times 10^8$ g cm⁻³. We refer to Table 5.1 on page 90 for the complete set of initial values. The initial velocity was set to zero on the entire domain. The resulting profiles of density, total energy, velocity, and concentration of ¹²C are plotted in Figure 5.1. It is evident, that the two constant states of burnt and unburnt material are separated by only one “mixed cell”, meeting the theoretical expectations. This result is in excellent agreement with Reinecke et al. (1999b). These authors also point out that the “passive

5. Results and discussion

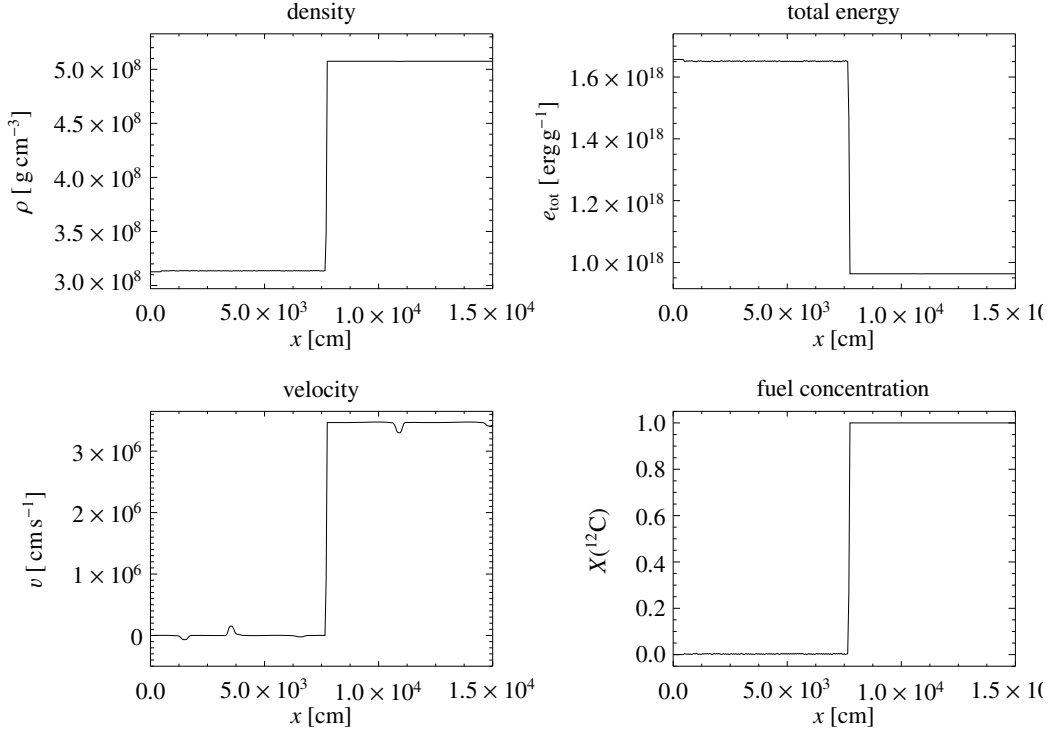


Figure 5.1.: Profiles of density, total energy, velocity and fuel concentration at $t = 0.8$ ms

implementation” of the level set method differs considerably from the results of the “complete implementation”. The former smears out the flame front over a number of grid cells and obscures the velocity profile.

We notice that there occur some minor bumps in the velocity profile of our implementation. These are probably caused in cases when the flame enters a new cell. To cure this problem, [Schmidt & Klein \(2001\)](#) suggest a special reconstruction procedure in case of small burnt or unburnt volume fractions, which is not applied here.

A second test concerned the propagation velocity of the flame front. This quantity was measured in the pseudo one-dimensional simulation described above. The reflecting boundary condition on the left hand side of the domain ensured zero velocity in the burnt material. Thus, together with a density jump of $\mu = \rho_u/\rho_b = 1.62$ equation (4.29) gives for the propagation velocity with respect to the grid

$$v_{\text{grid}} = v_u + s_l = \mu s_l = 9.06 \times 10^6 \text{ cm s}^{-1}. \quad (5.1)$$

Figure 5.2 compares this value with measurements from the simulation. The excellent agreement achieved here is not very surprising, since the value of the fluid velocity is exactly reproduced in the “complete implementation” (cf. Figure 5.1). On contrast, the

5.1. Some verification tests of the implementation

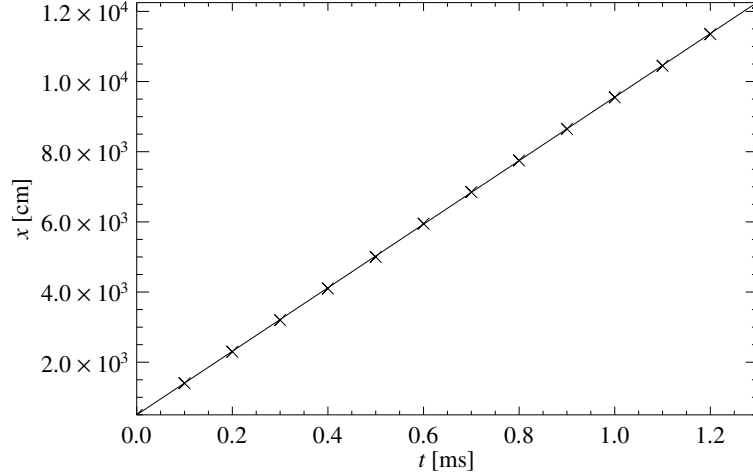


Figure 5.2.: Propagation of a one-dimensional flame front. The solid line indicates the expected motion with $v_{\text{grid}} = 9.06 \times 10^6 \text{ cm s}^{-1}$.

“passive implementation” deviates substantially in the flame propagation speed (see [Reinecke et al. \(1999b\)](#)), in that it lags behind the theoretical expectation.

In order to test the isotropy of the algorithm, a simulation of a spherically expanding flame was performed again setting the fuel density to $\rho_u = 5 \times 10^8 \text{ g cm}^{-3}$. In contrast to [Reinecke et al. \(1999b\)](#) this is done in a parallelized version of the code, where the domain was divided into four sub-squares. Deviations from the exact spherical shape (cf. [Figure 5.3](#)) occur after some time of flame evolution but are reasonably small. In comparison to the result of [Reinecke et al. \(1999b\)](#), no additional distortion of the flame shape due to the parallelization can be noted. However, the speed of the flame propagation considerably falls short of the theoretical expectation (cf. [Figure 5.3b](#)). This can be explained by the fact, that the velocity inside the circular flame deviates substantially from zero in contrast to the one-dimensional case. Thus, the prediction (5.1) does not hold for the flow field altered by the circular flame geometry, and the actual flame propagation lags behind it.

The next test concerned the ability of the implementation to handle topological changes. Four circular flames of different sizes were set up initially with a fuel density of $\rho_u = 5 \times 10^8 \text{ g cm}^{-3}$. [Figure 5.4](#) shows that the merging of the fronts happens smoothly. Also the burn-out of the “island” of fuel in the center of the four merged domains of burnt material causes no numerical difficulties. The slight deformation of the circular flames can be explained by the velocity fields generated between the flames. This numerical simulation demonstrates the superiority of the level set method over other techniques of front tracking in describing complicated topological situations without further numerical effort.

5. Results and discussion

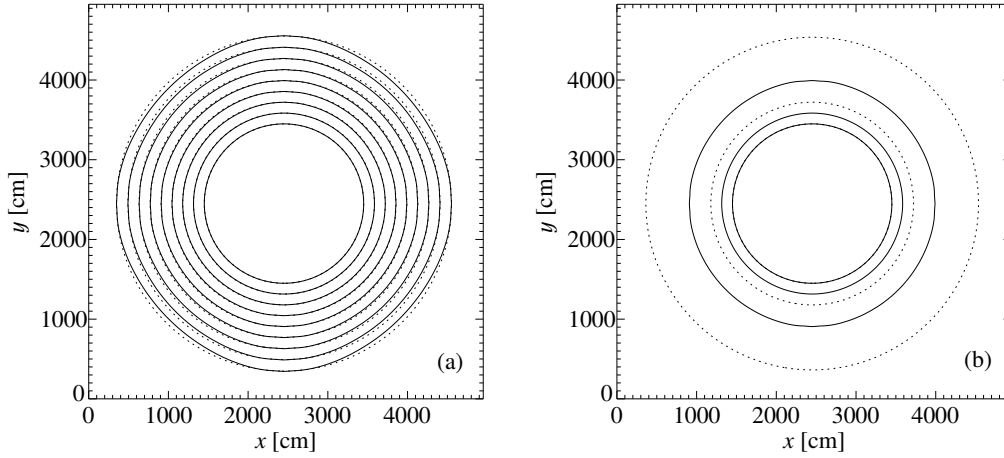


Figure 5.3.: Expansion of a circular flame front **(a)** each solid contour represents a timestep of 1.5×10^{-5} s; exact circles (dotted) given for comparison **(b)** flame front location at $t = 0$ s, $t = 1.5 \times 10^{-5}$ s, and $t = 6.0 \times 10^{-5}$ s (solid) and corresponding expected location (dotted)

The verification tests indicate that simulations applying the method specified in Chapter 4 adequately model the hydrodynamical situation. However, some numerical problems remain in the implementation. These will be discussed in the following section.

5.2. Problems with the numerical implementation

For reasons given in Section 5.1 and for comparison of the results with both theoretical expectations and experiments that will be presented below and in Chapter 6, we are confident that our numerical implementation reflects reality to a reasonable degree. However, numerical experiments (in particular those discussed in Section 5.4) can have only indicative character. Keeping this in mind, we will perform the forthcoming studies aiming on the exploration of possible behaviors of flame propagation.

In this section we would like to emphasize, that especially the “complete implementation” of the level set method is an intricate task. Some problems that still remain will be discussed in the following.

Reinecke et al. (1999b) reported on difficulties with the implementation of the complete version of the level set method. We examined our implementation in order to evaluate the improvements that could be achieved to stabilize the algorithm. Robustness of the reconstruction scheme is a prerequisite for its application to more complex simulations, such as flame evolution in presence of imprinted turbulence or Type Ia supernova explosions.

From given pre- and post-front states, which exactly fulfill the Rankine-Hugoniot jump conditions, Reinecke et al. (1999b) synthesize a mixed cell according to (4.19)–(4.21) for a

5.2. Problems with the numerical implementation

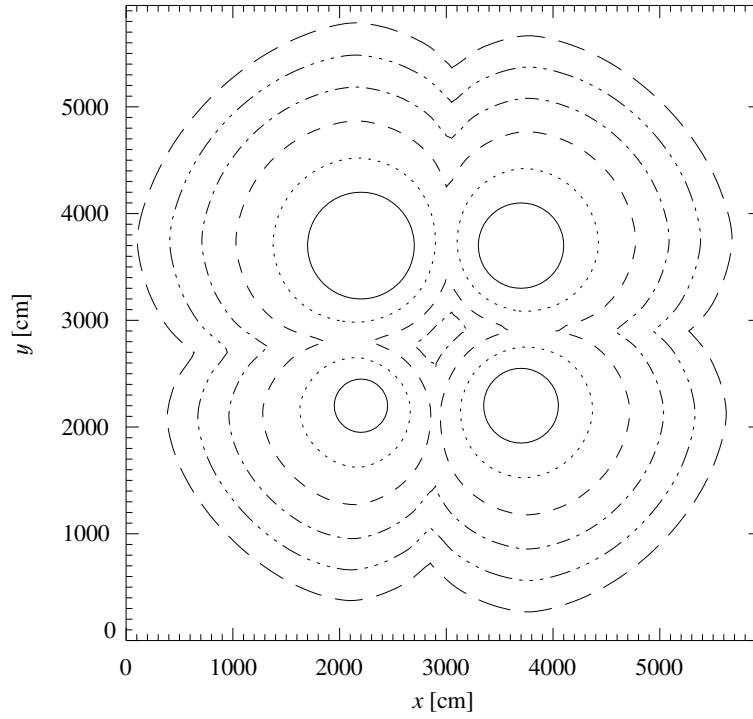


Figure 5.4.: Merging of four circular flame fronts, contours represent time steps of 3.0×10^{-5} s

given volume fraction of unburnt material α_0 . While trying to reconstruct for the burnt and unburnt states imposing an unburnt volume fraction α that deviates slightly from the exact value α_0 , they find that the solver for the nonlinear reconstruction equation system can enter regions for which the equation of state is undefined. It reaches values for the internal energy of the unburnt material, which are lower than the internal energy belonging to zero temperature. This, of course, means that the reconstruction fails. The problem is caused by the degenerate equation of state and is not observed in simulations of chemical deflagration fronts.

In simulations of thermonuclear flames this effect is a serious obstacle to build a stable implementation, because the flame front is linearly interpolated in mixed cells and therefore α usually deviates from the exact value. This deviation becomes most pronounced in highly curved front geometries. One would expect higher orders of interpolation to cure this problem. This, however, would strongly increase the number of topological uncertainties of the kind depicted in the rightmost sketch of Figure 4.2.

The described difficulty remains a critical issue in our simulations, although it is some-

5. Results and discussion

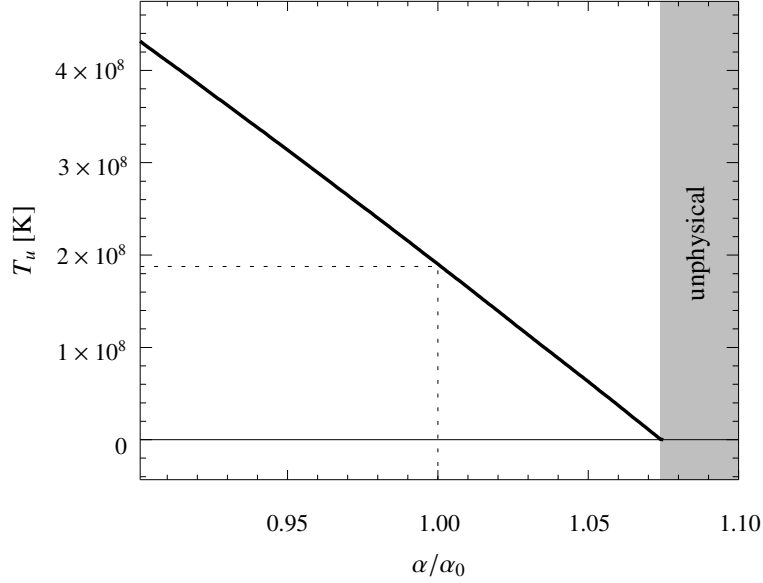


Figure 5.5.: Test of the reconstruction routine: T_u is the reconstructed temperature of the unburnt material in the mixed cell and α/α_0 denotes the deviation of the assumed volume fraction from the correct one.

what attenuated here. From Figure 5.5 it is obvious that the reconstructed temperature of the unburnt material enters unphysical values for a deviation of the assumed α from α_0 of more than 7%, while Reinecke et al. (1999b) report a tolerance in the volume fraction of only 2%. The reason for this may simply be that we assume the fuel to consist of pure carbon, while Reinecke et al. (1999b) apply a 50% mixture of carbon and oxygen. The energy release from the thermonuclear net reaction is thus in our case $\approx 9.3 \times 10^{17} \text{ erg g}^{-1}$ in contrast to $\approx 7.8 \times 10^{17} \text{ erg g}^{-1}$ for $1/2 \text{ C} + 1/2 \text{ O}$ fuel. Additionally, in the laminar flame speeds differ considerably in both cases and Reinecke et al. (1999b) even underestimate the energy release by assuming only $\approx 7.0 \times 10^{17} \text{ erg g}^{-1}$.

Nevertheless, in our simulations a failure of the reconstruction may still occur when the front is highly curved, which is especially the case for cusps of cellularly stabilized front geometries. Here situations are possible which lead to a large deviation of the α -value determined by linear interpolation from the intersection points of cell borders with zero level set of G and the actual α_0 given by the exact shape of the zero level line of G , as illustrated in Figure 5.6. In these cases energy is added to the cell in order to obtain a physical unburnt state with positive temperature. This, of course, makes our numerical scheme slightly non-conservative. Fortunately, the cases where cusps are aligned in an unfavorable manner with respect to the computational grid are rare. Of course, as stated by Reinecke et al. (1999b), a straight forward method to extenuate the problem is to limit the flame curvature by introducing a curvature-dependent effective burning velocity according to (5.3). In the presented simulations we did not explicitly prescribe such a burning law.

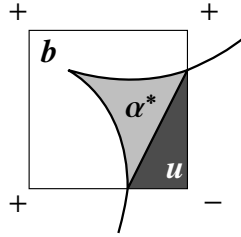


Figure 5.6.: Critical situation: the region marked with α^* is the deviation between the actual α_0 and α determined by linear interpolation

However, as will be discussed in Section 5.3.4, a Markstein-like behavior may be already present for numerical reasons, but an even larger Markstein length¹ might contribute to the robustness of the in-cell reconstruction scheme.

A further issue in the Reinecke et al. (1999b) implementation is that the implicit treatment of the source terms in the reconstruction scheme (see Section 4.5.2) was not applied. This leads to an additional deviation of energy and species distribution from the zero level set of the G -function. Implementation of this method in our code made the reconstruction scheme more reliable and may also contribute to the larger tolerance of the method to deviations in the volume fraction.

5.3. Flame propagation into quiescent fuel

The first task in this study is to investigate the evolution of a flame front that propagates into quiescent fuel. Objectives are to explore the general flame evolution and to quantify the effective flame propagation speed at various fuel densities. Niemeyer & Hillebrandt (1995) were able to confirm by means of a numerical simulation that the propagation of thermonuclear flames in degenerate matter under conditions that are to be expected in Type Ia supernovae is in fact subject to the LD instability. However, their simulations did not reach the nonlinear regime of flame front evolution. Thus, one question to be answered in this study is, whether or not the flame would stabilize in a cellular pattern as predicted from theoretical considerations (see Section 2.3.2) and as observed in terrestrial flames. Previous numerical studies addressing this question can be found in literature, but these either apply a numerical integration of the Sivashinsky equation (Blinnikov & Sasorov 1996) to describe the flame evolution and do not model the complete hydrodynamics or apply general analytical considerations based on certain assumptions (Bychkov & Liberman 1995).

The goal of this first part of our investigation is consequently, to model the nonlinear regime of flame evolution in a hydrodynamical simulation. After some remarks on the version of the implementation that is to be chosen for the forthcoming simulations and on the simulation setup, we study the linear regime of flame evolution. Here comparison with

¹This “Markstein length” would be artificially introduced for numerical reasons and is not to be confused with the original purpose of that quantity to model finite flame thickness.

5. Results and discussion

Landau’s dispersion relation (2.86) (page 36) provides a tool to judge the accuracy of our model. Following this, we will focus on the nonlinear evolution of the flame propagation. Additionally, measurements of the flame acceleration will be presented.

5.3.1. Passive vs. complete implementation

The question that has to be answered initially is, which of the two implementations of the level set technique is appropriate for our numerical simulations. The “passive implementation” (see Section 4.5) has the advantage, that it is much easier to implement and much more robust, while the “complete implementation” can cause difficulties in solving the reconstruction system of equations.

The basic assumption of the “passive implementation” is, that v_u needed in the G -evolution equation (4.16) can be approximated by the known average flow velocity in the mixed cells. The reason why this is an acceptable approach in large scale supernova simulations is, that these concentrate on early phases of the explosion where the density of the unburnt material is still high causing a small density jump over the flame front. Additionally, as pointed out by Reinecke (2001), the turbulent burning velocity is derived from a dimensional analysis there and only determined up to a factor of the order of unity. Both points obviously are not fulfilled in our studies. Therefore, the favorable method here is the “complete implementation”. The “passive implementation” can not be expected to provide an accurate flow field. This is, however, a prerequisite to describe the flame evolution under the influence of the Landau-Darrieus instability correctly, because the origin of that instability lies in the interaction of the flame propagation with the hydrodynamical flow (see Section 2.3.1).

In order to demonstrate the superiority of the “complete implementation” of the flame/flow coupling over the “passive implementation”, we compared the flame evolution for a fuel density of $5 \times 10^7 \text{ g cm}^{-3}$ for both methods. The physical domain was set to be periodic in y -direction. On the left boundary of the domain an outflow condition was enforced and on the right boundary we imposed an inflow condition with the unburnt material entering with the laminar burning velocity s_l . Together with additional measures this keeps the flame centered in the domain. Details of the setup will be described in the next section. A sinusoidal initial perturbation was imposed on the flame shape. The state variables were set up for a fuel density of $5 \times 10^7 \text{ g cm}^{-3}$ according to Table 5.1 on page 90. Keeping in mind the considerations of Section 3.1.2, the extent of the domain was chosen as $[3.2 \times 10^4 \text{ cm}]^2$.

The result is shown in Fig. 5.7. It illustrates very drastically that the “passive implementation” fails to reproduce theoretical expectations like an increase of the perturbation amplitude due to the LD instability or the stabilization of the flame in a cellular pattern. Both effects are present in the “complete implementation”. The difference can be attributed to the incorrect treatment of the flame propagation velocity in the G -evolution equation (4.16) in the “passive implementation”. This prevents the flow field from adjusting to the perturbed flame shape, which would cause the LD instability. It is evident that the “complete implementation” is the appropriate tool for our study. All simulations presented in the following are performed applying this method.

5.3. Flame propagation into quiescent fuel

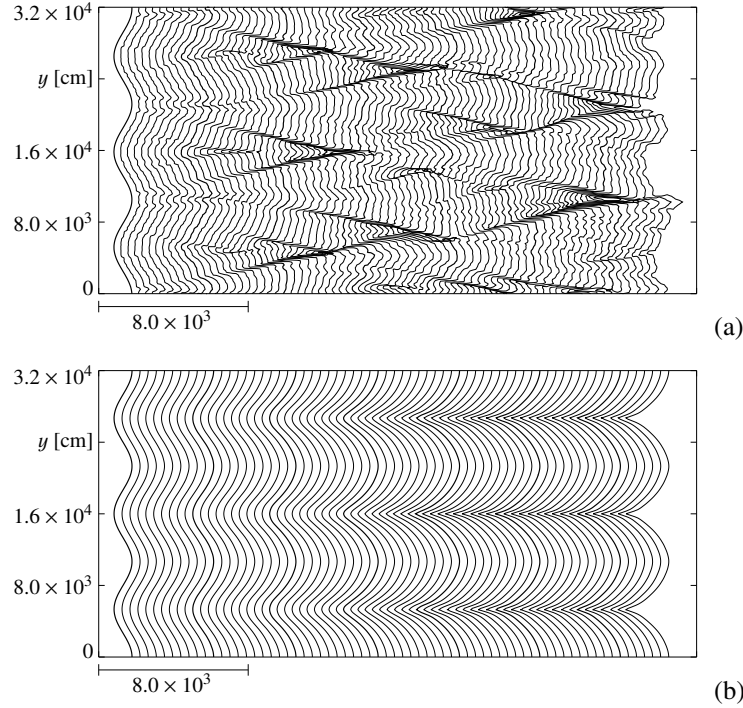


Figure 5.7.: Temporal evolution of the flame front at $\rho_u = 5 \times 10^7 \text{ g cm}^{-3}$ for a resolution of 200×200 cells: (a) “complete implementation”, (b) “passive implementation”; Each contour represents a timestep of 1.5 ms.

5.3.2. Simulation setup

From theoretical considerations (resulting for instance from the Sivashinsky equation), it can be expected that the general features of the evolution of the flame front shape depend significantly on the numerical setup used in the simulations. Possible parameters that influence the flame evolution are the overall geometry of flame propagation (i.e. planar or circularly expanding), the width of the computational domain compared to the length scale of perturbations, the resolution, the boundary conditions, sources of numerical noise (which is likely to be different when the simulation is parallelized to a varying number of sub-processes), and the initial flame shape. Therefore care has to be taken in choosing the specific setup depending on the questions that are addressed by the simulations as well as in the conclusions drawn from the simulation results. As will be discussed later, the separation between effects that can be expected in the astrophysical scenario and effects that are caused by the specifics of the numerical setup is a highly non-trivial issue.

The influence of some of the mentioned setup parameters on the flame evolution will be discussed here². First, we address the question of the overall geometry of flame propa-

²The questions of the effects of the resolution and the width domain compared to the wavelength of the initial

5. Results and discussion

gation. The two most obvious cases (that are commonly studied in literature) are an on average planar flame geometry and a flame that is on average circularly expanding. Although a naive approach would choose the second scenario for the supernova explosion, it is probably not the appropriate description of the flame propagation there. As discussed in Section 3.1.2, the flame evolution on scales of the star, where expansion effects are most pronounced, quickly becomes dominated by the Rayleigh-Taylor instability. This leads to a flame evolution completely diverging from a circular (or in three dimensions spherical) geometry (cf. Reinecke et al. 2002a). It rather proceeds in raising bubbles of burnt material. Nevertheless, it could be argued that these structures again partly resemble a spherically expanding geometry.

As has been pointed out in literature, the case of a circularly expanding flame reveals very interesting physical effects. Similar to the planar case, the flame will stabilize in a cellular pattern. However, as will be discussed in detail below, in a planar setup the tendency of the cells to merge forming a single domain-filling structure can be observed. This is not to be expected in a circular geometry. Here, expansion effects may lead to a mode splitting of the cells resulting in a fractalization of the flame front. This effect has been studied in the context of SN Ia explosions by Blinnikov & Sasorov (1996). They apply a semianalytical approach making use of the Sivashinsky and Frankel equations. It is interesting to test whether or not our implementation, which describes the hydrodynamics in a more realistic way, can reproduce these results. As Blinnikov & Sasorov (1996) point out, the effect of mode splitting depends on the density contrast over the flame. To this end we performed two *ad hoc* simulations with fuel densities of $5 \times 10^7 \text{ g cm}^{-3}$ and $5 \times 10^8 \text{ g cm}^{-3}$ (for the complete set of initial values cf. Table 5.1 on page 90). The corresponding density contrasts were $\mu = 2.41$ ($At = 0.413$) and $\mu = 1.62$ ($At = 0.237$), respectively, and the simulations were performed on a 1000×1000 cells grid. The result of the simulations is plotted in Figure 5.8. In both cases, the propagation of the circular flame is accelerated with respect to the motion of a planar or unperturbed circular flame front. This can be attributed to the surface increase by growing perturbations. This effect is more pronounced in the case of lower fuel density and a resulting higher Atwood number, which is consistent with the results of Blinnikov & Sasorov (1996). Cell splitting can be observed in both cases. It is, however, suspicious that it seems to be preferred in the directions parallel to the axes, indicating that—in contrast to the unperturbed circular flame (cf. Figure 5.3)—the isotropy is slightly broken here. However, a closer inspection reveals cell splitting also in tilted directions, at least for the $\rho_u = 5 \times 10^7 \text{ g cm}^{-3}$ simulation. The overall shape of the flame in Figure 5.8 is—up to a certain degree—similar to the results from the applications of the Sivashinsky equation or the Frankel-equation obtained by Blinnikov & Sasorov (1996), Filyand et al. (1994), and Kupervasser et al. (1996). However, in order to obtain significant results, the flame evolution would have to be followed for a much longer time. In our simple setup this requires prohibitively large computational domains.

Yet the objective of our study is somewhat different from the Blinnikov & Sasorov (1996) investigation. We aim on effects on scales around the Gibson length, at which global

flame perturbation will be postponed to the next sections.

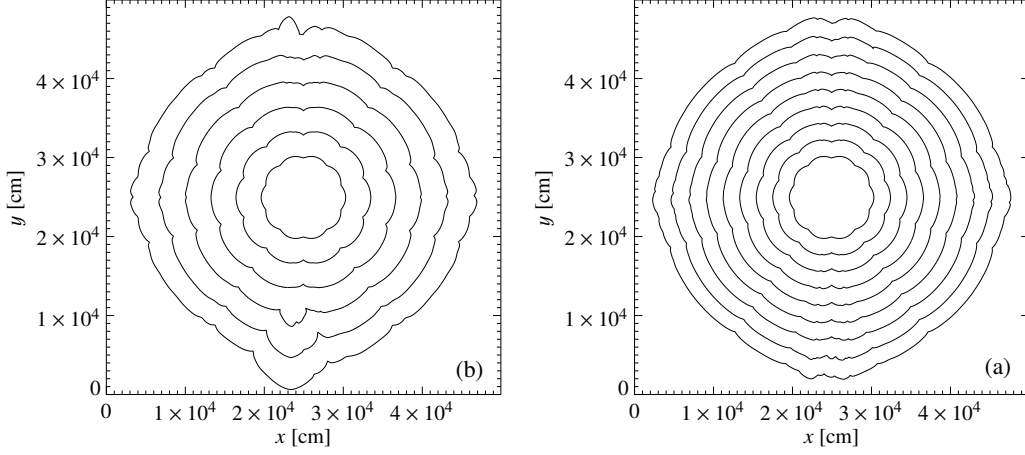


Figure 5.8.: Evolution of a circular flame with sinusoidal initial perturbation. **(a)** $\rho_u = 5 \times 10^7 \text{ g cm}^{-3}$, **(b)** $\rho_u = 5 \times 10^8 \text{ g cm}^{-3}$. Each contour corresponds to a timestep of $25\Delta x/s_l$, Δx denoting the width of one grid cell.

expansion effects are negligible. This has a technical advantage. It is much simpler to keep an overall planar flame in the center of the domain by choosing a comoving frame of reference. This enables us to study the long term flame evolution without requiring large computational domains. This is the reason why parameter studies (such as presented below) become possible at all.

The “experimental setup” applied in most of the simulations of the evolution of the flame subject to the LD instability is the following: The spatial extent of the computational domain was set to correspond to scales around the Gibson length and was fixed according to the discussion in Section 3.1.2 to $\sim 10^4$ cm. The flame was set up in the center of the domain in an on average planar vertical shape with the unburnt material on the right hand side and the burnt material on the left hand side, so that in laboratory frame of reference the flame would propagate to the right. The domain was set to be periodic in y -direction. These boundary conditions affect the global flame evolution, as will be discussed in the next section. On the left boundary of the domain an outflow condition was enforced and on the right boundary we imposed an inflow condition with the unburnt material entering with the laminar burning velocity s_l . This would yield a computational grid comoving with a planar flame. The LD instability leads to a growth of the perturbation and therefore increases the flame surface. This results according to equation (2.105) in an acceleration of the flame and therefore it is necessary to take additional measures in order to keep the mean position of the flame centered in the domain. One possibility is to detect the mean location of the flame and to simply shift the grid to keep the flame centered. The method is consistent with the boundary conditions applied in x -direction. The described method

5. Results and discussion

Label	ρ_u [g cm ⁻³]	ρ_b [g cm ⁻³]	μ	At	s_l [cm s ⁻¹] (TW)	$e_{i,u}$ [erg g ⁻¹]	$e_{i,b}$ [erg g ⁻¹]
1×10^7	9.969×10^6	2.691×10^6	3.70	0.575	2.39×10^5	1.619×10^{17}	8.59×10^{17}
1.25×10^7	1.232×10^7	3.830×10^6	3.22	0.526	2.86×10^5	2.005×10^{17}	8.99×10^{17}
2.5×10^7	2.484×10^7	8.69×10^6	2.86	0.482	5.01×10^5	2.56×10^{17}	9.50×10^{17}
5×10^7	4.988×10^7	2.071×10^7	2.41	0.413	8.74×10^5	3.584×10^{17}	1.051×10^{18}
7.5×10^7	7.50×10^7	3.345×10^7	2.24	0.383	1.21×10^6	4.29×10^{17}	1.13×10^{18}
1×10^8	1.00×10^8	4.789×10^7	2.09	0.352	1.53×10^6	4.89×10^{17}	1.182×10^{18}
1.25×10^8	1.25×10^8	6.21×10^7	2.01	0.336	1.83×10^6	5.373×10^{17}	1.22×10^{18}
5×10^8	5.05×10^8	3.11×10^8	1.62	0.238	5.58×10^6	9.614×10^{17}	1.654×10^{18}
1×10^9	1.00×10^9	6.80×10^8	1.47	0.190	9.75×10^6	1.27×10^{18}	1.96×10^{18}

Table 5.1.: Setup values for the simulations of the flame evolution.

allows the study of the long term flame evolution. In order to induce the development of perturbations, we usually imposed a sinusoidal perturbation on the initial flame.

The state variables were set up with values for the burnt and unburnt states obtained from (pseudo-)one-dimensional simulations performed with the “passive implementation” of the level-set method by [Reinecke et al. \(1999b\)](#), imposing a value for the density of the fuel. These values also served as initial guesses for solving the reconstruction equations. A compilation of the relevant setup values for different fuel densities is given in [Table 5.1](#). Note that frequently in this text fuel densities refer to a label of a specific set of values rather than giving the accurate fuel density. The laminar burning speed is calculated according to [equation \(2.73\)](#), although it is realized that this fit does not reproduce the simulation results of [Timmes & Woosley \(1992\)](#) as good as the authors claim. For high-precision explosion models a different fit is therefore advisable. However, owing to the more indicative character of our study, we settle for the results of [equation \(2.73\)](#).

5.3.3. General features of flame evolution

For all simulations presented henceforth we applied a simulation setup as described in [5.3.2](#) making use of the complete implementation of the level set technique. In this section, we describe some general features of the flame evolution for an exemplary case. We choose again $\rho_u = 5 \times 10^7$ g cm⁻³ as initial fuel density (see [Table 5.1](#) for the complete set of initial values). This will remain our standard numerical setup up to [Section 5.3.6](#)

[Figure 5.9](#) shows the result of a simulation for a grid resolution of 100×100 cells. Here, the flame evolution reveals two stages. First, in the linear regime of flame evolution, the perturbation grows due to the LD instability (see [Figure 5.9](#); snapshots at $t = 0.000$ s, $t = 0.001$ s, and $t = 0.002$ s). The second stage is the nonlinear regime, where a cusp forms at the intersection of two adjacent bulges of the front (see snapshot at $t = 0.004$ s). As theoretically predicted ([Section 2.3.2](#)), the formation of a cusp, where the propagation speed of the flame is increased, balances the perturbation growth and stabilizes the flame in a cellular pattern, i.e. in case of the simulation presented in [Figure 5.9](#) in a single domain-filling cusp-like structure. This structure is stable and the flame reaches a steady state as can be seen from the snapshots following $t = 0.004$ s.

5.3. Flame propagation into quiescent fuel

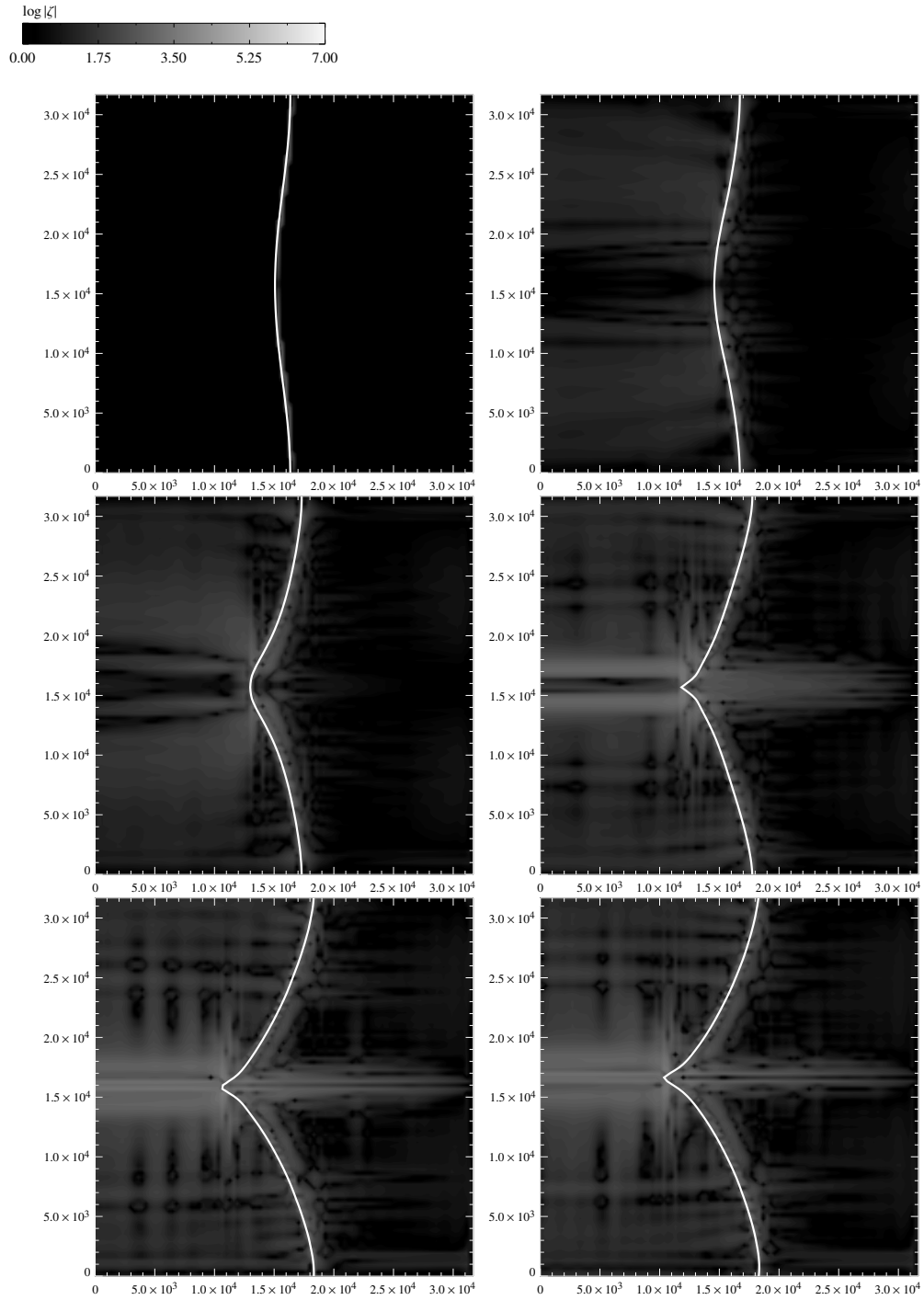


Figure 5.9.: Flame propagation into quiescent fuel, $\rho_u = 5 \times 10^7 \text{ g cm}^{-3}$, resolution: 100×100 cells, snapshots taken at $t = 0.000$ s, $t = 0.001$ s, $t = 0.002$ s, $t = 0.004$ s, $t = 0.090$ s, and $t = 0.150$ s (top left to bottom right).

5. Results and discussion

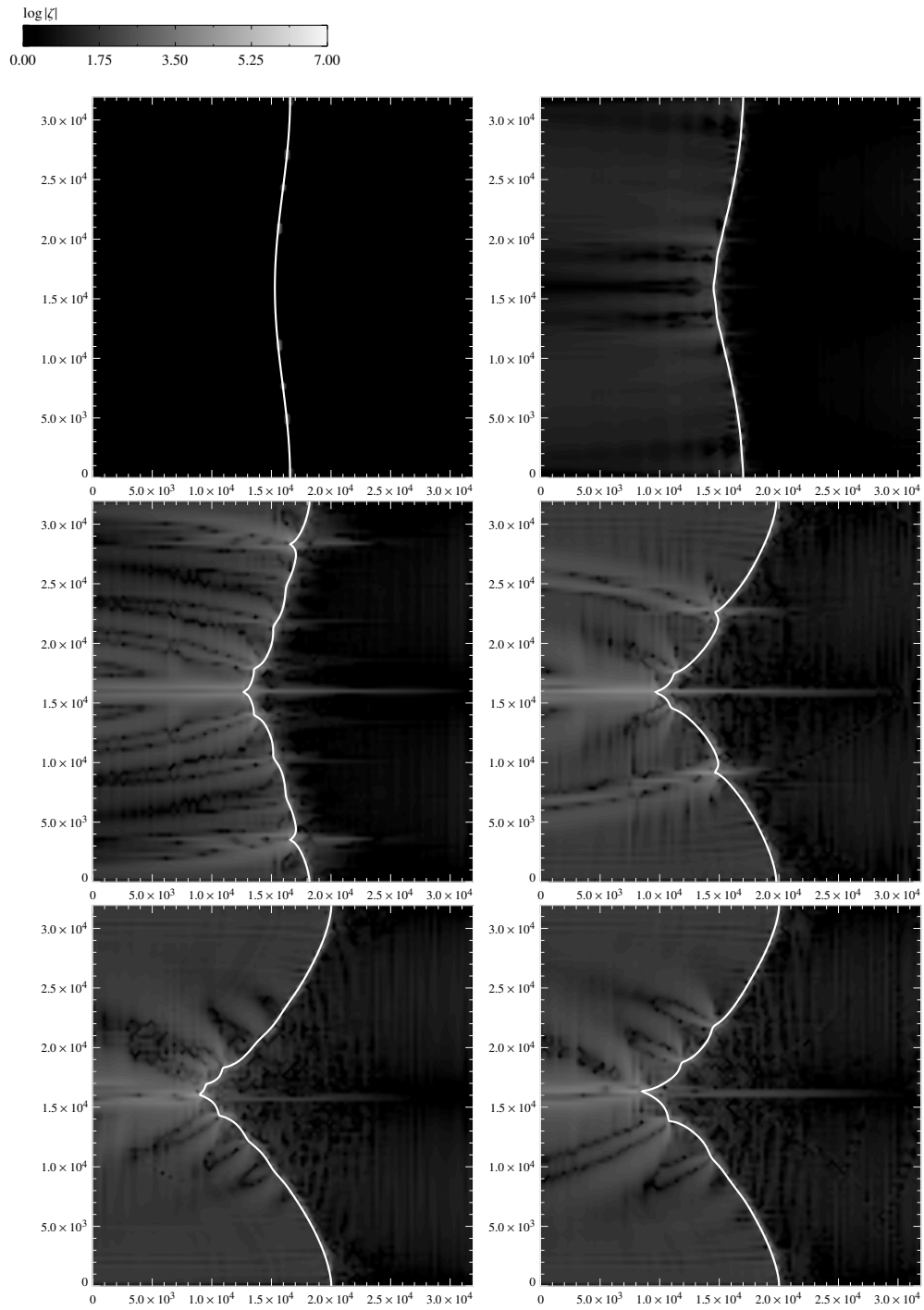


Figure 5.10.: Flame propagation into quiescent fuel, $\rho_u = 5 \times 10^7 \text{ g cm}^{-3}$, resolution: 400×400 cells, snapshots taken at $t = 0.000$ s, $t = 0.001$ s, $t = 0.002$ s, $t = 0.004$ s, $t = 0.090$ s, and $t = 0.150$ s (top left to bottom right).

5.3. Flame propagation into quiescent fuel

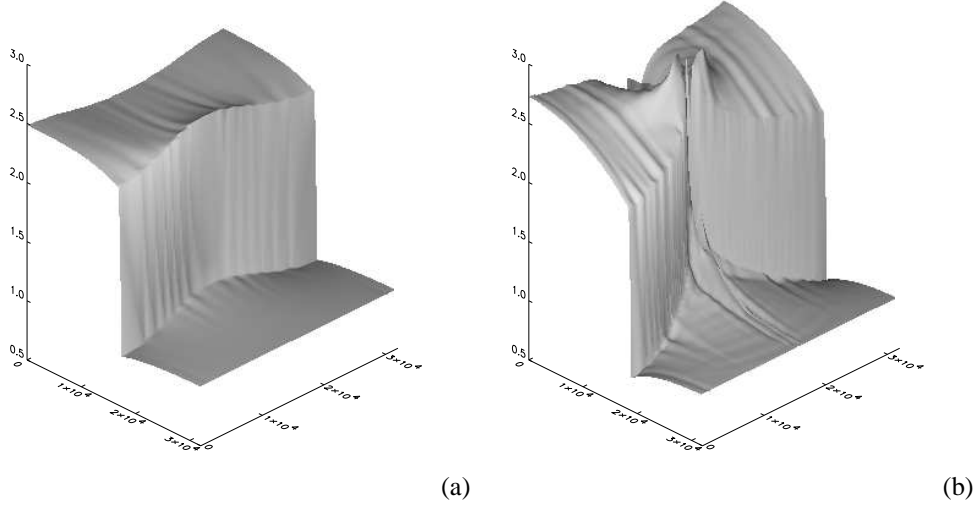


Figure 5.11.: Fluid velocity in the simulation with $\rho_u = 5 \times 10^7 \text{ g cm}^{-3}$ and 100×100 cells resolution. The x -axis and the y -axis show position in cm; the z -axis represents $|v|/s_i$; **(a)** snapshot at $t = 0.01 \text{ s}$, **(b)** snapshot at $t = 0.09 \text{ s}$

For higher resolutions of the computational domain the general features of perturbation growth in the linear regime and the stabilization in a large domain-filling cusp in the non-linear regime are similar to that described above. However, the flame evolution differs in detail. As can be seen from the simulation at a resolution of 400×400 cells (shown in Figure 5.10), the structure now becomes superimposed by a short-wavelength cellular pattern. This effect will be discussed in Section 5.3.5. In order to recheck the stability of our numerical implementation in the applied setup, we performed a simulation of a flame that was initially exactly planar. The resolution here was again 400×400 cells. Over the time that is covered by all other simulations we did not observe any deviation of the flame from its planar shape. This indicates rather low numerical noise in our numerical implementation.

It is certainly worth noticing that the basic shape underlying the flame structures observed in our simulations resembles the structures obtained via pole decomposition methods (cf. Figure 2.8).

In the snapshots of the flame evolution depicted in Figures 5.9 and 5.10 the vorticity of the flow field, $\zeta = \nabla \times \mathbf{v}$, is color-coded. For our two-dimensional simulations the (scalar) vorticity reads

$$\zeta = \frac{\partial v_y}{\partial x} - \frac{\partial v_x}{\partial y}. \quad (5.2)$$

Note that we color-code the logarithm of the absolute value of the vorticity and therefore even slight deviations from zero vorticity are visible. The flame produces vorticity in the burnt material. This effect is especially strong behind cusps. Analytical approximations

5. Results and discussion

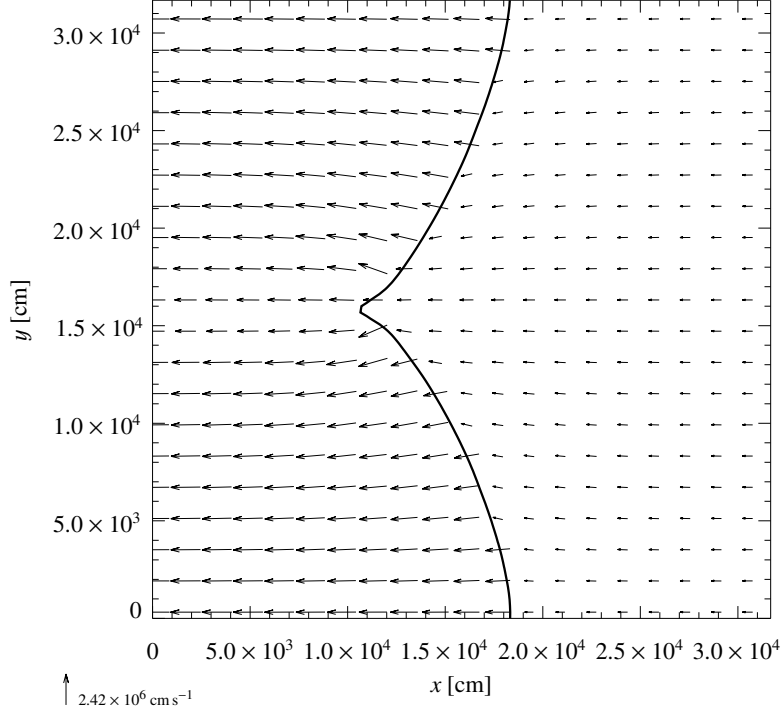


Figure 5.12.: Velocity field in the simulation $\rho_u = 5 \times 10^7 \text{ g cm}^{-3}$; 100×100 cells at $t = 0.09 \text{ s}$.

of the flame evolution frequently make the assumption of a potential flow ahead of the flame. In contrast to that, we observe the development of vorticity in the fuel region. This, however, is not surprising, since the flame propagates sub-sonically and the regions downstream and upstream of the flame are causally connected.

We will now discuss the development of the flow field in more detail, since this is the foundation of all effects connected to the LD instability and the cellular stabilization. For simplicity we refer to the simulation with 100×100 cells resolution.

The physical mechanism underlying the LD instability was described in Section 2.3.1. It is of purely hydrodynamical origin. The refraction of the streamlines at the flame front leads to the development of a flow field that causes the perturbation to grow. In the vicinity of bulges of the front the local fluid velocity is decreased, while it is increased near recesses due to deformation of the flow tubes. This can be observed in our simulations. Figure 5.11a depicts the absolute value of the fluid velocity normalized to the laminar burning velocity of the flame at $t = 0.01 \text{ s}$. It is well in agreement with what is expected from theory. Figure 5.11a illustrates clearly that the complete implementation of the level set method is capable

5.3. Flame propagation into quiescent fuel

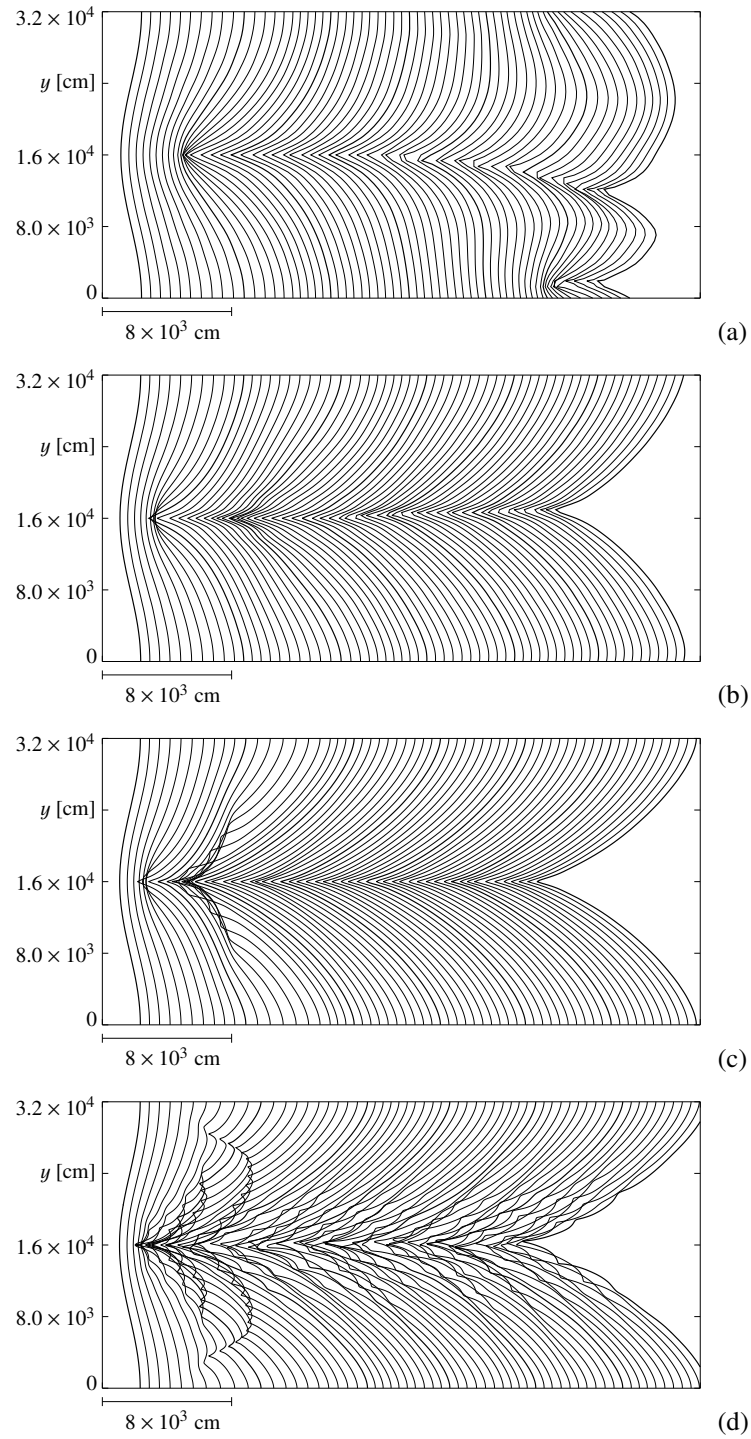


Figure 5.13.: Evolution of the flame front at $\rho_u = 5 \times 10^7 \text{ g cm}^{-3}$. The contours mark evolution steps of 2.5 ms; **(a)** resolution 50×50 cells; **(b)** resolution 100×100 cells; **(c)** resolution 200×200 cells; **(d)** resolution 400×400 cells;

5. Results and discussion

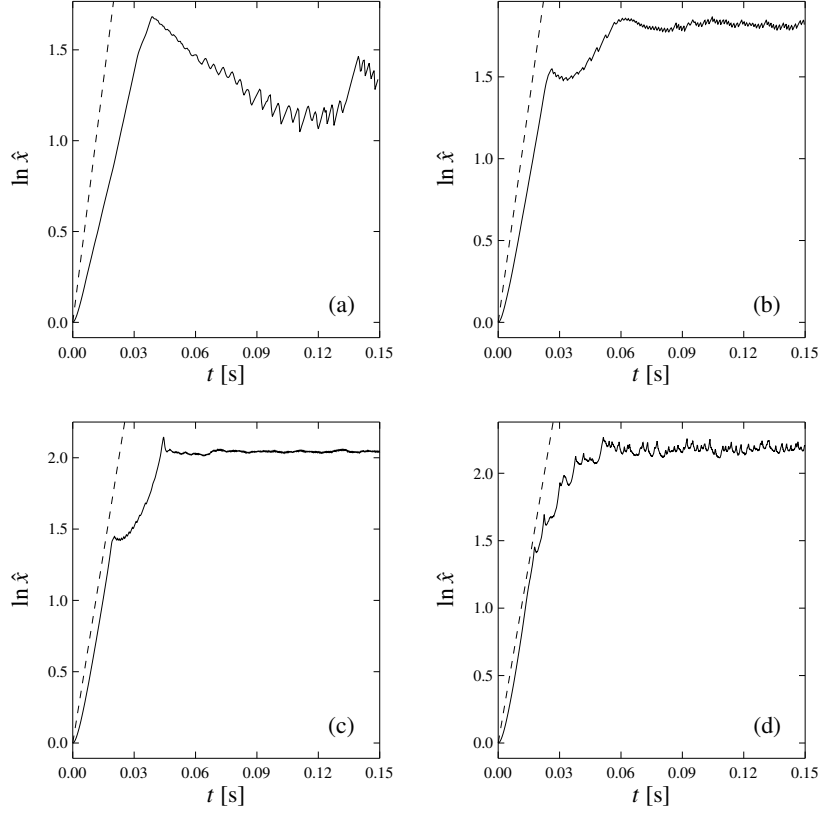


Figure 5.14.: Perturbation amplitudes $\ln \hat{x}$ as a function of time t ; (a) resolution 50×50 cells; (b) resolution 100×100 cells; (c) resolution 200×200 cells; (d) resolution 400×400 cells;

to reproduce the LD instability. This is not trivial as can be seen from the failure of the passive implementation to develop the correct flow field. Figure 5.11b shows the absolute value of the velocity after a cusp has formed.

The velocity field after the formation of a cusp is represented by arrows in Figure 5.12. Note, that the streamlines converge toward the cusp ahead of the front. This leads to the formation of a layer upstream of the front, in which the fluid velocity is directed toward the cusp. As will be discussed in Section 5.3.5, this is a crucial effect providing flame stability. In the downstream region, the flow diverges from the cusp.

To test the dependency of the results on the numerical resolution, a sequence of simulations was performed applying computational grids of 50×50 cells, 100×100 cells, 200×200 cells, 300×300 cells, and 400×400 cells. The results are given in Figure 5.13. In the plots, each contour is shifted artificially into the x -direction for better visibility and corresponds to a time evolution of 2.5 ms. The x -coordinate is stretched by a factor of about 2. We will now discuss the linear and nonlinear regimes of flame evolutions from these simulations.

5.3. Flame propagation into quiescent fuel

Case	ω [s ⁻¹]
Theory	88.7
50 × 50 cells	47.8
100 × 100 cells	69.0
200 × 200 cells	79.7
300 × 300 cells	90.0
400 × 400 cells	91.4

Table 5.2.: Growth rate of perturbation amplitude

5.3.4. The linear regime of flame evolution

In order to quantify the flame evolution in the linear regime, the growth of the amplitude of the perturbation was measured and compared to the theoretical prediction (equation (2.86) on page 36). This was done by a simple determination of the distance between the rightmost and the leftmost points of the flame front. Figure 5.14 shows the growth rates of the perturbation amplitudes over time. The dashed line corresponds to Landau's dispersion relation (2.86). All results share the feature that the growth of the amplitude is shifted in the beginning. This is due to the fact that we impose an initial perturbation but not the corresponding flow field. Thus some relaxation period is necessary for the correct velocities to establish in the vicinity of the flame front. In Figure 5.14, the linear regime of perturbation growth can be clearly distinguished from the later nonlinear stage, where the perturbation amplitude saturates. For now, we will discuss the linear part of the flame evolution.

It is evident from Figure 5.14 that the difference between the growth of the perturbation amplitude in our simulation and that predicted from theory decreases with resolution. According to Table 5.2 the deviation is about 46% for the 50 × 50 cells simulation and only about 10% for the 200 × 200 cells simulation. In the higher resolved runs the initial perturbation quickly gets superimposed with perturbations of higher wavenumber, so that the values of the growth rate can not safely be assigned to the largest wavelength of perturbation anymore. This is the reason why it exceeds the theoretical expectation slightly.

One could conclude from the results that the simulated growth rate matches the theoretical expectations better with higher resolution and converge for a resolution between 200 and 300 cells per dimension for our given fuel density. Alternatively an explanation could be given in terms of a finite effective flame thickness. Even with the special measures described in Section 4.5, l_f can not be expected to be smaller than one cell width. As mentioned in Section 2.2.4, a theoretical approximation of a finite flame width is the assignment of a curvature-dependent flame speed:

$$s_M = s_l(1 - l_M\kappa). \quad (5.3)$$

This burning law changes the dispersion relation depending on the Markstein length l_M . In our case one would expect the Markstein length to be higher for less resolved simulations.

The altered burning law (5.3) breaks the scale invariance of the theory connected to the LD instability. As explained in Section 2.3.1, it introduces a critical perturbation

5. Results and discussion

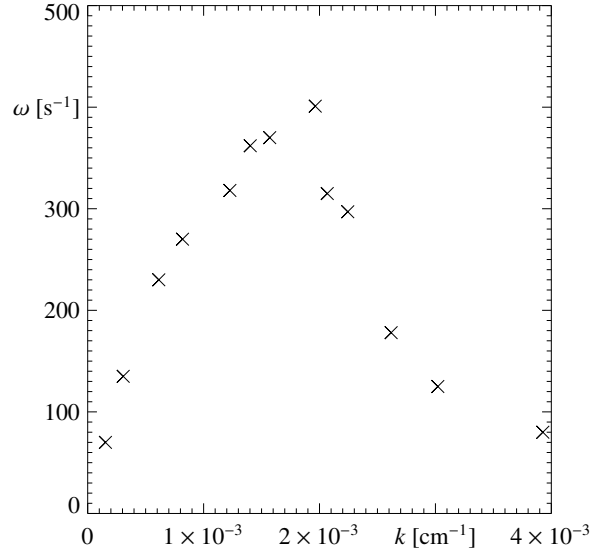


Figure 5.15.: Dispersion relation between the growth rate of the perturbation amplitude ω and the correspondig wavenumber of the perturbation k within the numerical simulations.

wavenumber leading to a maximum growth rate and a cutoff scale below which perturbations will not grow anymore. The measurement of the dispersion relation resulting from the Markstein burning law should be consistent with the plot shown in Figure 2.5. This, however, would at least require that other parameters than the wavenumber of the perturbation must be kept constant. In particular, the growth rates of all perturbations should be measured at the same numerical resolution. This, however, does not realistically reflect the situation in the simulations presented in this chapter. Since these aim on the study of the flame shape evolution, it is interesting to know, to what extent the altered dispersion relation of the LD instability (2.87) effects it. Here, of course, short-wavelength perturbations are less resolved. Therefore we measured the growth of the perturbation amplitude for different wavelengths keeping the width of a numerical grid cell Δx fixed. The result is plotted in Figure 5.15. The perturbation growth rate increases for higher wavenumbers until it reaches a maximum value after that it rapidly drops. However, a clear cutoff wavenumber is not visible. The shape of the dispersion relation in Figure 5.15 differs considerably from Figure 2.5.

The sequence of plots in Figure 5.14 shows increasing similarity of the overall evolution of the amplitudes with higher resolution. This indicates that our numerical model of the LD instability in thermonuclear flames converges in the global properties for resolutions between 200×200 and 400×400 cells.

5.3.5. The nonlinear regime of flame evolution

Figure 5.13 clearly shows the transition in flame propagation from the linear regime in the beginning—where perturbation growth by virtue of the LD instability dominates the dynamics—to the nonlinear burning regime. In accord with theoretical expectations (cf Section 2.3.2) this happens by the formation of cusps in recesses of the front. The flame adopts a cellular shape.

The global picture of the cellular regime is similar in all resolutions. We will now discuss some peculiarities in the details. The most prominent deviation occurs in the lowest resolved flame, where the cell splits and a two-cell structure forms. As reported by Joulin (1994) the phenomenon of cell splitting is not supported by analytical investigations of the nonlinear regime, but this could be owing to the restricted class of solutions studied there. Its invocation is usually attributed to numerical noise. This would explain why this feature is observed in the low-resolution simulation where the discretization errors are large.

All other runs share the feature that the final outcome is a single-cell structure, which steadily propagates forward. An effect contrary to the deviation in low resolved simulations is that with increasing resolution perturbations of smaller wavelength become observable that superimpose the initial long-wavelength perturbation. This is evident for the highest resolved run (Figure 5.13d). Again, the invocation of this phenomenon is discussed controversially in literature and Joulin (1994, 1989) argues that it should be attributed to numerical noise (as roundoff and truncation errors). It is even present in highly accurate numerical solutions of the Sivashinsky equation. However, a prerequisite for its observation is a wide enough computational domain (in our case a sufficiently high resolution in y -direction), as reported by Gutman & Sivashinsky (1990). This observation is consistent with our results, pointing to the fact that, as mentioned before, one important setup parameter that influences the final flame structure is the width of the domain. Figure 5.16 reprints a result from the semianalytical study of Gutman & Sivashinsky (1990). We note that our results (e.g. Figure 5.13d) are in good agreement with it.

The paradox why a superimposed smaller-wavelength cellular pattern does not destroy the global cusp-like structure—although its amplitude should grow faster due to the higher wavenumber (see equation (2.86))—was explained by Zel'dovich et al. (1980b) on the basis of a WKB-like linear analysis and by Joulin (1989) in the nonlinear regime (see Sections 2.4.1 and 2.4.3). Following the arguments of Zel'dovich et al. (1980b), the origin of the effect lies in a flow component parallel to the flame with increasing velocity toward the cusp. The velocity fields that establish in our simulations (see Figure 5.12) show this feature clearly. Therefore the superimposed perturbation is advected toward the cusp while its wavelength is stretched. In that way their growth is reduced until they disappear in the cusp. This is exactly what we observe in our highest-resolved simulation.

5.3.6. Increase in flame surface and acceleration of the flame

The wrinkling of the flame front amplified by the LD instability increases the flame surface. This causes the mean fuel consumption rate to grow and the flame is expected to propagate

5. Results and discussion

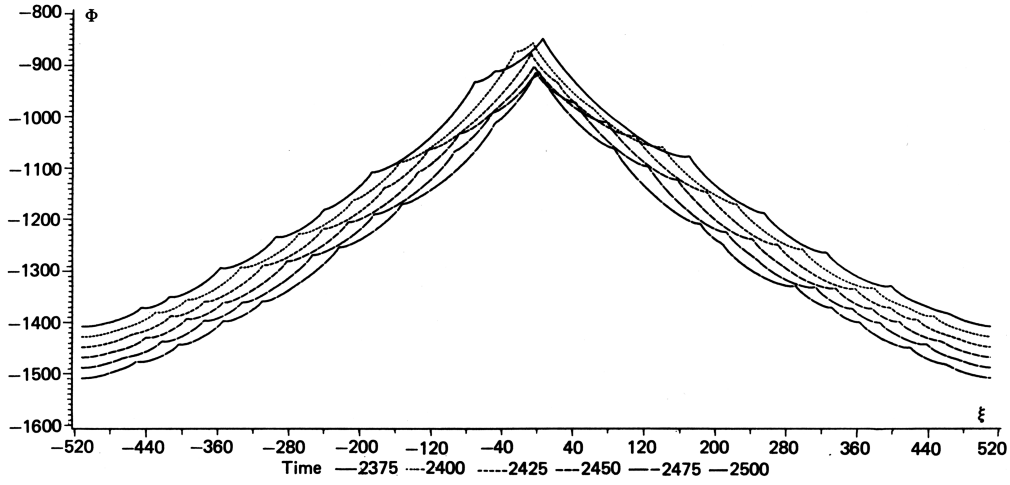


Figure 5.16.: Flame evolution (periodic boundary conditions) according to Gutman & Sivashinsky (1990)

with an increased mean velocity v_{mean} according to (2.105),

$$\frac{v_{\text{mean}}(t)}{v_{\text{mean}}(t_0)} = \frac{A(t)}{A(t_0)}, \quad (5.4)$$

where $A(t)$ denotes the flame surface area (i.e. length of the one-dimensional flame in our two-dimensional simulation) at time t .

In Figure 5.17 we present a measurement of the temporal evolution of the flame surface area and the mean velocity. As expected, the evolution of the velocities follows the growth of the initial perturbations in the beginning and saturates in the cellular regime. The flame area in Figure 5.17 is normalized to the flame area of our initial configuration whereas the mean velocity is normalized to the laminar flame speed. This results in a shift between $v_{\text{mean}}(t)/s_l$ and $A(t)/A(t_0)$ because the initial configuration is already perturbed from the planar shape and the corresponding value of the mean velocity deviates from s_l . The flow field needs some time to adapt to the initial flame geometry. Figure 5.17c depicts the difference between $v_{\text{mean}}(t)/s_l$ and $A(t)/A(t_0)$. Apart from the initial shift there is a deviation which can partly be explained by the different methods of measurement. While the mean propagation velocity was calculated from the flame positions (determined by the contents of ashes in the grid cells), the flame surface area was obtained by linear interpolation of the zero level-set of the G -function in the cells. Additionally one has to keep in mind that equation (5.4) holds strictly only for a burning velocity that is constant over the flame front. This is rigorous in the framework of the discontinuity model of the flame, ignoring any internal flame structure. Thus this relation may not exactly apply to our simulation, since we would expect an intrinsic Markstein-like behavior (see Section 5.3.4). Nevertheless, in the

5.3. Flame propagation into quiescent fuel

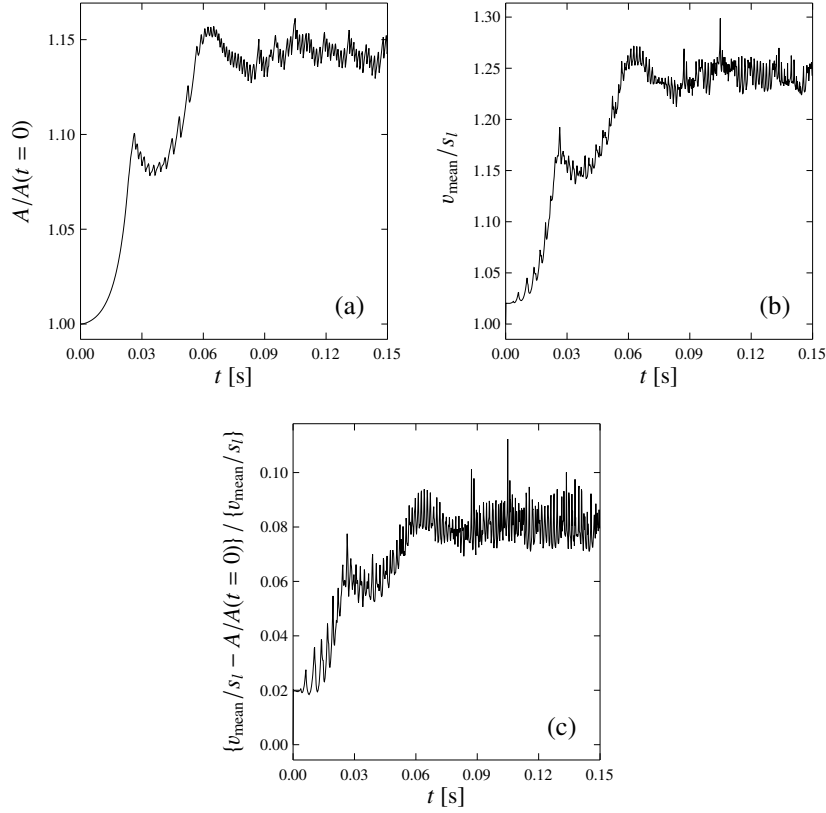


Figure 5.17.: (a) Growth of flame surface area and (b) mean velocity for a resolution of 100×100 cells; (c) deviation of area and velocity

following simulations we will use the increase in surface area of the flame as a measure of the flame acceleration.

The growth of the flame surface area for the simulations with different numerical resolution is plotted in Figure 5.18. All higher resolved simulations reveal roughly the same basic shape of the surface area profile reflecting the similar development of a cusp-like structure. However, in contrast to the growth of the perturbation area, a saturation in surface growth toward higher resolution can not be observed. This is due to the superposition of the flame with the short-wavelength cellular pattern, which does not alter the amplitude much, but increases the flame surface considerably. From theoretical approximations (see Section 2.3.2, equations (2.116, 2.117)), one would expect an increase in flame propagation velocity of $v_{\text{cell}} = 1.14s_l$, given $\rho_u = 5 \times 10^7 \text{ g cm}^{-3}$ and $\mu = 2.41$. Our results are consistent with this estimation (see Figure 5.18). The slight deviations are due to the uncertainties in the determination of the flame propagation velocity via the flame surface mentioned above. Furthermore, the theoretical prediction assumes a parabolic shape of the

5. Results and discussion

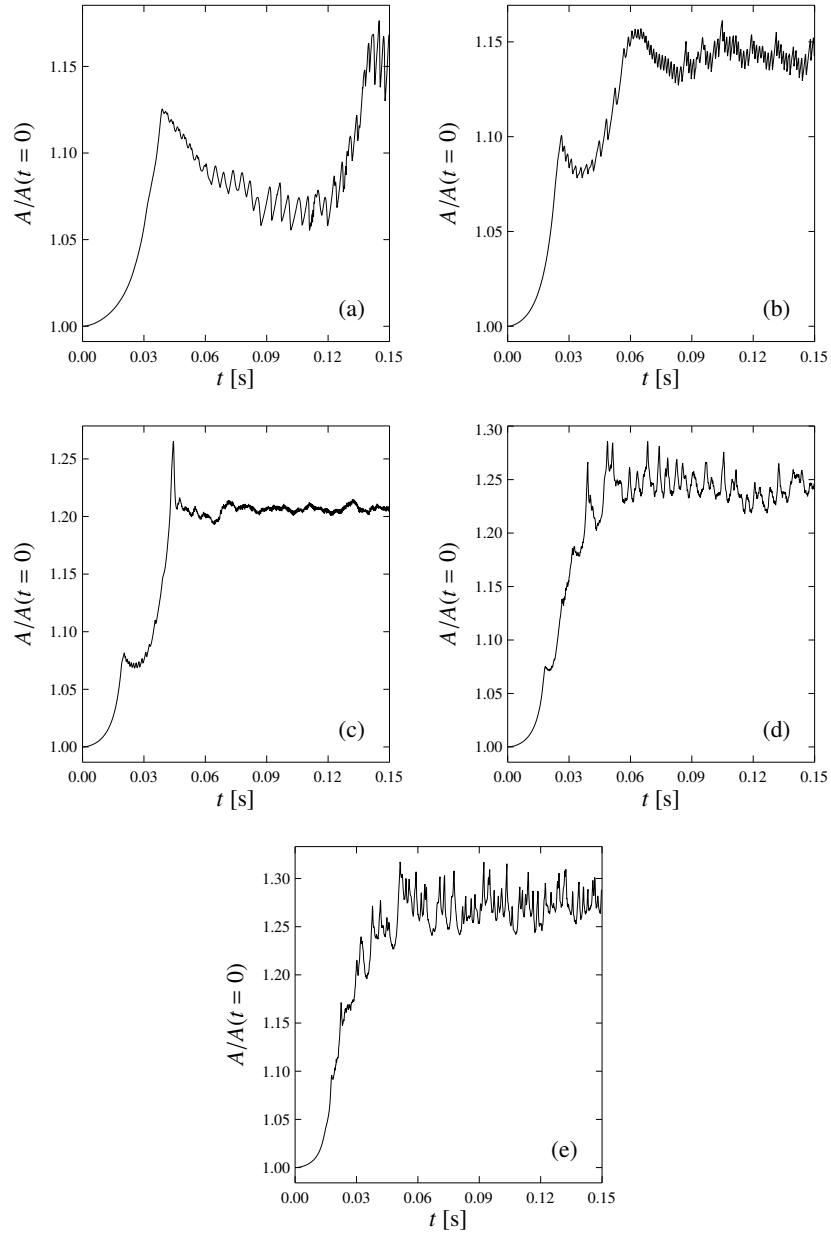


Figure 5.18.: Growth of flame surface area for a resolution of (a) 50×50 cells, (b) 100×100 cells, (c) 200×200 cells, (d) 300×300 cells, and (e) 400×400 cells.

5.3. Flame propagation into quiescent fuel

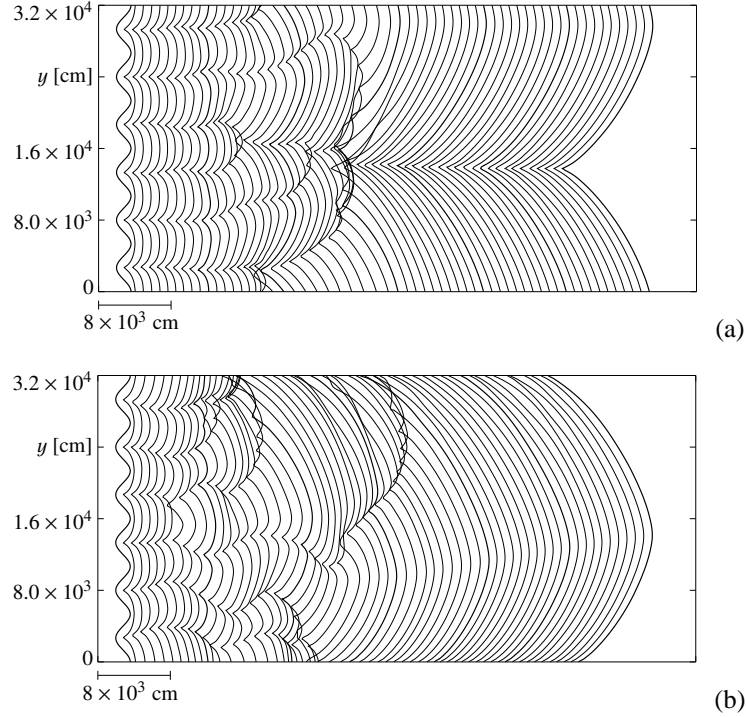


Figure 5.19.: Evolution of the flame front for $\rho_u = 5 \times 10^7 \text{ g cm}^{-3}$ **(a)** with periodic boundaries in y -direction, **(b)** with reflecting boundaries in y -direction. Each contour marks a time step of $0.5 \tau_{\text{LD}} (\lambda_{\text{pert}} = 3.2 \times 10^4 \text{ cm})$.

cells, which is only a crude approximation, and it does not take into account the development of a superimposed small-wavelength pattern.

5.3.7. Influence of the initial flame shape and the boundary conditions

One topic we have postponed so far is the influence of the shape of the initial flame perturbation and of the boundary conditions on the flame evolution. In order to test this, we performed two long-term simulations with the setup described above at a resolution of 200×200 grid cells with a cell width of $\Delta x = 160 \text{ cm}$. The fuel density was $5 \times 10^7 \text{ g cm}^{-3}$. In both cases we perturbed the flame front initially in a sinusoidal way with a wavelength of $1/6$ of the domain width, but we applied different boundaries transverse to the flame propagation. In the simulation whose result is plotted in Figure 5.19a, we applied periodic boundary conditions in y -direction. Figure 5.19b shows the result of the simulation with reflecting boundaries in y -direction. Both simulations were carried out over a time corresponding to 30 growth times $\tau_{\text{LD}} = \omega_{\text{LD}}^{-1}$ according to Landau's dispersion relation (2.86) and corresponding to a wavelength of the domain width (i.e. $3.2 \times 10^4 \text{ cm}$). Again, the

5. Results and discussion

flame contours are artificially shifted in x -direction for better visibility. The conclusions that can be drawn from these results are:

1. In the given setup, the initial perturbation shape is not retained, although the initial perturbation at first develops into a cellular structure of the same wavelength in the nonlinear regime. The flame shows the tendency to align in the shape of a single domain-filling cell. The transition to this steady-state pattern happens by growth of preferred cells from the initial perturbation and the disappearance of smaller cells in newly formed cusps. We will refer to this effect as “merging” of cells in the following.
2. The merging of the small cells proceeds smoothly without drastic effects on the flame shape. In particular it does not lead to a loss of flame stability.
3. The cases of reflecting and periodic boundary conditions differ in the alignment of the ultimately developed flame cell. In the case of periodic boundary conditions the cusp develops in the center of the domain and the crest tends toward the boundary. This result is consistent with numerical solutions of the Sivashinsky equation (Gutman & Sivashinsky 1990). For the reflecting boundary condition the pattern is reversed. Here, the crest centers in the domain.

These results support the generality of the simulations presented in the last sections. Although the restriction to an initial domain-filling perturbation wavelength may appear rather artificial, it avoids the time-consuming cell merging before the final steady-state flame structure is reached.

5.3.8. Flame stability at different fuel densities

Further numerical experiments addressed the flame stability at different fuel densities. With lower fuel density, the Atwood At number—defined as $At = |\rho_u - \rho_b|/(\rho_u + \rho_b)$ —(and, equivalently, the density contrast μ over the flame front) increases (cf. Table 5.1 on page 90). At the same time the laminar burning velocity of the flame decreases. Does this influence the flame stabilization? Originally, this question was raised by Niemeyer & Hillebrandt (1995), who reported on indications that the flame may destabilize at fuel densities $\lesssim 5 \times 10^7 \text{ g cm}^{-3}$. In the following tests of the flame stability at a variety of fuel densities will be presented. These use the setup introduced in Section 5.3.2 and we again refer to Table 5.1 for the complete set of setup values. The resolution chosen for this study was 200×200 cells.

Figure 5.20 shows the temporal evolution of the flame front for fuel densities of $2.5 \times 10^7 \text{ g cm}^{-3}$ and $5 \times 10^7 \text{ g cm}^{-3}$. In both cases the flame stabilizes in a single domain-filling cusp-like structure. Note, that the evolution time has been normalized to the growth time of the LD instability corresponding to the initial perturbation wavenumber $\tau_{LD} = \omega_{LD}^{-1}$. This offers comparability between the different simulations. The spacing between individual contours is, however, artificial since the original simulations were performed in the frame

5.3. Flame propagation into quiescent fuel

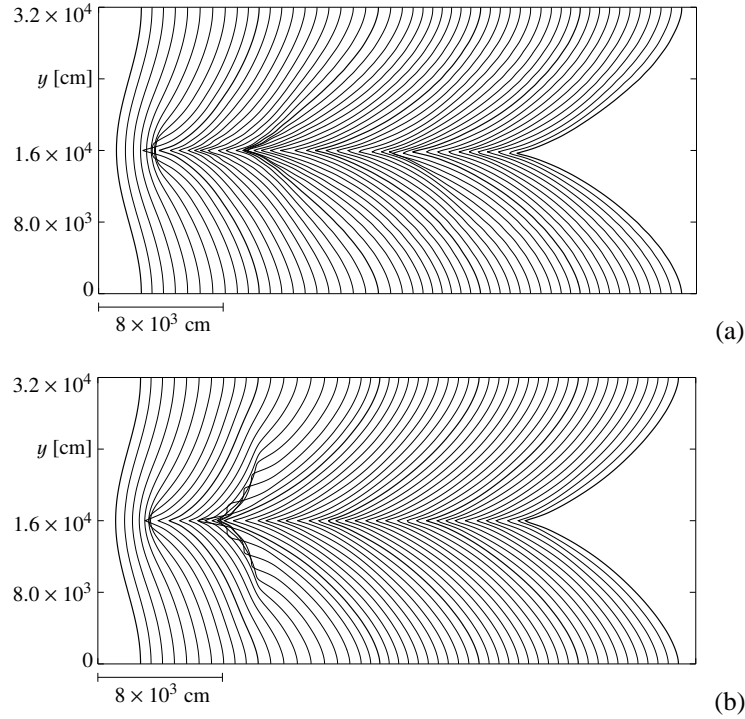


Figure 5.20.: Evolution of the flame front at **(a)** $\rho_u = 2.5 \times 10^7 \text{ g cm}^{-3}$ and **(b)** $\rho_u = 5 \times 10^7 \text{ g cm}^{-3}$. The contours mark evolution steps of $0.2 \tau_{LD}$.

of reference comoving with the flame. It has been chosen in a way that the contours fill the plot window and does not reflect flame propagation.

The outcome from simulations with even lower fuel density reveals a completely different flame evolution. Figure 5.21 shows the flame for fuel densities of $1 \times 10^7 \text{ g cm}^{-3}$ and $1.25 \times 10^7 \text{ g cm}^{-3}$. Although the initial flame evolution resembles that of $\rho_u \approx 5 \times 10^7 \text{ g cm}^{-3}$, the forming cusp lacks long term stability. As can be seen from the plots, the stable structure breaks up from the cusps outward and the flame subsequently evolves in an irregular pattern. The origin of these effects is most likely numerical. For a fuel density of $1 \times 10^7 \text{ g cm}^{-3}$ a simulation run with 600×600 cells resolution did not result in a disruption of the cusp anymore. Thus, a rather high grid resolution is required in order to describe a stable cusp properly at low fuel densities ($\lesssim 1.25 \times 10^7 \text{ g cm}^{-3}$). Nevertheless, if the reason for the disruption of the stable flame pattern is numerical noise, then one could argue that flames at lower fuel densities are likely to become more sensitive to velocity fluctuations in the fuel region. These, however, can be expected to be present in realistic scenarios of SN Ia explosions. Therefore we will address that question in Section 5.4.

A rather unexpected result is obtained from simulations for fuel densities around $1 \times 10^8 \text{ g cm}^{-3}$. Here, the flame does not propagate in a stable manner in the first stages of the flame evolution. This is illustrated by Figure 5.22. Small-wavelength perturbations super-

5. Results and discussion

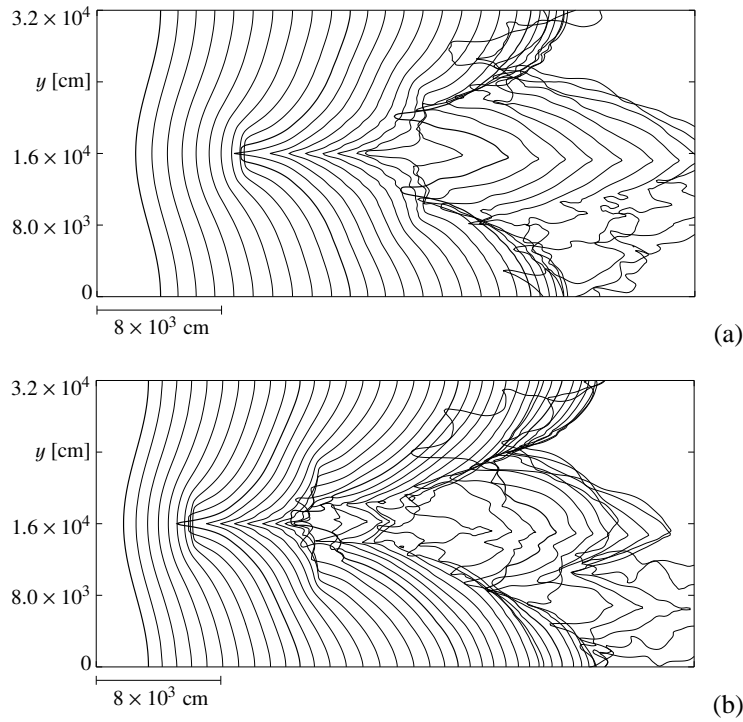


Figure 5.21.: Evolution of the flame front at (a) $\rho_u = 1 \times 10^7 \text{ g cm}^{-3}$ and (b) $\rho_u = 1.25 \times 10^7 \text{ g cm}^{-3}$. The contours mark evolution steps of $0.2 \tau_{LD}$.

pose the initial flame shape shortly after the beginning of the simulation. They appear to dominate the flame evolution (in particular in Figure 5.22b) for a while but then the flame stabilizes in the single-cell structure. This implies that *i*) the flame structure appears to be less stable against small-wavelength perturbations at these fuel densities and *ii*) the mechanism for a stabilization in a preferred long-wavelength pattern as analytically predicted (cf. Sections 2.4.1 and 2.4.3) does finally stabilize the flame evolution.

This initial flame destabilization becomes less pronounced in flame evolution at even higher densities. Figure 5.23 shows an example with $\rho_u = 1 \times 10^9 \text{ g cm}^{-3}$.

5.3. Flame propagation into quiescent fuel

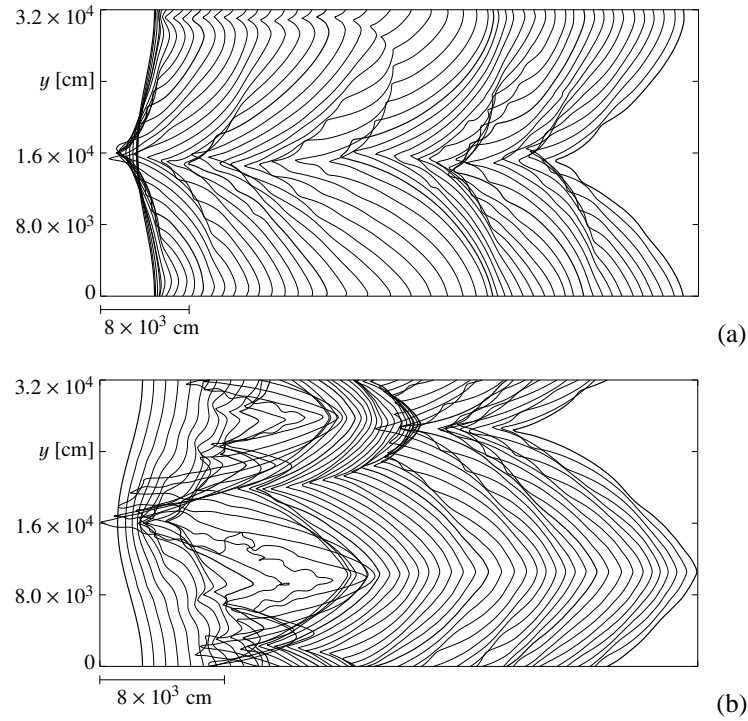


Figure 5.22.: Evolution of the flame front at (a) $\rho_u = 7.5 \times 10^7 \text{ g cm}^{-3}$ and (b) $\rho_u = 1 \times 10^8 \text{ g cm}^{-3}$. The contours mark evolution steps of $0.2 \tau_{LD}$.

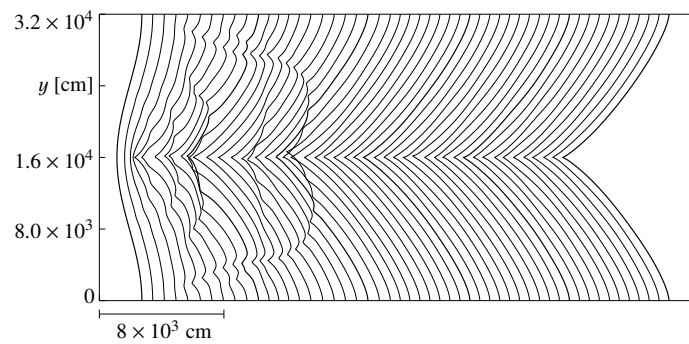


Figure 5.23.: Evolution of the flame front at $\rho_u = 1 \times 10^9 \text{ g cm}^{-3}$. The contours mark evolution steps of $0.2 \tau_{LD}$.

5. Results and discussion

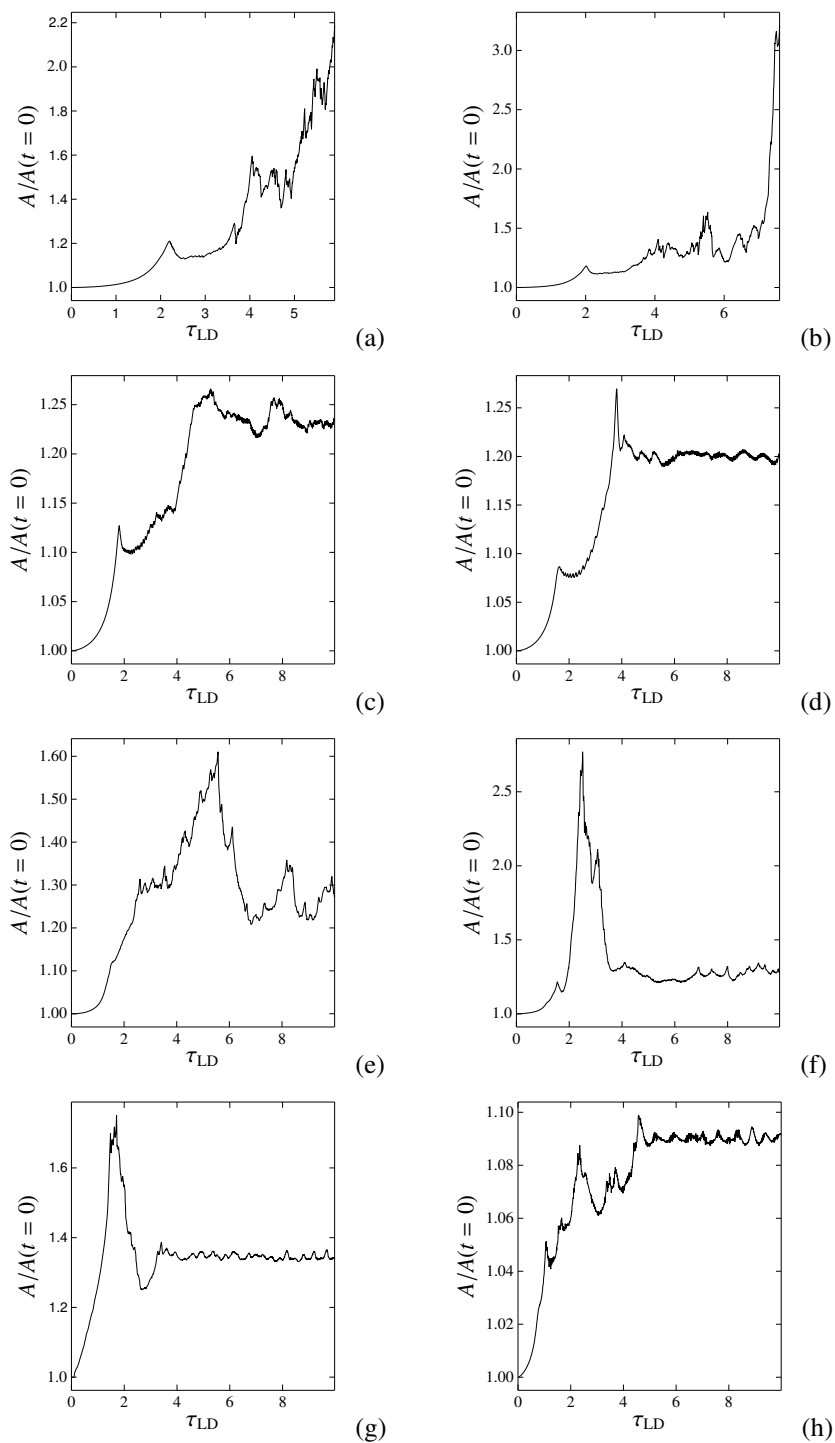


Figure 5.24.: Increase in flame surface area at fuel densities of
(a) $\rho_u = 1 \times 10^7 \text{ g cm}^{-3}$, **(b)** $\rho_u = 1.25 \times 10^7 \text{ g cm}^{-3}$,
(c) $\rho_u = 2.5 \times 10^7 \text{ g cm}^{-3}$, **(d)** $\rho_u = 5 \times 10^7 \text{ g cm}^{-3}$,
(e) $\rho_u = 7.5 \times 10^7 \text{ g cm}^{-3}$, **(f)** $\rho_u = 1 \times 10^8 \text{ g cm}^{-3}$,
(g) $\rho_u = 1.25 \times 10^8 \text{ g cm}^{-3}$, and **(h)** $\rho_u = 1 \times 10^9 \text{ g cm}^{-3}$.

5.4. Flame interaction with a vortical flow

ρ_u [g cm ⁻³]	v_{cell}/s_l (measured)	v_{cell}/s_l (according to eqs. (2.116, 2.117))
2.5×10^7	1.23	1.17
5×10^7	1.20	1.14
7.5×10^7	1.25	1.13
1×10^8	1.30	1.11
1.25×10^8	1.35	1.10
1×10^9	1.09	1.04

Table 5.3.: Flame propagation velocities in the cellular regime.

Again, we measured the flame acceleration in these simulations via the increase in flame surface area. The result is plotted in Figure 5.24. The final steady-state velocities of the cellular flames are compared to the theoretical predictions from equations (2.116, 2.117) in Table 5.3. Keeping in mind the limitations discussed in the previous paragraph, the measurements agree reasonably well with the theoretical predictions. However, the predicted trend of decreasing v_{cell}/s_l with increasing fuel density is obscured by the development of short-wavelength perturbations in some of the simulations.

5.4. Flame interaction with a vortical flow

The second part of our numerical investigations concerned the interaction of flames in the cellular regime with turbulent velocity fields as motivated from the presence of velocity fluctuations in Type Ia supernovae. These stem from pre-ignition convection or may be a relic from the turbulent cascade (see Sections 1.2.4 and 3.1.2).

5.4.1. Simulation setup

The numerical investigation of flame interaction with turbulence is generally an intricate issue. In principle, the straight forward way to go would be to produce an isotropic turbulence field by external forcing and to set up a flame in this field. The production of the turbulence field would have to be carried out in three dimensions and a two-dimensional cut could provide the velocity field to perform 2-d flame simulations in it. However, the numerical production of a turbulence field is very costly and combined with flame modeling it is far too expensive for the level of accuracy intended in our studies and given the parameter space that is to be explored.

For these reasons we follow a different approach. The inflow boundary condition is modified in order to induce a vortical flow field instead of quiescent fuel (as in the previous simulations). The flow field is not stirred anymore and turbulence is not actively produced inside the computational domain by external forcing. This means, that turbulence injected here partly decays before reaching the flame front. It turned out, that injection of a fully developed isotropic turbulence field was hampered by the fact that small scale fluctuations were damped quickly in our implementation.

5. Results and discussion

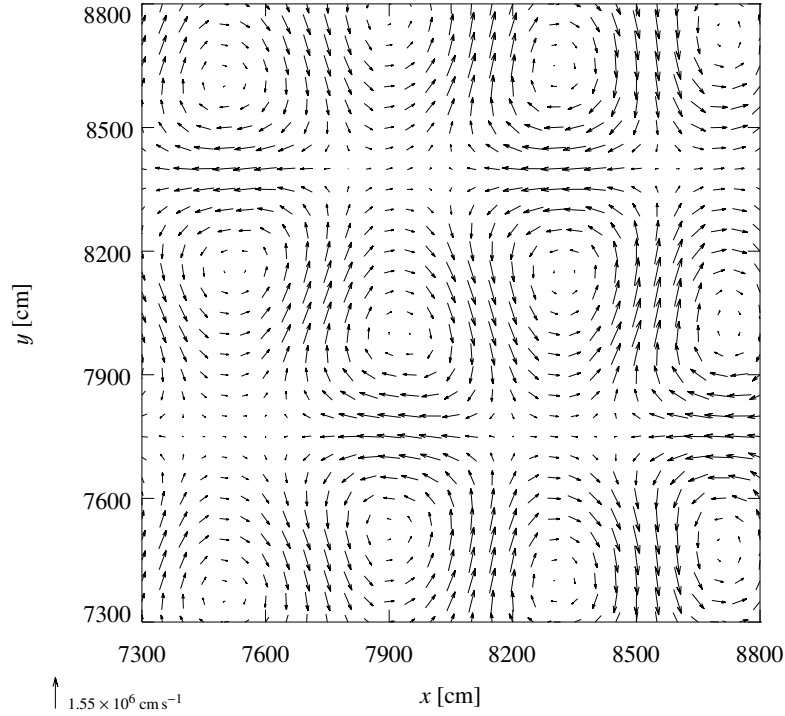


Figure 5.25.: Vortical flow field as applied in the simulations (here for the case $\rho = 5 \times 10^8 \text{ g cm}^{-3}$). The frame of reference is comoving with the vortices. The snapshot is taken after 1.5 flame crossing times over the entire computational domain.

Because of these difficulties we decided to step back to a simplified configuration. As suggested by [Helenbrook & Law \(1999\)](#) we applied an “oscillating” inflow boundary condition on the right hand side of the computational domain, which generates a vortical velocity field approaching the flame. The velocity at the boundary reads:

$$v_x = s_l \{-1 + v' \sin 2k\pi y \cos 2k\pi(x - ts_l)\} \quad (5.5)$$

$$v_y = s_l v' \cos 2k\pi y \sin 2k\pi(x - ts_l). \quad (5.6)$$

The parameter v' characterizes the strength of the imprinted velocity fluctuations. This produces what is termed “square vortices” by [Helenbrook & Law \(1999\)](#). A similar flow field is used by [Vladimirova et al. \(2003\)](#) who name it “cellular flow” and also [Zhu & Ronney \(1994\)](#) apply a flow with cellular vortices to study flame propagation in it. This specific flow has the advantage of being very simple—ideally containing only one Fourier mode. This helps to make the effects visible more clearly and simplifies the interpretation. Figure 5.25 illustrates the vortical flow applied in our simulations. It shows an example at a density of $\rho = 5 \times 10^8 \text{ g cm}^{-3}$. In Figure 5.26a the y -component of the velocity is

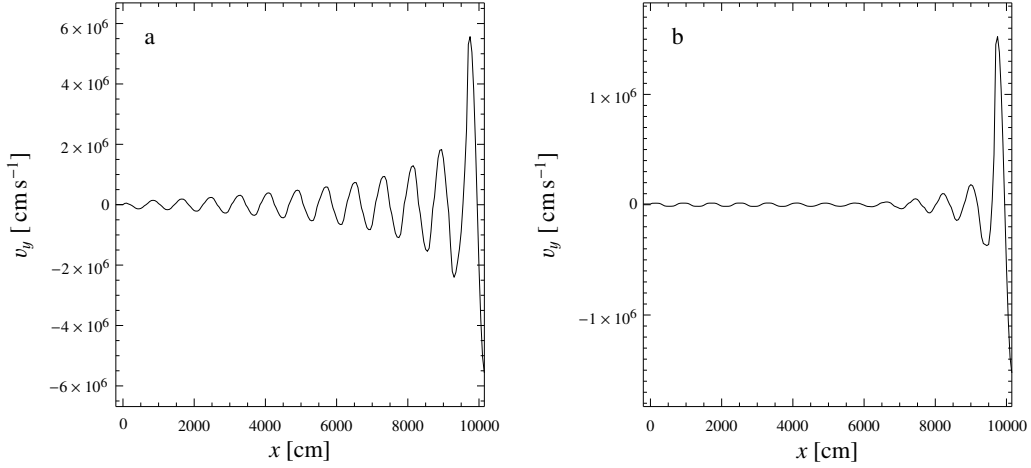


Figure 5.26.: Profile of the y -component of the vortical flow field parallel to the x -axis **(a)** $\rho = 5 \times 10^8 \text{ g cm}^{-3}$; **(b)** $\rho = 1 \times 10^8 \text{ g cm}^{-3}$. The snapshots are taken after 1.5 flame crossing times over the entire computational domain.

plotted against the x -coordinate for the same simulation. It is apparent that the velocity fluctuation is damped while propagating from the inflow boundary into the computational domain. The damping is even stronger for lower densities. Figure 5.26b shows a plot for $\rho = 1 \times 10^8 \text{ g cm}^{-3}$. This causes some problems in the interpretation of the simulation results that will be discussed below.

The other boundaries were set up in the same way as in section 5.3.2. In order to capture the full flame front in cases of strong deformation, we changed from a quadratic domain to a rectangle of 300×200 computational cells. Several experiments with initially planar flames yielded drastic responses of the flame shape when the vortices encountered it. This can be attributed to the high sensitivity of planar flames to perturbations. Consequently, in order to make the results of different simulations comparable and to enable a quantification of the flame evolution, the flame was perturbed initially in a sinusoidal way with eight periods fitting into the domain. This initial perturbation grows due to the LD instability and stabilizes in a cellular pattern, before the injected vortices reach the flame front. In this way it is possible to study the interaction of a stabilized flame with a vortical flow field preventing the incoming flow from unpredictably deforming the flame shape at the first encounter.

5.4.2. What can be expected?

Before we present the results of our numerical study we shall discuss what we actually are looking for in the simulations. That is, we will somehow have to define, how to discriminate between stable flame propagation and a breakdown of the stabilization. Why is this a question of definition? From the conjecture of active turbulent combustion it may appear

5. Results and discussion

that a breakdown of the stabilization must be obvious from a rapid and unlimited growth of the flame propagation velocity. However, this cannot be expected to occur in a numerical simulation where the growth of the flame surface accounting for that effect is limited by discretization and resolution. So, the maximum effect that can be anticipated is a rapid increase in flame surface and burning velocity and a saturation at some higher value. Another possibility is that with increasing strength the vortical flow starts to dominate the flame evolution.

On the other hand, how can we guarantee flame stabilization? Owing to the high computational costs it will not be possible to follow the flame propagation for an arbitrarily long time. However, in case of stabilization we can actually make use of the knowledge on the flame pattern that is to be expected in case of stability in our specific simulation setup. From Section 5.3 (see also Röpke et al. 2003) it is known that the flame propagating into quiescent fuel finally stabilizes in a single domain-filling cusp-like structure for the given setup. This structure may be superimposed by a smaller-scale cellular pattern in sufficiently resolved simulations. A similar result can be anticipated for interaction with weak imprinted vortices.

Thus we may expect two extremal behaviors of the flame. In case that the flame stabilizes and the incoming perturbation fails to break the cellular pattern, the cells of the stabilized small wavelength pattern caused by the initial perturbation of the flame front will merge forming the single domain-filling cusp which then propagates stably. On the other hand, if the intensity of the incoming vortices is high enough to break up the stabilization, no single domain-filling cusp will finally emerge, but the flame should rather show a transient pattern.

5.4.3. Simulation results

The general features of flame evolution in a vortical flow field will again be presented in exemplary cases. The intention is to give an overview over the possible behaviors. Some peculiarities will also be mentioned. The next section will then summarize the numerical experiments covering a certain parameter space.

First, we consider again the case of a fuel density amounting to $5 \times 10^7 \text{ g cm}^{-3}$ (cf. Table 5.1 on page 90). Figures 5.28 and 5.29 show snapshots of the flame evolution. Here, we applied incoming flows with two different strengths of vortices, namely $v'/s_l = 0.7$ and $v'/s_l = 2.5$. These values are imposed at the boundaries and will in the following be used to label the simulations. Note, however, that they do not necessarily represent the values experienced by the flame front for reasons given in section 5.4.1.

Figure 5.27 provides the comparison with flame propagation into quiescent fuel for the chosen setup. It resembles the features of the simulations presented in Section 5.3. Due to the LD instability, the initial perturbation grows and the flame stabilizes in a cellular pattern in the nonlinear regime. The following snapshots show the “merging” of the short-wavelength cells imprinted by the initial condition resulting in the formation of larger cells. The tendency to form a domain-filling cell is apparent. However, following the evolution until the steady-state of a cusp-like structure centered in the domain is reached

5.4. Flame interaction with a vortical flow

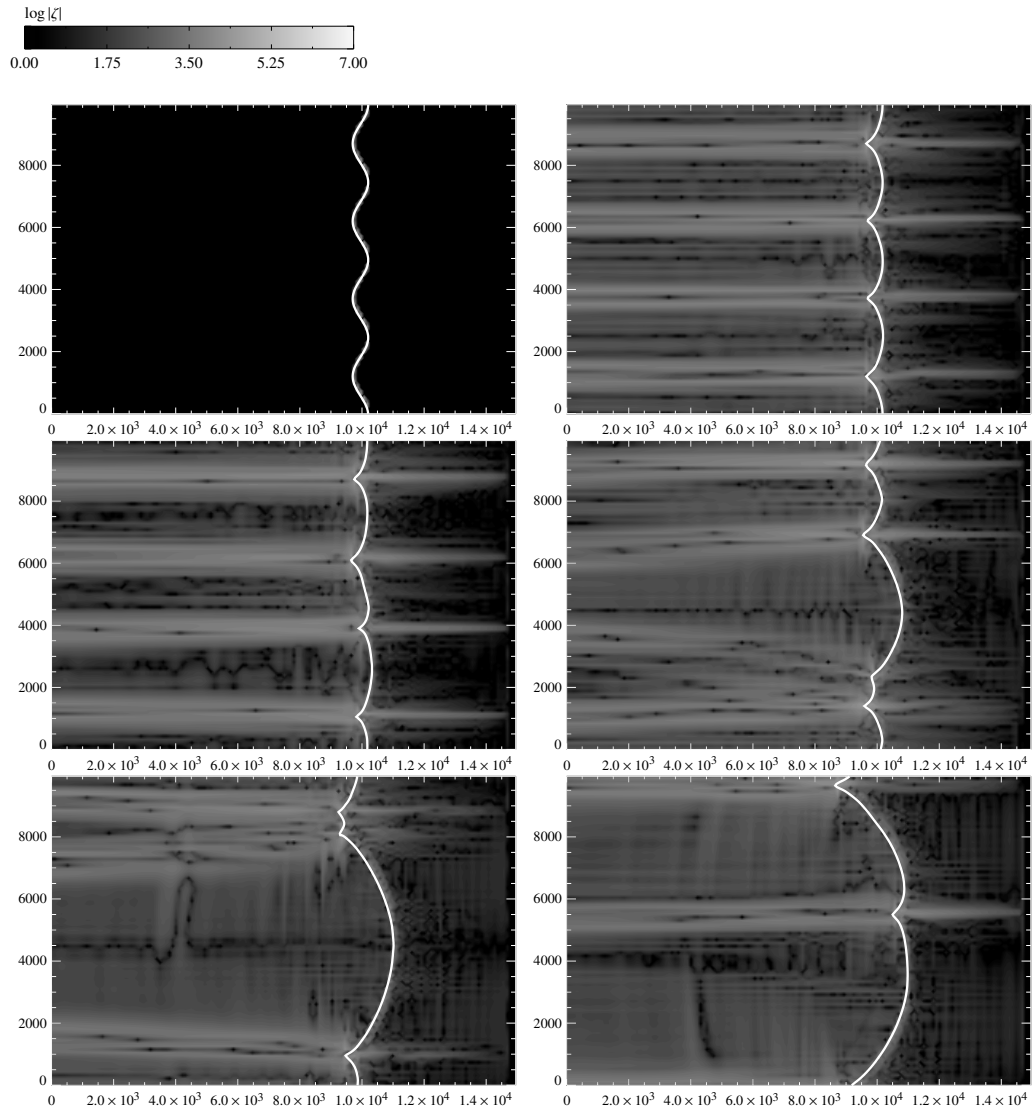


Figure 5.27.: Flame evolution for a fuel density of $5 \times 10^7 \text{ g cm}^{-3}$ and propagation into quiescent fuel. Snapshots taken at time steps $t = 0 \text{ s}$, $t = 8.0 \times 10^{-3} \text{ s}$, $t = 1.6 \times 10^{-2} \text{ s}$, $t = 2.4 \times 10^{-2} \text{ s}$, $t = 3.2 \times 10^{-2} \text{ s}$, and $t = 4.8 \times 10^{-2} \text{ s}$.

5. Results and discussion

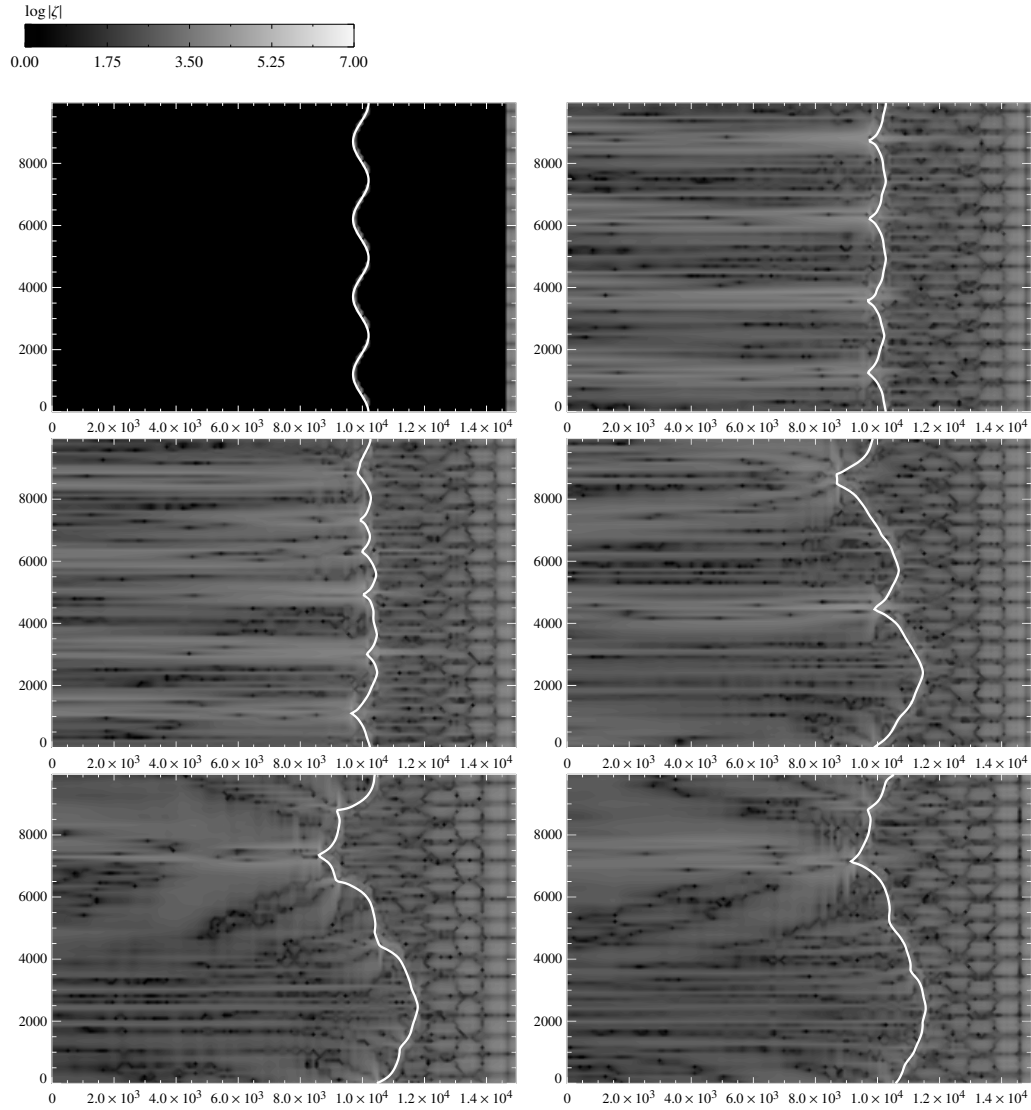


Figure 5.28.: Flame evolution for a fuel density of $5 \times 10^7 \text{ g cm}^{-3}$ and a velocity fluctuation of $v'/s_l = 0.7$ at the right boundary. Snapshots taken at time steps $t = 0 \times 10^{-3} \text{ s}$, $t = 1.2 \times 10^{-2} \text{ s}$, $t = 2.4 \times 10^{-2} \text{ s}$, $t = 3.2 \times 10^{-2} \text{ s}$, $t = 4.0 \times 10^{-2} \text{ s}$, and $t = 4.8 \times 10^{-2} \text{ s}$ (top left to bottom right).

5.4. Flame interaction with a vortical flow

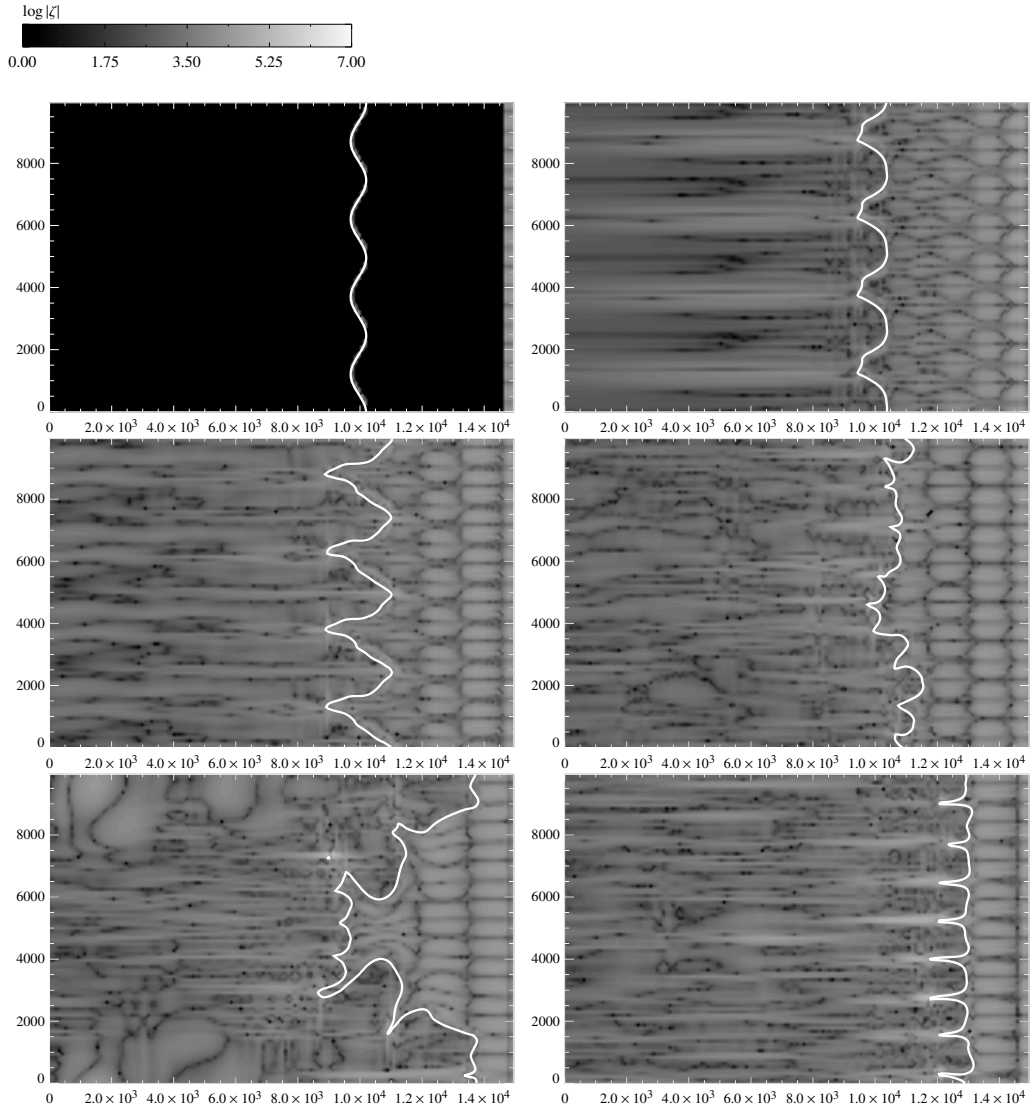


Figure 5.29.: Flame evolution for a fuel density of $5 \times 10^7 \text{ g cm}^{-3}$ and a velocity fluctuation of $v'/s_l = 2.5$ at the right boundary. Snapshots taken at time steps $t = 0 \times 10^{-3} \text{ s}$, $t = 4.0 \times 10^{-3} \text{ s}$, $t = 8.0 \times 10^{-3} \text{ s}$, $t = 1.6 \times 10^{-2} \text{ s}$, $t = 3.2 \times 10^{-2} \text{ s}$, and $t = 4.8 \times 10^{-2} \text{ s}$ (top left to bottom right).

5. Results and discussion

(as it would be expected from the results presented in section 5.3.5) is very expensive and shall not be tried here. This is certainly a drawback in the current study, but it was chosen as a compromise in order to be able to explore a larger parameter space with given computational resources.

Contrary to the flame evolution in Figure 5.27, Figure 5.29 clearly shows the disruption of the initial cellular pattern by interaction of the flame with vortices. Also, the formation of a single domain-filling cell is suppressed by the interaction. The overall flame shape evolution in this case can be interpreted as an adaptation to the imprinted vortical flow structure. The change in the flame evolution from the extreme cases depicted in Figures 5.27 and 5.29 does, however, not proceed abruptly, but rather in a smooth transition. Figure 5.28 presents an example of intermediate behavior. Similar simulations were also performed in some cases with higher resolution of the numerical grid in order to test whether or not insufficient resolution prevents small scale flame structures from developing. However, no significant difference to the flame evolution depicted in Figures 5.27–5.29 was noticed. This agrees with Helenbrook & Law (1999), who found in their simulations of chemical flames that the wavelength of perturbations that develop in interaction with a vortical flow is determined by the scale of the vortices.

5.4.4. A Parameter study

In order to quantify the the flame evolution as qualitatively described in the preceding section, we conducted a parameter study. It aimed on the determination of the trend of the flame behavior as a function of the strength of the vortices in the incoming flow and in dependence on the fuel density.

As discussed in Section 5.3.8, the cellular flame pattern loses stability at around $1.0 \times 10^7 \text{ g cm}^{-3}$, which, however, is attributed to numerics rather than being a physical effect. Correct description of cellular stabilization at these low fuel densities would therefore require unaffordable high numerical resolutions. On the other hand, it can be observed, that at higher fuel densities the sensitivity of the initial flame to small-wavelength perturbations increases. This causes difficulties in producing a stable flame configuration prior to the incoming vortices encountering the flame front. Because of these difficulties we restricted the study to four fuel densities: $\rho_u = 1.25 \times 10^7 \text{ g cm}^{-3}$, $\rho_u = 2.5 \times 10^7 \text{ g cm}^{-3}$, $\rho_u = 5 \times 10^7 \text{ g cm}^{-3}$, and $\rho_u = 7.5 \times 10^7 \text{ g cm}^{-3}$ (cf. Table 5.1 on page 90).

General features

Before we turn to a statistical evaluation of the parameter study, we will illustrate the flame evolution for the different fuel densities by presenting a sample of four simulations for each fuel density (see Figures 5.30 and 5.32–5.34). These differ in the strength of velocity fluctuations imposed on the boundary condition, but note, that the velocity fluctuations experienced by the flame do not scale directly with these values, as mentioned before. Therefore, the plots in Figures 5.30 and 5.32 to 5.34 are ordered according to the mean of the strength of velocity fluctuations at the flame front over a certain period of time. We

will make use of this quantification later in this section.

For comparison, in Figure 5.30 the flame evolution at a fuel density of $5 \times 10^7 \text{ g cm}^{-3}$ is given again for propagation into quiescent fuel and for velocity fluctuations of $v'/s_l = 0.7$, $v'/s_l = 2.0$, and $v'/s_l = 2.5$ at the inflow boundary. The general trends discussed in Section 5.4.3—as the tendency to form domain-filling cusp-like structures in case of low velocity fluctuations and adaptation to the incoming flow at high velocity fluctuations—are apparent here. The plots also reveal the gradual change from one extreme behavior to the other. For this example we will discuss the measurement of some quantities for this simulation. The measured flame surface area as a function of time is plotted in Figure 5.31a,b for the simulations with $v'/s_l = 0.7$ and $v'/s_l = 2.5$, respectively. Apart from fluctuations on a small time scale, the interaction with the vortical flow field introduces also considerable long term fluctuations. These are, of course, expected in the initial phase when the flame starts to react to the incoming vortices. But even at much later times the flame surface area does not reach a steady state. The reason for this effect will be discussed below. Two other quantities that are instructive for the examination of flame evolution are certainly the velocity fluctuations in the fuel upstream of the front and in the ashes downstream of it. As discussed above, the strength of the vortices created at the inflow boundary is not a reliable measure of what the flame actually experiences, since the velocity fluctuations get quickly damped when propagating toward the flame and bending of the flame front may lead to different velocity fluctuations at different locations on the flame. Moreover, the dependence of the damping on the fuel density hampers the comparison of simulations with a variety of these values. Therefore we determine the standard deviations of the velocity fields, $\sigma(v_u)$ and $\sigma(v_b)$, in a certain belt around the flame. It is obvious from plots 5.31c,d,e,f that both quantities fluctuate considerably.

Figures 5.32 and 5.33 indicate that at lower fuel densities the effect of the incoming vortices on the flame structure is generally more drastic. At $\rho_u = 2.5 \times 10^7 \text{ g cm}^{-3}$ (Figure 5.33) the tendency of the formation of the domain-filling structure is still visible in the case of propagation into quiescent fuel. This is not the case anymore for $\rho_u = 1.25 \times 10^7 \text{ g cm}^{-3}$ (Figure 5.32) for reasons discussed in Section 5.3.8. However, with increasing strengths of the imprinted velocity fluctuations, the flame still gradually adapts to the flow.

Figure 5.34 shows the flame evolution at a fuel density of $7.5 \times 10^7 \text{ g cm}^{-3}$. The trends are the same as for $\rho_u = 5 \times 10^7 \text{ g cm}^{-3}$. Only in case of propagation into quiescent fuel (Figure 5.34a) the initial destabilization with respect to small wavelength perturbations (cf. Section 5.3.8) alters the evolution for a transition period, before the flame stabilizes in a domain-filling single-cell structure.

Statistical quantification

In a statistical evaluation of our parameter study of the flame evolution for different fuel densities we will now address *i*) the dependency of the effective flame propagation velocity on the strength of the imprinted velocity fluctuations and *ii*) the amplification of the velocity fluctuation by the flame front. As was discussed above, all quantities necessary for this are not easy to determine, because they fluctuate considerably with time (see Fig-

5. Results and discussion

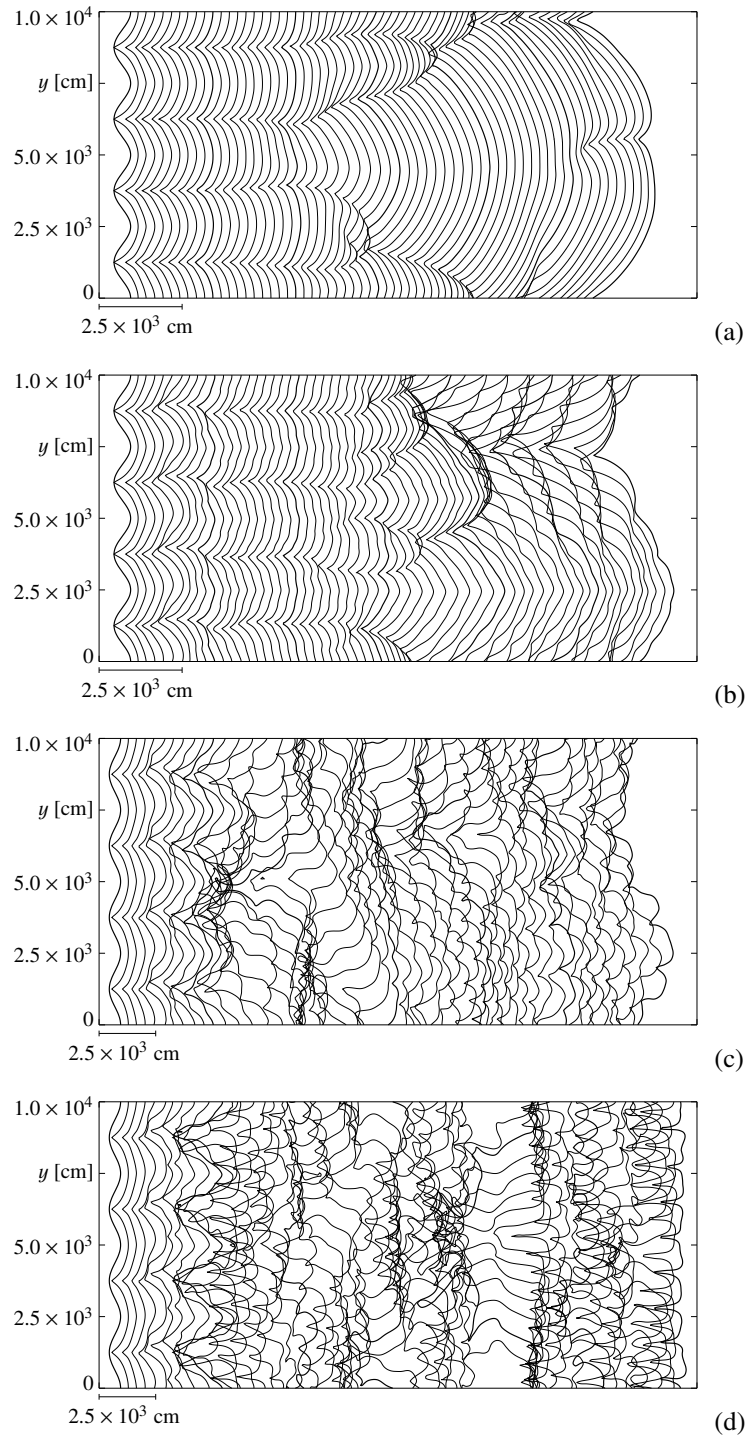


Figure 5.30.: Flame evolution for a fuel density of $5 \times 10^7 \text{ g cm}^{-3}$. **(a)** propagation into quiescent fuel and for velocity fluctuations at the right boundary of **(b)** $v'/s_l = 0.7$, **(c)** $v'/s_l = 2.0$, and **(d)** $v'/s_l = 2.5$. Each contour represents a time step of $8.0 \times 10^{-4} \text{ s}$ (a,b), and $2.4 \times 10^{-3} \text{ s}$ (c,d).

5.4. Flame interaction with a vortical flow

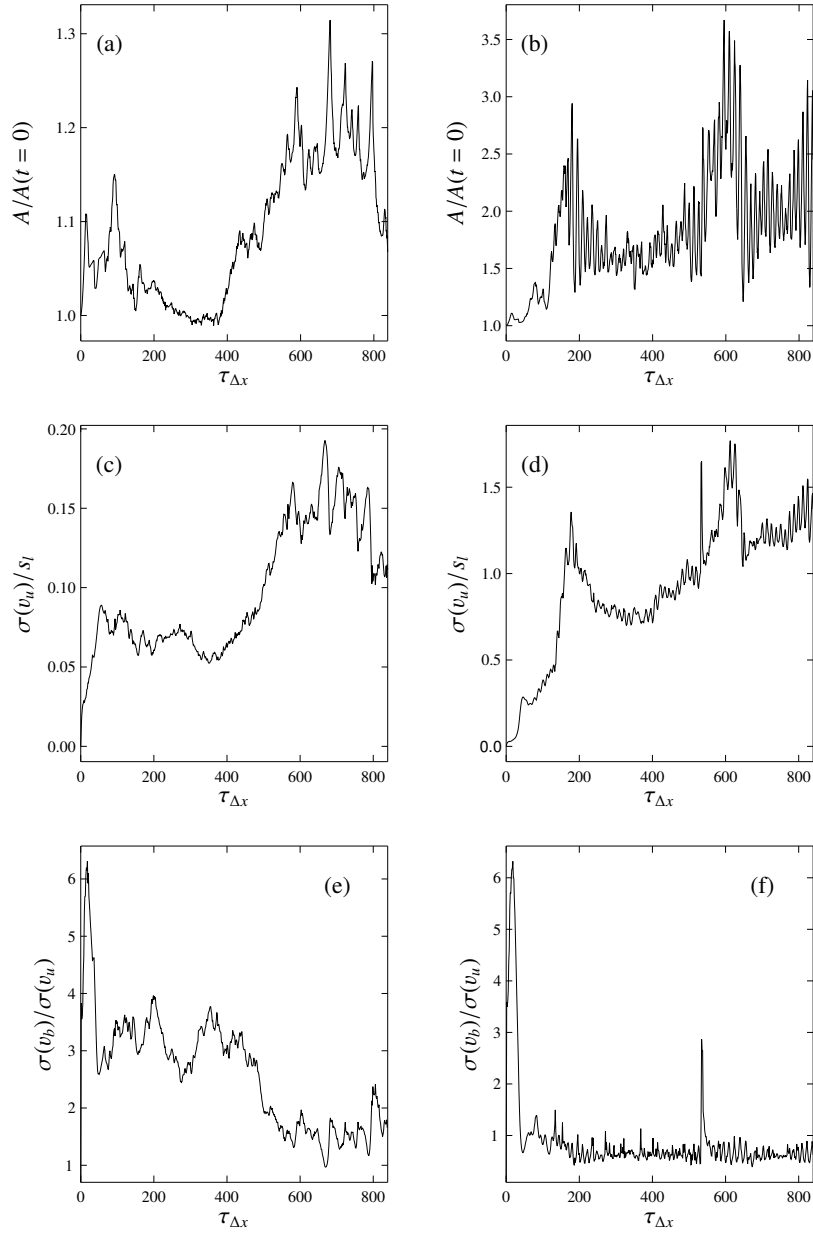


Figure 5.31.: (a,b) Flame surface area over time (c,d) standard deviation of the velocity field ahead of the front over time (e,f) ratio of the standard deviations of the velocity fields beyond and ahead of the flame over time (the time is normalized to the crossing time of the laminar flame over one grid cell $\tau_{\Delta x}$) The left and right columns of plots correspond to $v'/s_l = 0.7$ and $v'/s_l = 2.5$, respectively.

5. Results and discussion

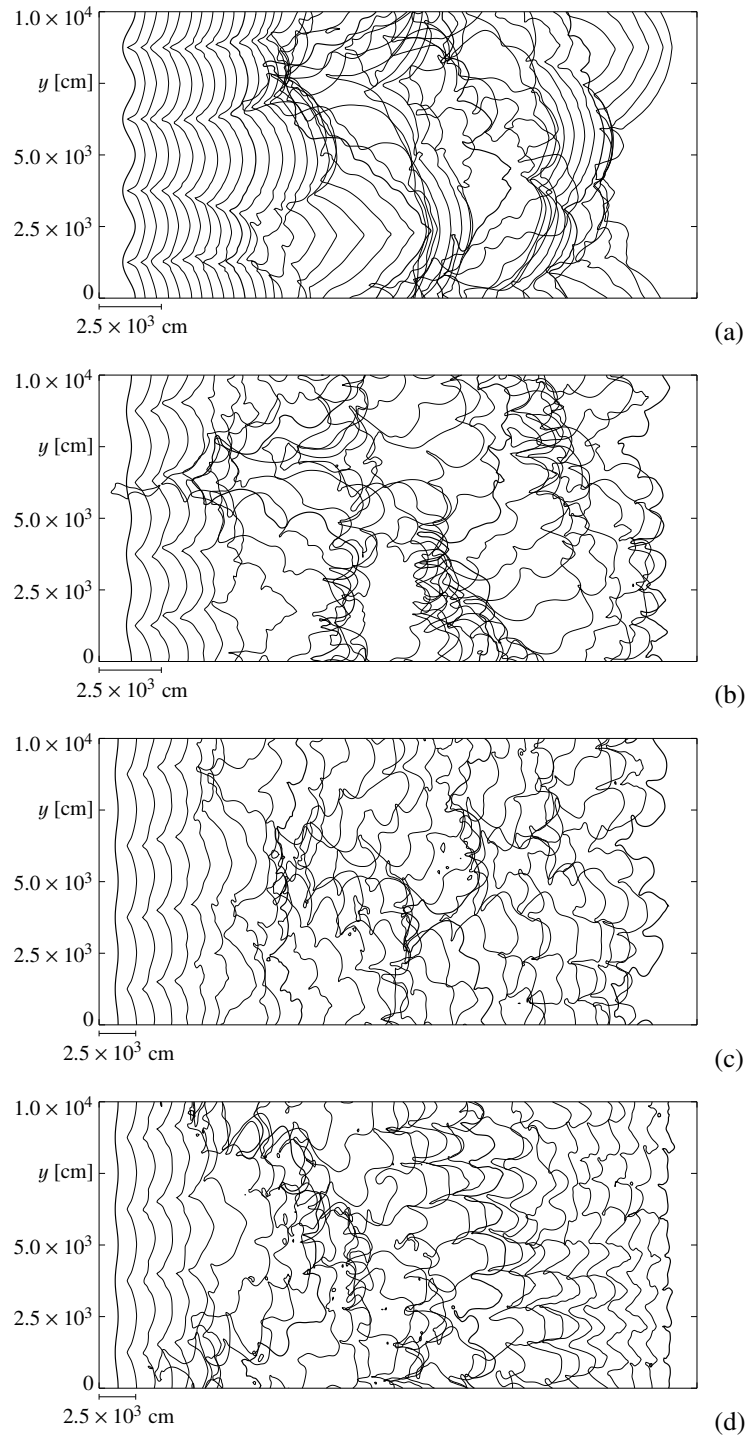


Figure 5.32.: Flame evolution for a fuel density of $1.25 \times 10^7 \text{ g cm}^{-3}$. **(a)** propagation into quiescent fuel and for velocity fluctuations at the right boundary of **(b)** $v'/s_l = 2.0$, **(c)** $v'/s_l = 2.5$, and **(d)** $v'/s_l = 3.0$. Each contour represents a time step of $4.2 \times 10^{-4} \text{ s}$.

5.4. Flame interaction with a vortical flow

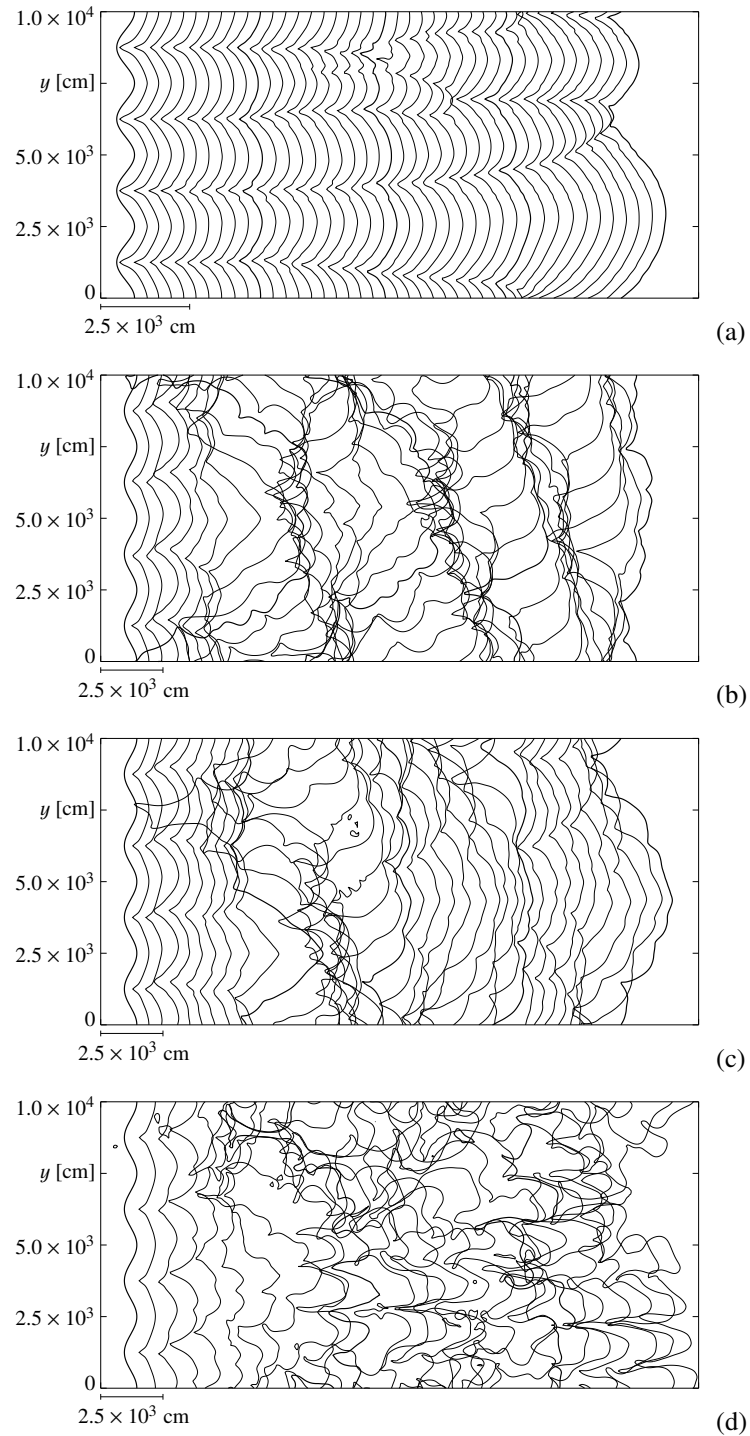


Figure 5.33.: Flame evolution for a fuel density of $2.5 \times 10^7 \text{ g cm}^{-3}$. **(a)** propagation into quiescent fuel and for velocity fluctuations at the right boundary of **(b)** $v'/s_l = 1.75$, **(c)** $v'/s_l = 1.5$, and **(d)** $v'/s_l = 3.5$. Each contour represents a time step of $1.2 \times 10^{-3} \text{ s}$ (a) and $2.4 \times 10^{-3} \text{ s}$ (b)–(d).

5. Results and discussion

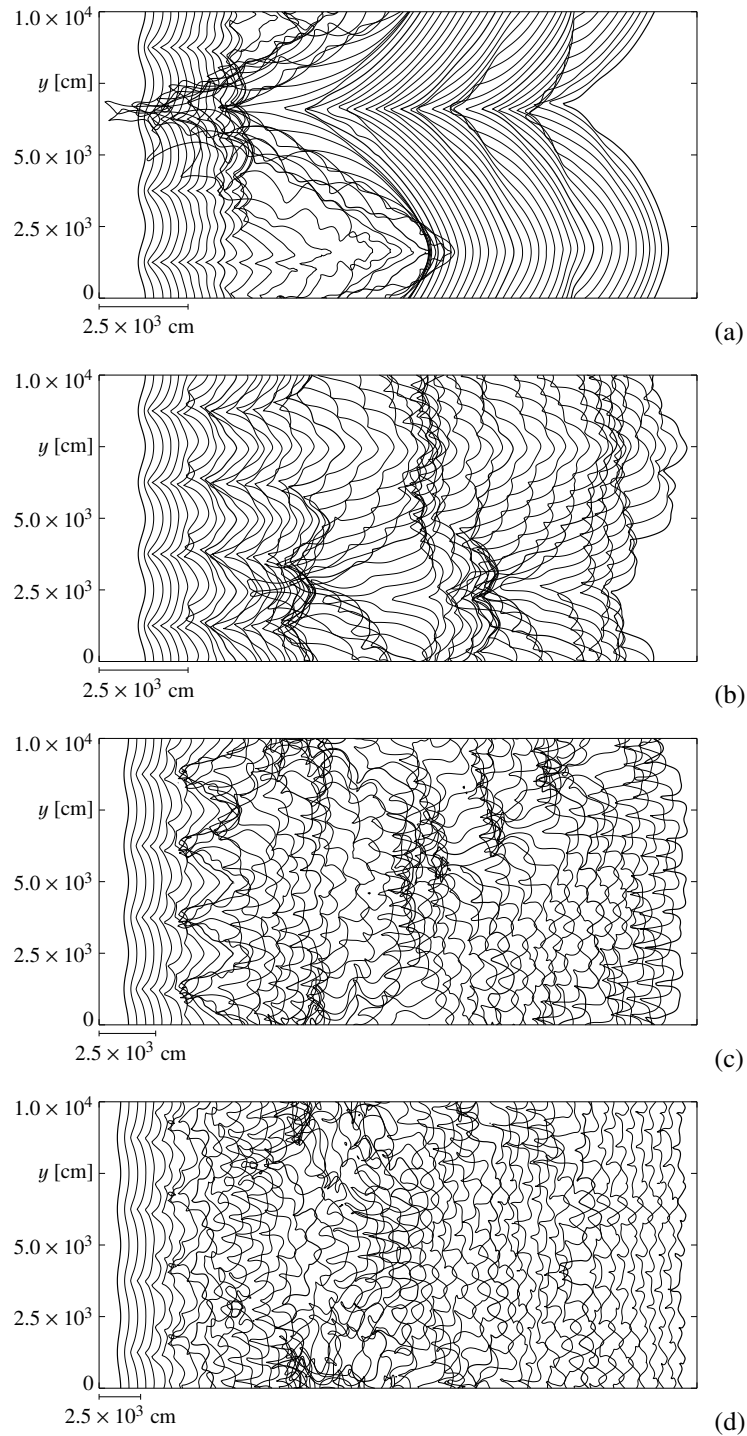


Figure 5.34.: Flame evolution for a fuel density of $7.5 \times 10^7 \text{ g cm}^{-3}$. **(a)** propagation into quiescent fuel and for velocity fluctuations at the right boundary of **(b)** $v'/s_l = 1.0$, **(c)** $v'/s_l = 2.0$, and **(d)** $v'/s_l = 3.0$. Each contour represents a time step of $8.3 \times 10^{-7} \text{ s}$.

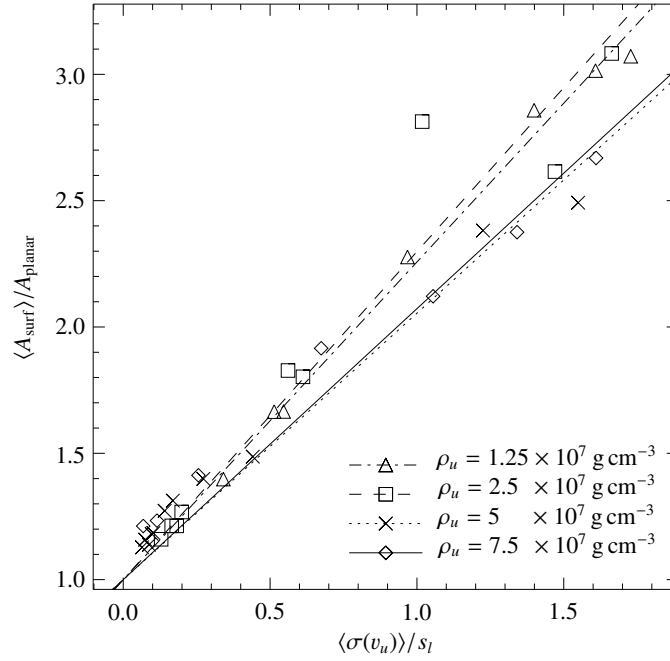


Figure 5.35.: Dependence of the flame surface area on the strength of the imprinted velocity fluctuations.

ure 5.31). Therefore we will have to average these quantities over a certain time. For this averaging we chose a time range from $480 \tau_{\Delta x}$ to $720 \tau_{\Delta x}$ ($\tau_{\Delta x}$ denotes the crossing time of the corresponding laminar flame over one grid cell). Additionally, in order to make the measurements for different fuel densities comparable, we scaled the belt around the flame in which the standard deviation of the velocity field was determined in a way that the time for flame crossing over the width of this belt remained the same for all fuel densities.

In Figure 5.35 the temporal mean value of flame surface area A_{surf} (normalized to the surface area of the corresponding planar flame front A_{planar}) is plotted against the temporal mean of standard deviation of the velocity in the fuel region (normalized to the laminar burning velocity of the flame). This measures according to Section 5.3.6 the flame propagation velocity in dependence on the imprinted velocity fluctuations.

The increase of the flame speed with stronger incoming velocity fluctuations is evident from Figure 5.35. However, there is quite a large scatter in the data. This has two reasons. Firstly, we certainly did not follow the flame evolution long enough to undoubtedly reach the steady state of the flame shape—which should ideally be the clearly distinct single domain-filling cusp-like structure in case of weak incoming vortices. To follow the flame propagation up to this stage would, however, be much too expensive for a parameter study. Secondly, some peculiar features of the flame shape may develop as a result of small

5. Results and discussion

ρ_u [g cm ⁻³]	a	b	c
1.25×10^7	1.25712 ± 0.0215	0.177654 ± 0.05236	1.28103 ± 0.004581
2.5×10^7	1.29816 ± 0.0797	0.180935 ± 0.01718	0.779895 ± 0.01982
5×10^7	1.05533 ± 0.04931	0.141428 ± 0.01171	0.558411 ± 0.01883
7.5×10^7	1.07245 ± 0.05131	0.150079 ± 0.2911	0.466975 ± 0.03134

Table 5.4.: Fit parameters according to fitting formulas (5.7) and (5.8) with corresponding asymptotic standard errors.

perturbations (e.g. due to numerical noise). In particular, this causes substantial deviations if it affects the long-wavelength structure of the flame and is primarily responsible for the scatter of the results in case of strong incoming velocity fluctuations. Our simulations suggest here, that the flame shape gradually adapts to the incoming flow, which has short-wavelength velocity fluctuations imprinted on it. The larger scale features here are only transient phenomena, that, however can alter the flame surface significantly. Again, this scatter could very likely be cured by taking the mean over longer time intervals.

Damköhler (1940) proposed a linear dependence of the effective flame propagation velocity on the turbulence intensity for turbulent combustion in what is today called flamelet regime. Our results are consistent with a linear growth. Linear fits to the data are included in Figure 5.35. Values for the fit parameter a according to the fitting formula

$$\frac{\langle A_{\text{surf}} \rangle}{A_{\text{planar}}} = 1.0 + a \frac{\langle \sigma(v_u) \rangle}{s_l} \quad (5.7)$$

are given in Table 5.4. It is evident from Figure 5.35 that interaction of the flame in the cellular regime with turbulent velocity fluctuation can lead to a substantial acceleration of the flame propagation velocity. It is certainly not possible from this parameter study to infer a clear trend of the slope depending on the fuel density.

In order to estimate the amplification of the velocity fluctuations across the flame for different densities, we investigated the strength of velocity fluctuations downstream of the flame in dependency of the strength of the imprinted vortices in the fuel. As already shown for the case of flame propagation into quiescent fuel (Section 5.3.3), the flame produces vorticity in the ashes. Here, the question is addressed, whether vorticity present in the fuel will be amplified in the flame, This question arises in connection with the conjecture of active turbulent combustion (Niemeyer & Woosley 1997, see also Section 2.6.3).

The result of the study for a variety of fuel densities is plotted in Figure 5.36. In this plot, trends show up much more clearly than in Figure 5.35. However, some scatter is still present in the data. But the reason for this scatter is only partly connected to the effects that cause the scatter in Figure 5.35. As can be seen from snapshots of the evolution of the flame front (an example is the bottom left snapshot in Figure 5.29), eventually the merging of cusps can produce transient “bursts” in vorticity beyond the flame. This is particularly prominent in case of changes in the long-wavelength flame structure, but not necessarily connected to it. From Figure 5.31f, where this “burst” in velocity fluctuation appears as a spike in the profile, it can be seen that the duration of those events is very short. Hence their

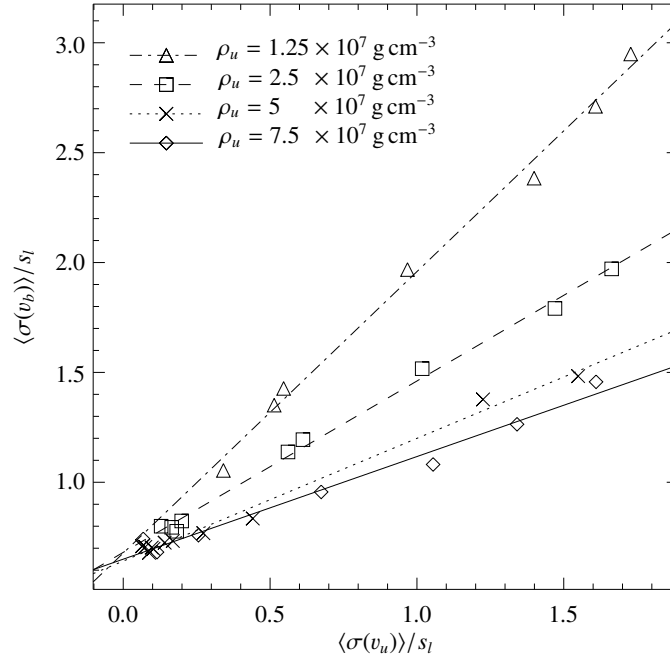


Figure 5.36.: Relation between velocity fluctuations upstream and downstream of the flame front.

contribution to the temporal mean is small (whereas the long-wavelength flame structure and thus the flame surface changes slowly). Consequently, the scatter in plot 5.36 is much smaller than in plot 5.35.

The data plotted in Figure 5.36 can be fit rather well by the assumption that the ratio $\langle \sigma(v_b) \rangle / \langle \sigma(v_u) \rangle$ is proportional to the incoming turbulence intensity, i.e.

$$\langle \sigma(v_b) \rangle = b + c \langle \sigma(v_u) \rangle. \quad (5.8)$$

Table 5.4 provides the fit parameters. In contrast to Figure 5.35, the plot in Figure 5.36 reveals a clear trend for the fuel density. The slope c increases with lower ρ_u . This is what would be expected taking into account the increased production of specific volume in the flame with lower ρ_u . In Figure 5.37 the factor c is plotted against the corresponding density ratio μ , accentuating the trend. Of course, a functional dependence cannot be inferred from this small sample of data. It is interesting to note that for $\rho_u \approx 2.5 \times 10^7 \text{ g cm}^{-3}$ the slope c becomes greater than unity, indicating a slight amplification of velocity fluctuation in this case.

We would like to mention here that the above interpretation of this result requires some caution, since the cellular stabilization of the flame has been shown to be weaker with lower fuel density. This seems to be a numerical rather than a physical effect, since

5. Results and discussion

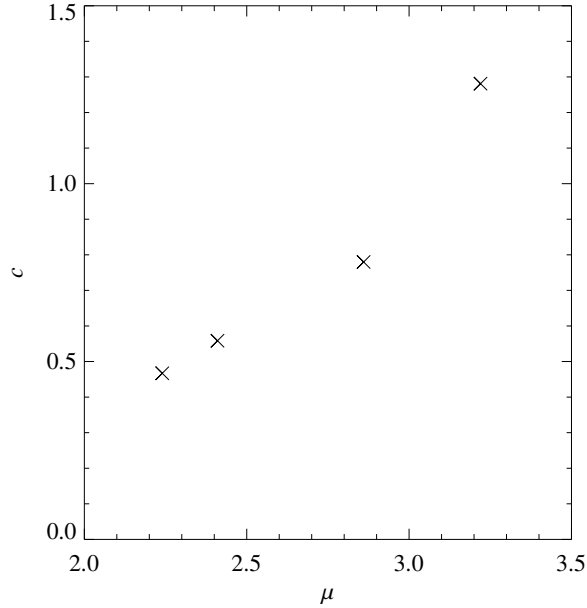


Figure 5.37.: Ratio of the velocities upstream and downstream of the flame front as a function of the density contrast μ over it.

the cusps become more stable with higher resolution. Thus, at the given resolution of our parameter study, the flame evolution shows peculiar behavior below a fuel density of $1.25 \times 10^7 \text{ g cm}^{-3}$. Cusps lose eventually stability distorting the flame shape, which then responds with accelerated propagation of the perturbed part for a short period, after that the flame stabilizes again. Here, the results can not be trusted anymore.

However, we do not observe such a flame evolution at higher fuel densities included in this parameter study. Thus, the dependency on the fuel density is likely to be (at least partially) of physical origin.

The result of the presented parameter study is that no drastic flame acceleration or turbulence production is observed even if the imprinted velocity fluctuations are strong enough to break up the original cellular stabilization of the flame front. We rather observe a gradual adaptation of the flame to the vortical flow field. This is consistent with the result of the numerical investigation of chemical flames by [Helenbrook & Law \(1999\)](#). Therefore the simulations performed in the parameter space of fuel densities ranging from $\rho_u = 7.5 \times 10^7 \text{ g cm}^{-3}$ down to $\rho_u = 1.25 \times 10^7 \text{ g cm}^{-3}$ and imprinted velocity fluctuations up to $\sigma(v_u)/s_l \sim 1.7$ reveal no indication of a deviation of the flame propagation in the flamelet regime of turbulent combustion.

6. Epilogue

Yet not every solution of the equations of motion, even if it is exact, can actually occur in Nature. The flows that occur in Nature must not only obey the equations of fluid dynamics, but also be stable.

— L. D. Landau & E. M. Lifshitz (1959)

6.1. Conclusions

The present study addresses the question of stability of thermonuclear flames in Type Ia supernova explosions. The underlying model of all investigations discussed in this work explains SNe Ia as thermonuclear explosions of a Chandrasekhar-mass white dwarf star composed of carbon and oxygen. The thermonuclear burning is confined to a very thin layer ($\lesssim 1$ cm), called a *flame*, which initially propagates in the subsonic deflagration mode, i.e. the combustion wave is mediated by microphysical transport processes.

Our study focuses on scales around the Gibson scale (see Sections 2.6.2 and 3.1.2) and we thus confined the typical width of the computational domain in that we performed our studies to $\sim 10^4$ cm. It is therefore well-justified to model the flame in the discontinuity approximation ignoring any inner structure of it. The reason for our interest in this scale range, which is orders of magnitude below the radius of the exploding WD ($\sim 10^8$ cm) is, that large scale SN Ia simulations (e.g. Reinecke et al. 2002b) trying to model the scales of the WD are unable to resolve it and therefore rely on the assumption of stability of the flame there. However, this has not been convincingly checked so far. Below the Gibson scale, the flame propagation is not affected anymore by the turbulent eddy cascade that is evoked by large-scale instabilities. Here, flame evolution is dominated here mainly by a hydrodynamic instability, known as the *Landau-Darrieus instability*. Theoretical considerations suggest that the flame stabilizes against this instability by a nonlinear mechanism. It should adopt a cellular shape. So far, there exists no numerical simulation including full treatment of the hydrodynamical flow that proves this conjecture for conditions that are expected in SN Ia explosions.

A key parameter to all deflagration SN Ia models is the effective flame propagation velocity. Wrinkling of the flame surface due to instabilities or interaction with turbulence increase the surface and this accelerates the flame speed beyond the value that corresponds to a planar flame geometry. Only this effect qualifies deflagration models as candidates to explain SNe Ia. Therefore it is highly desirable to determine the flame acceleration that results from the cellular pattern at scales we address in our simulations. Furthermore,

6. Epilogue

there have been speculations in literature about a possible breakdown of the cellular stabilization of the flame front and a following self-turbulization of the flame. This effect has been discussed under the term *active turbulent combustion* by Niemeyer & Woosley (1997), Niemeyer (1999), and Hillebrandt & Niemeyer (2000). It would have drastic consequences for SN Ia explosion models and could eventually lead to a transition of the flame propagation mode from subsonic deflagration to supersonic detonation. From one-dimensional empirical supernova models it is known that such a transition at low fuel densities of ~ 1 to $5 \times 10^7 \text{ g cm}^{-3}$ (i.e. late in the explosion phase, when the star has already considerably expanded) produces spectra that are in good agreement with observations. Furthermore, Niemeyer & Hillebrandt (1995) reported on a loss of flame stability at a fuel density of $5 \times 10^7 \text{ g cm}^{-3}$. We therefore focussed our investigation on effects at rather low fuel densities.

In Section 1.4 we raised a number of questions that were to be answered in the framework of the present study. According to the results from our numerical studies presented in Chapter 5 and the discussion therein, we can state:

1. Both the Landau-Darrieus instability¹ and the nonlinear cellular stabilization balancing it exist for thermonuclear flames in Type Ia supernova explosions. The latter has been shown in the framework of the present study for the first time applying full treatment of the hydrodynamical flow.
2. The presented numerical method based on the level set approach and comprising in-cell reconstruction and flux-splitting techniques was shown to be capable of appropriately modeling the propagation of the flame in the discontinuity approximation. The measured growth rate of perturbations of the planar flame shape in the linear stage of flame evolution was in agreement with Landau's dispersion relation. In contrast, the "passive implementation" of the level set method applied in the large-scale supernova simulations by Reinecke et al. (2002b) has been shown to be unable to reproduce the expected behavior. This was attributed to the fact that unlike the "passive implementation", the scheme used in the present study provides correct coupling between flame propagation and the hydrodynamical flow.
3. In the nonlinear regime of flame evolution the flame adopts a cellular pattern. In the simulation setup we applied, the steady-state shape of the flame front is a domain-filling single-cell structure that may be superimposed with a short-wavelength cellular pattern at sufficient numerical resolution. This result does not depend on the shape of perturbation that was initially imposed on the flame. The alignment of the large cell in the computational domain depends on the boundary conditions applied in the direction transverse to that of flame propagation. In case of periodic boundary conditions, the cusp centers in the computational domain while in case of reflection boundary conditions the crest of the pattern tends to align in the domain

¹This part is in accord with the result by Niemeyer & Hillebrandt (1995)

6.2. Comparison with experiments

center. All these results are consistent with predictions resulting from analytical and semi-analytical studies.

4. For the steady-state cellular flame structure we measured an effective flame propagation velocity of $\sim 1.1s_l$ depending on the fuel density. Keeping in mind the discussion from Section 5.3.8 the agreement with theoretical predictions is reasonable.
5. In contrast to Niemeyer & Hillebrandt (1995), we found no indication for a decrease of flame stability at a fuel density of $5 \times 10^7 \text{ g cm}^{-3}$. The loss of stability of the cusps of the cellular flame structure at $\rho_u \approx 1 \times 10^7 \text{ g cm}^{-3}$ observed in our simulations can be attributed to insufficient numerical resolution. To our surprise, we observed a loss of flame stability at $\rho_u \sim 10^8 \text{ g cm}^{-3}$. This, however, was identified as a transient phenomenon and the flame stabilized finally in a domain-filling cell. We thus may conclude that our simulations did not reveal significant flame destabilization at the density range under consideration (1×10^7 to $1 \times 10^9 \text{ g cm}^{-3}$), although some peculiarities were observed.
6. If the cellularly stabilized flame interacts with vortices of sufficient strengths, then the initial cellular pattern can break up in the sense that the initial shape is lost and the flame adapts to the incoming vortical flow. The tendency of the flame to form a single-cell structure is suppressed by this effect. However, we do not observe a sharp transition but rather a gradual change in the flame behavior.
7. Our numerical simulations suggest that the flame smoothly adapts to the incoming vortical flow with increasing turbulence intensity. No drastic effects were observed. Although we measured an amplification of the strength of the velocity fluctuation across the flame for $\rho_u = 2.5 \times 10^7 \text{ g cm}^{-3}$, we could not observe a deviation from a linear scaling between the flame surface area (and thus the effective flame propagation speed) and the strength of the imprinted velocity fluctuations.

We conclude from that, that the results of our study are consistent with flame propagation in the so-called flamelet regime. Thus our simulations do not conflict with the assumptions of large-scale supernova models on the stability on small unresolved scales. Although we can probably not completely rule out the possibility of active turbulent combustion, we found no convincing hint for such an effect in our numerical investigations. Our simulations indicate that effects resulting from the cellular regime of flame propagation are unlikely to trigger a presumed deflagration to detonation transition.

6.2. Comparison with experiments

One question that is still unanswered is to what degree does our numerical model reflect the flame evolution in nature? Of course, comparison with experiments is usually not possible in astrophysics owing to the extreme conditions in the objects studied here. However,

6. Epilogue

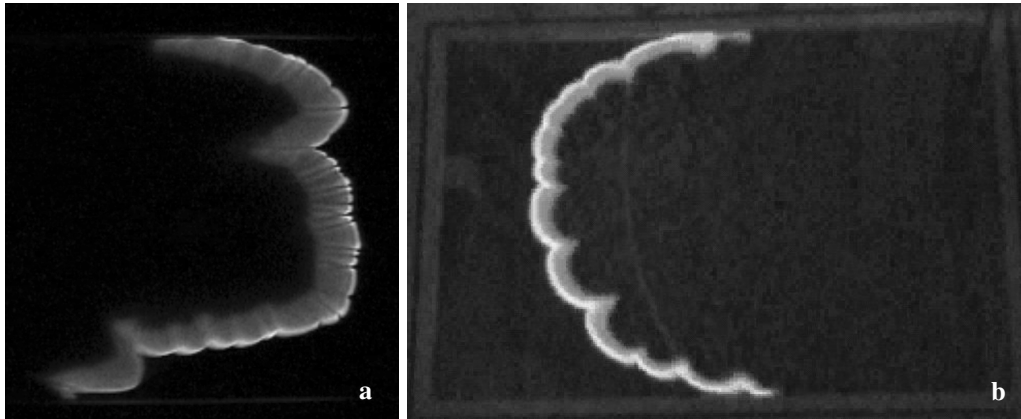


Figure 6.1.: Flame propagation in Hele-Shaw cells **(a)** in a 7.3 % propane – 92,7 % air mixture and **(b)** in a 6.8 % methane – 93.2% air mixture (courtesy of P. D. Ronney, Figure (b) is taken from the *eFluids Gallery of Fluid Flow Images*, <http://www.efluids.com/efluids/gallery/Premixed-gas.htm>)

we can compare our results with terrestrial flames. Although this cannot provide a quantitative validation of our results, one can still judge from that comparison, whether the basic physical concepts that enter our model are appropriate to describe real flames to a certain degree.

Experiments that are suitable for comparison with our results are investigations of the propagation of premixed gaseous chemical flames in so-called *Hele-Shaw cells*, performed in the group of P. D. Ronney at the Department of Aerospace and Mechanical Engineering, University of Southern California, Los Angeles (Sharif et al. 1999, Abid et al. 1999). The Hele-Shaw cells applied there consist of two Plexiglas plates separated by a thin aluminum frame and form a combustion chamber that essentially restricts flame evolution to two dimensions. The chamber is filled with the fuel mixture (typically hydrocarbon and air) and the flame is ignited on one side of the chamber by one or more sparks. Figure 6.1 shows two examples.

In the comparison with our results one has to keep in mind that the Lewis number Le for the chemical flames in the experiments is orders of magnitude lower than in thermonuclear flames under conditions of SN Ia explosions. Therefore the pattern of these chemical flames is not solely caused by the LD instability, but also by the diffusional-thermal instability (cf. Section 2.3).

Nevertheless, the basic features we observe in our simulations are present in the experiments:

1. The flame stabilizes in a cellular pattern.
2. The flame front shows the tendency to form a one-cell structure that fills the entire width of the combustion chamber (see Figure 6.1b; this feature is also apparent in many other snapshots and movies from the experiments that cannot be shown here)

3. The one-cell flame structure aligns with the crest centered in the combustion chamber, as is the case in our simulations when reflecting boundary conditions are applied transverse to the direction of flame propagation. These would be adequate in models of Hele-Shaw cells anyway.
4. The long-wavelength structure is superimposed by a small-wavelength cellular pattern, consistent with our highest-resolved simulations.

Thus, although a quantitative comparison is not possible, we conclude that our numerical model reflects at least the phenomenology of flame propagation in nature to a reasonable degree.

6.3. Implications for SN Ia models

As stated above, our study corroborates the assumption of flame stability at unresolved scales in large-scale SN Ia explosion models. This is an important contribution that our small-scale model makes to the credibility of those simulations. At least at fuel densities above $\rho_u \approx 2.5 \times 10^7 \text{ g cm}^{-3}$ no deviations from burning in the flamelet regime can be expected from our result. The slight amplification of the turbulent velocity fluctuations across the flame at $\rho_u = 2.5 \times 10^7 \text{ g cm}^{-3}$ (and possibly even more pronounced below that value) may have no significant impact on the current SN Ia models, since the flame width at those densities will become non-negligible anymore (cf. the data given by [Timmes & Woosley 1992](#)). Then the burning is expected to enter the distributed regime of turbulent combustion, which requires completely different numerical approaches. In case of SN Ia explosions, an approach to study this regime was discussed by [Lisewski et al. \(2000b\)](#).

Although the increase in effective flame propagation resulting from the cellular regime will be negligible compared to the increase in flame speed at larger scales where the flame is affected by the turbulent cascade, it may be significant in the early stages of the explosion. In the current large-scale models, the flame is assumed to propagate with its laminar flame velocity before the rising RT bubbles establish the turbulent cascade. This may cause a problem with the nucleosynthetic yields from the SN Ia explosion ([Reinecke 2001](#)). Since the laminar flame speed is very low, the WD expands slowly in the beginning of the explosion and thus the combustion products remain at rather high densities for a considerable time. This effect leads to a neutronization of the material by electron capture and an overproduction of neutron-rich heavy nuclei ([Nomoto & Kondo 1991](#), [Brachwitz et al. 2000](#)), eventually even leading to a collapse of the star. Taking into account the velocity increase resulting from the cellular regime, this problem could be extenuated. As has been shown in this study, this may be in particular the case if strong velocity fluctuations left over from the pre-ignition convection interact with the flame. However, the strength of turbulence resulting from pre-ignition effects is not well-determined yet. [Höflich & Stein \(2002\)](#) claim surprisingly high values of $\sim 10^7 \text{ cm s}^{-3}$.

In the current SN Ia models by [Reinecke et al. \(2002b\)](#), the effective flame propagation velocity is determined as the maximum of the value derived from a subgrid model and the

6. Epilogue

laminar burning velocity according to equation (2.73). Our study suggests that the lower cutoff value corresponding to s_l may underestimate the actual propagation velocity taking into account the effects in the cellular mode of flame propagation. We therefore propose a higher cutoff value for the flame speed corresponding to the velocity of the cellular flame at the Gibson scale.

6.4. Future work

Directions for further work resulting from our study concern on the one hand the numerical scheme applied here and on the other hand the physical effects.

Throughout this work, we restricted our study of the flame evolution to two dimensions only. This was mainly due to the fact that extending our numerical scheme to three dimensions is highly non-trivial. The in-cell reconstruction is based on the assumption that the position flame front inside a computational cell can be linearly interpolated from intersections of the zero level set of the G -function with the cell interfaces. Already in two dimensions this caused a topological uncertainty (see Section 4.5.1). In three dimensions one would have to deal with a much higher number of ambiguous geometries. One can even easily imagine situations, where the intersections of the flame with the cell interfaces do not span a plane. However, a three-dimensional study of the cellular flame stabilization would be desirable. Furthermore, the sensitivity of the reconstruction to deviations in the unburnt volume fraction of the mixed cell (cf. Section 5.2) hampers the application of the scheme to large-scale SN Ia models. Nevertheless, since the “complete implementation of the level-set method provides a more accurate flame description, it would be worth trying to implement this scheme in large scale SN Ia models (at least in a two-dimensional version).

The nonlinear flame evolution investigated in this work is partly determined by the setup in an on average planar flame shape. It would be interesting to study the flame propagation in case of circularly expanding geometries, since these are expected to reveal cell-splitting and consequent fractalization of the flame fronts in contrast to the cell merging observed in our simulations. Moreover, there exists rich literature on this problem (e.g. Blinnikov & Sasorov 1996, Filyand et al. 1994). All studies so far employed the Sivashinsky equation or its descendants. A comparison of hydrodynamical simulations to those results has the potential to reveal interesting nonlinear physics.

A further field for investigation is the nucleosynthetic yield of large-scale supernova models when an initial flame propagation velocity higher than the laminar value is prescribed. According to our study, this new value depends on the velocity fluctuations present in the WD matter at the ignition time. The strength of those, however, needs further investigation. A possible result from the proposed study could be the attenuation of the problem of neutronization of the burning products in the early stages of the SN Ia explosion.

Finally, the question on the possibility of a deflagration to detonation transition is still open. Although recent three dimensional large scale deflagration models (Reinecke et al. 2002b, Gamezo et al. 2003) suggest, that this transition may not be necessary for the ex-

plosion energetics, still nucleosynthetic arguments favor a delayed detonation. It would provide a way to burn the fuel that is still left in the center of the exploding star because of the fingers of fresh material sinking in between the rising RT bubbles. This unburnt material may ultimately be in conflict with spectra from observations². Although we did not find an effect that could account for this transition in the scale space under consideration, the possibility of active turbulent combustion cannot be completely ruled out by our numerical experiments. Another approach would be to look for a mechanism to trigger the transition at even lower fuel densities when burning proceeds in the distributed regime. However, [Lisewski et al. \(2000a\)](#) concluded that this turbulent burning regime is unlikely to establish the conditions required for a deflagration to detonation transition.

Currently, the observation of Type Ia supernovae is a very active field of astronomy, providing observational constraints of increasing accuracy. Together with the cosmological relevance of these astrophysical events, this makes the theoretical and numerical modeling of Type Ia supernovae an exceptional fascinating and absorbing subject of astrophysical research.

²This is speculative since the corresponding observations are still missing and a nucleosynthetic evaluation of the SN Ia models is not yet complete. However, both issues are currently being tackled.

A. Derivation of the Sivashinsky equation for a hydrodynamical model of the flame

We shall now briefly repeat the main ideas included in the derivation of the Sivashinsky equation (2.119), following the simplified case presented by Sivashinsky & Calvin (1987). This approach focuses on the description of the hydrodynamic instability and neglects diffusional and thermal effects. The perturbed flame front is parametrized by

$$x = \phi(y, t). \quad (\text{A.1})$$

Assuming the flame propagation velocity relative to the burnt material to be constant yields the condition

$$\mathbf{v}_+ \cdot \mathbf{n} - D = 1 \quad (\text{A.2})$$

at $x = \phi(y, t)$, where

$$\mathbf{n} = \frac{(1, -\phi_y)}{\sqrt{1 + \phi_y^2}}, \quad (\text{A.3})$$

$$D = \frac{\phi_t}{\sqrt{1 + \phi_y^2}}, \quad (\text{A.4})$$

$$(\text{A.5})$$

and the subscript '+' denotes quantity in the burnt material, while a '-' will refer to the unburnt values in the following. The subscripts y and t stand for the corresponding partial derivatives. Describing the flame as a surface of density discontinuity and modeling the fluid as incompressible and non-viscous yields the following form of the Euler equations for the hydrodynamic development of the system in two spatial dimensions:

$$\frac{\partial \mathbf{v}_\pm}{\partial t} + (\mathbf{v}_\pm \cdot \nabla) \mathbf{v}_\pm = -\frac{1}{\rho} \nabla p_\pm, \quad \nabla \cdot \mathbf{v}_\pm = 0, \quad \mathbf{v}_\pm = (u_\pm, v_\pm). \quad (\text{A.6})$$

A convenient choice of reference values gives the density on both sides of the front in the nondimensional form

$$\rho_+ = 1, \quad \rho_- = (1 - \gamma)^{-1}. \quad (\text{A.7})$$

Continuity of mass and momentum flow across the flame front now reads

$$\rho_+(\mathbf{v}_+ \cdot \mathbf{n} - D) = \rho_-(\mathbf{v}_- \cdot \mathbf{n} - D), \quad (\text{A.8})$$

$$\rho_+(\mathbf{v}_+ - D\mathbf{n})(\mathbf{v}_+ \cdot \mathbf{n} - D) + p_+\mathbf{n} = \rho_-(\mathbf{v}_- - D\mathbf{n})(\mathbf{v}_- \cdot \mathbf{n} - D) + p_-\mathbf{n}, \quad (\text{A.9})$$

A. Derivation of the Sivashinsky equation for a hydrodynamical model of the flame

respectively, which can be rewritten using (A.2) giving

$$\mathbf{v}_+ \cdot \mathbf{n} = \gamma + \mathbf{v}_- \cdot \mathbf{n}, \quad (\text{A.10})$$

$$\mathbf{v}_+ \cdot \mathbf{t} = \mathbf{v}_- \cdot \mathbf{t}, \quad (\mathbf{t} \cdot \mathbf{n} = 0), \quad (\text{A.11})$$

$$p_+ = -\gamma + p_-. \quad (\text{A.12})$$

The basic solution of the system (A.2), (A.6), (A.8), and (A.9) corresponding to a plane flame ($\phi = 0$) is given as

$$u_+^{(b)} = 1, \quad v_+^{(b)} = 0, \quad p_+^{(b)} = 1 \quad \text{for } x > 0; \quad (\text{A.13})$$

$$u_-^{(b)} = 1 - \gamma, \quad v_-^{(b)} = 0, \quad p_-^{(b)} = 1 + \gamma \quad \text{for } x < 0. \quad (\text{A.14})$$

This model does not contain a characteristic length scale and therefore the coordinates x and y can be assumed to be of the order of unity. Under the assumption $\gamma \ll 1$ Sivashinsky (1977) estimates the following states for the perturbed flame based on a linearized stability analysis:

$$\phi \sim \gamma; \quad u_{\pm} - u_{\pm}^{(b)} \sim \gamma^2; \quad v_{\pm} - v_{\pm}^{(b)} \sim \gamma^2; \quad p_{\pm} - p_{\pm}^{(b)} \sim \gamma^2; \quad x, y \sim 1; \quad t \sim \gamma^{-1}. \quad (\text{A.15})$$

This leads to the introduction of scaled variables:

$$\begin{aligned} u_+ &= 1 + \gamma^2 U_+; & v_+ &= \gamma^2 V_+; & p_+ &= 1 + \gamma^2 P_+; \\ u_- &= 1 - \gamma + \gamma^2 U_-; & v_- &= \gamma^2 V_-; & p_- &= 1 + \gamma + \gamma^2 P_-; \end{aligned} \quad \phi = \gamma \Phi; \quad \gamma t = \tau, \quad (\text{A.16})$$

which, together with the transformation to curvilinear coordinates ξ, η attached to the front

$$\xi = x - \gamma \Phi(y, \tau), \quad \eta = y \quad (\text{A.17})$$

lead to the following form of (A.6):

$$\frac{\partial U_{\pm}}{\partial \xi} + \frac{\partial P_{\pm}}{\partial \xi} = -\gamma \frac{\partial U_{\pm}}{\partial \tau} + O(\gamma^2), \quad (\text{A.18})$$

$$\frac{\partial V_{\pm}}{\partial \xi} + \frac{\partial P_{\pm}}{\partial \eta} = -\gamma \frac{\partial V_{\pm}}{\partial \tau} + \gamma \Phi_{\eta} \frac{\partial P_{\pm}}{\partial \xi} + O(\gamma^2), \quad (\text{A.19})$$

$$\frac{\partial U_{\pm}}{\partial \xi} + \frac{\partial V_{\pm}}{\partial \eta} = \gamma \Phi_{\eta} \frac{\partial V_{\pm}}{\partial \xi}. \quad (\text{A.20})$$

Conditions (A.10), (A.11), (A.12), and (A.2) become

$$U_+ - U_- = -\frac{1}{2} \gamma \Phi_{\eta}^2 + O(\gamma^2), \quad (\text{A.21})$$

$$V_+ - V_- = -\Phi_{\eta} + O(\gamma^2), \quad (\text{A.22})$$

$$P_+ - P_- = 0, \quad (\text{A.23})$$

$$\Phi_{\tau} + \frac{1}{2} \Phi_{\eta}^2 = U_+ - \gamma V_+ \Phi_{\eta} + O(\gamma^2). \quad (\text{A.24})$$

As an ansatz for the solution of system (A.18)–(A.24) the asymptotic expansion

$$\Phi = \Phi^{(0)} + \gamma\Phi^{(1)} + \dots \quad (\text{A.25})$$

$$U_{\pm} = U_{\pm}^{(0)} + \gamma U_{\pm}^{(1)} + \dots \quad (\text{A.26})$$

$$V_{\pm} = V_{\pm}^{(0)} + \gamma V_{\pm}^{(1)} + \dots \quad (\text{A.27})$$

$$P_{\pm} = P_{\pm}^{(0)} + \gamma P_{\pm}^{(1)} + \dots \quad (\text{A.28})$$

is chosen, which in the first approximation yields

$$\frac{\partial U_{\pm}^{(0)}}{\partial \xi} + \frac{\partial P_{\pm}^{(0)}}{\partial \xi} = 0, \quad (\text{A.29})$$

$$\frac{\partial V_{\pm}^{(0)}}{\partial \xi} + \frac{\partial P_{\pm}^{(0)}}{\partial \eta} = 0, \quad (\text{A.30})$$

$$\frac{\partial U_{\pm}^{(0)}}{\partial \xi} + \frac{\partial V_{\pm}^{(0)}}{\partial \eta} = 0, \quad (\text{A.31})$$

$$U_{+}^{(0)} - U_{-}^{(0)} = 0, \quad (\text{A.32})$$

$$V_{+}^{(0)} - V_{-}^{(0)} = -\Phi_{\eta}^{(0)}, \quad (\text{A.33})$$

$$P_{+}^{(0)} - P_{-}^{(0)} = 0, \quad (\text{A.34})$$

$$\Phi_{\tau}^{(0)} + \frac{1}{2}(\Phi_{\eta}^{(0)}) = U_{+}^{(0)}. \quad (\text{A.35})$$

The solution of (A.29)–(A.31) can be written as

$$\begin{aligned} U_{\pm}^{(0)} &= \frac{\partial \Pi_{\pm}^{(0)}}{\partial \xi} + R_{\pm}^{(0)}(\eta, \tau) \\ V_{\pm}^{(0)} &= \frac{\partial \Pi_{\pm}^{(0)}}{\partial \eta} \\ P_{\pm}^{(0)} &= \frac{\partial \Pi_{\pm}^{(0)}}{\partial \xi}, \end{aligned} \quad (\text{A.36})$$

where the potential $\Pi_{\pm}^{(0)}$ is a solution of the Laplace equation

$$\frac{\partial^2 \Pi_{\pm}^{(0)}}{\partial \xi^2} + \frac{\partial^2 \Pi_{\pm}^{(0)}}{\partial \eta^2} = 0 \quad (\text{A.37})$$

in the form

$$\Pi_{\pm}^{(0)} = \frac{1}{2\pi} \iint Q_{\pm}^{(0)}(\eta', \tau) e^{ik(\eta - \eta') \mp |k|\xi} dk d\eta'. \quad (\text{A.38})$$

The function $R_{\pm}^{(0)}$ is related to the flow vorticity:

$$\frac{\partial U_{\pm}^{(0)}}{\partial \eta} - \frac{\partial V_{\pm}^{(0)}}{\partial \xi} = \frac{\partial R_{\pm}^{(0)}}{\partial \eta}. \quad (\text{A.39})$$

A. Derivation of the Sivashinsky equation for a hydrodynamical model of the flame

Assuming the flow ahead of the flame to be irrotational yields

$$R_-^{(0)} = 0. \quad (\text{A.40})$$

Now, (A.36) and (A.40) can be inserted into (A.32)–(A.34) giving

$$R_+^{(0)} = 0, \quad Q_+^{(0)} = -\frac{1}{2}\Phi^{(0)}, \quad Q_-^{(0)} = \frac{1}{2}\Phi^{(0)}. \quad (\text{A.41})$$

Hence,

$$U_{\pm}^{(0)} = \pm \frac{1}{2}I\{\Phi^{(0)}\}, \quad I\{\Phi^{(0)}\} = \frac{1}{4\pi} \iint |k|\Phi^{(0)}(\eta', \tau)e^{ik(\eta-\eta') \mp |k|\xi} dk d\eta', \quad (\text{A.42})$$

which is inserted into (A.35) giving

$$\Phi_{\tau}^{(0)} + \frac{1}{2}(\Phi_{\eta}^{(0)})^2 = \frac{1}{2}I\{\Phi^{(0)}\}. \quad (\text{A.43})$$

Returning to the original variables this yields

$$\phi_t + \frac{1}{2}\phi_y^2 = \frac{\gamma}{2}I\{\phi\}, \quad (\text{A.44})$$

which is a simplified version of the original Sivashinsky equation, here derived from a purely hydrodynamic model of flame propagation. $I\{\cdot\}$ represents a linear singular nonlocal operator defined by (A.42), which is responsible for the LD instability.

Sivashinsky & Calvin (1987) continue with the derivation of the second approximation which, however, leaves the qualitative picture of flame front dynamics unchanged. The equation resulting from the second approximation yields a dispersion relation consistent with the result from Landau's stability analysis (2.86).

B. Vectors of the general reactive flow equation

The vectors used in equation (4.1) on page 64 read

$$\mathbf{U} = \begin{pmatrix} \rho \\ \rho v_x \\ \rho v_y \\ \rho v_z \\ \rho X_i \\ \rho e_{\text{tot}} \end{pmatrix} \quad \mathbf{I} = \begin{pmatrix} \rho v_x \\ \rho v_x^2 + p \\ \rho v_y v_x \\ \rho v_z v_x \\ \rho X_i v_x \\ (\rho e_{\text{tot}} + p)v_x \end{pmatrix} \quad \mathbf{J} = \begin{pmatrix} \rho v_y \\ \rho v_x v_y \\ \rho v_y^2 + p \\ \rho v_z v_y \\ \rho X_i v_y \\ (\rho e_{\text{tot}} + p)v_y \end{pmatrix}$$

$$\mathbf{K} = \begin{pmatrix} \rho v_z \\ \rho v_x v_z \\ \rho v_y v_z \\ \rho v_z^2 + p \\ \rho X_i v_z \\ (\rho e_{\text{tot}} + p)v_z \end{pmatrix} \quad \mathbf{L} = \begin{pmatrix} 0 \\ \tau_{xx} \\ \tau_{xy} \\ \tau_{xz} \\ \rho v_{i,x}^D X_i \\ \tau_{xx}v_x + \tau_{yx}v_y + \tau_{zx}v_z + q_x \end{pmatrix}$$

$$\mathbf{M} = \begin{pmatrix} 0 \\ \tau_{yx} \\ \tau_{yy} \\ \tau_{yz} \\ \rho v_{i,y}^D X_i \\ \tau_{xy}v_x + \tau_{yy}v_y + \tau_{zy}v_z + q_y \end{pmatrix} \quad \mathbf{N} = \begin{pmatrix} 0 \\ \tau_{zx} \\ \tau_{zy} \\ \tau_{zz} \\ \rho v_{i,z}^D X_i \\ \tau_{xz}v_x + \tau_{yz}v_y + \tau_{zz}v_z + q_z \end{pmatrix}$$

$$\mathbf{Q} = \begin{pmatrix} 0 \\ 0 \\ 0 \\ 0 \\ \rho \omega_{X_i} \\ \rho S \end{pmatrix}$$

C. Nomenclature

The following list of notations is not complete and contains only identifiers that are most important to the work or frequently used in it. The symbols follow as much as possible the general conventions. Auxiliary variables are defined in the text and will not be included. Multiple use of identifiers could not always be avoided, but in those cases the meaning should be clear from the context. The similarity numbers are defined in Table 2.1 on page 21.

Greek

Δx	cell size
Π	pressure tensor
Φ	gravitational potential
α	volume fraction containing unburnt material
β	Zel'dovich number; interface fraction
ζ	scalar vorticity
ζ	vorticity
κ	bulk viscosity; curvature
κ_{cond}	conductive opacity
κ_{rad}	radiative opacity
λ	wavelength
λ_i	interaction rate
μ	density contrast ρ_u/ρ_b over the flame; shear viscosity
ρ	(mass) density
σ	thermal conductivity; standard deviation
σ_{SB}	Stefan-Boltzmann constant
τ	viscous stress tensor
ϕ	flame front
ω	growth rate
ω_{X_i}	reaction rate of species i

C. Nomenclature

Uppercase Latin

A	flame surface
A_i	atomic mass of species i
D_{ik}	binary diffusion coefficient
E_A	activation energy
E_F	Fermi energy
F, \mathcal{F}	Fermi integrals
G	level set function
\mathcal{G}	gravitational constant
L	integral scale of turbulence
M_{Ch}	Chandrasekhar mass
\mathcal{R}	universal gas constant
ρS	energy source term due to reaction
T	temperature
V	volume; specific volume
X_i	mass fraction of species i
Y_i	specific abundance

Lowercase Latin

a_i^n	discretized value (cell i , time t_n)
c_p	specific heat at constant pressure
c_s	sound speed
e_{int}	specific internal energy
e_{tot}	specific total energy
f	specific external force
g	gravitational acceleration
h	specific enthalpy
\mathbf{j}	flux density vector
k	wavenumber
k_B	Boltzmann's constant
l	length scale
l_f	flame width
\mathbf{n}	normal vector
n_i	number density of species i
p	pressure
\mathbf{q}	heat flux vector
s_l	laminar burning velocity
t	time
\mathbf{v}	velocity
v'	velocity fluctuation
\mathbf{v}_i^D	diffusion velocity of species i
\mathbf{x}	position
\hat{x}	amplitude

Indices

☉	solar
*	nondimensional quantity
Gibs	Gibson
K	Kolmogorov
KH	Kelvin-Helmholtz
LD	Landau-Darrieus
M	Markstein
RT	Rayleigh-Taylor
<i>b</i>	post-front (burnt) state
eff	effective
ref	(dimensional) reference value
<i>u</i>	pre-front (unburnt) state

Following abbreviations were used frequently in the text:

Abbreviations

ATC	active turbulent combustion
DDT	deflagration to detonation transition
KH	Kelvin-Helmholtz
LD	Landau-Darrieus
RT	Raleigh-Taylor
SN(e) Ia	Type Ia supernova(e)
WD	white dwarf

Bibliography

- Abid, M., Aung, K., Ronney, P. D., Sharif, J., Wu, M.-S. (1999): Studies of premixed laminar and turbulent flames at microgravity (NASA grant no. NAG3-2124), in *Fifth International Microgravity Combustion Workshop*, National Center for Microgravity Research, Cleveland, Ohio. (available online: <http://www.ncmr.org/events/combustion1999/proceedings.html>)
- Arnett, D., Livne, E. (1994a): The delayed-detonation model of a Type Ia supernovae. 1: The deflagration phase, *Astrophys. J.* **427**, 315–329
- Arnett, D., Livne, E. (1994b): The delayed-detonation model of Type Ia supernovae. 2: The detonation phase, *Astrophys. J.* **427**, 330–341
- Arnett, W. D. (1969): A possible model of supernovae: Detonation of ^{12}C , *Astrophys. Space Sci.* **5**, 180–212
- Arnett, W. D. (1982): Type I supernovae. I—Analytic solutions for the early part of the light curve, *Astrophys. J.* **253**, 785–797
- Arnett, W. D., Branch, D., Wheeler, J. C. (1985): Hubble’s constant and exploding carbon-oxygen white dwarf models for Type I supernovae, *Nature* **314**, 337–338
- Audi, G., Wapstra, A. H. (1995): The 1995 update to the atomic mass evaluation, *Nucl. Phys. A* **595**(4), 409–480
- Baade, W., Zwicky, F. (1934): Remarks on super-novae and cosmic rays, *Phys. Rev.* **46**, 76–77
- Balberg, S., Shapiro, S. L. (2000): The properties of matter in white dwarfs and neutron stars, in *Handbook of Elastic Properties of Solids, Liquids, and Gases*, edited by M. Levy, H. Bass, R. Stern, Academic Press, volume 4, chapter 15. (preprint available: astro-ph/0004317)
- Barenblatt, G. I., Zel’dovich, Y. B., Istratov, A. G. (1962): On the diffusional-thermal stability of a laminar flame, *Zh. Prikl. Mekh. Tekh. Fiz.* **4**, 21–26
- Benz, W. (1997): Three-dimensional simulations of core ignition in sub-Chandrasekhar mass models, in *Thermonuclear Supernovae*, edited by P. Ruiz-Lapuente, R. Canal, J. Isern, Kluwer Academic Publishers, Dordrecht, pp. 457–474

Bibliography

- Benz, W., Cameron, A. G. W., Press, W. H., Bowers, R. L. (1990): Dynamic mass exchange in doubly degenerate binaries. I—0.9 and 1.2 solar mass stars, *Astrophys. J* **348**, 647–667
- Blinnikov, S. I., Khokhlov, A. M. (1986): Development of detonations in degenerate stars, *Soviet Astronomy Letters* **12**, 131–134
- Blinnikov, S. I., Sasorov, P. V. (1996): Landau-Darrieus instability and the fractal dimension of flame fronts, *Phys. Rev. E* **53**(5), 4827–4841
- Bolgiano, R. (1959): Turbulent spectra in a stably stratified atmosphere, *J. Geophys. Res.* **64**(12), 2226–2229
- Borghi, R. W. (1985): On the structure and morphology of turbulent premixed flames, in *Recent advances in the aerospace sciences*, edited by C. Casci, Plenum Publishing Corporation, New York, chapter 7, pp. 117–138
- Boury, G., Joulin, G. (2002): Nonlinear response of premixed-flame fronts to localized random forcing in the presence of a strong tangential blowing, *Combust. Theory Modelling* **6**, 243–261
- Brachwitz, F., Dean, D. J., Hix, W. R., Iwamoto, K., Langanke, K., Martínez-Pinedo, G., Nomoto, K., Strayer, M. R., Thielemann, F., Umeda, H. (2000): The role of electron captures in Chandrasekhar-mass models for Type Ia supernovae, *Astrophys. J.* **536**, 934–947
- Brahe, T. (1573): *De nova et nullius aevi memoria prius visa stella, iam pridem á nato Christo 1572, mense Novembri primum conspecta, contemplatio mathematica*, Copenhagen
- Branch, D. (1998): Type Ia supernovae and the Hubble constant, *Annu. Rev. Astron. Astrophys.* **36**, 17–56
- Branch, D., Fisher, A., Nugent, P. (1993): On the relative frequencies of spectroscopically normal and peculiar Type Ia supernovae, *Astron. J.* **106**, 2383–2391
- Bychkov, V., Liberman, M. A. (1995): Hydrodynamic instabilities of the flame front in white dwarfs, *Astron. Astrophys.* **302**, 727–734
- Cappellaro, E., Turatto, M., Tsvetkov, D. Y., Bartunov, O. S., Pollas, C., Evans, R., Hamuy, M. (1997): The rate of supernovae from the combined sample of five searches, *Astron. Astrophys.* **322**, 431–441
- Caughlan, G. R., Fowler, W. A. (1988): Thermonuclear reaction rates V, *Atomic Data and Nuclear Data Tables* **40**, 283–334
- Chandrasekhar, S. (1961): *Hydrodynamic and Hydromagnetic Stability*, Clarendon Press, Oxford

- Chapman, S., Cowling, T. G. (1960): *The Mathematical Theory of Non-uniform Gases*, Cambridge University Press, Cambridge
- Colella, P., Glaz, H. M. (1985): Efficient solution algorithms for the Riemann problem for real gases, *J. Comp. Phys.* **59**, 264–289
- Colella, P., Woodward, P. R. (1984): The piecewise parabolic method (PPM) for gas-dynamical simulations, *J. Comp. Phys.* **54**, 174–201
- Colgate, S. A., McKee, C. (1969): Early supernova luminosity, *Astrophys. J.* **157**, 623–643
- Contardo, G., Leibundgut, B., Vacca, W. D. (2000): Epochs of maximum light and bolometric light curves of Type Ia supernovae, *Astron. Astrophys.* **359**, 876–886
- Courant, R., Friedrichs, K. O., Lewy, H. (1928): Über die partiellen Differentialgleichungen der mathematischen Physik, *Math. Ann.* **100**, 32–74
- Cox, J. P., Giuli, R. T. (1968): *Principles of Stellar Structure*, volume 2, Gordon and Breach, New York
- Damköhler, G. (1940): Der Einfluß der Turbulenz auf die Flammgeschwindigkeit in Gasgemischen, *Z. f. Elektroch.* **46**(11), 601–652
- Darrieus, G. (1938): Propagation d'un front de flamme. Communication presented at *La Technique Moderne*, Unpublished.
- Diehl, R., Timmes, F. X. (1998): Gamma-ray line emission from radioactive isotopes in stars and galaxies, *Publ. Astron. Soc. Pac.* **110**, 637–659
- Döring, W. (1943): On detonation processes in gases, *Ann. Physik* **43**, 421–436
- Drell, P. S., Loredó, T. J., Wasserman, I. (2000): Type Ia supernovae, evolution, and the cosmological constant, *Astrophys. J.* **530**, 593–617
- Dursi, J. Zingale, M., Calder, A. C., Fryxell, B., Timmes, F. X., Vladimirova, N., Rosner, R., Caceres, A., Lamb, D. Q., Olson, K., Ricker, P. M., K., R., A., S., Truran, J. W. (2003): The response of model and astrophysical thermonuclear flames to curvature and stretch, *Astrophys. J.* (in press) Preprint available: astro-ph/0306176
- Filippenko, A. V. (1997): Optical spectra of supernovae, *Annu. Rev. Astron. Astrophys.* **35**, 309–355
- Filyand, L., Sivashinsky, G. I., Frankel, M. L. (1994): On self-acceleration of outward propagating wrinkled flames, *Physica D* **72**, 110–118
- Frankel, M. L. (1990): An equation of surface dynamics modeling flame fronts as density discontinuities in potential flows, *Phys. Fluids A* **2**, 1879–1883

Bibliography

- Fryxell, B., Olson, K., Ricker, P., Timmes, F. X., Zingale, M., Lamb, D. Q., MacNeice, P., Rosner, R., Truran, J. W., Tufo, H. (2000): FLASH: An adaptive mesh hydrodynamics code for modeling astrophysical thermonuclear flashes, *Astrophys. J. Suppl.* **131**, 273–334
- Fryxell, B. A., Müller, E., Arnett, W. D. (1989): *Hydrodynamics and nuclear burning*, MPA Green Report 449, Max-Planck-Institut für Astrophysik, Garching
- Gamezo, V. N., Khokhlov, A. M., Oran, E. S., Chtchelkanova, A. Y., Rosenberg, R. O. (2003): Thermonuclear supernovae: Simulations of the deflagration stage and their implications, *Science* **299**, 77–81
- Garcia-Senz, D., Woosley, S. E. (1995): Type Ia supernovae: The flame is born, *Astrophys. J.* **454**, 895–900
- Godunov, S. K. (1959): Finite difference method for numerical computation of discontinuous solution of the equations of fluid dynamics, *Matematicheskii Sbornik* **47**, 271
- Green, D. A., Stephenson, F. R. (2003): Historical supernovae, in *Supernovae and Gamma-Ray Bursters*, edited by K. W. Weiler, Springer-Verlag, Berlin Heidelberg New York, volume 598 of *LNP*, pp. 7–20. (preprint available: astro-ph/0301603)
- Gröbl, A. (1999): *Simulation von Flammenfronten in Wasserstoff-Luft-Gemischen*, Diplomarbeit, Technische Universität München
- Gutman, S., Sivashinsky, G. I. (1990): The cellular nature of hydrodynamic flame instability, *Physica D* **43**, 129–139
- Hamuy, M., Phillips, M. M., Suntzeff, N. B., Schommer, R. A., Maza, J., Aviles, R. (1996): The absolute luminosities of the Calan/Tololo Type Ia supernovae, *Astron. J.* **112**, 2391–2397
- Hansen, C. J., Kawaler, S. D. (1994): *Stellar Interiors: Physical Principles, Structure, and Evolution*, Astronomy and Astrophysics Library, Springer-Verlag, New York
- Harkness, R. P., Wheeler, J. C. (1990): Classification of supernovae, in *Supernovae*, edited by A. G. Petschek, Springer-Verlag, New York, pp. 1–29
- Helenbrook, B. T., Law, C. K. (1999): The role of Landau-Darrieus instability in large scale flows, *Combustion and Flame* **117**, 155–169
- Hillebrandt, W., Niemeyer, J. C. (2000): Type Ia supernova explosion models, *Annu. Rev. Astron. Astrophys.* **38**, 191–230
- Hillebrandt, W., Niemeyer, J. C., Reinecke, M., Röpke, F., Travaglio, C. (2003): Multidimensional simulations of Type Ia supernova explosions and nucleosynthesis, *Nucl. Phys. A* **718**, 229c–238c

- Höflich, P., Khokhlov, A. (1996): Explosion models for Type Ia supernovae: A comparison with observed light curves, distances, h_0 , and q_0 , *Astrophys. J.* **457**, 500–528
- Höflich, P., Stein, J. (2002): On the thermonuclear runaway in Type Ia supernovae: How to run away?, *Astrophys. J.* **568**, 779–790
- Hoyle, F., Fowler, W. A. (1960): Nucleosynthesis in supernovae, *Astrophys. J.* **132**, 565–590
- Iben, I., Tutukov, A. V. (1984): Supernovae of type I as end products of the evolution of binaries with components of moderate initial mass (m not greater than about 9 solar masses), *Astrophys. J. Suppl.* **54**, 335–372
- Ivanova, L. N., Imshennik, V. S., Chechetkin, V. M. (1974): Pulsation regime of the thermonuclear explosion of a star's dense carbon core, *Astrophys. Space Sci.* **31**, 497–514
- Iwamoto, K., Brachwitz, F., Nomoto, K., Kishimoto, N., Umeda, H., Hix, W. R., Thielemann, F. (1999): Nucleosynthesis in Chandrasekhar mass models for Type Ia supernovae and constraints on progenitor systems and burning-front propagation, *Astrophys. J. Suppl.* **125**, 439–462
- Joulin, G. (1989): On the hydrodynamic stability of curved premixed flames, *J. Phys. France* **50**, 1069–1082
- Joulin, G. (1994): Nonlinear hydrodynamic instability of expanding flames: Intrinsic dynamics, *Phys. Rev. E* **50**, 2030–2047
- Kasen, D., Nugent, P., Wang, L., Howell, D. A., Wheeler, J. C., Höflich, P., Baade, D., Baron, E., Hauschildt, P. H. (2003): Analysis of the flux and polarization spectra of the Type Ia supernova SN 2001el: Exploring the geometry of the high-velocity ejecta, *Astrophys. J.* (in press) Preprint available: astro-ph/0301312
- Kerstein, A. R. (1996): Scaling properties of the burning velocity in freely propagating turbulent premixed flames, *Combust. Sci. Technol.* **118**, 189–201
- Khokhlov, A. (1993): Flame modeling in supernovae, *Astrophys. J. Lett* **419**, L77–L80
- Khokhlov, A. M. (1991): Delayed detonation model for Type Ia supernovae, *Astron. Astrophys.* **245**, 114–128
- Khokhlov, A. M. (1995): Propagation of turbulent flames in supernovae, *Astrophys. J.* **449**, 695–713
- Khokhlov, A. M., Oran, E. S., Wheeler, J. C. (1997): Deflagration-to-Detonation Transition in Thermonuclear Supernovae, *Astrophys. J.* **478**, 678–688
- Kluge, G., Neugebauer, G. (1994): *Grundlagen der Thermodynamik*, Spektrum Akademischer Verlag, Heidelberg Berlin Oxford. (in German)

Bibliography

- Kolmogorov, A. N. (1941): The local structure of turbulence in incompressible viscous fluid for very large reynolds numbers, *Dokl. Akad. Nauk SSSR* **30**, 299–303. In Russian
- Kupervasser, O., Olami, Z., Procaccia, I. (1996): Geometry of developing flame fronts: Analysis with pole decomposition, *Phys. Rev. Lett.* **76**(1), 146–149
- Landau, L. D. (1944): On the theory of slow combustion, *Acta Physicochim. URSS* **19**, 77–85
- Landau, L. D., Lifshitz, E. M. (1959): *Fluid Mechanics*, volume 6 of *Course of Theoretical Physics*, Pergamon Press, Oxford
- Leibundgut, B. (2000): Type Ia supernovae, *Astron. Astrophys. Rev.* **10**, 179–209
- Leibundgut, B. (2001): Cosmological implications from observations of Type Ia supernovae, *Annu. Rev. Astron. Astrophys.* **39**, 67–98
- LeVeque, R. J. (1998): Nonlinear conservation laws and finite volume methods, in *Computational Methods for Astrophysical Flows*, edited by O. Steiner, A. Gautschy, Springer, Berlin Heidelberg New York, Saas-Fee Advanced Course 27, pp. 1–159
- Li, W. D., Filippenko, A. V., Riess, A. G., Treffers, R. R., Hu, J. Y., Qiu, Y. L. (2000): A high peculiarity rate for Type Ia SNe, in *Cosmic Explosions: Tenth Astrophysics Conference*, edited by S. S. Holt, W. W. Zhang, American Institute of Physics, Melville, New York, volume 522 of *AIP Conference Proceedings*, pp. 91–94
- Liñan, A., Williams, F. A. (1993): *Fundamental Aspects of Combustion*, Oxford University Press, Oxford, New York
- Lisewski, A. M., Hillebrandt, W., Woosley, S. E. (2000a): Constraints on the delayed transition to detonation in Type Ia supernovae, *Astrophys. J.* **538**, 831–836
- Lisewski, A. M., Hillebrandt, W., Woosley, S. E., Niemeyer, J. C., Kerstein, A. R. (2000b): Distributed burning in Type Ia supernovae: A statistical approach, *Astrophys. J.* **537**, 405–413
- Livio, M. (1996): Type Ia supernovae and supersoft X-ray sources, in *Supersoft X-Ray Sources*, edited by J. Greiner, Springer-Verlag, Berlin Heidelberg New York, volume 472 of *LNP*, pp. 183–191
- Livne, E., Arnett, D. (1995): Explosions of sub-Chandrasekhar mass white dwarfs in two dimensions, *Astrophys. J.* **452**, 62–74
- Mandelbrot, B. B. (1983): *The fractal geometry of nature*, W. H. Freeman, New York
- Markstein, G. H. (1951): Experimental and theoretical studies of flame-front stability, *J. Aeronaut. Sci.* **18**, 199–209

- Mikhel'son, V. A. (1889): *On the normal ignition rate of fulminating gas mixtures*, Ph.D. thesis, Univ. Moscow. See *Collected works*, Vol. 1, Novyi Agronom Press, Moscow (1930)
- Minkowski, R. (1941): Spectra of supernovae, *Publ. Astron. Soc. Pac.* **53**, 224–225
- Mochkovitch, R., et al. (1997): The merging of white dwarfs, in *Thermonuclear Supernovae*, edited by P. Ruiz-Lapuente, R. Canal, J. Isern, Kluwer Academic Publishers, Dordrecht, pp. 187–204
- Moré, J. J., Garbow, B. S., Hillstrom, K. E. (1980): *User Guide for MINPACK-1*, Argonne National Laboratory Report ANL-80-74, Argonne National Laboratory, Argonne, Ill.
- Müller, E. (1998): Simulation of astrophysical fluid flow, in *Computational Methods for Astrophysical Flows*, edited by O. Steiner, A. Gautschy, Springer, Berlin Heidelberg New York, Saas-Fee Advanced Course 27, pp. 343–494
- Nandkumar, R., Pethick, C. J. (1984): Transport coefficients of dense matter in the liquid metal regime, *MNRAS* **209**, 511–524
- Niemeyer, J. C. (1995): *On the Propagation of Thermonuclear Flames in Type Ia Supernovae*, Ph.D. thesis, Technical University of Munich. Also available as MPA Green Report 911
- Niemeyer, J. C. (1999): Can deflagration-detonation transitions occur in Type Ia supernovae?, *Astrophys. J. Lett.* **523**, L57–L60
- Niemeyer, J. C., Hillebrandt, W. (1995): Microscopic instabilities of nuclear flames in Type Ia supernovae, *Astrophys. J.* **452**, 779–784
- Niemeyer, J. C., Hillebrandt, W. (1997): Microscopic and macroscopic modeling of thermonuclear burning fronts, in *Thermonuclear Supernovae*, edited by P. Ruiz-Lapuente, R. Canal, J. Isern, Kluwer Academic Publishers, Dordrecht, pp. 441–456
- Niemeyer, J. C., Hillebrandt, W., Woosley, S. E. (1996): Off-center deflagrations in Chandrasekhar mass Type Ia supernova models, *Astrophys. J.* **471**, 903–914
- Niemeyer, J. C., Kerstein, A. R. (1997a): Burning regimes of nuclear flames in SN Ia explosions, *New Astronomy* **2**, 239–244
- Niemeyer, J. C., Kerstein, A. R. (1997b): Numerical investigation of scaling properties of turbulent premixed flames, *Combust. Sci. Technol.* **128**(1-6), 343–358
- Niemeyer, J. C., Woosley, S. E. (1997): The thermonuclear explosion of Chandrasekhar mass white dwarfs, *Astrophys. J.* **475**, 740–753
- Nomoto, K., Iben, I. (1985): Carbon ignition in a rapidly accreting degenerate dwarf—A clue to the nature of the merging process in close binaries, *Astrophys. J.* **297**, 531–537

Bibliography

- Nomoto, K., Kondo, Y. (1991): Conditions for accretion-induced collapse of white dwarfs, *Astrophys. J. Lett.* **367**, L19–L22
- Nomoto, K., Thielemann, F.-K., Yokoi, K. (1984): Accreting white dwarf models of Type I supernovae. III—Carbon deflagration supernovae, *Astrophys. J.* **286**, 644–658
- Obukhov, A. M. (1959): O vliyani arkhimedovykh sil na struktury temperaturnogo polya v turbulentnom potoke, *Dokl. Akad. Nauk SSSR* **125**(6), 1246–1248
- Osher, S., Sethian, J. A. (1988): Fronts propagating with curvature-dependent speed: Algorithms based on Hamilton-Jacobi formulations, *J. Comp. Phys.* **79**, 12–49
- Paczyński, B. (1972): Carbon ignition in degenerate stellar cores, *Astrophys. Lett.* **11**, 53–55
- Paquette, C., Pelletier, C., Fontaine, G., Michaud, G. (1986): Diffusion coefficients for stellar plasmas, *Astrophys. J. Suppl.* **61**, 177–195
- Perlmutter, S., Aldering, G., Goldhaber, G., Knop, R. A., Nugent, P., Castro, P. G., Deustua, S., Fabbro, S., Goobar, A., Groom, D. E., Hook, I. M., Kim, A. G., Kim, M. Y., Lee, J. C., Nunes, N. J., Pain, R., Pennypacker, C. R., Quimby, R., Lidman, C., Ellis, R. S., Irwin, M., McMahon, R. G., Ruiz-Lapuente, P., Walton, N., Schaefer, B., Boyle, B. J., Filippenko, A. V., Matheson, T., Fruchter, A. S., Panagia, N., Newberg, H. J. M., Couch, W. J., The Supernova Cosmology Project (1999): Measurements of Omega and Lambda from 42 high-redshift supernovae, *Astrophys. J.* **517**, 565–586
- Peters, N. (1986): Laminar flamelet concepts in turbulent combustion, in *Twenty-First Symposium (International) on Combustion*, The Combustion Institute, Pittsburgh, pp. 1231–1250
- Peters, N. (1999): The turbulent burning velocity for large-scale and small-scale turbulence, *J. Fluid Mech.* **384**, 107–132
- Pope, S. B. (2000): *Turbulent Flows*, Cambridge University Press, Cambridge
- Powell, M. J. D. (1970): A hybrid method for nonlinear algebraic equations, in *Numerical Methods for Nonlinear Algebraic Equations*, edited by P. Rabinowitz, Gordon and Breach, London, pp. 87–114
- Rahibe, M., Aubry, N., Sivashinsky, G. I., Lima, R. (1995): Formation of wrinkles in outwardly propagating flames, *Phys. Rev. E* **52**(4), 3675–3686
- Reinecke, M., Hillebrandt, W., Niemeyer, J. C. (1999a): Thermonuclear explosions of Chandrasekhar-mass C+O white dwarfs, *Astron. Astrophys.* **347**, 739–747
- Reinecke, M., Hillebrandt, W., Niemeyer, J. C. (2002a): Refined numerical models for multidimensional Type Ia supernova simulations, *Astron. Astrophys.* **386**, 936–943

- Reinecke, M., Hillebrandt, W., Niemeyer, J. C. (2002b): Three-dimensional simulations of Type Ia supernovae, *Astron. Astrophys.* **391**, 1167–1172
- Reinecke, M., Hillebrandt, W., Niemeyer, J. C., Klein, R., Gröbl, A. (1999b): A new model for deflagration fronts in reactive fluids, *Astron. Astrophys.* **347**, 724–733
- Reinecke, M., Niemeyer, J. C., Hillebrandt, W. (2002c): On the explosion mechanism of SNe Type Ia, *New Astronomy Review* **46**, 481–486
- Reinecke, M. A. (2001): *Modeling and simulation of turbulent combustion in Type Ia supernovae*, Ph.D. thesis, Technical University of Munich
- Richardson, L. F. (1922): *Weather prediction by numerical process*, Cambridge University Press, Cambridge. (republished Dover 1965)
- Riess, A. G., Filippenko, A. V., Challis, P., Clocchiatti, A., Diercks, A., Garnavich, P. M., Gilliland, R. L., Hogan, C. J., Jha, S., Kirshner, R. P., Leibundgut, B., Phillips, M. M., Reiss, D., Schmidt, B. P., Schommer, R. A., Smith, R. C., Spyromilio, J., Stubbs, C., Suntzeff, N. B., Tonry, J. (1998): Observational evidence from supernovae for an accelerating universe and a cosmological constant, *Astron. J.* **116**, 1009–1038
- Riess, A. G., Filippenko, A. V., Li, W., Treffers, R. R., Schmidt, B. P., Qiu, Y., Hu, J., Armstrong, M., Faranda, C., Thouvenot, E., Buil, C. (1999): The rise time of nearby Type Ia supernovae, *Astron. J.* **118**, 2675–2688
- Röpke, F. K., Niemeyer, J. C., Hillebrandt, W. (2003): On the small-scale stability of thermonuclear flames in Type Ia supernovae, *Astrophys. J.* **588**, 952–961
- Saio, H., Nomoto, K. (1985): Evolution of a merging pair of C+O white dwarfs to form a single neutron star, *Astron. Astrophys.* **150**, L21–L23
- Schmidt, H. (2001): *Ein numerisches Verfahren zur Verfolgung von Vormischflammen unter Berücksichtigung instationärer Frontstrukturen*, Ph.D. thesis, Gerhard-Mercator-Universität Duisburg. (in German)
- Schmidt, H., Klein, R. (2001): Private communication
- Sethian, J. A. (1996): *Level Set Methods*, Cambridge University Press, Cambridge
- Sharif, J., Abid, M., Ronney, P. D. (1999): *Premixed-gas flame propagation in Hele-Shaw cells*, Technical report, Spring Technical Meeting, joint U. S. Sections, Combustion Institute, Washington D. C.
- Shchelkin, K. I. (1940): The effect of the roughness of a tube on the development and propagation of detonation in gases, *Zh. Eksp. i Theor. Fiz.* **10**, 823
- Sivashinsky, G. I. (1977): Nonlinear analysis of hydrodynamic instability in laminar flames—I. derivation of basic equations, *Acta Astronautica* **4**, 1177–1206

Bibliography

- Sivashinsky, G. I. (1983): Instabilities, pattern formation, and turbulence in flames, *Ann. Rev. Fluid Mech.* **15**, 179–199
- Sivashinsky, G. I., Calvin, P. (1987): On the nonlinear theory of hydrodynamic instability in flames, *J. Phys. (Paris)* **48**, 193–198
- Smiljanovski, V., Moser, V., Klein, R. (1997): A capturing-tracking hybrid scheme for deflagration discontinuities, *Combustion Theory and Modelling* **1**, 183–215
- Sorokina, E., Blinnikov, S. (2003): Light curves of Type Ia supernovae as a probe for an explosion model, in *From Twilight to Highlight: The Physics of Supernovae*, edited by W. Hillebrandt, B. Leibundgut, Springer-Verlag, Berlin Heidelberg, ESO Astrophysics Symposia, pp. 268–275
- Steinmetz, M., Muller, E., Hillebrandt, W. (1992): Carbon detonations in rapidly rotating white dwarfs, *Astron. Astrophys.* **254**, 177–190
- Stephenson, F. R., Green, D. A. (2002): *Historical Supernovae and their Remnants*, Oxford University Press, Oxford
- Strang, G. (1968): On the construction and comparison of difference schemes, *Siam Journal Numerical Analysis* **5**, 506–517
- Sussman, M., Smereka, P., Osher, S. (1994): A level set approach for computing solutions to incompressible two-phase flow, *J. Comp. Phys.* **114**(1), 146–159
- Thual, O., Frisch, U., Hénon, M. (1985): Application of pole decomposition to an equation governing the dynamics of wrinkled flame fronts, *J. Phys. (Paris)* **46**, 1485–1494
- Timmes, F. X., Woosley, S. E. (1992): The conductive propagation of nuclear flames. I. degenerate c+o and o+ne+mg white dwarfs, *Astrophys. J.* **396**
- Tonry, J. L., Schmidt, B. P., Barris, B., Candia, P., Challis, P., Clocchiatti, A., Coil, A. L., Filippenko, A. V., Garnavich, P., Hogan, C., Holland, S. T., Jha, S., Kirshner, R. P., Krisciunas, K., Leibundgut, B., Li, W., Matheson, T., Phillips, M. M., Riess, A. G., Schommer, R., Smith, R. C., Sollerman, J., Spyromilio, J., Stubbs, C. W., Suntzeff, N. B. (2003): Cosmological results from high-z supernovae. (in press) Preprint available: astro-ph/0305008
- Truran, J. W., Arnett, W. D., Cameron, A. G. W. (1967): Nucleosynthesis in supernova shock waves, *Canad. J. Physics* **45**, 2315–2332
- Vladimirova, N., Constantin, P., Kiselev, A., Ruchayskiy, O., Ryzhik, L. (2003): Flame enhancement and quenching in fluid flows, *Combustion Theory and Modelling* (in press) Preprint available: physics/0212057

- von Neumann, J. (1942): *Theory of detonation waves*, Prog. Rept. No. 238; O.S.R.D. Rept. No. 549, Ballistic Research Laboratory File No. X-122, Aberdeen Proving Ground, MD
- Wang, L., Baade, D., Hoefflich, P., Khokhlov, A., Wheeler, J. C., Kasen, D., Nugent, P. E., Perlmutter, S., Fransson, C., Lundqvist, P. (2003): Spectropolarimetry of SN 2001el in NGC 1448: Asphericity of a normal Type Ia supernova, *Astrophys. J.* (in press) Preprint available: astro-ph/0303397
- Webbink, R. F. (1984): Double white dwarfs as progenitors of R Coronae Borealis stars and Type I supernovae, *Astrophys. J.* **277**, 355–360
- Wosley, S. E. (1990): Type Ia supernovae: Carbon deflagration and detonation, in *Supernovae*, edited by A. G. Petschek, Springer-Verlag, New York, pp. 182–212
- Wosley, S. E., Weaver, T. A. (1986): The physics of supernova explosions, *Annu. Rev. Astron. Astrophys.* **24**, 205–253
- Wosley, S. E., Weaver, T. A. (1994): Massive stars, supernovae, and nucleosynthesis, in *Les Houches Session LIV: Supernovae*, edited by S. Bludman, R. Mochovitch, J. Zinn-Justin, North-Holland, Amsterdam, pp. 63–154
- Zel'dovich, Y. B. (1940): On the theory of the propagation of detonations in gaseous systems, *J. Exp. Theor. Phys. USSR* **10**, 542–568
- Zel'dovich, Y. B. (1966): An effect which stabilizes the curved front of a laminar flame, *Journal of Appl. Mech. and Tech. Physics* **1**, 68–69. English translation
- Zel'dovich, Y. B., Barenblatt, G. I., Librovich, V. B., Makhviladze, G. (1980a): *The Mathematical Theory of Combustion and Explosions*, Nauka, Moscow. English translation 1985 Consultants Bureau (Plenum), New York.
- Zel'dovich, Y. B., Istratov, A. G., Kidin, N. I., Librovich, V. B. (1980b): Flame propagation in tubes: Hydrodynamics and stability, *Combust. Sci. Technol.* **24**, 1–13
- Zel'dovich, Y. B., Librovich, V. B., Makhviladze, G. M., Sivashinsky, G. I. (1970): On the development of detonation in a nonuniformly heated gas, *Astronaut. Acta* **15**, 313–321
- Zhu, J., Ronney, P. D. (1994): Simulation of front propagation at large non-dimensional flow disturbance intensities, *Combust. Sci. Technol.* **100**, 183–201

Danksagung

An dieser Stelle möchte ich mich bei meinem Betreuer Wolfgang Hillebrandt herzlich bedanken. Er hat zur Bearbeitung des Themas angeregt und durch konstante Unterstützung die vorliegende Arbeit ermöglicht. Besonders die Freude und das Engagement mit der die Astrophysik betreibt sind ein Beispiel, das mich – wie schon viele andere Studenten vor mir – für dieses Fachgebiet begeistert hat.

Jens Niemeyer danke ich dafür, daß er mir durch fachlichen Rat und freundliche Hilfe die Erschließung des Gebiets der astrophysikalischen Flammen erleichtert hat. In Diskussionen hat er oft durch Ideen neue Perspektiven eröffnet.

Die Einarbeitung in die Programmierung und die Umsetzung der numerischen Implementierung des Flammenmodells wären ohne die Unterstützung durch Martin Reinecke wohl nicht so reibungslos verlaufen. Für seinen Rat und seine exzellente Vorarbeit, auf die ich zurückgreifen konnte, gebührt ihm besonderer Dank. In der der Anfangsphase der Arbeit hat mich Anton Gröbl hilfreich unterstützt.

Bei Sergei Blinnikov möchte ich mich ganz herzlich dafür bedanken, daß er mir durch zahlreiche Hinweise und Anregungen ermöglicht hat, den Blickwinkel der wissenschaftlichen Einordnung des Themas zu erweitern. P. D. Ronney hat dankenswerterweise Ergebnisse seiner Experimente für den Vergleich mit den Modellen der vorliegenden Arbeit zur Verfügung gestellt.

Hervorzuheben ist die angenehme Atmosphäre am Max-Planck-Institut für Astrophysik in Garching, die sicherlich allen Mitarbeitern hier zu danken ist und für die ich stellvertretend Thomas Janka und Ewald Müller nennen möchte. Besonders die vielen wissenschaftlichen und allgemeinen Gespräche mit Florian, Christoph, Daniel, Wolfram, Harry, Leonhard, Tobias, Robi und vielen anderen, wie auch die Abende beim „Hydro-Kegeln“ und auf Schloß Ringberg sollen hier Erwähnung finden.

Die Bereitstellung eines „Knotens“ des IBM Regatta Systems durch das Rechenzentrum der Max-Planck-Gesellschaft in Garching hat die zahlreichen aufwendigen Simulationen ermöglicht, auf denen die vorliegende Arbeit gegründet ist.

Meinen Eltern und meinen Schwestern (samt Familie) bin ich dankbar, daß sie mich in der Zeit der Doktorarbeit unermüdlich unterstützt und auch hin und wieder für die nötige Ablenkung gesorgt haben.

Besonders bedanken möchte ich mich bei meiner Nele. Daß ich die vergangenen drei Jahre in schöner Erinnerung behalten werde, ist ihr Verdienst.

Lebenslauf

<i>Name</i>	<u>Friedrich Konrad Röpke</u>	
<i>Geburtsdatum</i>	9. Juli 1974	
<i>Geburtsort</i>	Blankenburg (Harz)	
<i>Staatsangehörigkeit</i>	deutsch	
<i>Familienstand</i>	verheiratet	
<i>Schulbildung</i>	1981–1983	17. Polytechnische Oberschule in Rostock
	1983–1989	9. Polytechnische Oberschule in Rostock
	1989–1993	Spezialschule mathematisch-naturwissenschaftlich-technischer Richtung in Rostock (ging 1990 in das Jugenddorf-Christophorus-Gymnasium Rostock über) Abitur im Mai 1993
<i>Zivildienst</i>	1993–1994	
<i>Studium</i>	1994–2000	an der Friedrich-Schiller-Universität Jena, Studienrichtung Physik/Diplom
	Sept. 1996	Abschluß des Vordiploms
	1997–1998	an der University of Virginia, Charlottesville, VA, U.S.A.
	1999–2000	Diplomarbeit am Theoretisch-Physikalischen Institut der Friedrich-Schiller-Universität Jena, Thema: „Thermodynamik rotierender Objekte in der Gravitationstheorie“
<i>Promotion</i>	seit dem 1. Juli 2000	Doktorand am Max-Planck-Institut für Astrophysik, Garching.

Garching, 19. Juni 2003